CIVIL ENGINEERING JOURNAL

číslo 2/2025

Obsah:

CIVIL ENGINEERING JOURNAL

Article no. 11

THE CIVIL ENGINEERING JOURNAL 2-2025

REBAR-CONCRETE DEBONDING EFFECT ON THE SEISMIC PERFORMANCE OF REINFORCED CONCRETE SHEAR WALLS: AN EXPERIMENTAL STUDY

Afshin Hossein Sharifzadeh[1] and Saeed Tariverdilo[2]

1. *Department of Engineering, Faculty of Civil Engineering, Salmas Branch, Islamic Azad University, Salmas, Iran*
2. *University of Urmia, Faculty of Civil Engineering, Urmia, Iran; s.tariverdilo@urmia.ac.ir*

Received: *12.08.2024*

Received in revised form: *01.01.2025*

Accepted: *22.05.2025*

ABSTRACT

Diverse criteria are taken for seismic design of shear walls due to their buckling failure in various regulations. Despite extensive studies on the topic, no practical mechanism has been widely adopted to effectively mitigate out-of-plane buckling in reinforced concrete shear walls. This study presents a novel approach to address this issue by experimentally investigating the effect of rebar-concrete debonding on the seismic performance of boundary elements in shear walls with minimum reinforcement. Plastic sleeves, applied to rebar at varying lengths (80 mm, 150 mm, and 220 mm), were used to induce debonding and thus modify the stress transfer mechanisms and crack propagation within the concrete. Five experimental samples of shear wall boundary element were designed and constructed with minimum reinforcement. Samples were subjected to non-uniform cyclic loading to study rebar debonding effect on crack distribution, rebar strain, and out-of-plane instability in boundary element. The results indicate that debonding leads to a reduction in the lateral stiffness of the boundary elements, postponing rebar buckling, and also provides a 12% enhancement in the tensile capacity of the rebar. Findings illustrate rebar-concrete debonding results in a reduction in lateral stiffness of boundary element. Similarly, comparing to a debonding free element, buckling member occurs at more minimal strains. It is also revealed that to prevent buckling, larger dimensions are required for sleeved sample. Moreover, robust evidence proved that increasing rebar debonding length enlarges crack width near sleeves, while sleeve length does not affect the first buckling or axial length of samples. This study provides a practical and innovative mechanism for addressing buckling challenges in minimum-reinforcement boundary elements, contributing to safer and more efficient structural design practices.

KEYWORDS

Boundary elements, Out-of-plane buckling, Rebar debonding, Reinforcement fracture, Shear walls

INTRODUCTION

An overriding damage can occur as a result of failure in considering the mechanical forces' effect [1-4]. Accordingly, part of the energy, such as earthquakes and wind, imposed on the structure via external factors must be dissipated with minimal damage in a safe manner through plastic deformation of different members. Such proceeding prevents the structure from instability against loads. Furthermore, innumerable concrete structures are mostly torn down and rebuilt due to unpermitted steady-state deformations and high costs of post-earthquake reconstruction. Distinct mechanisms can be taken to use up a large bulk of exerted energy on the structures' principal members. Hitherto, in recent years, dozen studies have exclusively addressed the performance of reinforced, strengthened concrete shear walls [5-7].

Cook et al. [8] examined failure causes in shear walls under 2010 Chilean earthquake and detected an identical failure in walls. In such type, crack concentration and rebar fracture were observed. According to ACI regulations, the plastic joint length should be approximately half the length of the wall. However, in this study, the minimum length was set to two to three times the wall thickness, which is considered minimal. Henceforth, insufficient plastic deformation capacity leads to insufficient ductility and finally minimum deformations under a seismic load arise reinforcement fracture. Previous studies have extensively investigated the behavior of reinforced concrete elements under seismic loading, particularly focusing on structures with minimum reinforcement. Hoult et al. [9] analyzed the seismic performance of U-shaped shear walls with less than 0.5% longitudinal reinforcement ratio and observed that strain concentration in the reinforcement tends to localize in a single crack, often leading to rebar fracture. This finding highlights the susceptibility of minimum-reinforced shear walls to failure due to inadequate strain distribution, emphasizing the need for strategies to mitigate such risks. Fantili et al. [10] empirically examined the effect of reinforcement diameter on the behavior of concrete beams with minimum reinforcement, demonstrating that larger reinforcement diameters influence crack propagation and strain distribution. These results underline the critical role of reinforcement characteristics in governing the performance of concrete elements under loading. Han et al. [11] surveyed the effect of boundary element details on seismic deformation of shear walls. In this research, shear walls with different reinforcement conditions and boundary element shapes were examined. It achieved conclusive findings revealing that the first flexural crack appears at a relative displacement of 0.17%–0.25% in the lower part of the boundary element. If steel tensile strength at initial crack location (cracked section) is higher than that of concrete (un-cracked section), flexural cracks could develop. Henceforth, boundary reinforcement is concentrated along the wall edges (boundary element). Khalfallah [12] performed a crack analysis on reinforced concrete tensile members. The study concluded post-cracking behavior of reinforced concrete member depends on parameters such as concrete strength, development length for reinforcement, concrete-rebar connection, and distance between rebars. Chrysanidis et al. [13] discussed tensile strain effect on lateral buckling of wall boundary element. Their study revealed instability and lateral buckling increase in tensile strain of rebar of shear wall boundary element.

Rebar-concrete bond effect on longitudinal reinforcement strain distribution could be considered as other effective parameter affecting concrete shear walls behavior [14-16]. Such issue constituted a research topic for numerical researchers in this domain [17-19]. Fantili et al. [20] studied members' bond-slip behavior under tension at cracked section. Findings demonstrated tensile force exerted on crack location member is carried by rebar, and so applied force to concrete is via bonding force. Muhamad et al. [21] experimentally studied load-slip relationship of tensile reinforcement in reinforced concrete members. In this study, flexural members' deformation divided into continuous and non-continuous (deformation). Hong and Park [22] investigated rebar-concrete bond-slip relationship and provided a new behavioral model for slip-shear stress along the interface between rebar and concrete. In another empirical study, Tastani et al. [23] examined rebar indentation area effect on strain penetration and rebar-concrete debonding. This study concludes strain penetration will reduce through an increase in indentation surface area. Naghipour et al. [24] empirically evaluated bonding stress and rebar slip behavior in concrete under reciprocating static loading as well as concrete confinement effect. Guizani et al. [25] examined bond-slip behavior via previous models to consider stirrup placement effect in medium-ductility reinforced concrete structures. The study observed stirrup confinement increase along bond strength between rebar and concrete. Bao et al. [26] introduced a method to prevent and reduce progressive collapse risk in reinforced concrete structures. In this method, rebar-concrete debonding (sleeving) was applied to improve ductility around 30%. This phenomenon also converted strain concentration in a cracked expansion in beam into strain propagation along sleeve and hence delayed fracture. Hussein et al. [27] studied bonding and debonding effect of reinforced rebar in concrete structures' vibration behavior with normal and high-strength concrete. The study displayed rebar-concrete debonding could increase beams ductility. Opabola et al. [28] investigated slip and shear deformations influence on the elastic response of RC components. The study achieved reliable evidences in damage reduction as well as absorption increase of seismic energy. Furthermore, findings revealed diagonal reinforcement strain uniformity as well as its independency from flexural stress. Henceforth, diagonal deformation increases and rebar usage reduction emerge.

The seismic performance of reinforced concrete shear walls is critical for the safety and resilience of structures in earthquake-prone regions. Despite advancements in design approaches, one persistent challenge is the out-of-plane buckling of boundary elements, which undermines the structural integrity of shear walls. Existing studies have extensively investigated factors influencing buckling and crack propagation in these elements. However, these studies have largely focused on traditional reinforcement strategies without exploring innovative mechanisms to mitigate buckling in structures with minimum reinforcement. This research aims to address this gap by introducing and experimentally evaluating the effects of rebar-concrete debonding through the use of plastic sleeves. By strategically isolating sections of the rebar, the study investigates how this technique impacts strain distribution, crack behavior, and buckling in boundary elements under seismic loading. The findings of this research have the potential to influence industry practices by providing a practical solution for improving the seismic performance of reinforced concrete shear walls, particularly in cost-sensitive projects requiring minimum reinforcement. Moreover, the results could inform future updates to seismic design codes and regulations, promoting the adoption of rebar-concrete debonding as a viable strategy for mitigating buckling and enhancing structural safety.

Walls with minimum reinforcement ratios are more prone to instability because they lack the necessary resistance to buckling and stress distribution. The minimal reinforcement leads to a higher concentration of stresses at crack locations, reduced ductility, and early fracture of reinforcement. These factors make such walls more vulnerable to failure under seismic loading. This research focuses on improving the performance of these walls by investigating the effect of rebar-concrete debonding, which can potentially reduce buckling and enhance stability in walls with minimal reinforcement. Almost all literature review revealed a high demand for tensile rebar strain at crack location. It is also emerged that tensile rebar strain at crack location is the momentous failure in shear walls with minimum longitudinal reinforcement ratio which ultimately leads them to rebar fracture. On the other hand, findings of the current study demonstrate method of debonding, elimination or concrete-rebar bond reduction could increase beams and columns ductility. Accordingly, ultimate goal of the present study is to examine experimental distribution of longitudinal rebar strain in boundary element of shear walls via minimum reinforcement. As a pioneer study in this field, it also considers the effect of such process on buckling stability of shear walls considering local rebar-concrete debonding (sleeving). Such a consequential issue is conducted taking several experimental tests on various samples for boundary element of reinforced concrete shear walls. The firm claim is that changes in tensile force at the base of shear wall are smaller than the wall height due to low bending moment gradient. Henceforth, considering this hypothesis, a prismatic element under tension at two ends can be applied to model shear wall boundary element. Accordingly, four different samples without rebar debonding were subjected to cyclic loading followed by three samples with different sleeve lengths. Then, rebar strain distribution and failure mode, including cracks and buckling distribution, were examined to evaluate sleeving effect on seismic behavior of shear wall boundary element.

METHODS

Initially, three rebar debonding free samples were subjected to monotonic and cyclic loading to evaluate sleeving effect on seismic behavior of shear wall. Then, three samples with different sleeve lengths were subjected to cyclic loading, and strain distribution in rebar and failure mode, including crack distribution and buckling, were studied. Steps for selection, samples' dimensions and methodology are as follows: Selection of sample's dimensions, Selection of rebar and concrete strength, Conduction of Rockwell tests on rebars prior than principal experiment, Design of laboratory setup for sample testing, Selection of loading protocol, Placement and testing of samples, and registration of experimental data, Destruction of samples after their loading and Rockwell tests.

Seven prismatic samples with section dimensions of 150 mm × 150 mm and a length of 1000 mm are opted to evaluate seismic behavior of shear wall boundary element. Fig. 1 displays the geometric properties of samples under study. Two of samples (BM2 and BM3) were sleeveless and subjected to cyclic loading as reference samples. Moreover, three sleeved samples (DC1, DC2, and DC3) were subjected to cyclic loading. The dimension selection and sample preparation were conducted considering two issues; the operating limits of testing device (motion range of the jack) and ACI318R-14 regulations [29] in such a way that an element does not undergo overall buckling during loading. Concrete foundations with dimensions of 600 mm × 450 mm × 150 mm were applied to meet two purposes: to connect prismatic piece to loading jack and laboratory rigid floor and to provide development length of reinforcement. Fig. 1b illustrates the experimental setup prepared at Infrastructure Research Center at Urmia University. Furthermore, having observed the minimum vertical reinforcement ratio in shear wall based on ACI318R-14, the study applied indented type 10T longitudinal reinforcement. It should be nominated that reinforcement ratio of cross section was higher than that recommended by ACI318R-14. Plain 6T rebars placed at distances of 75 mm were used to concrete confinement at element core.

The experimental dimensions and parameters were carefully chosen to represent realistic scenarios encountered in reinforced concrete shear walls with minimum reinforcement while allowing for controlled laboratory testing. The test specimens were designed to reflect typical dimensions and reinforcement ratios used in real-world reinforced concrete shear walls, with a height-to-width ratio of 2.5:1 to simulate slender boundary elements. Due to laboratory constraints, the specimens were scaled to manageable sizes while maintaining realistic proportions, ensuring the relevance of the experimental results to actual field conditions. The longitudinal reinforcement ratio of 0.351% was selected to align with the minimum reinforcement requirements specified in seismic design codes and to facilitate comparison with similar studies.

The sleeve lengths of 80 mm, 150 mm, and 220 mm were selected to represent varying degrees of rebar debonding commonly encountered in construction. The 80 mm length simulates minimal debonding, which might be used in cases where only slight improvements to strain distribution are needed. The 150 mm length corresponds to moderate debonding, reflecting a common approach in seismic design to balance reinforcement efficiency and performance. Finally, the 220 mm length represents a more substantial debonding, suitable for high-performance applications where significant strain redistribution is necessary to prevent premature failure. These lengths were chosen based on practical considerations and typical construction practices, ensuring that the experimental results are relevant to real-world applications in reinforced concrete shear wall design. The choice of sleeving lengths (80 mm, 150 mm, and 220 mm) was informed by preliminary trials and literature observations indicating that localized detachment can influence strain distribution and crack patterns in reinforced concrete elements. These lengths were chosen to cover a range of detachment effects, from minimal to more significant, enabling a comprehensive analysis of the technique's impact. By grounding the experimental setup in established research while introducing innovative parameters, such as the sleeving mechanism, this methodology ensures both relevance to practical applications and the ability to draw meaningful comparisons with prior studies.

CIVIL ENGINEERING JOURNAL

Article no. 11

THE CIVIL ENGINEERING JOURNAL 2-2025

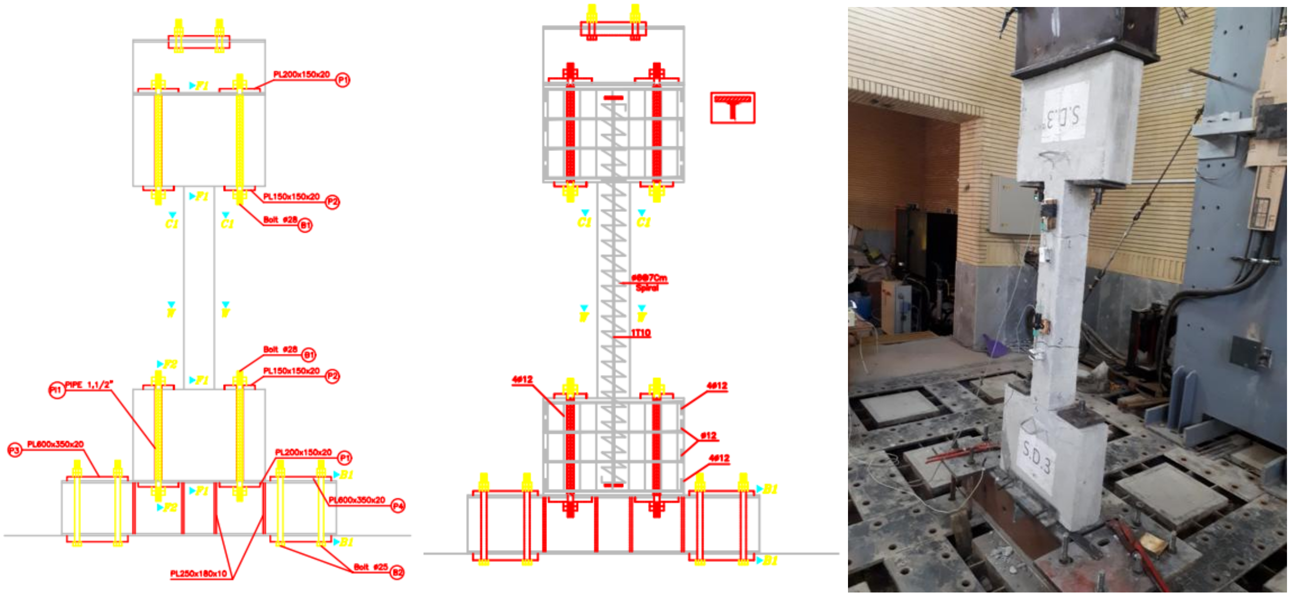

a b

c d

Fig. 1 - (a) Geometric properties of samples under study; (b) experimental setup and method of samples installing; (c) rebar sleeving method; (d) reinforcement and construction details of concrete boundary element before concrete placement

To investigate the effect of rebar separation on the seismic behavior of the shear wall boundary element and the stress distribution in the longitudinal rebar, three laboratory specimens were prepared. A plastic hose, matching the diameter of the rebar, was used as the sheath to create debonding. The sheaths were placed at the mid-height of the specimens with lengths of 80 mm, 150 mm, and 220 mm. Before positioning the sheaths, the rebars were greased at the specified locations to minimize interaction between the rebar and the sheath body, ensuring effective debonding at the designated lengths. The plastic sleeves were subsequently and securely positioned at specified locations on the rebar, as shown in Figure 1c. These sleeves were carefully placed to ensure uniform debonding along the reinforcement. Following the installation of the sleeves, all three specimens were subjected to seismic loading according to a standardized loading protocol. This protocol was designed to replicate realistic seismic conditions and assess the performance of the specimens under cyclic loading, ensuring consistency in the testing procedure across all samples. The summary of the specifications of the samples and the load application method employed in the experimental study is shown in Table 1.

Tab. 1 - A summary of the specifications of the samples and the method of load application utilized in the experimental study

Sample No.	Loading Type	Lateral Reinforcement	Longitudinal Reinforcement	Percentage of Reinforcement (%)	Sleeve Length (mm)
BM2	Monotonic	φ6@70 mm	T10	0.351	--
BM3	Monotonic	φ6@70 mm	T10	0.351	--
BC1	Cyclic	φ6@70 mm	T10	0.351	--
BC2	Cyclic	φ6@70 mm	T10	0.351	--
DC1	Cyclic	φ6@70 mm	T10	0.351	80
DC2	Cyclic	φ6@70 mm	T10	0.351	160
DC3	Cyclic	φ6@70 mm	T10	0.351	240

Direct tension tests were conducted on the rebars, as outlined in reference [30], to evaluate their tensile strength and deformation characteristics under controlled conditions. Corresponding stress-strain curves of rebar is displayed in Figure 2a. Direct tension test findings demonstrate ISIRI3132 reinforcement is S400 grade and exactly meets tensile strength requirements and elongation of reinforcement. Given sample dimensions and concrete coating thickness on lateral reinforcement, the study used C30 concrete to prepare samples both via a suitable mix design selection and maximum grain size observation. The characteristic compressive strength in 28-day concrete cylinder samples with dimensions of 100×300 reaches 30 MPa. Figure 2b depicts compressive test of concrete cylindrical test.

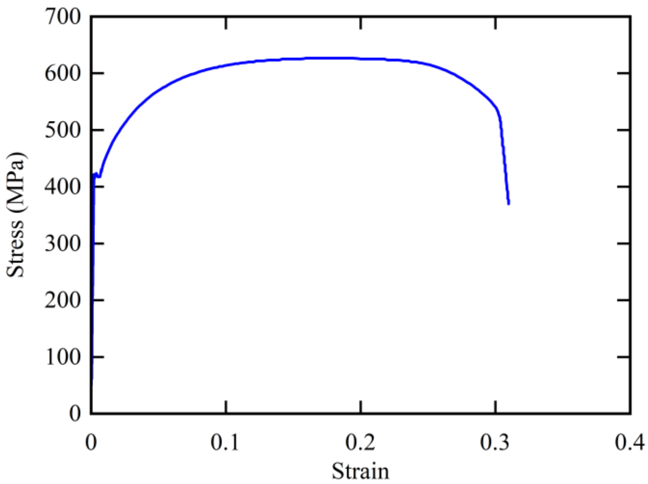

a

b

Fig. 2 - (a) Stress-strain curve of rebar; (b) Determination of compressive strength of the concrete

Wall fracture in minimum longitudinal reinforced sheer walls is substantially controlled due to tensile load on boundary elements. Henceforth, boundary elements are not required to endure a serious compressive load. An asymmetric loading protocol, similar to ACI 355.2 protocol [31], was considered for cyclic loading. Such loading protocol comprised of symmetric cycles of increasing axial strain around 0.003. This figure achieves after continuously stable increase is notified in tensile loading range, while compressive strain ends at 0.003. Applied cyclic loading protocol has been illustrated in Figure 3. The protocol consists of asymmetrical displacement cycles with increasing amplitudes to simulate seismic loading conditions. The initial cycles represent lower displacement values to assess the elastic behavior of the specimens, while subsequent cycles introduce larger displacements to evaluate the capacity for energy dissipation, crack propagation, and eventual failure modes under realistic seismic conditions.

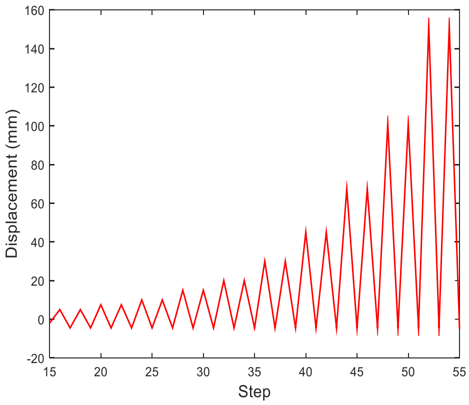

Fig. 3 - Applied loading protocol in large-displacement asymmetrical loading tests. The graph shows the cyclic loading sequence applied to the shear wall boundary elements during the experimental tests.

Since the expansion of cracks in the boundary element of the shear wall has led to a decrease in lateral stiffness, so that the buckling of the boundary element can occur before the buckling and rupture of the longitudinal bar. In this regard, Dashti et al. [32] realized the relationship between the horizontal displacement of the middle of the wall and the buckling of the wall and presented the equation (1) relating the lateral displacement with the reinforcement ratio.

$$\xi = \frac{\delta}{b} \leq 0.5\left(1 + 2.35\frac{\rho f_y}{f_c^{'}} - \sqrt{5.53\left(\frac{\rho f_y}{f_c^{'}}\right)^2 + 4.70\frac{\rho f_y}{f_c^{'}}}\right) \tag{1}$$

in which δ is the lateral displacement of the middle of the element, b is the section dimension, and ρ is the reinforcement ratio in the border element of the shear wall. The average critical strain caused by plate buckling for a sample with one layer of reinforcement can be estimated according to the following equation.

$$\varepsilon_{cr} = 4\left(\frac{b}{l_o}\right)^2 \xi_{cr} \tag{2}$$

RESULTS

This section addresses findings for sleeveless samples BC1 and BC2 (reference samples), sleeved samples DC1, DC2, and DC3 based on cyclic loading test via loading protocol. Loading test was continued until the rebar fracture occurs.

The BC1 sample was subjected to cyclic loading based on the defined loading protocol to study the seismic behavior of boundary elements in shear walls with minimum reinforcement. The load-displacement curve is displayed in Figure 4. In subsequent cycles, cracks appeared abruptly as the load force increased (e.g., cracks 3 and 5) and were closely spaced (as shown in Figure 4b). At these locations, failure initiated with concrete crushing followed by longitudinal reinforcement buckling between two cracks. A further increase in load led to fatigue fracture of the reinforcing rebar, with the ultimate tensile deformation upon failure reaching approximately 88 mm. At these locations, failure initiated with crushing of concrete followed by buckling of longitudinal reinforcement between two cracks. Further increase in load leads to fatigue fracture of reinforcing rebar. Maximum or ultimate tensile deformation upon failure was about 88 mm.

CIVIL ENGINEERING JOURNAL

Article no. 11

THE CIVIL ENGINEERING JOURNAL 2-2025

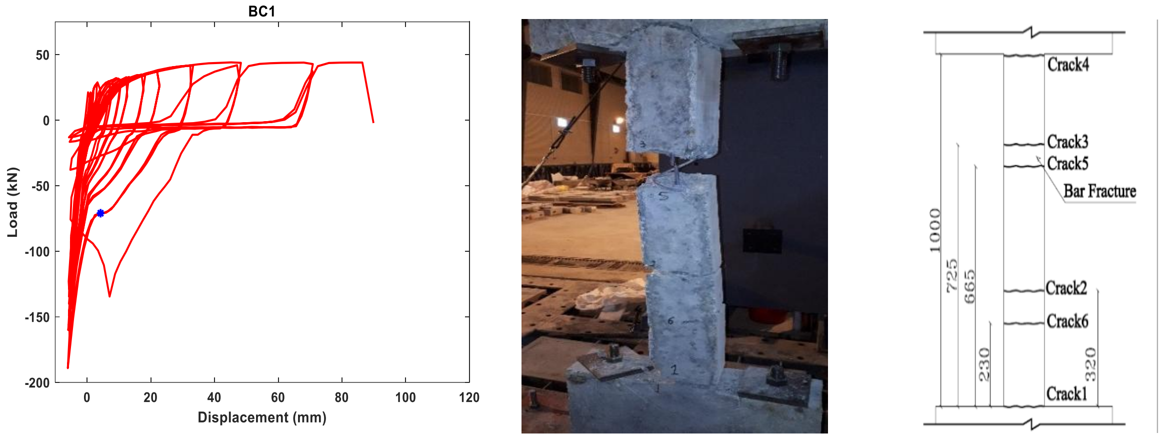

a b c

Fig. 4 - (a) Load-displacement graph under cyclic loading for BC1 sample. This graph shows the relationship between the applied load and displacement, with the initial steep slope indicating elastic behavior and the flattening of the curve reflecting stiffness reduction due to crack formation. (b) Crack geometry showing the distribution and locations of cracks. (c) Crack shape highlighting the morphology of cracks, emphasizing the primary cracks leading to rebar fracture.

Similar to other samples, in BC2, the first crack occurred in fifth cycle at distance 325 mm from joint region along element and foundation via applied cyclic loading. Additional cyclic loading leads to second crack at joint region along element and upper foundation. Then, further cyclic loading makes the third and fourth cracks in ninth and tenth cycles at distance 710 mm from joint region along element and footing; and element and foundation, respectively. Figure 5a displays load-elongation graph of sample under cyclic loading. Also, Figure 5 illustrates crack distribution along sample. Although failure location of Crack 3 initiated in concrete crushing and global buckling forms, ultimate failure happened as rebar fracture at the first crack location (Crack 1).

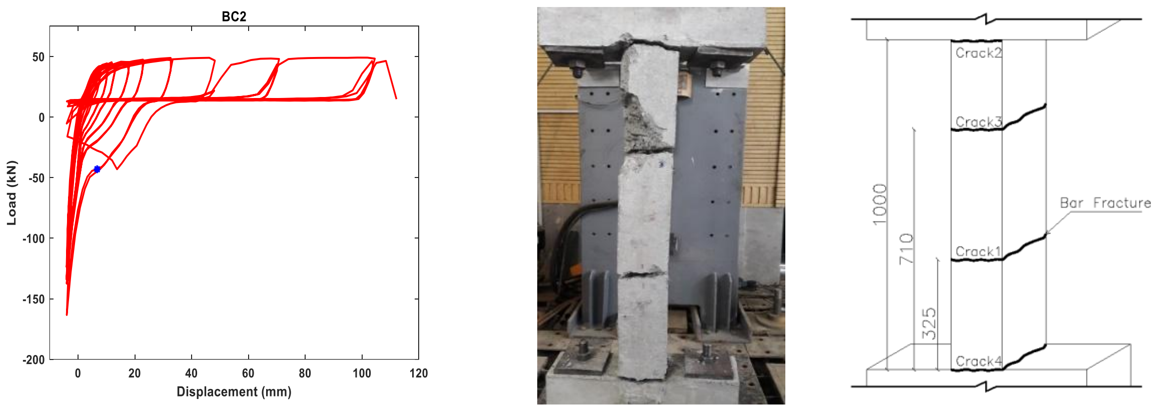

a b c

Fig. 5 - (a) Load-displacement graph under cyclic loading for BC2 sample, showing initial elasticity and stiffness reduction as cracks form. (b) Crack geometry and (c) crack shape, highlighting crack distribution and key fractures leading to rebar failure.

In DC1, with rebar-concrete debonding sleeves in the middle of height with a length 80 mm, the first crack occurred with applied cyclic loading at joint region along element and foundation. Figure 6 displays schematic diagram of failure and load-displacement graph. According to Figure 6, as load increases in subsequent cycles, three other cracks appeared at distances of 80 mm, 210 mm, and 390 mm. These cracks were mainly concentrated in the lower part of sample. As shown in Figure 6, with further loading, buckling failure occurs during 20th cycle. After Crack 5 appears at joint region along sample and foundation, another crushing failure occurs at Crack 3 during 22nd cycle. The ultimate failure happened as rebar fracture in Crack 2 under the sleeve.

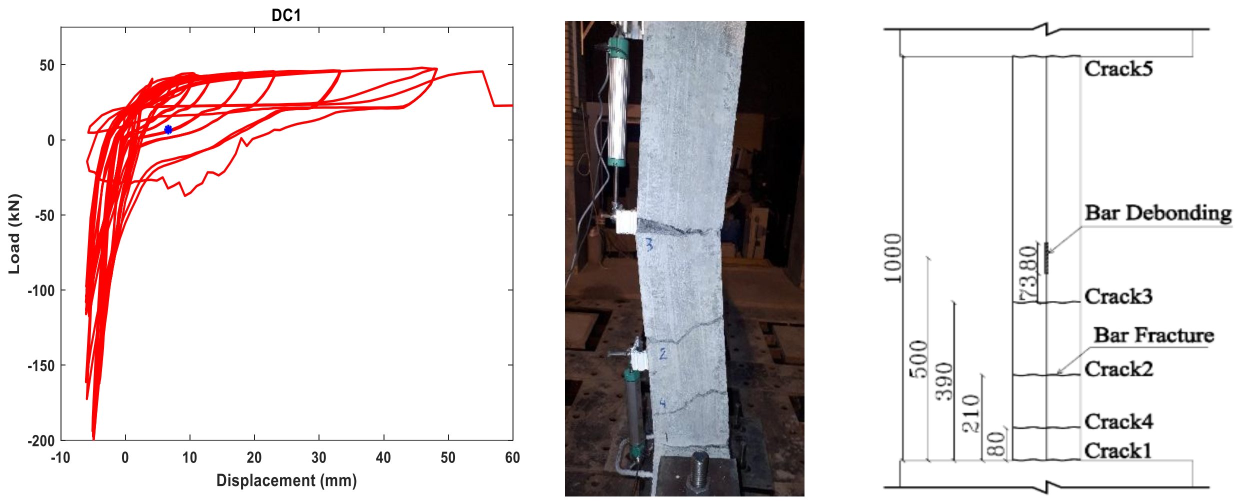

a b c

Fig. 6 - (a) Load-displacement graph under cyclic loading for DC1 sample, showing the load-displacement relationship with stiffness reduction as cracks form. (b) Crack geometry and (c) crack shape, highlighting the distribution and key fractures leading to rebar failure.

In DC2, with the rebar-concrete debonding sleeves in the middle of height with a length 60 mm, as shown in Figure 7, the first crack occurred at distance 385 mm from joint region along element and foundation. Increasing load produces crack width increase to 16 mm under tension during 23rd cycle. In next cycle, concrete crushing at horizontal crack and vertical crack propagation along rebar appeared. The ultimate failure occurred without any new cracks as rebar fracture at Crack 1 under sleeve. Absence of any crack propagation and initiation along sample produced no lateral buckling. Comparing to other samples, absence of initiation of secondary cracks in DC2 lead to overall deformation of sample at minimum level. Henceforth, rebar fracture occurred at low cycles.

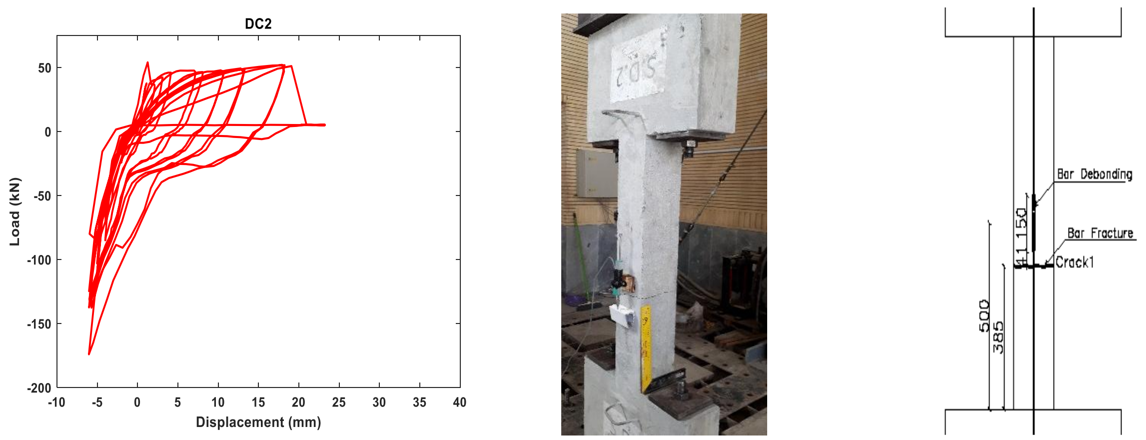

a b c

Fig. 7 - (a) Load-displacement graph under cyclic loading for DC2 sample, showing the load-displacement relationship with stiffness reduction as cracks form. (b) Crack geometry and (c) crack shape, highlighting the distribution and key fractures leading to rebar failure.

The occurrence of early fractures in some samples highlights the complex interplay between the debonding mechanism, crack patterns, and strain distribution. While the sleeving mechanism improves fracture strain in certain scenarios, it also introduces new stress concentrations near the sleeve boundaries. These observations suggest that careful consideration must be given to the length and placement of the sleeves to optimize their effectiveness. In seismic design, this underscores the need for a balance between achieving strain redistribution and avoiding localized vulnerabilities that could compromise the overall performance of the boundary element. The ultimate failure occurred without any new cracks as rebar fracture at Crack 1 under sleeve. Absence of any crack propagation and initiation along sample produced no lateral buckling. Comparing to other samples, absence of initiation of secondary cracks in DC2 lead to overall deformation of sample at minimum level. Henceforth, rebar fracture occurred at low cycles.

In DC3, with the rebar-concrete debonding sleeves in the middle of height with a length 220 mm, the first crack occurred in the third cycle at distance 280 mm from joint region along element and foundation. Load-displacement graph and crack geometry of this sample are displayed in Figure 8. Increasing load produced second crack 5th cycle at distance 785 mm from joint region along element and foundation. As illustrated in Figure 7, the third and fourth cracks occurred in 9th and 11th cycles, respectively, at two ends of elements at joint region with foundation. The element failure in 26th cycle occurred as global buckling (instability), and cracks along longitudinal reinforcement were observed during 36th cycle at Cracks 1 and 2 along concrete weight coating. Finally, rebar fractured at Crack 1 during 39th cycle in a way that widths of Cracks 1 to 4 were 6 mm, 11 mm, 26 mm, and 35 mm, respectively. Similar to reference samples (BC1 and BC2) and sleeved sample (DC1), in the present sample, failure occurred as out-of-plane buckling with concrete crushing at crack location before rebar fracture. Findings for Rockwell are illustrated in Figure 9.

The sleeve length significantly influences the crack width in shear walls with rebar debonding. As the sleeve length increases, the debonding effect becomes more pronounced, redistributing strain and leading to wider cracks near the sleeve. This can enhance energy dissipation and strain redistribution, improving the seismic performance and ductility of the structure. However, wider cracks also weaken the bond between the concrete and rebar, reducing the concrete's ability to transfer forces effectively. This can lead to localized failure in the concrete, potentially compromising the wall's overall integrity. Therefore, sleeve length must be carefully balanced to optimize seismic performance while minimizing the risk of localized damage from excessive crack widths.

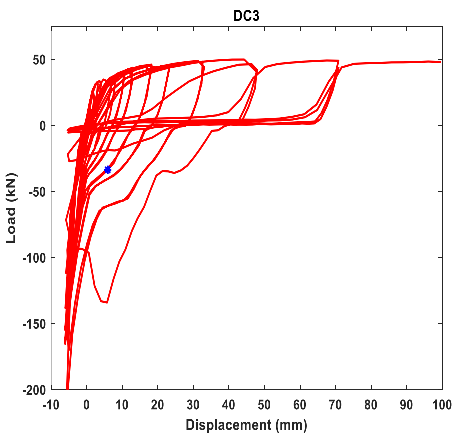

a

b

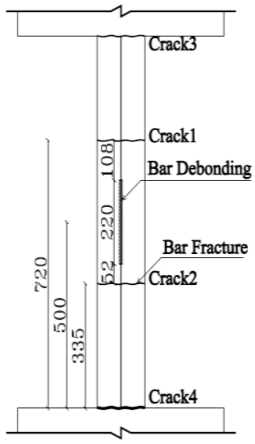

c

Fig. 8 - (a) Load-displacement graph under cyclic loading for DC3 sample, showing the load-displacement relationship with stiffness reduction as cracks form. (b) Crack geometry and (c) crack shape, highlighting the distribution and key fractures leading to rebar failure.

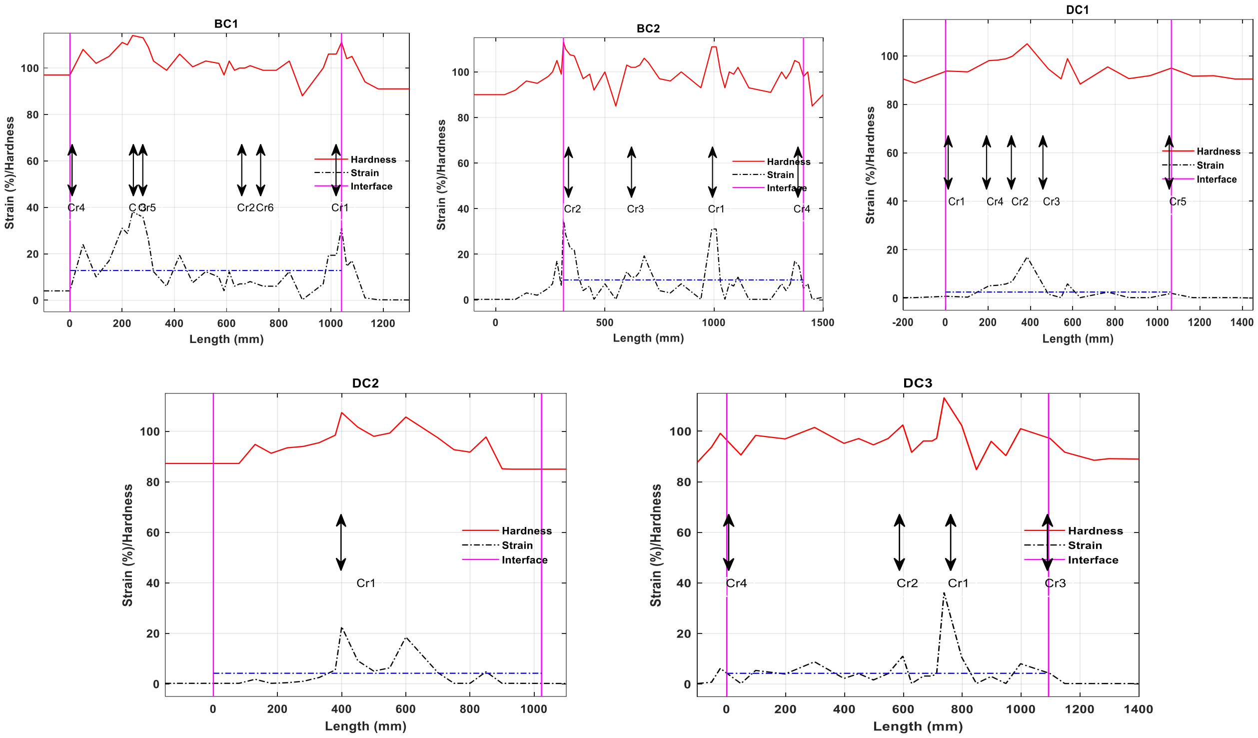

Fig. 9 - Strain distribution along the reinforcement in various samples, illustrating the variation in strain at different locations along the reinforcement for each sample.

For cyclic loading tests, the cracking pattern is highly similar to observed monotonic loading. Because of strain penetration into foundation, in samples subjected to cyclic loading, rebar fracture occurred for both BM2 and BM3 at joint region along member and foundation element. In addition, out-of-plane buckling is an overriding reason for change in rebar fracture location. Out-of-plane buckling is also a substantial reason for rebar fracture in the middle region. Nevertheless, numbers and patterns of cracks in sleeved samples (DC1 and DC3) are diverse and various, out-of-plane buckling in both samples occurred at the average strain. Such evidence confirms the relationship between buckling and average axial deformation. Since crack widths do not represent strain distribution before buckling, henceforth, no analysis could be practiced on uniform elongation of such samples. Subsequently, rebar-concrete debonding effect on boundary element's seismic behavior in shear wall with minimum reinforcement is investigated via two perspectives:

1) Impact of longitudinal reinforcement strain on buckling instability
2) Impact of longitudinal reinforcement strain on drift

Table 2 summarizes findings for cracking in sleeved and sleeveless samples under cyclic loading. It covers both buckling and corresponding state to rebar fracture. Based on demonstrated findings in Table 2 and also taking into account the average strain upon buckling for both sleeved and sleeveless samples, it is more likely to deduce that comparing to sleeveless samples, sleeved samples experience buckling at minimum strains. Furthermore, it can be claimed that sleeve length does not play a crucial role in buckling control of boundary element. The experimental results demonstrate that the fracture strain of the rebar increases from 0.088 in the case of no sheath to 0.098 when a sheath with a length of 240 mm is used. This represents a 12% improvement in the fracture strain of the rebar. This enhancement highlights the potential of the rebar-concrete debonding mechanism to improve the ductility and deformation capacity of reinforcement, thereby contributing to better seismic performance of shear wall boundary elements. With the weakening of the bond between the rebar and concrete near the sleeve, the ability of the concrete to transfer axial and shear forces to the reinforcement is diminished. This can result in premature rebar fracture or failure at the sleeve location, which could limit the wall's overall capacity to resist seismic forces.

Tab. 2 - Summary for cracking in different elements under study

Sample	Failure Mode	Crack Number and Width (mm)						Sample Elongation (mm)	Average Strain εsm1
		1	2	3	4	5	6		
BC1	Buckling	5	4	9*	7	7	-	32	0.032
	Rebar Fracture	20	19	14**	21	25	12	88	0.088
BC2	Buckling	10*	5	9	8	--	--	32	0.032
	Rebar Fracture	25	19**	22	18	--	--	84	0.084
DC1	Buckling	3	6*	5	4	--	--	18	0.018
	Rebar Fracture	7	24**	23	6	5	--	65	0.065
DC3	Buckling	5	7*	2	4	--	--	18	0.018
	Rebar Fracture	24	36**	6	32	--	--	98	0.098

*Maximum crack width upon initial buckling in sample
**Rebar fracture

One of the key applications of the strain distribution diagram along the element is to assess both the maximum local strain within the reinforcement and the uniform strain distribution along the entire length of the element. This analysis is crucial for understanding the strain variation and identifying potential points of failure within the reinforcement during loading. The uniform strain is calculated by dividing the total elongation, which is derived from summing all local strains along the reinforcement, by the total length of the reinforcement. The values for both the uniform and maximum strains, as measured in the sleeved and sleeveless samples, are presented in Table 3. It is totally worthwhile to notify that maximum strain values obtained are not caused only by axial deformation. They are also dramatically affected by bending deformation. As the sleeve length increases, the debonding effect becomes more pronounced, leading to a concentration of strain near the sleeve edges. This can cause localized concrete cracking or spalling, reducing the concrete's ability to transfer forces effectively and compromising the overall structural integrity.

The observed instability in sleeved samples at lower strains can be attributed to stress concentrations near the edges of the sleeves. The debonding effect, induced by the plastic sleeves, weakens the bond between the rebar and concrete, leading to a redistribution of strain along the reinforcement. This redistribution causes localized stress concentrations near the sleeve edges, which can initiate buckling or other forms of instability at lower strains compared to unsleeved samples.

Tab. 3 - Elongation and Deformation Data Taken from Samples

Sample	Average Elongation (mm)	Average Strain *	Uniform Strain **	Maximum Strain **	Permissible Drift †	εcr‡	εcr
BC1	88	0.088	0.085	0.361	0.041	0.032	0.0176
BC2	84	0.084	0.087	0.357	0.031	0.032	0.0176
DC1	65	0.065	0.0251	0.170	0.023	0.018	0.0176
DC2	25	0.025	0.0418	0.226	0.009	---	0.0176
DC3	98	0.098	0.0423	0.382	0.035	0.018	0.0176

* Ratio of elongation to sample length
** Obtained via relationship between stiffness and strain.
† Obtained via Dezhdar and Adebar's proposed method [33].
‡ Tensile strain corresponding to first out-of-plane buckling.

Figure 10 compares expected and actual drift capacity of samples. Such capacities are compared to rebar strain in various samples under study. Based on findings, regarding sleeved and sleeveless samples, there are sufficient evidences to deduce that an increase in sleeve length can somehow affect drift capacity of element. On the other hand, crack and strain concentration in DC2 brings about weak drift capacity. Henceforth, failure occurs as a result of rebar fracture at minimum deformations before buckling.

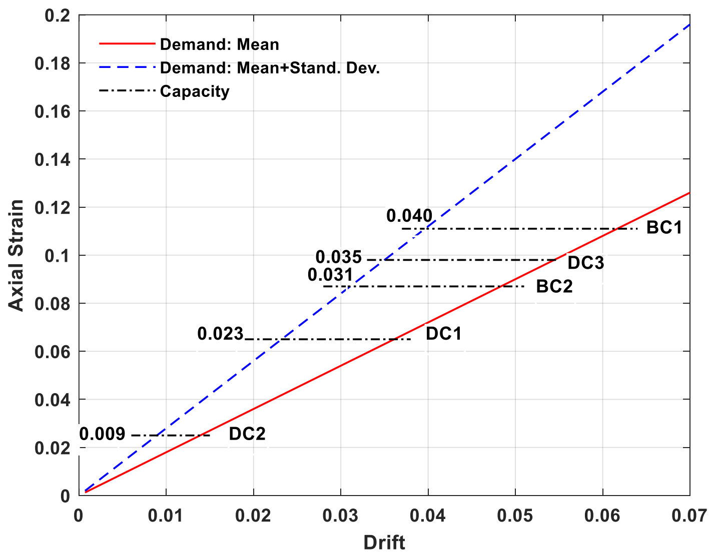

Fig. 10 - Comparison of expected and actual drift capacities of samples compared to rebar strain

The findings indicate that while rebar-concrete debonding can enhance strain distribution and delay buckling, improper implementation may lead to premature failure. These results suggest that design guidelines for implementing rebar debonding mechanisms should consider not only the benefits but also the potential risks of localized strain concentration. Future work could explore optimized sleeve geometries and material properties to mitigate these risks, thereby improving the seismic resilience of reinforced concrete shear walls. Building on these insights, our study hypothesizes that introducing a rebar-concrete detachment mechanism (via plastic sleeves) can address the strain concentration and improve strain distribution along the rebar. This approach aims to reduce the likelihood of localized fractures, as observed by Hoult et al. [9], and to optimize the behavior of the reinforcement, extending the principles identified by Fantili et al. [10] to the context of shear walls. By experimentally investigating this hypothesis, we seek to provide a novel mechanism for enhancing the seismic performance of minimum-reinforced boundary elements.

While rebar-concrete debonding offers significant benefits, such as improved strain redistribution and energy dissipation, it also introduces potential risks. The concentration of stress near the sleeve edges can cause localized concrete failure, reduce force transfer between the concrete and rebar, and increase the likelihood of premature rebar fracture or buckling. Therefore, the use of debonding must be carefully controlled to balance its seismic benefits with the risks of localized damage and reduced lateral stiffness. This study presents a novel investigation into the effect of rebar-concrete debonding in shear walls with minimum reinforcement, an area that has not been extensively studied in the literature. While previous research has focused on traditional reinforcement strategies, our findings provide new insights into the seismic performance of walls with minimum reinforcement, revealing both the benefits, such as improved strain redistribution, and the risks of localized failure due to stress concentrations near the sleeve edges.

Based on the findings of this study, several recommendations for updating seismic design guidelines are proposed. First, standardizing sleeve dimensions within a range of 80 mm to 220 mm would provide flexibility in addressing different levels of rebar debonding effects while maintaining structural integrity. Second, optimal sleeve placement should be considered, with sleeves placed at mid-height or near critical regions of the shear wall to ensure effective strain redistribution and minimize stress concentrations. Finally, sleeve length and placement could be adjusted according to the seismic risk of the region. In areas with higher seismic activity, longer sleeves may be necessary to enhance strain redistribution, while in lower seismic risk regions, shorter sleeves could be more appropriate to achieve the desired performance without compromising the overall stability of the wall.

CONCLUSION

The present study experimentally investigated rebar debonding effects on boundary element's seismic performance in reinforced-concrete shear walls with minimum reinforcement. Thereupon, fully experimental tests were conducted on diverse samples applying asymmetric cyclic loading for both sleeved and sleeveless samples. Ultimately, evaluation developed at strain distribution along element and buckling of boundary element. Based on conducted experiments and analyses:

- Concrete-rebar debonding reduces the lateral stiffness of boundary element. Hence, compared to debonding free element, buckling occurs at minimum strains.
- Larger dimensions are required for sleeved sample to prevent buckling. For instance, under a longitudinal reinforcement ratio of 0.351%, the maximum tensile strain prior to buckling is approximately 0.02 for unsheathed specimens and 0.032 for sheathed specimens. These values are notably lower than the anticipated tensile strain capacity of the elements. Such values are less than expected tensile strain capacity for elements.
- Sleeved rebars experience cracks at distances 5φ to 7.5φ (φ is the diameter of the longitudinal rebar) from end of sleeve location. Cracks adjacent to sleeved length have the largest width. This crack is expected to release deformation along sleeve.
- The results indicate that the fracture strain of the rebar increases from 0.088 in specimens without a sheath to 0.098 in those utilizing a 240 mm-long sheath. This enhancement represents a 12% improvement in the fracture strain of the rebar.
- An increase in rebar debonding length increases the crack width near sleeving. Nevertheless, sleeving length does not affect first buckling of sample or axial elongation of samples.
- Rebar-concrete debonding using plastic sleeves offers a practical method to redistribute strain, delay buckling, and improve fracture strain capacity in reinforcement. This technique can enhance the seismic performance of shear walls in cost-sensitive, minimum-reinforcement projects. Proper sleeve length and placement are crucial to maximize benefits and minimize localized strain concentrations.
- The findings suggest the need for updated design guidelines to incorporate rebar debonding mechanisms. Recommendations should address sleeve dimensions, placement, and materials to encourage safer and more resilient seismic designs in reinforced concrete structures.

This study introduces a novel mechanism for mitigating out-of-plane buckling in shear wall boundary elements by leveraging rebar-concrete debonding. By selectively incorporating sleeving around the rebar, the study demonstrates the potential to improve strain distribution, increase fracture strain capacity, and delay buckling under seismic loading. This approach is particularly beneficial for structures with minimum reinforcement, where conventional methods may fail to prevent premature buckling. These findings provide a practical and cost-effective strategy for enhancing the seismic performance of reinforced concrete shear walls, offering a significant advancement over existing design methods.

The findings of this study have significant practical implications, especially for retrofit projects and cost-sensitive scenarios where minimum reinforcement is common. Rebar-concrete debonding provides a cost-effective method to improve seismic performance in both existing structures and new buildings, where budget constraints may limit the amount of reinforcement. This technique enhances energy dissipation and reduces the risk of premature buckling, offering a valuable solution for improving structural resilience without significant additional costs.

REFERENCES

[1] Barghlame H, Ferdousi A, Mousavi Ghasemi SA, 2021. Investigation into the behavior of an upgraded section used for Concrete-Filled Steel Tubular Columns (Upgraded CFT) under Cyclic Loading. Journal of Structural and Construction Engineering, vol. 9, p. 86-100. https://doi.org/10.22065/jsce.2021.309337.2601.

[2] Khosravi S, Amirsardari S, Goudarzi MA, 2024. Dynamic Behavior of Rectangular Tanks with Limited Freeboard Under Seismic Loads: Experimental, Analytical and Machine Learning Investigations. Journal of Pressure Vessel Technology, p. 1-34. https://doi.org/10.1115/1.4066967.

[3] Khosravi S, Goudarzi MA, 2023. Seismic risk assessment of on-ground concrete cylindrical water tanks. Innovative Infrastructure Solutions, vol. 8, p. 68. https://doi.org/10.1007/s41062-022-01002-8.

[4] Barmaki S, Sheidaii MR, Azizpour Miandoab O, 2021. Progressive collapse resistance of steel moment frames with different types of beam-to-column welded connections in various column removal scenarios. Journal of Structural and Construction Engineering, vol. 9, p. 59-71. https://doi.org/10.22065/jsce.2021.294557.2492.

[5] Mo J, Uy B, Li D, Thai H-T, Tran H, 2021. A review of the behaviour and design of steel–concrete composite shear walls. Structures, vol. 31, p. 1230-1253. https://doi.org/10.1016/j.istruc.2021.02.041.

[6] Kourehpaz P, Molina Hutt C, Marafi NA, Berman JW, Eberhard MO, 2021. Estimating economic losses of midrise reinforced concrete shear wall buildings in sedimentary basins by combining empirical and simulated seismic hazard characterizations. Earthquake Engineering & Structural Dynamics, vol. 50, p. 26-42. https://doi.org/10.1002/eqe.3325.

[7] Zhang J, Zhao Y, Li X, Li Y, Dong H, 2021. Experimental study on seismic performance of recycled aggregate concrete shear wall with high-strength steel bars. Structures, vol. 33, p. 1457-1472. https://doi.org/10.1016/j.istruc.2021.05.033.

[8] Cook DT, Liel AB, DeBock DJ, Haselton CB, 2021. Benchmarking FEMA P-58 repair costs and unsafe placards for the Northridge Earthquake: Implications for performance-based earthquake engineering. International Journal of Disaster Risk Reduction, vol. 56, p. 102117. https://doi.org/10.1016/j.ijdrr.2021.102117.

[9] Hoult R, Appelle A, Almeida J, Beyer K, 2019. Seismic response of thin, singly reinforced U-shaped walls: Overview and large-scale experimental tests. Proceedings of Concrete, vol. 43, p. 56-69.

[10] Fantilli AP, Ferretti D, Rosati G, 2005. Effect of bar diameter on the behavior of lightly reinforced concrete beams. Journal of Materials in Civil Engineering, vol. 17, p. 10-18. https://doi.org/10.1061/(ASCE)0899-1561(2005)17:1(10).

[11] Oh YH, Han SW, Lee LH, 2002. Effect of boundary element details on the seismic deformation capacity of structural walls. Earthquake Engineering & Structural Dynamics, vol. 31, p. 1583-1602. https://doi.org/10.1002/eqe.177.

[12] Khalfallah S, 2006. Cracking analysis of reinforced concrete tensioned members. Structural Concrete, vol. 7, p. 111-116. https://doi.org/10.1680/stco.2006.7.3.111.

[13] Chrysanidis T, 2014. Size of seismic tensile strain and its influence on the lateral buckling of highly reinforced concrete walls. IOSR Journal of Mechanical and Civil Engineering, vol. 11, p. 18-22.

[14] Esmaeili J, Khoshkanabi SP, Andalibi K, Kasaei J, 2023. An innovative method for improving the cyclic performance of concrete beams retrofitted with prefabricated basalt-textile-reinforced ultra-high performance concrete. Structures, vol. 52, p. 813-823. https://doi.org/10.1016/j.istruc.2023.04.004.

[15] Ghaderi M, Maleki VA, Andalibi K, 2015. Retrofitting of unreinforced masonry walls under blast loading by FRP and spray-on polyurea. Fen Bilimleri Dergisi (CFD), vol. 36, p. 4. https://doi.org/10.17776/CSJ.82511.

[16] Ismaili J, Andalibi K, Kasaei J, 2015. Investigation of the effects of adding nano-alumina on the mechanical properties of concrete. In: 10th International Congress of Civil Engineering, Faculty of Civil Engineering, Tabriz.

[17] Hu H, Wang J, Yan X, 2022. Cracking analysis of members connected by grouted splice sleeves under axial tension. Construction and Building Materials, vol. 322, p. 126487. https://doi.org/10.1016/j.conbuildmat.2022.126487.

[18] Schlicke D, Dorfmann EM, Fehling E, Tue NV, 2021. Calculation of maximum crack width for practical design of reinforced concrete. Civil Engineering Design, vol. 3, p. 45-61. https://doi.org/10.1002/cend.202100004.

[19] Yao G, Xiong X, Ge Y, 2021. Cracking behavior of full-scale pre-tensioned prestressed concrete double-Tee members with steel-wire meshes. Journal of Building Engineering, vol. 44, p. 102658. https://doi.org/10.1016/j.jobe.2021.102658.

[20] Fantilli AP, Mihashi H, Vallini P, 2009. Multiple cracking and strain hardening in fiber-reinforced concrete under uniaxial tension. Cement and Concrete Research, vol. 39, p. 1217-1229. https://doi.org/10.1016/j.cemconres.2009.08.020.

[21] Muhamad R, Ali MM, Oehlers D, Sheikh AH, 2011. Load-slip relationship of tension reinforcement in reinforced concrete members. Engineering Structures, vol. 33, p. 1098-1106. https://doi.org/10.1016/j.engstruct.2010.12.022.

[22] Hong S, Park SK, 2012. Uniaxial bond stress-slip relationship of reinforcing bars in concrete. Advances in Materials Science and Engineering, vol. 2012, p. 1-12. https://doi.org/10.1155/2012/328570.

[23] Tastani S, Pantazopoulou SJ, 2013. Reinforcement and concrete bond: State determination along the development length. Journal of Structural Engineering, vol. 139, p. 1567-1581. https://doi.org/10.1061/(ASCE)ST.1943-541X.0000725.

[24] Naghipour M, Khalili A, Hasani SMR, Nematzadeh M, 2022. Experimental investigation of natural bond behavior in circular CFTs. Steel and Composite Structures, vol. 42, p. 191-207. https://doi.org/10.12989/scs.2022.42.2.191.

[25] Guizani L, Chaallal O, Mousavi SS, 2017. Local bond stress-slip model for reinforced concrete joints and anchorages with moderate confinement. Canadian Journal of Civil Engineering, vol. 44, p. 201-211. https://doi.org/10.1139/cjce-2015-0333.

[26] Bao Y, Lew HS, Sadek F, Main J, 2013. A simple means for reducing the risk of progressive collapse. Concrete International, vol. 35, p. 33-38.

[27] Hussien O, Elafandy T, Abdelrahman A, Abdel Baky S, Nasr E, 2012. Behavior of bonded and unbonded prestressed normal and high strength concrete beams. HBRC Journal, vol. 8, p. 239-251. https://doi.org/10.1016/j.hbrcj.2012.10.008.

[28] Opabola EA, Elwood KJ, 2020. Simplified approaches for estimating yield rotation of reinforced concrete beam-column components. ACI Structural Journal, vol. 117, p. 279-291. https://doi.org/10.14359/51724667.

[29] Belarbi A, 2014. ACI 318-14. Building Code Requirements for Structural Concrete. American Concrete Institute, Farmington Hills.

[30] Pouraminian M, Akbari Baghal AE, Andalibi K, Khosravi F, Arab Maleki V, 2024. Enhancing the pull-out behavior of ribbed steel bars in CNT-modified UHPFRC using recycled steel fibers from waste tires: A multiscale finite element study. Scientific Reports, vol. 14, p. 19939. https://doi.org/10.1038/s41598-024-68682-3.

[31] Mahrenholtz C, Eligehausen R, Hutchinson TC, Hoehler MS, 2017. Behavior of post-installed anchors tested by stepwise increasing cyclic crack protocols. ACI Structural Journal, vol. 114, p. 621. https://doi.org/10.14359/51689023.

[32] Dashti F, Dhakal RP, Pampanin S, 2018. Evolution of out-of-plane deformation and subsequent instability in rectangular RC walls under in-plane cyclic loading: Experimental observation. Earthquake Engineering & Structural Dynamics, vol. 47, p. 2944-2964. https://doi.org/10.1002/eqe.3115.

[33] Dezhdar E, Adebar P, 2015. Estimating seismic demand on concrete shear wall buildings. In: The 11th Canadian Conference on Earthquake Engineering, Canadian Association for Earthquake Engineering, Victoria, BC, Canada.

Article no. 12

THE CIVIL ENGINEERING JOURNAL 2-2025

SEISMIC PERFORMANCE EVALUATION OF PREFABRICATED BRIDGE SUBSTRUCTURE CONNECTED BY GROUTED SLEEVES

Jingsong Shan[1], Fang Wang[1], Ranshu Liu[1], Deqing Liu[2], Jiayuan Zhang[3] and Ruifeng Nie[1]*

1. *Shandong University of Science and Technology, Shandong Key Laboratory of Civil Engineering Disaster Prevention and Mitigation, Qingdao, 266590, China; skd994189@sdust.edu.cn; 202282040012@sdust.edu.cn; qingdaonieruifeng@163.com*
2. *Shandong Quanjian Engineering Detection CO.; LTD., Jinan, 250000, China*
3. *The Second Construction Limited Company of China Construction Eighth Engineering Division, Jinan, 250014, China*

Received: *02.05.2024*

Received in revised form: *19.12.2024*

Accepted: *22.05.2025*

ABSTRACT

In this study, the seismic performance of prefabricated bridges connected by grouted sleeves has been evaluated. 12 sleeve specimens and 4 cast-in-place specimens with varying anchorage lengths and water-to-cementitious material ratios were fabricated to investigate the bond-slip performance by uniaxial tension test based on the constitutive relationship of grouted sleeves and bond-slip behaviour between rebar and concrete. A finite element (FE) model was proposed to analyse the prefabricated bridge substructure, considering bond and slip between rebar and sleeve. The corresponding seismic performance under simulated seismic effects was investigated using a multi-angle analysis method. Also, parametric investigation using FE analysis was performed to examine the influence of various parameters on the seismic performance of the specimens. The experiment results showed minimal bonding performance differences between the grouted sleeve specimens and the cast-in-place specimens, indicating that the grouted sleeve connection satisfies the connection performance requirements. The simulation results show that the typical damage form of the prefabricated bridge substructure connected by grouted sleeves is bending, the shape of the hysteresis loop is either shuttle or bow, with the slope of the descending section of the skeleton curve varied not significantly because of the excellent ductility, and the ultimate bearing capacity and cumulative energy consumption of prefabricated Pier- Bent Cap were 83.3% and 82.0% of RC specimen, separately. The results corroborate the excellent seismic performance of prefabricated bridge substructures connected by grouted sleeves.

KEYWORDS

Bond-slip test, Grouted sleeve, Prefabricated bridge substructure, Finite element analysis (FEA), Seismic performance

INTRODUCTION

In recent years, rapid advancement in assembly technology has been seen due to its advantages, such as reduced construction time, low pollution [1]. In addition, the development of prefabricated bridges is also relatively rapid, and prefabricated abutment technology become a new research area in bridge engineering for its fast construction, low interference, and small post-earthquake residual displacement [2]. However, prefabricated bridges have not gained significant attention due to their instability under seismic excitations [3]. When an earthquake occurs, the substructure is the most vulnerable to damage, leading to structural damage to the entire bridge. Therefore, ensuring the safety and stability of the substructure is crucial. Since the safety and stability of the substructure focus on the connection between the columns and pile cap, as well as between piers and the cover beam [4]. Consequently, whether the connection type can meet the requirements of connection performance and improve the seismic performance of prefabricated bridge substructure must be addressed.

Many studies have been performed on the connection between precast concrete members. Among all the connections, the grouted sleeve connections are among the most effective connections for prefabricated bridge substructures [5,6]. Many factors affect the connection performance of the grouted sleeve, such as the location of the sleeve connector, the anchorage length of the reinforcement, and the performance of the grout. Lu et al. [7] concluded that grouted sleeves with threads exhibit better connection properties. However, most studies were mainly focused on one type of connector. Comparative studies on the mechanical performance of two types of connections (grouted sleeve and cast-in-place) are still sparse. In addition, prefabricated bridges are primarily used in low-seismic and non-seismic fortification areas, with limited application in moderate and high-intensity regions mainly due to the uncertainty of the seismic performance of prefabricated bridges. Liu et al. [8] and Haber et al. [9] conducted a large number of tests to confirm that prefabricated bridge substructures with grouted sleeve connections have seismic performance comparable to that of cast-in-place, indicating that the sleeve joints significantly affect on the hysteretic response when they are at the location of the plastic hinge. There are two widely used methods to study the seismic performances of prefabricated bridges: the first uses model experiments [9,10], which is accurate but with significantly high experimental effort, whereas the other method is realized by finite element (FE) simulation [11], which is computationally efficient and easy. Nevertheless, it cannot determine the actual force in the grouted sleeve and the influence of the sleeve connections on the whole prefabricated bridge substructure. Thus, the simulation results are usually not accurate enough. Besides, in the current simulations, the bond-slip effects of reinforcement and concrete are generally ignored, which may also reduce the simulation accuracy. There are relatively few studies on sleeve connectors with different parameters and fabricated bridge substructures with other parameters, and they have not formed a systematic control analysis. Therefore, conducting relevant experimental and numerical simulation studies is imperative to fill the research gaps in parametric analyses.

As is well known, the results of full-scale tests can be replaced effectively by finite element based reasonable constitutive and parameter values, and costs reduced significantly. Therefore, results of sleeve connections tests used as the original parameters for full-scale seismic performance analysis of prefabricated Pier- Bent Cap is an effective solution. In this paper, the mechanical properties of sleeve connectors were experimentally analyzed to clarify the reliability of sleeve connections and the constitutive relations to be subsequently used in finite element analysis (FEA). Afterward, FE-based models were developed to delve into the seismic performance of bridge substructures that employ sleeve connections under earthquake. These models were then used to conduct a parametric investigation to provide a deeper understanding of how the critical parameters affect the seismic performance of the assembled bridge substructure.

CIVIL ENGINEERING JOURNAL

Article no. 12

THE CIVIL ENGINEERING JOURNAL 2-2025

MATERIAL AND METHOD

Raw materials

In order to study the connection performance of the grouted sleeve connectors, 12 sleeve connection specimens were designed and fabricated, with two specimens in each set. Using TT represented grouted sleeve connection specimens. TT-120-0.1 represents the anchorage length of this connection specimen, which is 120 mm, and its water-material ratio is 0.1. Cast-in-place comparative specimens were designed and labelled as XJ. The developed specimens were cured in an underground curing room. Specimen preparation is shown in Fig. 1. The material properties and parameters of the grouted sleeve were determined following JG/T398-2019 [12]. The cast-in-place specimens were formed by C40 concrete, and the cubic compressive strength of the concrete was measured at 42.9 MPa. In this test, HRB400 rebar with d=12mm and C40 concrete were chosen. In order to determine the bonding strength of grout, the bond-slip test was conducted, which showed that the initial bond-slip of grout with different water-to-cementitious material ratios is greater than 300 mm, and all grout could meet the workability requirement. In addition, the compressive strength of the grout was tested according to GBT17671-2021[13], confirming that all grouts met the target strength requirement.

a) Sleeve test piece grouting preparation

b) Sleeve test piece grouting

c) Pouring concrete

Fig. 1 – Specimen preparation

Sensor arrangement and Loading process

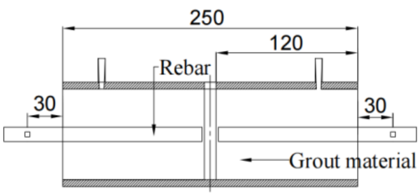

a) Sleeve specimen reinforcing steel strain gauge arrangement

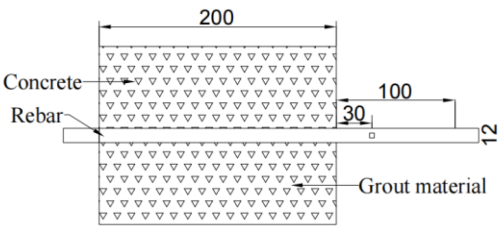

b) Cast-in-place specimen reinforcemen strain gauge arrangement

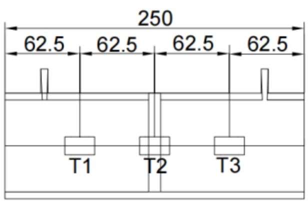

c) Sleeve strain gauge arrangement

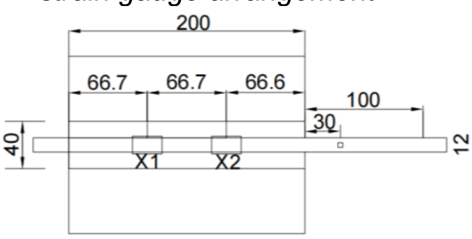

d) Concrete strain gauge arrangement

Fig. 2 – Measurement point arrangement

DOI 10.14311/CEJ.2025.02.0012

Strain gauges for rebar were arranged 30 mm away from the top and bottom of the sleeve (as shown in Figure 2(a) or 30 mm away from the concrete edge of the cast-in-place specimen (as shown in Figure 2(b). The sleeve specimen was divided into four equal-length parts, and then six strain gauges were affixed axially and symmetrically at the equal points, numbered T1-T6, as shown in Figure 2(c). Meanwhile, the cast-in-place specimen was divided into three equal parts. Four strain gauges were affixed axially and symmetrically in each equal part, labelled X1-X4, as shown in Figure 2(d). For displacement sensors, one was arranged 50 mm away from the top and bottom of the sleeve or 50 mm away from the concrete edge of the cast-in-place specimens. MTS universal testing machine was used in this test. The force-controlled loading mode was selected with a rate of 500N/s before specimen yielding, while the displacement-controlled mode was adopted with a rate of 0.25mm/s after yield.

TEST RESULTS AND DISCUSSION

Test phenomenon and failure patterns

Failure patterns and grouting failure for these sleeve specimens under uniaxial tension are shown in Figure 3 and Figure 4. When critical damage occurred, when the two bonds reached the maximum bond strength and the reinforcement did not reach the ultimate strength, the reinforcement was pulled out. The sleeve connector specimens showed slight displacement of the reinforcement first, followed by a yielding phase. Microcracks appeared in the grout, and the slip between the grout and the rebar increased significantly. Then, the slip of both continued to increase, and the grout at the ports spalled off.

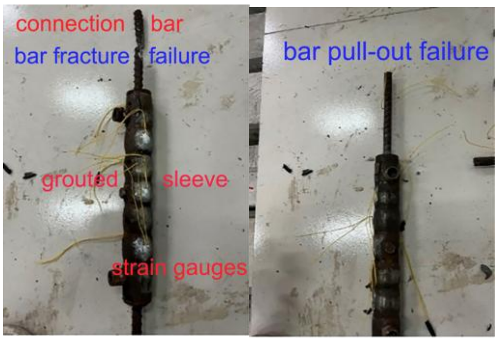

a) Bar fracture failure *b) Bar pull-out failure*

Fig.3 – Failure patterns of the grout sleeves

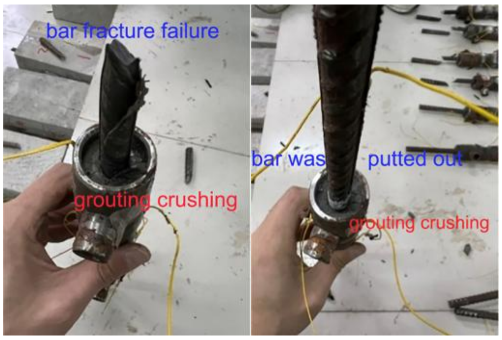

a) Bar fracture failure *b) Bar pull-out failure*

Fig.4 – Grouting crushing

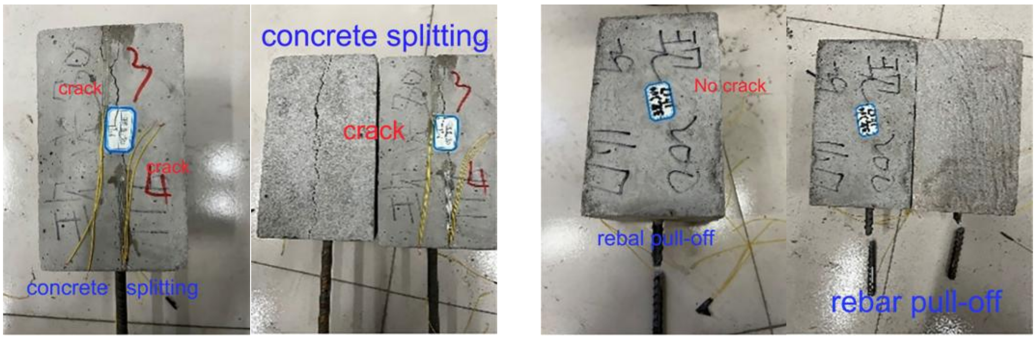

a) Concrete splitting *b) Rebar pull-off*

Fig. 5 – Failure patterns of cast-in-place specimens

Failure patterns for these cast-in-place (CIP) specimens under uniaxial tension are shown in Figure 5. As the specimens yielded, concrete microcracks appeared and developed from the

DOI 10.14311/CEJ.2025.02.0012

boundary to the center, and the rebar showed significant slippage. As the specimens entered the strengthening stage, a small amount of concrete was dislodged, cracks of varying degrees appeared, and slip continued to increase in this stage.

Load-strain curves

Figure 6 shows the load-strain curves of some grouted sleeve specimens. The sleeve strains of all specimens showed an overall increasing trend. The strains（T2, T5) in the middle of the sleeve are larger than the other four strains (T1, T4 & T3, T6). Since the reinforcement did not yield, the surface of the embedded rebar portion remained in contact with the grout, and the tensile force of the rebar was effectively transmitted to the inner wall of the sleeve through the grout. The strain of the corresponding sleeve increased from the outside to the inwards, with the maximum strain occurring in the middle of the sleeve. However, it began to elongate and thin when the steel at the end of the sleeve entered the yielding phase. Consequently, the outer surface of the rebar was no longer in close contact with the grout. Subsequently, wedge-shaped damage occurred, resulting in a reduced tensile force transmitted to this section of the sleeve through the grout and decreased strain in the end region of the sleeve. Then, the effective restraint of the sleeve on the rebar shifted inward, and the corresponding strain inside the sleeve continued to increase, with the maximum strain value still occurring in the middle of the sleeve. Figure 7 shows the reinforcement strain inside the grouted sleeve to explore the stress-strain relationship. The maximum and minimum strains of the rebar were around 3000×10^{-6} and 2000×10^{-6}, respectively. The strain in the upper reinforcement of the TT-0.10-100 specimen was only about 1500×10^{-6}, while the reinforcement did not reach the yield point. The strains in the upper reinforcement in all four specimens (TT-0.10-70, TT-0.12-100, TT-0.12-70&TT-0.12-50) were around 2000×10^{-6}, and the strain value also did not meet the requirement for the reinforcement to yield. In summary, the upper reinforcement inside the grouted sleeve was either yielding or not yielding. In the meantime, the lower reinforcement reaches its ultimate strength, and the strain of the lower reinforcement is greater than that of the upper reinforcement. As the length of the embedded rebar increased, the restraining effect of the sleeve on the rebar became more pronounced.

Figure 8 shows the load-strain curve of CIP specimens. It is found that the strain of CIP specimens gradually increased with the load. Except for the strain at X2 of XJ-120-C40, which was greater than -250×10^{-6}, the strains of other specimens were less than -150×10^{-6}. The strains (X2, X4) were approximately -250×10^{-6}, while the strains (X1, X3) were approximately -40×10^{-6}. The strain increase of the lower concrete (X2, X4) of the specimens was significantly faster than that of the upper concrete (X1, X3), which is attributed to the strain disparity in the upper and lower parts of the specimens. The load-strain curve for reinforcement of the CIP specimen is shown in Figure 9. The reinforcement strain on XJ-200-C40 was more than 3000×10^{-6}, and the reinforcement strains on XJ-160-C40 and XJ-80-C40 were not more than 2500×10^{-6}, indicating a slight difference.

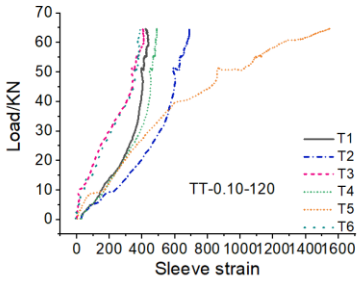

a) TT-0.10-120

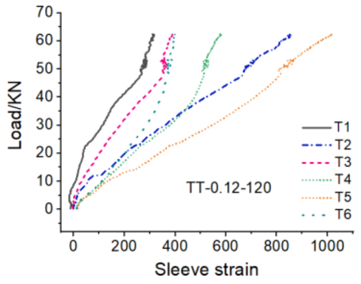

b) TT-0.12-120

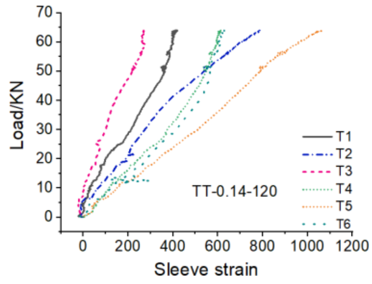

c) TT-0.14-120

Fig. 6 – Load-strain curves of grouted sleeve

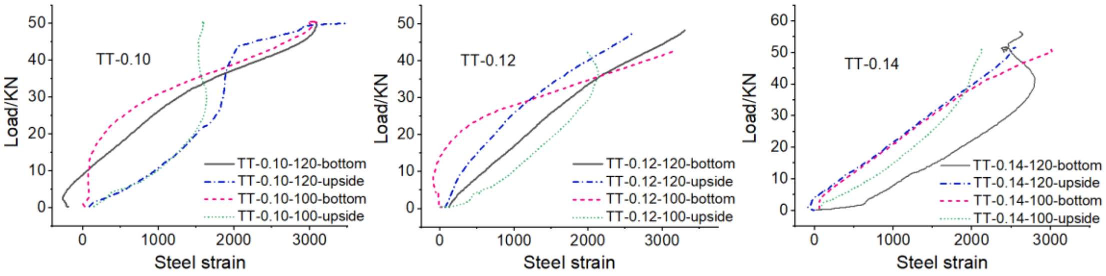

a) TT-0.10 b) TT-0.12 c) TT-0.14

Fig. 7– Load-strain curves of reinforcement inside the grouted sleeve

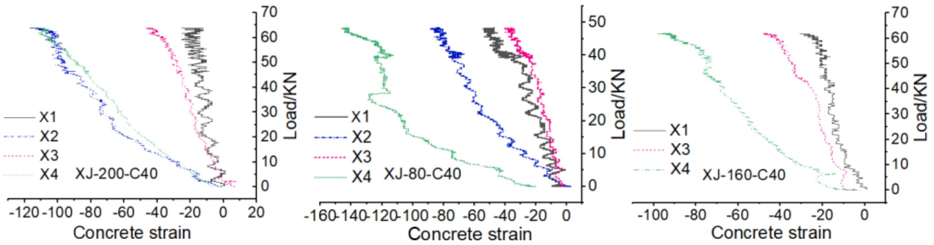

a) XJ-200-C40 b) XJ-160-C40 c) XJ-80-C40

Fig. 8 – Load-strain curves of CIP specimens

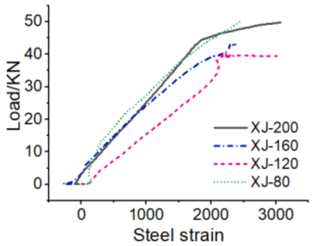

Fig. 9 – Load-strain curves of reinforcement inside the CIP specimens

Bond stress and slip of the connections

The average bond stress τ of the reinforcement and grout and concrete is the ratio of the peak load to the anchorage area, as given in Equation (1). The slip of the rebar S_s is the difference between the displacement of specimen S and the elongation of the rebar necking is defined in Equation (2).

$$\tau = \frac{P_\mu}{\pi d l} \tag{1}$$

$$S_s = S - \frac{4 P_\mu \Delta l}{\pi d^2 E_s} \tag{2}$$

where P_μ is the peak load; l is the anchorage length; Δl is the distance between the fixture and the top of the bonded area; E_s is the elasticity modulus of reinforcement.

The average bond stress and slip of the grouted sleeve and cast-in-place connectors could be obtained based on the equations and experimental data. It can be seen that when the water-to-cementitious material ratio was 0.10, the specimens experienced fracture failure of the rebar. When the water-to-cementitious material ratios were 0.12 and 0.14, the TT-0.12-50 and TT-0.14-50 specimens exhibited pull-out failure of rebar. The average bonding stress of the TT-0.12-50 and TT-0.14-50 specimens was 1.92 and 2.23 times the 120mm anchorage length under the same conditions, respectively. The rebar slips of the TT-0.12-50 specimen increased by 25.6% compared to the TT-0.12-120 specimen. The average bonding stress of the XJ-200-C40 and XJ-120-C40 specimens was determined as 8.51MPa and 11.89MPa, respectively, while the corresponding rebar slips were 9.20mm and 9.49mm. The disparity in the average bonding stress is because the contact area between the reinforcement bar and the grout was increased with the increasing anchorage length, and the stress transfer between the grout and the reinforcement was strengthened. Therefore, to avoid pull-out failure of rebar in the actual project and to ensure the safety and stability of the component, it is recommended that the anchorage length of the sleeve specimen be taken as≥8.3l_α and the anchorage length of the cast-in-place specimen be taken as ≥10l_α.

It is inferred from Table 1 that the TT-0.10-120 specimen and the XJ-200-C40 specimen exhibited the best mechanical performance among the two connection types. In addition, the table enlists a performance comparison of the two specimens, revealing minimal differences in peak load and slip between the sleeve and cast-in-place connections, indicating that the grouting sleeve connection meets the bond performance requirements.

Tab. 1 - Average bond stress and slip of specimens

Serial No.	Peak load/kN	Reinforcing bar stress/MPa	Average bond stress/MPa	Slip/mm
TT-0.10-120	64.81	573	14.33	9.32
TT-0.10-100	63.33	560	16.81	10.53
TT-0.10-70	61.65	545	23.37	11.28
TT-0.10-50	60.37	534	32.04	12.45
TT-0.12-120	64.33	569	14.23	10.31
TT-0.12-100	63.09	558	16.74	10.93
TT-0.12-70	61.03	540	23.14	11.27
TT-0.12-50	60.84	538	32.29	12.95
TT-0.14-120	64.60	571	14.29	10.67
TT-0.14-100	62.86	556	16.68	11.30
TT-0.14-70	62.96	557	23.87	13.84
TT-0.14-50	60.05	531	31.87	9.38
XJ-200-C40	64.13	567	8.51	9.20
XJ-160-C40	61.90	547	10.27	11.55
XJ-120-C40	53.76	475	11.89	9.49
XJ-80-C40	48.92	432	16.23	6.10

FINITE ELEMENT ANALYSIS (FEA)

The seismic performance of the assembled bridge substructure was analyzed using the ABAQUS finite element (FE) method. First, the bond-slip constitutive relationship for reinforced concrete was proposed. Then finite element models (FEMs) were developed based on this constitutive relation. In order to ensure the reliability of the subsequent calculations, the numerical results were verified against test results to validate the rationality and reliability of the proposed method. Then the FEMs of assembled bridge substructure specimens and cast-in-place bridge substructure specimens were developed on this basis to assess the seismic performance of assembled bridge substructure from multiple angles.

FE Models

FEA was used to simulate to assess the damage mechanism of the assembled bridge substructure. Three sets of FEMs, PC-01, PC-02, and RC, were designed in this section. FEM comprises a bearing platform, cover beam, column, sleeve, and reinforcements, where the reinforcement ratio of the piers was 1.14%, which meets the requirements of the code in the range of 0.6%~5%, as shown in Figure 10. The parameters of the model specimen and material are shown in Table 2 and Table 3, respectively. The concrete was modeled by C3D8R, while the reinforcement was simulated by T3D2. One difficulty in the modeling was simulating the bond stress-slip relationship between the reinforcement and grout. Bond behavior between reinforcement and grout is little available in the literature. Thus, the bond-slip relationship between reinforcement and concrete is proposed using experimental data.

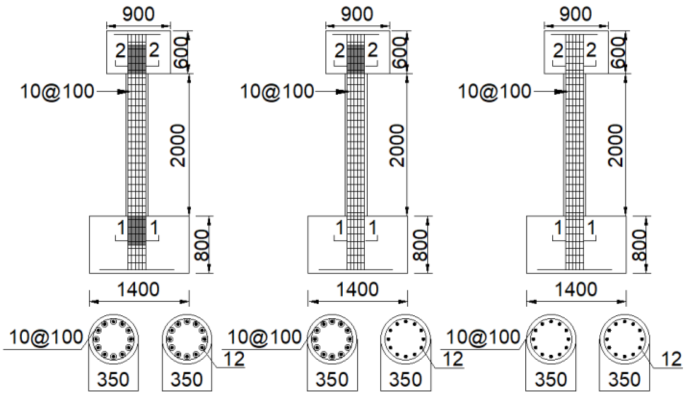

a) PC-01 b) PC-02 c) RC

Fig. 10 – Dimensions and reinforcement of three sets of models

Tab. 2 - Model parameters

Specimen No.	Connection of Pier- Bent Cap	Connection of Pier-Pile Cap	Axial Pressure Ratio	Reinforcement Rate
PC-01	grouted sleeve connection	Grouting sleeve connection	0.3	1.14%
PC-02	grouted sleeve connection	cast-in-place	0.3	1.14%
RC	cast-in-place	cast-in-place	0.3	1.14%

Tab. 3 - Material parameter values

Material	Elastic Modulus /GPa	Poisson's Ratio	Yield Strength /MPa	Ultimate Strength /MPa	Invariant Stress Ratio	Expansion Angle	Strain hardening exponent	Viscosity Coefficient
Sleeve	210.0	0.3	395	600	/	/	/	/
Steel Bar	200.0	0.3	335	429	/	/	/	/
Concrete	32.5	0.2	/	/	0.67	38	0.1	0.005
Grouting	41.0	0.2	/	/	0.67	38	0.1	0.005

Bond-Slip Constitutive Relation

Based upon the sub-section titled ‘Bond stress and slip of the connections, a constitutive

Article no. 12

THE CIVIL ENGINEERING JOURNAL 2-2025

relation considering bond-slip between reinforcement and concrete was proposed. A three-stage constitutive model was selected to simulate the bond-slip constitutive relation of reinforced concrete under uniaxial tension, as shown in Equation (3) [14]. The bond-slip curves of the connectors can be divided into the micro-slip stage, the slip acceleration stage, and the decline stage.

$$\tau = \begin{cases} \frac{\tau_s}{S_s} S & (0 < S \leq S_s) \\ \tau_s + \frac{\tau_s - \tau_\mu}{(S_s - S_\mu)}(S - S_s)^2 & (S_S < S \leq S_\mu) \\ \tau_\mu + \frac{\tau_r - \tau_\mu}{(S_r - S_\mu)}(S - S_\mu)^2 & (S_\mu < S \leq S_r) \end{cases} \quad (3)$$

where s is the end point of the micro-slip, and the corresponding bond stress and slip are expressed by τ_s and S_s; μ is the maximum point of the bond-slip curve; τ_μ and S_μ denote the corresponding bond stress and slip; r is the break point of the connection reinforcement; the corresponding bond stress and slip are expressed by τ_r and S_r.

The characteristic points (s, μ, r) in the three-stage constitutive model for the connection were decided based on the statistical analysis of the bond-slip data, as listed in Table 4. Then, using Equation (3), the bond-slip curves of TT-0.10-12 and XJ-200-C40 were fitted. It could be seen that the fitting results are approximately the same as the test results, indicating that the three-stage constitutive model matches the bond-slip curves of the two specimens well, as shown in Figure11. And the probability of bond-slip damage in XJ-200-C40 is greater than TT-0.12-200. Therefore, the fitted bond-slip curve of XJ-200-C40 was selected as the bond-slip constitutive relation of reinforced concrete for numerical simulations.

Tab.4 - Parameter values for the characteristic points

Specimen No.	τ_s /MPa	S_s /mm	τ_μ/MPa	S_μ/mm	τ_r /MPa	S_r/mm
XJ-200-C40	6.7	1.79	8.51	9.20	7.46	10.89
TT-0.10-120	11.25	1.19	14.33	9.32	11.63	12.57

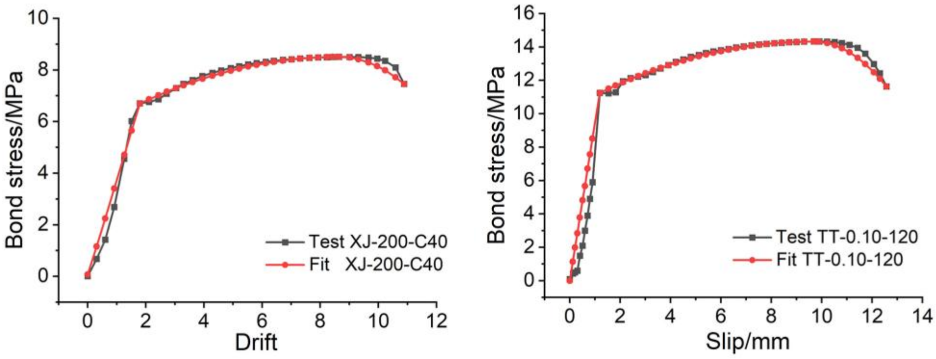

a) XJ-200-C40 *b) TT-0.10-120*

Fig. 11– Comparison of bond-slip curves

Model validation

In this paper, the test data were taken from the mechanical performance test of a prefabricated bridge pier by Huang [15]. ABAQUS was used to simulate the static performance of the prefabricated pier connected by the grouted sleeve, and the reasonable parameters were compared with the experimental results.

The failure pattern, stress nephogram, compressive damage nephogram, and tensile damage nephogram of specimens are shown in Figure 12 to Figure 13. The ultimate failure was represented by concrete crushing and peeling on the loading direction of the pier. The corner (lower left corner of Figure 12) was severely affected by concrete crushing and peeling. In addition, within approximately 20 cm from the base of the pier, the concrete was completely damaged, with compressive-flexural failure being the primary type of failure. The FE simulation successfully matched the cracking development, and the model failure patterns were identical to the specimens.

DOI 10.14311/CEJ.2025.02.0012

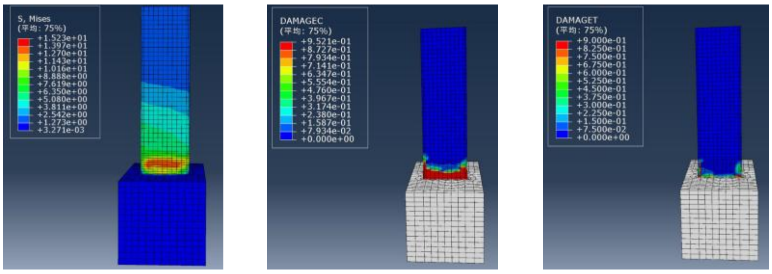

a) Stress *b) Compressive damage* *c) Tensile damage*

Fig.12– Failure pattern

Fig. 13– Nephogram of stress,compressive damage and tensile damage

The hysteresis and skeleton curves of the FEA and prefabricated specimens are shown in Figure 14. The hysteresis loops of the FEA and prefabricated specimens became gradually complete with increasing displacement. The envelopes of hysteresis curves were quite similar and showed excellent pinching effects and energy dissipation. The numerical simulation result of the skeleton curve was consistent well with the experimental result. The ultimate load and displacement simulation errors were 1.7% and 4.2%, respectively, validating model accuracy.

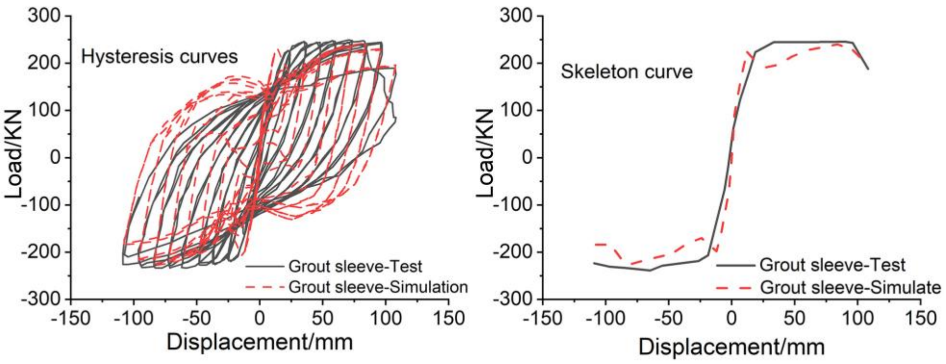

a) Hysteresis curve *b) Skeleton curve*

Fig. 14 – Hysteresis curve and Skeleton curve of grouting sleeve specimen

FEA results

Analysis of damage pattern

Figure 15 (a)-(f) showed the stress distribution of the FEM. Significant bulging occurred as significant stress was experienced on both sides of the loading direction. The stress was concentrated in the plastic hinge area at the bottom of PC-02, but was mainly exhibited at the top and middle of PC-01. Compared with PC-01 and PC-02, the maximum yield stress value and larger yield area indicate that the RC model had the best overall stability, as shown in Figure 15 (a)-(f). Then, Figure 15 (g)-(l) further revealed the damage process of the model. First, the model experienced cracks on both sides of the column, which gradually developed into 45-degree diagonal cracks and rapidly expanded toward the point of concentrated load. Due to the effect of grouted sleeves, the plastic hinge region at the bottom of PC-02 was longer than the RC specimens, and higher compressive damage was experienced at the bottom of the column. The plastic hinge region at the bottom of PC-01 was similar to the RC specimens. The concrete at the bottom of the column was stripped and failed, and the rebar yielded with the cracks developed, resulting in the specimen being crushed. The specimen exhibited a bending failure mode. The specimen experienced severe tension damage on both sides of the concrete, which gradually developed towards the column.

Concrete at the bottom of the column for PC-01 and PC-02 experienced significantly higher tension damage than the RC specimen. The RC specimen experienced the least tension damage, indicating excellent stability. The PC-01 experienced moderate tension damage and did not exhibit a propensity to propagate towards the column, whereas PC-02 experienced the most severe tension damage and tended to develop to the column. Lastly, Equivalent plastic strain clouds of the model are presented in Figure 15 (m)-(o). Significant equivalent plastic strain at both sides of the column gradually developed towards the column. The equivalent plastic strain at the bottom of the PC-01 and PC-02 was more significant than the RC specimen. No slip phenomenon was observed at the bottom of PC-02 and RC columns, while there was a noticeable slip phenomenon at PC-01.

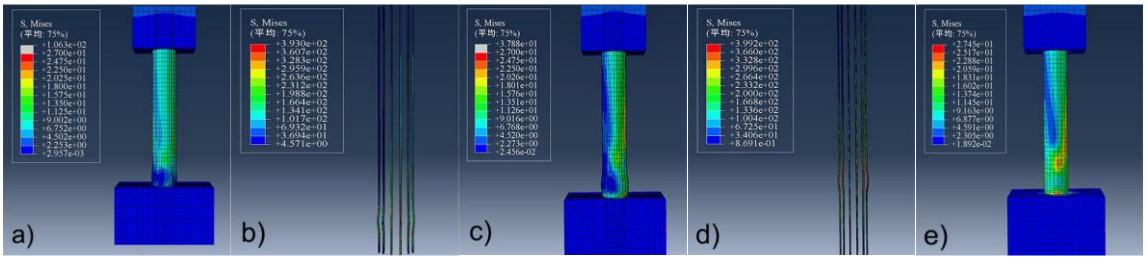

a) PC-01 stress cloud *b) PC-02 stress cloud* *c) RC stress cloud* *d) PC-01 steel stress cloud* *e) PC-02 steel stress cloud*

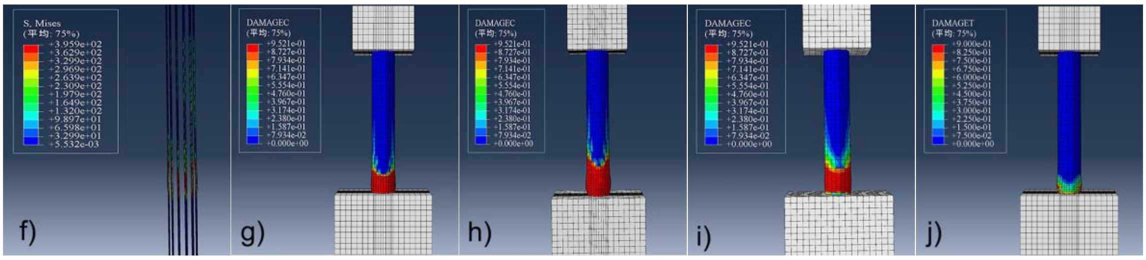

f) RC steel stress cloud *g) PC-01 compressive damage cloud* *h) PC-02 compressive damage cloud* *i) RC compressive damage cloud* *j) PC-01 tensile damage cloud*

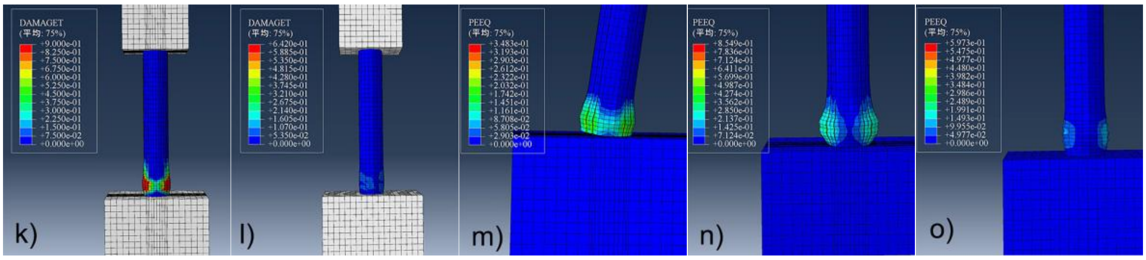

k) PC-02 tensile damage cloud *l) RC tensile damage cloud* *m) PC-01 equivalent plastic strain cloud* *n) PC-02 equivalent plastic strain cloud* *o) RC equivalent plastic strain cloud*

Fig. 15– Stress-yield, compressive-tensile damage, and equivalent plastic strain clouds for models

Comparative analysis of seismic performance

The seismic performance response of cast-in-place bridge substructure (RC) and grouted sleeve connection precast bridge substructure (PC) are shown in Figure 16 through Figure 18 and Table 5. Figure 16 and Figure 18 show minimal differences between the hysteretic and skeleton curves between the RC and PC. The hysteretic curves of the three specimens showed a full or shuttle shape, indicating the specimens with strong plastic deformation ability. In addition, the pinching phenomenon of the hysteresis curve of PC-01 was a bit obvious. The ultimate bearing capacities of the PC-01, PC-02, and RC are 136.9 kN·m, 153.1 kN·m, and 183.8 kN·m, respectively. The RC specimen had the highest ultimate bearing capacity compared with PC-02 and PC-01. The ultimate bearing capacity of PC-01 was 74.5% of RC. Similarly, PC-02 was 83.3% of RC. In Figure 17, it can be seen that the cumulative energy consumption of RC and PC were similar. The final cumulative energy consumption of RC is 18% higher than that of PC-02; meanwhile, PC-01 is 27.2% lower than that of PC-02. In summary, the final cumulative energy consumption of PC-01 was slightly lower than that of RC, but PC-02 exhibited a similar level to that of RC. Further, Figure 18 shows that the stiffness degradation curves of RC and PC were almost identical. First, the slope of stiffness degradation was large in the initial stage and then gradually tended to level. The maximum cut-line stiffness of PC-01, PC-02, and RC were 22639.2kN·m, 23930.4kN·m, and 24561.7kN·m, respectively. The initial stiffness of PC-01 was smaller than that of RC, while the stiffness degradation of PC-02 was slightly greater than that of RC. Based on Table 5, the yield displacement of PC-01, PC-02, and RC were 6.3mm, 6.5mm, and 8.1mm, respectively. Meanwhile, the ultimate displacement of PC-01, PC-02, and RC were 21.5mm, 21.6mm, and 25.2mm, respectively. The displacement ductility coefficient of PC-01and PC-02 were 110.6% and 107.7% respectively, when compared with RC. Indicating that the prefabricated bridge substructure with grouted sleeve connection had better ductility. In summary, the seismic performance of PC reached a similar degree to that of RC.

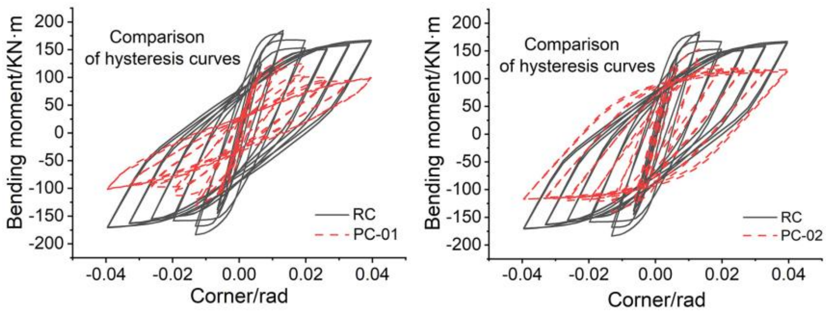

a) PC-01 and RC *b) PC-02 and RC*

Fig.16 – Hysteresis curves of the developed models

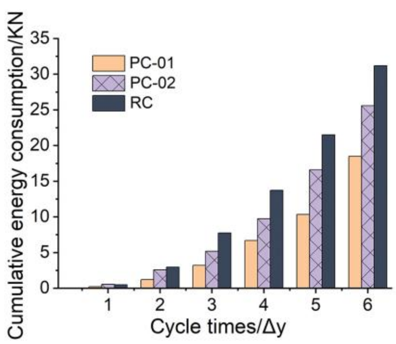

Fig.17– Cumulative energy dissipation of the developed models

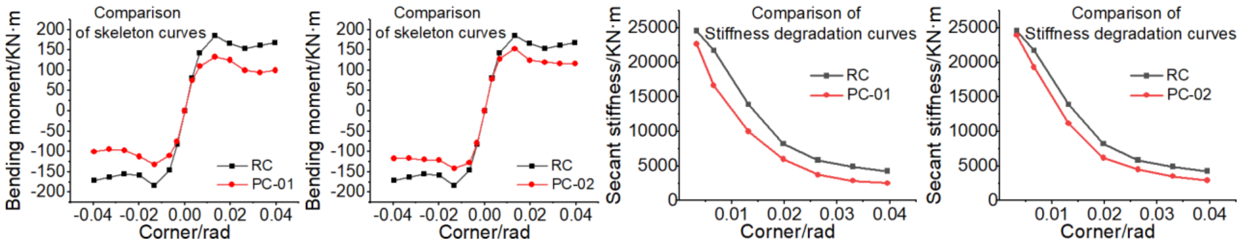

a) PC-01 and RC skeleton curves

b) PC-02 and RC skeleton curves

c) PC-01 and RC stiffness degradation curves

d) PC-02 and RC stiffness degradation curves

Fig.18 – Skeleton curves and Stiffness degradation of the developed models

Tab.5 - Results of the FEMs

No.	Ultimate bearing capacities /kN·m	Yield displacement /mm	Ultimate displacement /mm	cumulative energy consumption/kN·m	Maximum cut-line stiffness/kN·m	Ductility
PC-01	136.9	6.3	21.5	40.2	22639.2	3.44
PC-02	153.1	6.5	21.6	58.2	23930.4	3.35
RC	183.8	8.1	25.2	77.7	24561.7	3.11

PARAMETRIC INVESTIGATION

Determination of parameters

A parametric investigation to analyze the effect of different design variables (axial compression ratio, hoop reinforcement ratio, and concrete strength) on the seismic performance of prefabricated bridge substructure with grouted sleeve is presented in this section. PC-01 was selected as the control specimen for the parametric analysis. Each subsection is briefly described in terms of adjusted variables, and the outcomes are discussed.

Effect of axial pressure ratio

The axial pressure ratios of the developed models were 0.3, 0.2, and 0.1, respectively, while other parameters were the same. Seismic performance response parameters of the prefabricated bridge substructure connected by the grouted sleeve with a different axial pressure ratio are shown in Figure 19, which indicate that the axial pressure ratio had a remarkable effect on the seismic performance of the prefabricated bridge substructure. It is also observed that the ultimate bearing capacity and cumulative energy consumption increased by 28.4% and 14%, respectively, with the axial pressure ratio increasing from 0.1 to 0.2. Meanwhile, the ductility factor increased by 28.1% (Table 6). With the axial pressure ratio of the model increased from 0.2 to 0.3, the ultimate bearing capacity and cumulative energy consumption increased by 18.6% and 29.3%, respectively, while the ductility factor of displacement decreased by 4.4%. In addition, the maximum secant stiffness values for models were 14,969.4kN·m, 20,307.9kN·m, and 22,639.3kN·m, respectively. When the axial pressure ratio of the model increased from 0.1 to 0.3, the ratio of final cut-line stiffness to initial cut-line stiffness was 9.3%, 10.1%, and 11.2%, respectively. As the axial pressure ratio increased, the peak bearing capacity, cumulative energy consumption, and stiffness obviously increased, the ductility factor of displacement increased and then decreased.

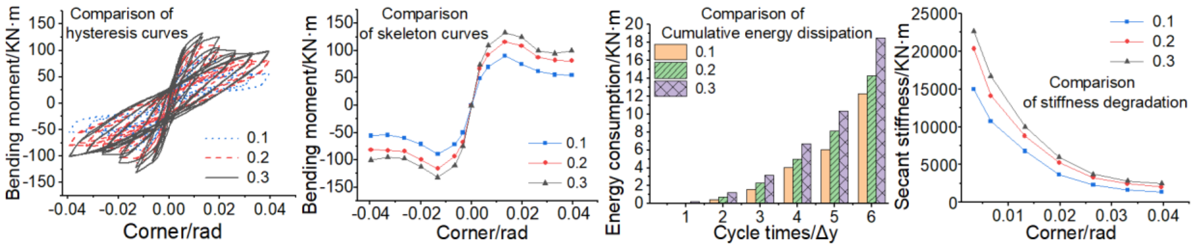

a) Hysteresis curves b) Skeleton curves c) Cumulative energy dissipation d) Stiffness degradation

Fig. 19 – Comprehensive evaluation curve of seismic performance with different axial pressure ratios

Effect of hoop diameter

The hoop diameters of the developed models were 10mm, 12mm, and 14mm, respectively, and other parameters are the same. Subfigures 1 and 2 show the hysteresis and skeleton curves of the model with different hoop diameters. The increase in the hoop diameter led to a slight increase in the peak bearing capacity, whereas the ultimate bearing capacity and hysteresis loop area did not change much. Subfigures 3 and 4 show that as the hoop diameter increased, there was no significant change in cumulative energy consumption and stiffness. Table 6 indicates that the ductility factor was increased by 0.87% and 2.61%, respectively, when the hoop diameter increased from 10mm to 12mm or 14mm. The variation in hoop diameter had little influence on the ductility. The comparisons of the diagrams showed that the hoop diameter had little effect on the seismic performance of the prefabricated bridge substructure.

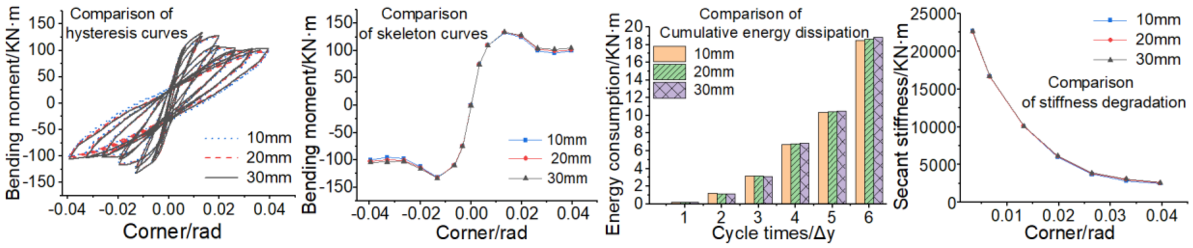

a) Hysteresis curves b) Skeleton curves c) Cumulative energy dissipation d) Stiffness degradation

Fig. 20 – Comprehensive evaluation curve of seismic performance with different hoop diameters

Effect of concrete strength

The concrete compressive strengths of the developed models were C40, C30, and C50, respectively, while the other parameters were the same. Subfigures 1 and 2 show the hysteresis and skeleton curves of the model with different concrete strengths. As the concrete grade changed from C30 to C40 or C50, the ultimate bearing capacity was increased by 12.7% and 21.9%, respectively. Strength change led to a pronounced increase in the ultimate bearing capacity and hysteresis loop area. Subfigures 3 and 4 indicate that the concrete strength significantly influenced the cumulative energy consumption and stiffness. The initial stiffness and cumulative energy consumption increased as the concrete strength increased; however, stiffness degradation became severe. Table 6 indicates that with the concrete changed from C30 to C40 or C50, the ductility was decreased by 11.1% and 10.1%, respectively. The comparisons of the diagrams showed that improving concrete strength is beneficial to enhancing seismic performance.

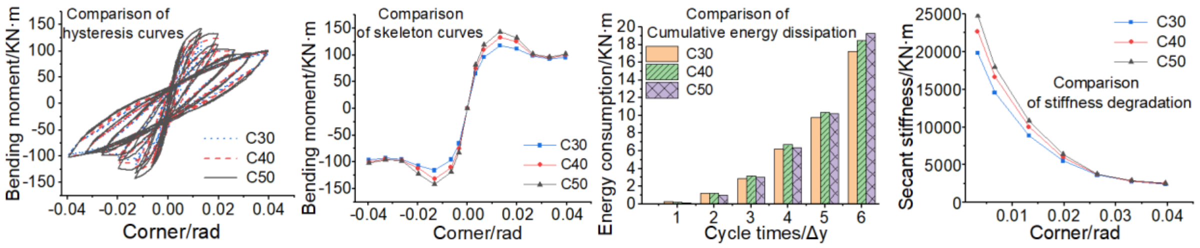

a) Hysteresis curves *b) Skeleton curves* *c) Cumulative energy dissipation* *d) Stiffness degradation*

Fig. 21– Comprehensive evaluation curve of seismic performance with different concrete strengths

Tab.6 - Ductility factors for different design variables

Variable		Positive Yield Displacement/m	Ultimate Displacement /m	Negative Yield Displacement/m	Ultimate Displacement /m	Ductility
Axial	0.1	0.0068	0.0191	0.0065	0.0182	2.81
Pressure	0.2	0.0061	0.0229	0.0060	0.0206	3.60
Ratio	0.3	0.0063	0.0232	0.0062	0.0198	3.44
	10	0.0063	0.0232	0.0062	0.0198	3.44
Hoop	12	0.0063	0.0234	0.0063	0.0203	3.47
Diameter	14	0.0064	0.0237	0.0063	0.0212	3.53
	C30	0.0065	0.0254	0.0063	0.0242	3.87
Concrete	C40	0.0063	0.0232	0.0062	0.0198	3.44
	C50	0.0062	0.0220	0.0060	0.0203	3.48

CONCLUSIONS

In this paper, the seismic performance of prefabricated bridge substructures using grouted sleeve connectors and CIP bridge substructures was compared by FEA, and a parametric investigation was performed to assess the seismic performance of prefabricated bridges. main conclusions as follows:

(1) The uniaxial tension tests indicate that extend the anchorage length was shown to enhance connection capacity, and it is recommended that the anchorage length of the grouted sleeve connection be taken as ≥8.3 *lα* and ≥10 *lα* for the cast-in-place connections.

(2) The bond-slip constitutive relation was proposed based on the experimental results to refine the FE model, considering bond and slip between reinforcement and sleeve or concrete, and elucidating the bond-slip constitutive relation of the grouted sleeve joint and the simulation method.

(3) Failure modes of the prefabricated bridge substructure connected by the grouted sleeve were the same as the cast-in-place bridge substructure, and the hysteresis responses of the models were similar. PC-02 had ultimate bearing capacity, cumulative energy consumption, ultimate displacement, maximum cut-line stiffness and ductility values of 83.3%, 82.0%, 74.5%, 92.2% and 107.7%, respectively, when compared with RC.

(4) Parametric investigation results showed that concrete strength and axial compression ratio remarkably affected seismic performance. As the concrete strength and axial compression ratio increased, the bearing capacity, cumulative energy consumption, and stiffness increased significantly. The effect of hoop diameter on seismic performance is not significant.

(5) The relevant FEMs, methods, and research results can provide reference and inspiration for the prefabricated bridges substructure connected by grouted sleeves.

ACKNOWLEDGMENT

This work was supported by Shandong Provincial Natural Science Foundation, China [grant number ZR2020ME241]; Shandong Provincial Natural Science Foundation, China [grant number ZR2021ME004]; Shandong housing and urban rural construction science and technology plan project, China [grant number 2020-K4-12].

REFERENCES

[1] Song L., Kai P., 2021. Seismic performance of grouted sleeve connected precast pier based on steel hysteretic model, Earth and Environmental Science, vol. 634:012133.

[2] Bao L., Zhao J., Teng F., et al.,2023. Experimental study on the seismic performance of prefabricated frame piers. Structures, vol. 52:651-665.

[3] Luo X., Long H., et al., 2021. Study on finite element model of the prefabricated reinforced concrete beam-column joints with grouted sleeves. Advances in Civil Engineering, vol.5552380.

[4] Cheng Y., Chen W., Xu T., et al., 2016. Analysis of susceptibility of bridge construction process in aftershock areas. Engineering Mechanics, vol. 33: 251-256.

[5] Li X., Zhang G., Han Q., et al., 2023. Shear Behavior of Low-Aspect-Ratio Precast Bridge Columns with Grouted Sleeve Connection Considering the Effect of Axial Load Ratios. Journal of Bridge Engineering, vol.281: 115755.

[6] Liu H., Chen J., Xu C., et al.,2020. Seismic performance of precast column connected with grouted sleeve connectors. Journal of Building Engineering, vol. 31: 101410.

[7] Lu Z., Huang J., Li Y., et al.,2019. Mechanical behavior of grouted sleeve splice under uniaxial tensile loading. Engineering Structure, vol. 186:421-435.

[8] Liu Y., Li X., Zheng X., Song Z., et al.,2020. Experimental study on seismic response of precast bridge piers with double-grouted sleeve connections. Engineering Structures, vol. 221: 111023.

[9] Haber Z B., Saiid M., David S., et al.,2014. Seismic performance of precast column with mechanically spliced column-footing connection. ACI Structural Journal, vol. 111:639-650.

[10] Zhang G., Han Q., Xu K., et al., 2023. Numerical analysis and design method of UHPC grouted RC column- footing socket joints. Engineering Structures, vol. 281: 115755.

[11] Li X., Zhang G., Han Q., et al.,2023. Mechanical behavior of splice joints for bridge columns connected by grouted sleeves. Soil Dynamics and Earthquake Engineering, Vol.173: 108078.

[12] Ministry of Housing and Urban-Rural Development of the People's Republic of China. Grouting sleeves for reinforcing steel connections: JG/T398-2019. Beijing, China Standard Press. 2019.

[13] State Administration of Market Supervision and Administration. Test method of cement mortar strength: GB/T 17671-2021. Beijing: China Standard Press. 2021.

[14] Ministry of Housing and Urban-Rural Development of the People's Republic of China. Code for design of concrete structures: GB 50010-2010, Beijing, China Architecture & Building Press, 2011.

[15] Huang Y.,2016. Research on the seismic performance of assembled reinforced concrete bridge piers. M.A. dissertation, Dalian University of Technology, Dalian, China.

CIVIL ENGINEERING JOURNAL

Article no. 13

THE CIVIL ENGINEERING JOURNAL 2-2025

MECHANICAL PROPERTIES ANALYSIS OF A CABLE-STAYED BRIDGE WITHOUT BACKCABLES UNDER THE INFLUENCE OF TEMPERATURE AND INCLINATION ANGLE

Dandan Hu[1], Liangxiang Guo[2] and Xuezhao Xu[3]

1. *School of Civil and Architectural Engineering, Harbin University, No.109 Zhongxing Road, Harbin, Heilongjiang Province, China; Hardandan@163.com*
2. *Engineering Department, Guangzhou Highway Engineering Group Co. LTD, No. 6 Shuiyin Erheng Road, Guanzhou, Guangdong Province, China; 854364064@qq.com*
3. *Engineering Department, Guangzhou Expressway Co., LTD, No.17 Fenghuang San Road, Guanzhou, Guangdong Province, China; 759408235@qq.com*

Received:	*10.08.2024*
Received in revised form:	*01.01.2025*
Accepted:	*24.07.2025*

ABSTRACT

Cable-stayed bridge without backcables is an important branch of the cable-stayed bridge family. It tilts the bridge tower to one side and removes the cable behind it. It balances the cable force of the cable-stayed cable with its own weight. This paper relies on the construction project of the main bridge, and uses finite element analysis software to establish a space model to simulate and analyze the construction process, focusing on the influence of the bridge tower inclination and temperature. When the inclination angle of the bridge tower changes within a certain range, it has little effect on the stiffness and strength of the structure, but under the condition that the stress of the tower girder is roughly the same, the greater the inclination angle of the tower, the greater the counterweight of the tower, and the greater the material consumption of the tower. Angle of the tower, the greater the counterweight of the tower, and the greater the material consumption of the tower. When the bridge tower is 52 °, 55 ° and 58 °, the stress on the left side of the bridge tower is -5.8 MPa, -4.1 MPa and 0.7 MPa, respectively.

KEYWORDS

Cable-stayed bridge without back cable, Tilt angle of the main tower, Temperature variation, Parameter analysis

INTRODUCTION

Cable-stayed bridge's main feature is to use the stay cable as the elastic support of the girder span, reduce the section bending moment of the trabecular span, reduce the weight of the main girder, and improve the crossing ability of the main girder [1].

Since the 1990s, with the development of the world's cable-stayed bridge construction technology, China's cable-stayed bridge ushered in a new development opportunity and opportunity, have built a lot of span more than 500 m long span cable-stayed bridges [2-4]. It has trained many bridge design and construction talents, and accumulated a lot of valuable construction experience and technology. After the construction of a number of world-leading kilometer-level cable-stayed bridges, through decades of hard work and independent innovation, China's cable-stayed bridge construction level is moving towards the world's top level [5, 6].

In the continuous development of cable-stayed bridges, people have found that it is completely possible to increase the tower tilt angle, and finally form a more unique and novel structural form - cable-free cable-stayed bridges [7-10]. Remove the cable from one side of a single-pylon cable-stayed bridge, and tilt the cable tower to that side to balance the cable-stayed force with its own weight [11]. The characteristics of cable-less cable-stayed bridge are that the positive bending distance of the main beam is all balanced by the overturning moment generated by the cable from the tilt of the bridge tower, and the force is more complex, especially at the joint of the tower, beam and pier, not only the axial force, shear force and bending moment of the main beam, but also the torque and the joint action between them.

In terms of visual effects, the bridge has a strong impact, enough to attract people's attention, and after construction, it has become a representative building of the city, which is favored by designers and local governments [12-15]. However, this type of bridge is not built in the world, the analysis of the reasons, first of all, the force state of this type of bridge is complicated, there are many factors to consider, and the related design work is limited. [16-18].

Cable-stayed bridges without backcables are more and more favored by designers because of their beautiful shape and economical applicability. draw some useful conclusions, solve the problems encountered in the construction of cable-stayed bridges, and provide reference for design and construction.

ENGINEERING BACKGROUND

Bridge is located in Jinzhou District of Dalian City. The central pile number of the bridge is K2+300.00. The tower adopts single column concrete tower, the tower is inclined, and the angle between the tower and the horizontal is 55°. The full height of the tower is 124.2 m, the lower tower column is a variable section box section, the upper tower column is a variable section rectangular section.

The main bridge adopts the consolidation system of pier, tower and girder. The approach bridge adopts 40 m hole by hole cast-in-place prestressed concrete continuous box girder, and the lower structure adopts inverted vase type double column pier, drilled pile foundation and expanded foundation. Elevation drawing of the main bridge of Jinzhou bridge is shown in Figure 1.

Fig. 1 - Elevation drawing of the main bridge of Jinzhou bridge

Cable

The cable is a steel strand cable, and the cable is arranged in the shape of a harp. The standard cable distance on the main beam is 12.0 m, the longest cable is 196.056 m, the shortest is 44.732 m. The cable is arranged in the shape of a harp. The standard cable distance on the main beam is 12.0 m. The longest cable is 196.056 m and the shortest cable is 44.732 m.

Girder

The bridge main girder is divided into concrete box girder, steel box girder and steel-concrete composite box girder. The concrete box girder is the main girder at the consolidation of pier, tower and girder. The length of the concrete box girder is 10.0 m, and the height of the central girder is 3.0 m. The bridge concrete girder cross-sectional diagram is shown in Figure 2. The bridge steel-concrete composite girder cross-sectional diagram is shown in Figure 3, and the bridge steel girder cross-sectional diagram is shown in Figure 4.

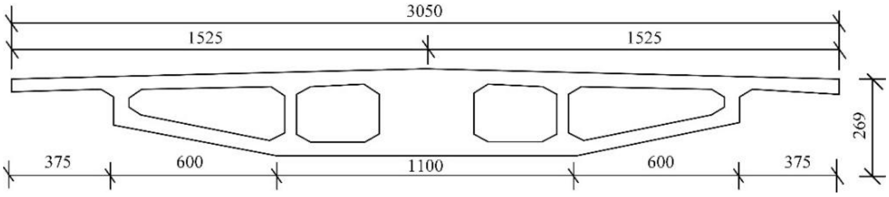

Fig. 2 -The bridge concrete girder cross-sectional diagram (mm)

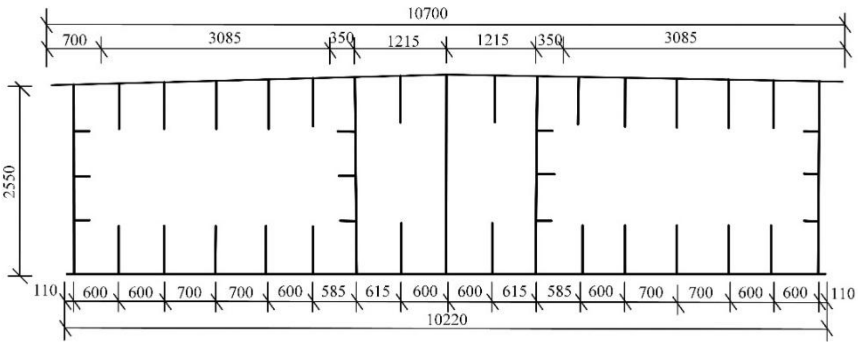

Fig. 3 - The bridge steel-concrete composite girder cross-sectional diagram (mm)

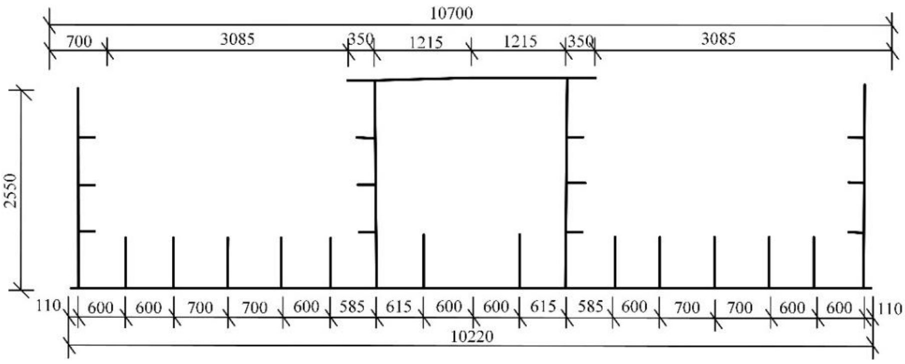

Fig. 4 - The bridge steel girder cross-sectional diagram (mm)

Cable tower

The tower adopts a single column concrete Leaning Tower with a horizontal inclination of 55° and a rear inclination of 35°. The cable is arranged in the shape of a harp. The transverse distance of the cable anchorage point on the girder is 1.6 m, and the standard distance of the cable on the main girder is 12.0 m. There are three cable specifications, each specification 6, a total of 18. The tower is 124.2 m. The lower tower column is a variable section box section, and the size is 24.574

m×5.142 m~16.509 m×3.5 m. The upper column is a rectangular section with variable section and the size is 10.862m×4.5m~5.0 m×4.5 m.

ANALYSIS OF CONSTRUCTION DIFFICULTIES OF CABLE-STAYED BRIDGE WITHOUT BACK CABLE

1. Construction facilities are difficult to meet the requirements of leaning tower construction

The vertical length of the horizontal projection of the tower is 77.3 m. The leaning tower tilts 35°, and the average height of each meter is offset by 0.7 m, which makes the structure of the tower crane attached to the wall complex, and the supporting rod needs 20m length, and the installation of the attached wall is extremely difficult.

The 35° inclined climbing structure is different from the vertical tower climbing structure in essence, and the vertical tower climbing structure bears a single vertical load, and the force condition of each side is the same. In addition to bearing vertical loads, the inclined tower climbing frame still has to bear a large overturning moment, and the stress conditions on each side are different, so the frame structure, track anchorage system and dynamic system need innovative design.

2. The variable shape structure leads to the diversification of construction technology

The tower can be divided into three sections from bottom to top: tower section C with double-chamber box section, tower girder consolidation transition section B with rectangular solid section and cable section A with large dip angle. Due to the large arc and large folding angle connection of the middle pier girder consolidation transition section B, the tower construction must adopt different technological methods to deal with the construction, including the full support of the tower section C and B, and the climbing mold construction of the upper pier section A.

3. The difficult installation of rigid skeleton and reinforcement

Whether the positioning of the rigid skeleton is accurate or not and whether the connection meets the strength requirements plays a key role in the construction quality, safety and linear shape of the tower. As the first process of tower segment construction, and the tower tilts back 35°, the installation stage is basically suspended in mid-air construction, resulting in the positioning and installation of the entire rigid skeleton is very difficult.

4. Influence of stay cable on climbing form construction

The cable tower is an inclined solid structure, the cable anchor teeth are all set in the lateral groove of the dark side, the length of the cable tube is up to 21.249 m, involving 3 to 4 construction segments, such a long cable tube is the most construction, and the general cable tower structure is difficult to install. The installation of anchor cable tube is the most difficult in the construction of cable tower, and it needs to find a different environment.

5. Many types of embedded parts and high requirements

In addition to the anchor cable pipe, the embedded parts of the cable tower also have access road, lightning protection grounding, tower crane, elevator, construction walkway and other structures or construction embedded parts, especially the access road adopts bolt connection structure, the embedded parts in addition to high density, the installation position requirements are obviously high.

6. The anti-crack control of the cable tower runs through the whole construction process

All the cable tower from the pier girder consolidated above are rectangular solid sections. How to ensure the quality of high grade tower concrete pouring is particularly important for the concrete joints of tower piers, and the upper tower columns with large self-weight moment. It is a difficult and important point in construction to prevent structural cracks induced by temperature difference cracks. Therefore, it is difficult to control the temperature difference cracks and the structural cracks of the leaning tower throughout the whole construction process.

7. **Concrete appearance quality control**

The concrete structure of bridge is an important part of urban bridge landscape. It is always a difficult point in the construction of urban bridge because it needs to meet the functional requirements and have considerable ornamental value. In particular, the construction of the Leaning Tower is difficult and there are many safety hazards. During the construction process, under the premise of ensuring the internal quality of concrete, efforts are made to ensure the roundness of the line and the smoothness of the joint, and improving its appearance quality is a continuous exploration process.

STRUCTURAL ANALYSIS MODEL ESTABLISHMENT

The modeling and analysis of the main bridge of Jinzhou Bridge are performed using the Midas/Civil finite element analysis software. A spatial truss system model is established. According to the calculation method of finite element analysis, before building the model, the structure needs to be discretized. The discretization should follow certain principles. Otherwise, the built model will either require excessive computation time for the same level of accuracy or have significant discrepancies in the stress distribution compared to the actual structure. In this study, for computational convenience and considering the construction sequence, the structure is divided into 262 units. The division of the entire bridge units is shown in Figure 5. The main beam, the main tower and the bridge pier are all made of beam elements, and the cable is made of truss elements. The pier bottom is consolidated. The link between the cable, beam and tower is a rigid connection.

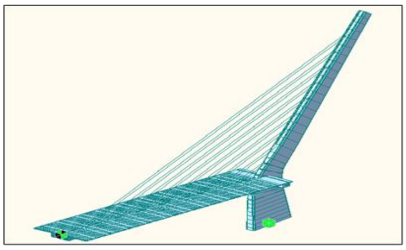

Fig. 5 - Finite element discretization diagram of the structure

When simulating the main girder, the stiffness (torsional stiffness, lateral bending stiffness, and vertical bending stiffness) and mass of the main girder are all concentrated on the central axis of the main girder. The constraints on the main girder at the pier are modeled using general supports that constrain the horizontal lateral displacement Dy, vertical displacement Dz, and rotation around the z-axis Rz, based on the actual types of supports set.

THE IMPACT OF LOCAL TEMPERATURE DIFFERENCES

The effect of local temperature differences on cable-stayed bridges without backstays is complex. Assuming a temperature difference of 5 °C between the sunny and shaded sides of the bridge tower, and a temperature increase of 10 °C for the cables, the local temperature difference in the main girder can be determined using the vertical temperature gradient curve shown in the diagram below, according to the design specifications.

The effect of local temperature differences on the displacement and stress values of the main girder and bridge tower in the completed bridge state is shown in Figure 6 - Figure 12. In this case, the bridge deck is paved with 10 cm of asphalt concrete, resulting in temperatures T1 of 14 °C for the cast-in-place concrete section and steel box girder with bridge deck panels, and T2 of 5.5 °C.

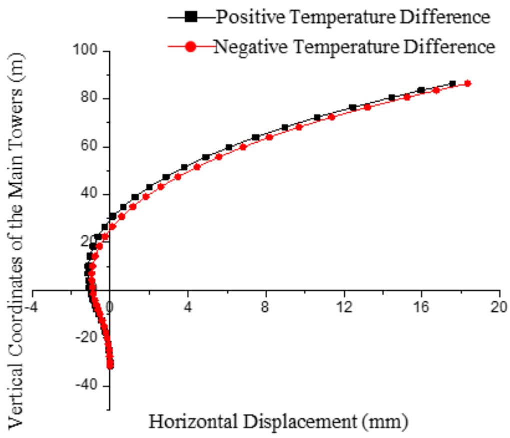

Fig. 6 - The temperature effect on the bridge tower displacement

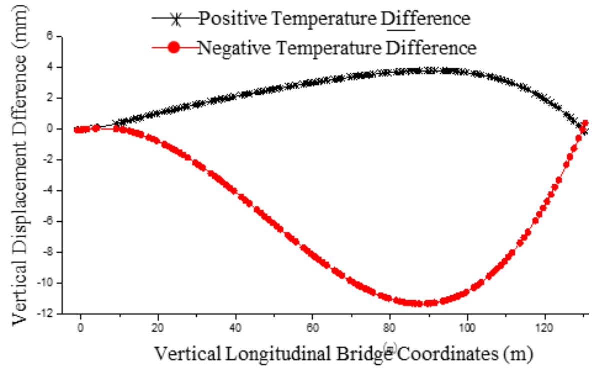

Fig. 7 - The temperature effect on the girder displacement

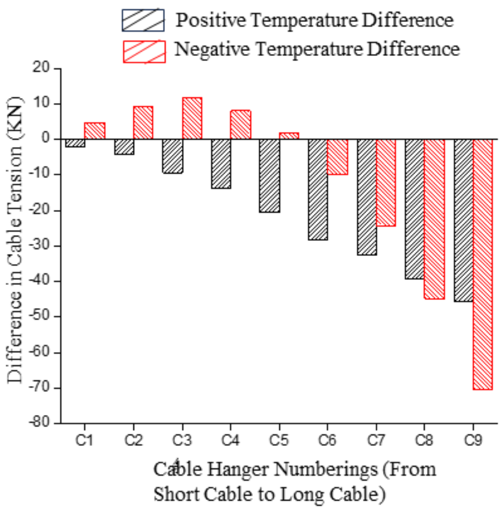

Fig. 8 - The temperature effect on the cables

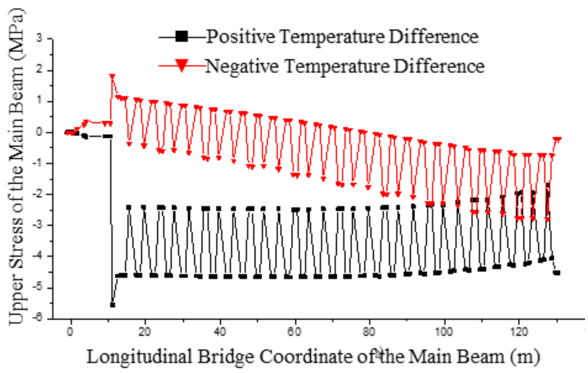

Fig. 9 - The temperature effect on the girder stress

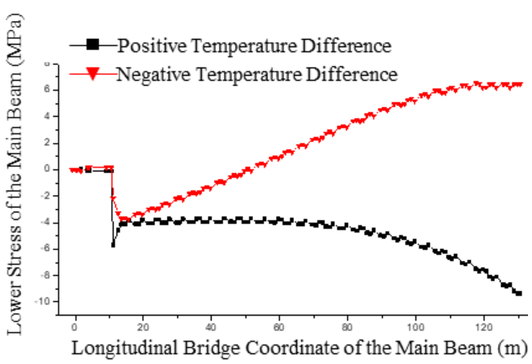

Fig. 10 - The effect of local temperature difference on the stress variation of the lower flange of the main girder

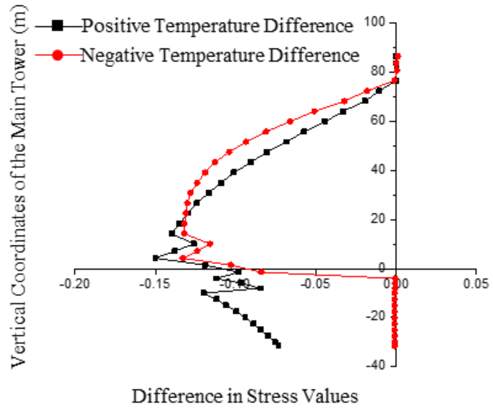

Fig. 11 - Localized temperature difference results in stress variation on the left side of the tower

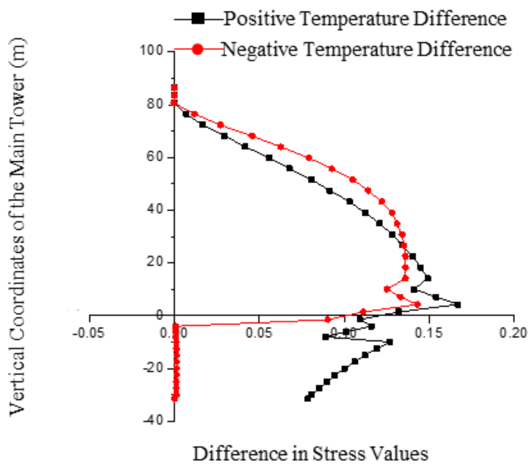

Fig. 12 - The local temperature difference causes stress variation on the right side of the tower

According to Figure 6 - Figure 12, it can be observed that the deformation of the bridge structure is significantly affected by localized temperature differences. The main girder experiences a downward displacement of 11.3 mm, while the upper part of the bridge tower moves horizontally towards the abutment, with a maximum displacement of 18.4 mm. The localized temperature differences have the greatest impact on the tension force of cable C9, while their influence on the cables at the bridge tower is relatively small. The stress impact on the main girder is within 10MPa, indicating a minor effect. The bridge tower is minimally affected, with a maximum tensile stress change of 0.15 MPa.

From the above analysis, it can be seen that the effects of localized temperature differences and overall temperature differences on the displacement and tension force of the main tower are significant. However, due to the complex nature of localized temperature variations, it is difficult to accurately consider their impacts in calculations. In order to avoid the influence of localized temperature differences on construction, it is recommended to carry out construction processes that have a significant impact on the elevation of the main girder and structural forces, such as cable tensioning, when the structure is in a uniform temperature state. Measurements of tension forces, elevation, and stress at control points should also be conducted in a uniform temperature state.

INCLINATION ANGLE ON STRUCTURAL FORCES INFLUENCE

The unique structure of cable-stayed bridges without backstays leads to distinctive mechanical characteristics. The inclination angle of bridge towers can vary in the hands of different designers, and different inclination angles correspond to different structural features. This paper takes the main bridge of Jinzhou Bridge as an example to study the influence of different inclination angles on the structural performance under loading.

The study investigated three different cases: inclination angles of 52°, 55° (design angle), and 58°. The inclination angle refers to the acute angle between the axis of the bridge tower and the axis of the main girder. The models with inclination angles of 52° and 58° were modified from the model with a 55° inclination angle that was established in this study. When the bridge tower is 52 °, 55° and 58°, the stress on the left side of the bridge tower is -5.8MPa, -4.1MPa and 0.7MPa, respectively. Only the coordinates of the nodes corresponding to the bridge tower were modified while keeping other parameters, such as cross-section characteristics and material properties, unchanged. The model only considers the bridge in its completed state, i.e., the structural state formed when the

DOI 10.14311/CEJ.2025.02.0013

bridge is fully assembled. The established models are shown in Figure 13 and Figure 14.

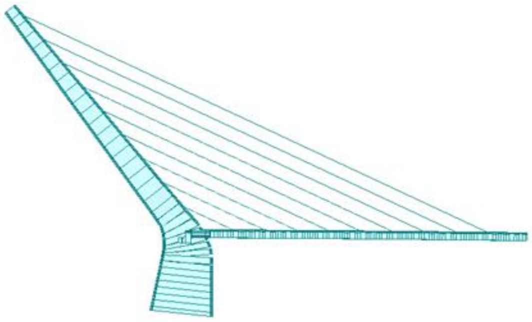

Fig. 13 - Analysis model for an inclination angle of 52°

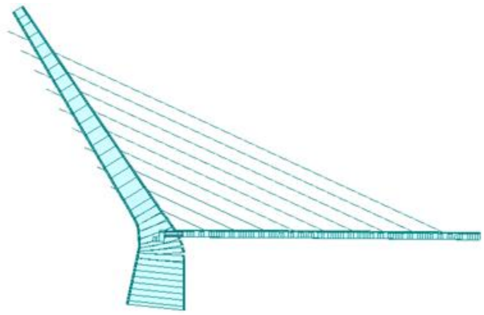

Fig. 14 - Analysis model for an inclination angle of 58°

The model considers the combined effects of dead load and live load and performs a comparative analysis of the results for the three different inclination angles. The analysis includes the changes in cable forces and displacements under the action of live load and the stresses resulting is shown in Figure 15 - Figure 21.

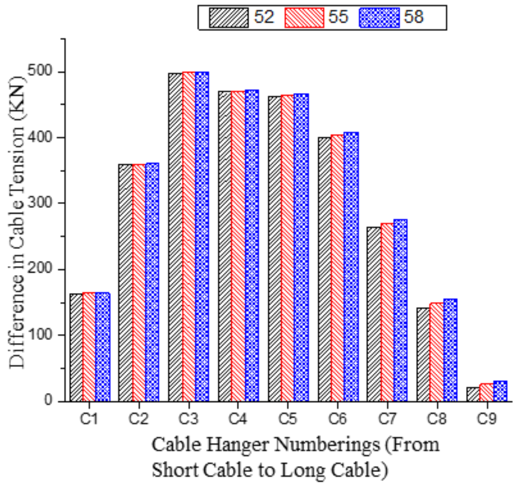

Fig. 15 - Comparison of cable forces for different inclination angles

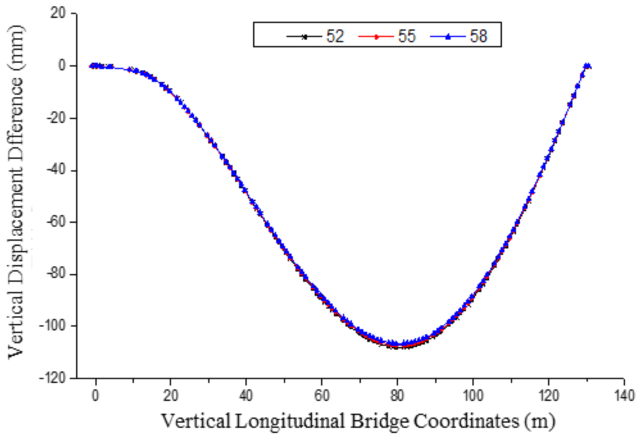

Fig. 16 - Girder deflections comparison at different inclination angles

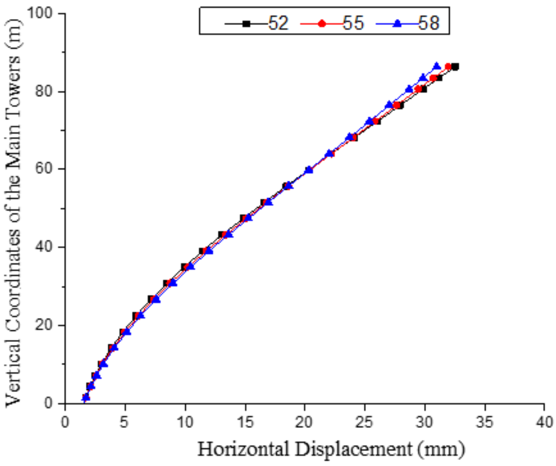

Fig. 17 - Bridge towers displacements

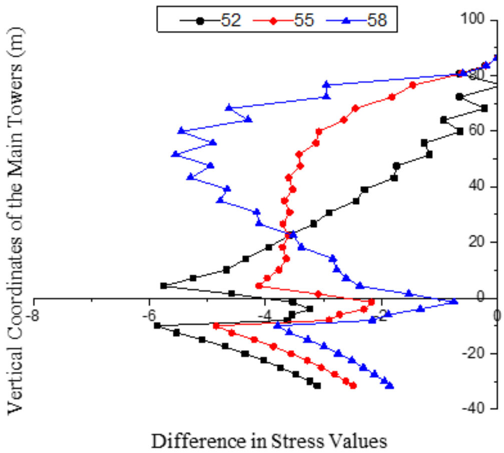

Fig. 18 - Bridge towers left side stress comparison

DOI 10.14311/CEJ.2025.02.0013

comparison at different inclination angles *at different inclination angles*

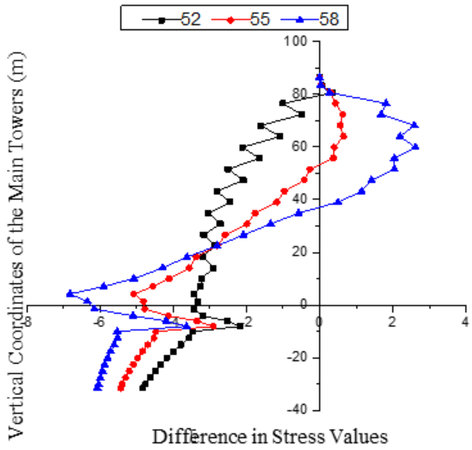

Fig. 19 - Bridge tower rightside stress comparison at different inclination angles

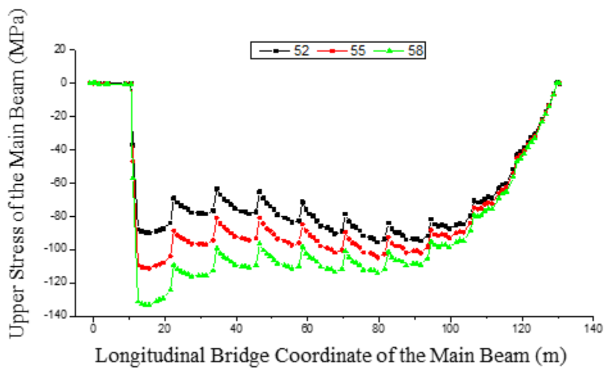

Fig. 20 - Girders upper surface stress comparison at different inclination angles

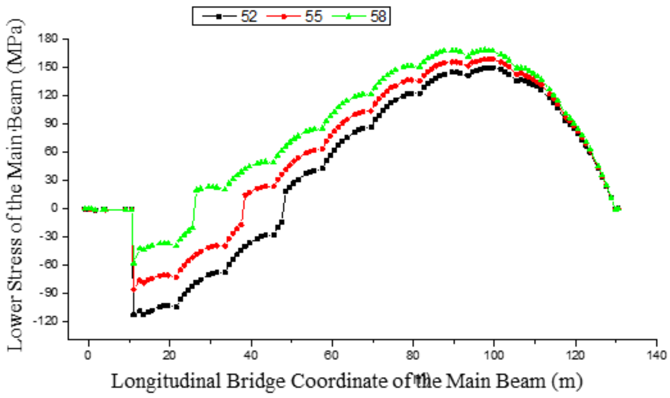

Fig. 21 - Girder lower surface stress comparison at different inclination angles

Based on the results calculated from the three different inclination angles mentioned above, it can be concluded:

Under the action of live loads, the tension force in the inclined cables increases with the increasing inclination angle. However, the displacement of the main girder and the bridge tower is not significantly affected by the inclination angle under live load.

Under the combined action of dead load and live load, the stress on the left side of the bridge tower decreases with increasing inclination angle below a vertical coordinate of 20 m, while it increases above 20 m. On the right side of the bridge tower, the stress increases below a vertical coordinate of 20 m with increasing inclination angle, but decreases above 20 m as the inclination angle increases.

Under the combined action of dead load and live load, the tensile stress on the upper surface of the main girder increases with increasing inclination angle, while the compressive stress on the lower surface decreases with increasing inclination angle. There is a peak tensile stress at the 100 m position of the main girder. The variation of the upper and lower surface stresses is significant before the 100 m mark for different inclination angles, but becomes smaller after that. A 55° inclination angle is considered reasonable for the main bridge of the Jinzhou Bridge.

CONCLUSION

(1) When the inclination angle of the bridge tower changes within a certain range, it has little

effect on the stiffness and strength of the structure, but under the condition that the stress of the tower girder is roughly the same, the greater the inclination angle of the tower, the greater the counterweight of the tower, and the greater the material consumption of the tower. When the bridge tower is 52°, 55° and 58°, the stress on the left side of the bridge tower is -5.8 MPa, -4.1 MPa and 0.7 MPa, respectively.

(2) Under the combined action of dead load and live load, the stress on the left side of the bridge tower decreases with increasing inclination angle below a vertical coordinate of 20 m, while it increases above 20 m. On the right side of the bridge tower, the stress increases below a vertical coordinate of 20 m with increasing inclination angle, but decreases above 20 m as the inclination angle increases.

(3) In addition to the general characteristics of cable-stayed bridge, this bridge also has its own characteristics, that is, the influence of the tower's dead weight on the structure is greater than that of the straight tower cable-stayed bridge, especially the influence on the horizontal displacement and self-stress.

REFERENCES

[1] Li H, Ou J.,2016. The State of the Art in Structural Health Monitoring of Cable-stayed Bridges. Journal of Civil Structural Health Monitoring, vol. 6, p. 43-67. ISSN 2190-5452, https://doi.org/10.1007/s13349-015-0115-x

[2] Ren W X, Peng X L, Lin Y Q., 2005. Experimental and Analytical Studies on Dynamic Characteristics of a Large Span Cable-stayed Bridge. Engineering Structures, vol. 27, n. 4, p. 535-548. ISSN Engineering Structures, https://doi.org/10.1016/j.engstruct.2004.11.013

[3] Feng Y, Lan C, Briseghella B,. 2022. Cable Optimization of a Cable-stayed Bridge Based on Genetic Algorithms and the Influence Matrix Method. Engineering Optimization, vol. 54, n. 1, p. 20-39. ISSN 1084-0702, https://doi.org/10.1080/0305215X.2020.1850709

[4] Pan H, Azimi M, Yan F,. 2018. Time-frequency-based Data-driven Structural Diagnosis and Damage Detection for Cable-stayed Bridges. Journal of Bridge Engineering, vol.23, n. 6, p. 04018033. ISSN 1084-0702, https://doi.org/10.1061/(ASCE)BE.1943-5592.0001199

[5] Shao Y, Shao X, Li L., 2018. Optimum Combination of Bridge and Deck Systems for Superspan Cable-stayed Bridges. Journal of Bridge Engineering, vol. 23, n. 1, p. 04017112. ISSN 1084-0702, https://doi.org/10.1061/(ASCE)BE.1943-5592.00011

[6] Tome E S, Pimentel M, Figueiras J., 2018. Structural Response of a Concrete Cable-stayed Bridge under Thermal Loads. Engineering Structures, vol. 176, p. 652-672. ISSN 0141-0296, https://doi.org/10.1016/j.engstruct.2018.09.029

[7] Zeng Y, Zheng H, Jiang Y., 2022. Modal Analysis of a Steel Truss Girder Cable-stayed Bridge with Single Tower and Single Cable Plane. Applied Sciences, vol. 12, n. 15, p. 7627. ISSN 2076-3417, https://doi.org/10.3390/app12157627

[8] Zheng X, Cui Y., 2022. Analysis of Static Performance of Cable-stayed Arch Cooperative Bridge without Back Cable. Archives of Civil Engineering, p. 531-548. ISSN 2300-3103

[9] Huynh T C, Park J H, Kim J T.,2016. Structural Identification of Cable-stayed Bridge under Back-to-back Typhoons by Wireless Vibration Monitoring. Measurement, vol. 88, p. 385-401. ISSN 0263-2241, https://doi.org/10.1016/j.measurement.2016.03.032

[10] Zhang K, Qi T, Xue X W., 2020. Study on the Influence of Cable/sling Damage on the Natural Vibration Characteristics of Special-shaped Cable-stayed Arch Bridge without Back Cable. Stavební obzor-Civil Engineering Journal, vol. 29, n. 4. ISSN 1210-4027, https://doi.org/10.14311/CEJ.2020.04.0044

[11] Straupe V, Paeglitis A., 2012. Analysis of Interaction Between the Elements in Cable-stayed Bridge. The Baltic Journal of Road and Bridge Engineering, vol. 7, n. 2, p. 84-91. ISSN, 1822-427X, https://doi.org/10.3846/bjrbe.2012.12

[12] Chen D W, Au F T K, Tham L G., 2000. Determination of Initial Cable Forces in Prestressed Concrete Cable-stayed Bridges for Given Design Deck Profiles Using the Force Equilibrium Method. Computers & Structures, vol. 74, n. 1, p. 1-9. ISSN 0045-7949, https://doi.org/10.1016/S0045-7949(98)00315-0

[13] Hao H, Tang E K C., 2010. Numerical Simulation of a Cable-stayed Bridge Response to Blast Loads, Part II: Damage Prediction and FRP Strengthening. Engineering Structures, vol. 32, n. 10, p. 3193-3205. ISSN 0141-0296, https://doi.org/10.1016/j.engstruct.2010.06.007

[14] Su X, Kang H, Chen J., 2019. Experimental Study on In-plane Nonlinear Vibrations of the Cable-stayed Bridge. Nonlinear Dynamics, vol. 98, p. 1247-1266. ISSN 0924-090X, https://doi.org/10.1007/s11071-019-05259-0

[15] Le L X, Siringoringo D M, Katsuchi H., 2022. Stay Cable Tension Estimation of Cable-stayed Bridge under Limited Information on Cable Properties using Artificial Neural Networks. Structural Control and Health Monitoring, vol. 29, n. 10, p. e3015. ISSN 1545-2263, https://doi.org/10.1002/stc.3015

[16] Li S, Li H, Liu Y., 2014. SMC Structural Health Monitoring Benchmark Problem Using Monitored Data from an Actual Cable-stayed Bridge. Structural Control and Health Monitoring, vol. 21, n. 2. p. 156-172. ISSN 1545-2255, https://doi.org/10.1002/stc.1559

[17] Ma C, Duan Q, Liao H,. 2018. Experimental Investigation on Aerodynamic Behavior of a Long Span Cable-stayed Bridge under Construction. KSCE Journal of Civil Engineering, vol. 22, 2492-2501. ISSN 1226-7988, https://doi.org/10.1007/s12205-017-0402-7

[18] Kim H K, Kim K T, Lee H., 2013. Performance of Unpretensioned Wind Stabilizing Cables in the Construction of a Cable-stayed Bridge. Journal of Bridge Engineering, vol. 18, n. 8, p. 722-734. ISSN 1084-0702, https://doi.org/10.1061/(ASCE)BE.1943-5592.0000405

USE OF CONTACTLESS SPATIAL DATA COLLECTION METHODS FOR SNOW COVER MONITORING: CASE STUDIES FROM CZECH MOUNTAINS

Jan Pacina, Ondřej Soukup, Dominik Brétt, Petr Novák and Jan Popelka

J. E. Purkyne University, Faculty of Environment, Department of Geoinformatics, Ústí nad Labem, Pasteurova 1, Czech Republic; jan.pacina@ujep.cz

Received:	*02.12.2024*
Received in revised form:	*15.04.2025*
Accepted:	*17.06.2025*

ABSTRACT

Accurate documentation of snow cover is critical for hydrological modeling, climate adaptation planning, and risk assessment in mountainous regions. This study presents a comprehensive methodology for snow cover monitoring using UAV-based LiDAR scanning, tailored to the specific environmental and technical constraints of Central European mountain ranges. Field campaigns were conducted across several Czech border mountain locations (Ore Mountains, Giant Mountains, Beskids Mountains), utilizing DJI Matrice 300 RTK equipped with Zenmuse L1 or L2 LiDAR sensors. Due to limitations in deploying traditional ground control points (GCPs) in remote and protected areas, the methodology emphasizes reliance on GNSS RTK corrections and minimal GCP use. The influence of two GNSS reference networks (CZEPOS and TopNet) was evaluated through photogrammetric analysis, revealing systematic elevation biases and spatial autocorrelation, with TopNet yielding slightly better results.

Various point cloud post-processing workflows were tested, including smoothing and noise filtering in DJI Terra, TerraSolid, and CloudCompare. The best visual and statistical results were obtained using a combined approach supplemented by a single foldable GCP. Ground point classification methods were assessed in both snow-free and snow-covered conditions. The most reliable method for snow-free filtering was the Spatix-based algorithm in TerraSolid, while snow-covered scenes required custom multi-criteria filtering in CloudCompare.

Validation was performed using over 4,500 RTK GNSS ground points and manual snow probe measurements. The methodology proved robust despite uncertainties from vegetation interference and manual measurement limits. This study delivers practical guidelines for operational snow cover documentation under constrained field conditions, and proposes improvements for future automation and validation.

KEYWORDS

UAV LiDAR, Snow cover, GNSS RTK, Point cloud processing, Bare ground filtering, Mountain environments

INTRODUCTION

Modeling snow cover is essential for understanding the dynamics of the hydrological cycle [1], managing water resources, and predicting the impacts of climate change [2]. Snow serves as a significant reservoir of water, influencing runoff in watersheds [3], water availability during dry seasons [4], and overall ecological stability [5]. Accurate snow cover models enable us to estimate the amount of water stored in snow (known as snow water equivalent, SWE) and provide critical data for water resource management [6], particularly in regions where snow is the primary source of water for populations and agriculture [7]. Another key reason for modeling snow cover is monitoring the impacts of climate change [8], [9]. In warmer regions or seasons, the snowline is shifting, the total volume of snow is decreasing, and snowmelt is occurring earlier, affecting both ecological and socioeconomic systems [10]. Models based on accurate snow cover data help scientists and policymakers understand these changes in the landscape and facilitate better planning for adaptation to new climate conditions [11].

Beyond environmental and hydrological applications, snow cover modeling is also crucial for winter sports [12], transportation [13], and energy production [14]. In mountainous areas, models can optimize infrastructure maintenance and safety measures [15]. Wind and hydroelectric power facilities can use snow cover models to improve energy management [16]. Precise information about snow cover and its dynamics is critical for a wide range of applications, from local to global scales [17].

Snow cover can be measured using various methods. Manual methods are traditional approaches to snow measurement that require direct physical presence in the field. The simplest method is to use a snow gauge rod or measuring rod, where the depth of the snow cover is measured on site [18]. This method is undemanding in terms of equipment, but time-consuming and dependent on the availability of the measured locations [19]. More detailed snow analysis is made possible by measuring snow profiles, where a profile is dug in the snow layer and its structure, density and temperature are evaluated. This information is crucial for avalanche risk prediction or hydrological modelling, but the method requires expertise and careful implementation in the field [20].

With the growing need for more accurate data and frequent monitoring of snow cover, automated methods have become popular. Among the most widespread are ultrasonic snow gauges, which measure the distance between the sensor and the snow surface using ultrasonic waves [21]. This method allows for continuous measurements and is commonly installed at weather stations.

Remote sensing and photogrammetry allow monitoring of snow cover over large areas using various sensors located on satellites, aircraft or UAVs. Aerial and ground-based LiDAR (Light Detection and Ranging) allows detailed measurements of changes over time [22], while SAR radar systems (e.g. Sentinel-1) provide information on snow cover even in cloudy conditions [23].

Optical images from satellites such as Landsat or Sentinel-2 allow mapping of the presence of snow and its spectral properties, but their accuracy is lower than that of radar methods. UAV photogrammetry provides detailed models of snow cover by comparing images before and after snowfall, while historical photos can in some cases be used to reconstruct the evolution of snow conditions in the past. Another option is to use sensors in the field, such as temperature and humidity sensors, which provide indirect information about the properties of the snow. For comprehensive analysis, data from these methods are often combined with numerical models that allow simulation of snow accumulation and melting based on meteorological data, remote sensing and other input parameters.

In the following text, we will focus mainly on the documentation of snow cover using LiDAR data. Laser scanning (LiDAR) and point cloud analysis have revolutionized the accuracy of snow cover modeling. These technologies allow for detailed mapping of the Earth's surface both before and after snowfall, enabling precise quantification of snow layer thickness. The high spatial resolution of LiDAR captures fine-scale variations in snow cover, which is crucial for studying local microclimatic conditions and their influence on snow melting or accumulation. The results of such modeling are not only valuable for hydrological applications but also for mitigating risks such as avalanches or extreme flooding caused by rapid snowmelt.

The use of LiDAR scanners in combination with UAVs allows for fast, cheap and operative documentation of snow cover even in hard-to-reach areas. Our research presented in this paper is focused on verifying the possibilities of using mobile laser scanning in combination with UAVs in our national conditions (Czech Republic, Europe), especially focusing on data quality and accuracy. When working in remote mountainous and difficult-to-reach areas, we are limited by the quality of the GNSS RTK solution, the very limited ability to deploy control points and the problematic validation of the obtained data. The aim of the presented research is to define possible qualitative parameters of the resulting snow cover data, methodological recommendations for their processing and the presented validation of the results in the field with application in the border mountains of the Czech Republic, as the snow data was collected and processed as part of a research project of the Technology Agency of the Czech Republic called „Analysis of spatio-temporal dynamics of snow cover for the purposes of prediction and prevention of hydrological extremes and dimensioning of adaptation measures within land consolidation“ (TA CR SNOW).

MATHERIALS AND METHODS

The TA CR SNOW project was solved for a total of 3 years (2022 – 2024). During the individual years of the project, there was a gradual improvement of the surveying technology and thus changes in the methodology of data collection. With regard to the very warm winters in the monitored period in Central Europe, activities aimed at monitoring the snow cover were directed to the border areas of the Czech Republic – the Ore Mountains, the Giant Mountains and the Beskids Mountains.

Areas of interest

The area for testing the accuracy of individual methods and verifying the methodology of data collection and processing was chosen in the Ore Mountains – the ridge part at an altitude of about 900 m above sea level (see Figure 1). This area was chosen with regard to the existence of previous ground measurements, the combination of open spaces (mountain meadows) and forest, proximity to the state border (most of the snow monitoring within the TA CR SNOW project was carried out in border areas), which brings aspects such as poor mobile signal coverage and possible problematic RTK solutions, the possibility of using UAVs without permission. Within the localities in the Ore Mountains, the Giant Mountains and the Beskids Mountains, data collection and processing were carried out on the basis of the methodology presented in the following text. However, due to the inaccessibility of many sites in the Giant Mountains and Beskids Mountains during winter, extensive validation measurements could not be performed there. Therefore, detailed accuracy analysis is presented only for the Ore Mountains, while field campaigns in the other regions helped to confirm the general applicability of the methodology and identify potential limitations. The data processed within the area of Giant Mountains and the Beskids Mountains are thus not presented within this paper.

Fig. 1 - Area of interest

Hardware and software used for data acquisition and processing

The data collection was carried out by a DJI Matrice 300 RTK drone (carrier), which is a UAV (Unmanned Aerial Vehicle) suitable for mapping. It can carry multiple sensors and is equipped with a device to receive real-time GNSS RTK corrections. In the course of our research, we used the DJI Zenmuse P1 (full-frame camera), DJI Zenmuse L1, and DJI Zenmuse L2 LiDAR sensors.

The following software tools were used for data processing: DJI Terra Pro – raw LiDAR data processing, TerraSolid and CloudCompare – LiDAR data postprocessing, ArcGIS Pro – LiDAR data processing, visualization and analysis, Agisoft Metashape – image data processing from the DJI P1 sensor.

The point clouds are exported in DJI Terra in the ETRS89 UTM 33N coordinate system, while the exact NTv2 grid transformation to the Czech national coordinate system S-JTSK (EPSG 5514) is not possible in this software. External software using the certified transformation key was used for transformation to EPSG 5514.

GNSS correction networks

A total of two GNSS reference networks were used for field data collection. The CZEPOS network provides correction data for GNSS measurements in real time with high accuracy. According to testing carried out by the Land Survey Office and Cadastral Offices on 150 trigonometric points in 25 locations throughout the Czech Republic, the following mean errors were achieved for RTK services: horizontal accuracy (m_{xy}): 1–2 cm and vertical accuracy (m_h): 2–3 cm [24]. The TopNet network works with similar accuracies [25]. However, it is important to note that accuracy may be affected by distance from the reference station and current environmental conditions. In general, accuracy can decrease as the distance from the reference station increases. The RTK method states a horizontal accuracy of approximately 10 - 20 mm + 1 ppm (part per million), which means 1 mm for every kilometer of distance from the reference station. Vertical accuracy tends to be slightly lower. Thus, at a distance of 10 km from the reference station, the horizontal error would be approximately 10 mm (basic error) + 10 mm (1 mm/km × 10 km) = 20 mm. There are studies that suggest that RTK accuracy does not decrease significantly with distances up to 80 km from the reference station

[26],[27]. However, further publications confirm the dependence of accuracy on the distance from the reference station [26],[28].

Data collection methodology

The methodology of data collection assumes that snow cover data are measured in mountainous, hard-to-reach locations. It is necessary to transport equipment with a total weight of 52.4 kg (drone, battery, sensor, means of transport) to the selected location. Most of the Czech border mountains are included in large-scale protected areas (Protected Landscape Areas, National Parks). Access to the sites (especially during winter) is difficult and in most cases, it is not possible to use motor vehicles. Movement within a given locality is in many cases, with regard to the rugged terrain, the amount of snow, the wintering grounds of the game, impossible or even forbidden. The presented methodology of data collection and processing thus reflects the possible shortcomings that we may encounter when collecting data in such conditions.

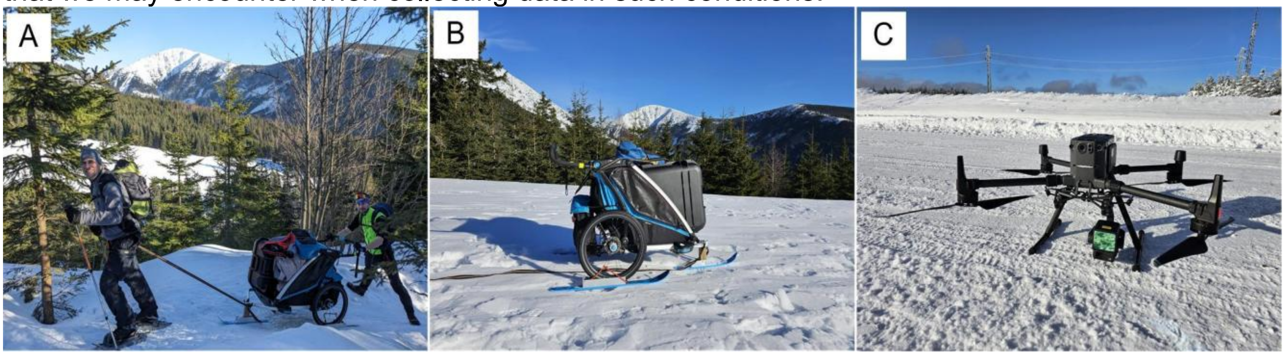

Fig. 2 A and B - drone transportation in the mountainous area; C - DJI Matrice 300 RTK equipped with Zenmuse L2 LiDAR scanner

For the analysis of snow cover, it is necessary to process data from two-time horizons (landscape with snow and without snow). For data collection, we had the opportunity to try a number of different sensors and approaches - classic photogrammetry, aerial laser scanning and laser scanning where a drone was used as a carrier.

All these methods have one common weak point – the very problematic or impossible placement of ground control points (GCPs) within the site of interest, which make the collection of LiDAR data more accurate. GCP for LiDAR scanning must be large and provided with a high-quality reflective layer. At a flight altitude of 100 m AGL, the recommended size of the edge of a square GCP is 70 – 80 cm [30]. The 6 GCP set can thus weigh well over 10 kg. These bulky and heavy GCPs are difficult to transport to remote locations when moving on foot, or it is problematic to deploy these GCPs within the site at all. Mountainous areas are in most cases forested and therefore the precise targeting of GCP centers using GNSS is problematic. As part of the presented methodology, we will focus on evaluating the quality of the data obtained only with the help of RTK solutions on a drone. At the Lesná test site, the use of the so-called folding GCP was verified, which was located at the launch site and the center coordinates were measured with RTK GNSS. In the Results chapter, the effect of the application of the detected "corrections" from this one GCP on the entire resulting point cloud will be tested.

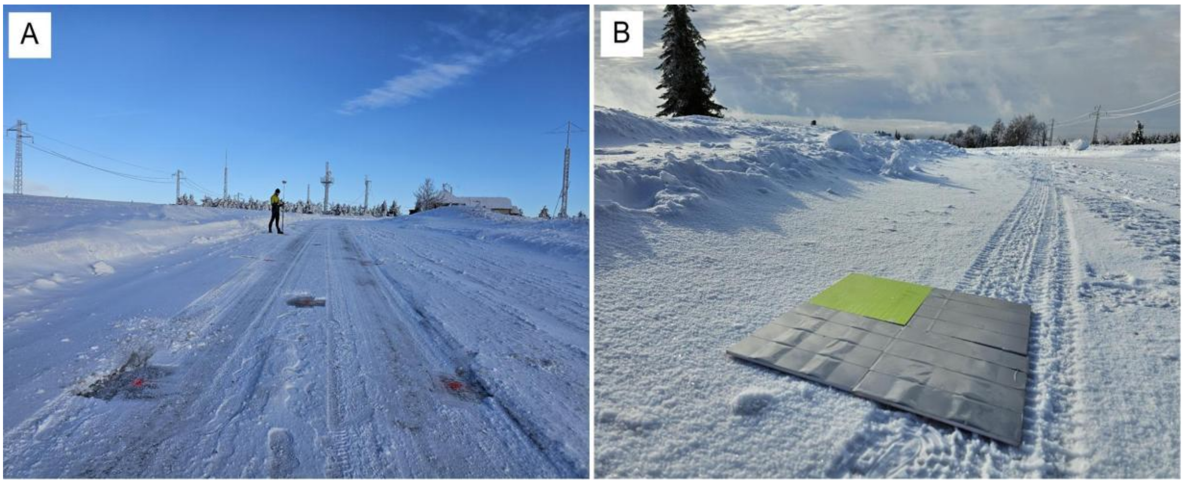

Fig. 3 A - measurement of control points on the road; B - foldable Ground Control Point with different reflective materials

Before starting the actual data collection, it is necessary to select a suitable sensor. Within the TA CR SNOW project, data collection was carried out using both a photogrammetric sensor (DJI P1) and LiDAR sensors. With regard to the character of the landscape (forested areas), photogrammetry seems to be an unsuitable method in most cases. Since it is very difficult (if at all) to model (snowy) terrain under trees in densely overgrown terrain.

The actual preparation for the flight is no different from the preparation for a normal flight - it is only necessary to ensure that the batteries for the drone are warm at all times. The flight was always planned from a height of 100 m AGL, with the Terrain Follow function activated, which ensures that the drone's flight altitude follows changes in the topography of the terrain. When taking test images with the DJI P1 sensor, at an altitude of 100 m AGL, the resulting resolution of the acquired image data is 0.88 cm/pixel. However, photogrammetric snow cover photography requires a specific approach according to [30] it is advisable to shoot in low sunlight (the relief is better rendered on snow) and the camera needs to be set to take underexposed images (ideally in RAW format for possible post-processing). When using the DJI Zenmuse L1 sensor, 3 reflections of the laser beam were set, while the DJI Zenmuse L2 sensor had 5 reflections. The resulting density of the point cloud is approximately 530 points/m^2 from DJI L1 and 600 points/m^2 from DJI L2.

We rely on GNSS correction data for our own data collection. It receives the drone in real time via the RTK service. RTK correction data available within public (mostly commercial) reference networks are dependent on the coverage of the area by the mobile signal, which is needed for real-time data transmissions. During our measurements, we had access to two reference networks – the national Czepos network and the commercial TopNet network. Having active access to two reference networks proved to be practical in case there was a problem with finding an RTK solution and fixing the position with cm accuracy when using the (preferred) Czepos network.

The correction data of our flights has always been received through the so-called virtual reference station, which should be located automatically within the scanned location, while the corrections are derived from the surrounding reference stations. Experience has shown that it is advisable to manually disconnect the drone from the reference network before the start of the mission and then connect it again – this will in many cases correct the position of the virtual reference station to the data collection point.

Data processing methodology

A suitable way of data processing is crucial to obtaining the quality data needed to create an accurate snow cover model. Photogrammetric images, which contain coordinates of the center of the image and values of Yaw, Pitch and Roll in EXIF, were processed in a standard way in the Agisoft

Metashape SW environment. Data derived from photogrammetric images (DSM, point clouds) are not suitable for modeling snow cover in areas covered by forest. We mention this method here only for the complexity of the methodology, and in the following text we will focus mainly on LiDAR data processing.

The raw data from the DJI L1 and DJI L2 sensors needs to be processed in the native DJI Terra program as part of the first step. For data processing in our research, we used the DJI Terra Pro program, which is a paid version of the DJI Terra tool. One of the main differences between the "free" version and the paid "Pro" version is the ability to use the Optimize Point Cloud function to process data from the LiDAR sensor. According to information from the DJI website [31], this function is suitable for removing noise, improving point alignment, smoothing out dense clouds, correcting errors caused by drone movement. The research did not identify an expert study that would verify the effect of this function on the resulting point cloud. However, according to discussions within DJI community groups, user experiences suggest that this feature makes sense and leads to an increase in the quality of the resulting point cloud. In our research, we focused on empirically verifying the influence of this function on the resulting data.

However, DJI Terra Pro only processes the raw data, performs point cloud optimization, and exports the LAS file for the area of interest. Further processing takes place in TerraSolid SW, where we perform further filtering/smoothing.

The last step in data processing is the removal of noise (so-called isolated points), which can still be identified in the data even after applying the optimization functions in the DJI Terra Pro and TerraSolid environments. Here we use the CloudCompare software and the Statistical Outlier Removal function (SOR).

Another problematic aspect that affects the quality of the resulting data is point filtering. To analyze snow cover, we need so-called "bare ground" data. There are many software tools that allow this – we will focus on the possibilities of filtering "ground" points in the TerraSolid, CloudCompare and ArcGIS Pro environments. Each of these software products contains different algorithms for filtering points, the influence of which on data quality will be verified.

Methodology for verifying the quality of measurement

In our research, we used two reference networks (Czepos, TopNet), the accuracy of which is defined by tests carried out by network operators (see the previous text). Verification of the use of the reference network in combination with UAVs was analyzed, for example in [32]. In our case, we wanted to verify the accuracy of our two reference networks. For this purpose, test photogrammetric imaging was carried out at an open site. Within this locality, 7 GCPs were deployed, where these points will be used to evaluate differences in coordinates [X, Y, Z]. In addition, 75 control points in the field were surveyed, which will be used to verify the Z coordinate. All points were surveyed by RTK GNSS – the resulting coordinate is the result of an average of 20 observations at the point. Claimed accuracy m_{xy} = 1 cm, m_h = 1 – 2 cm. The entire site was then covered with photogrammetric images from two flights – the first using the Czepos reference network, the second using the TopNet network (consequent flights). The data were photogrammetrically processed in the Agisoft Metashape environment. The coordinates [X, Y, Z] were read on the derived data (orthophoto, DSM) and compared with the directly measured data. The analysis of the differences of individual coordinates allows us to see the differences in the accuracies of individual reference networks. In the DJI Terra environment, it is possible to find the coordinates of the virtual reference station in the "Base center point settings" settings to verify that the virtual reference station has been placed in a suitable position.

Verification of the quality of LiDAR data was carried out at the Lesná test site (see Fig. 1). A total of 46 points on the surface of the road that passes through the area of interest were marked here (see Fig. 3-A). These points were again surveyed using RTK GNSS (20 observations at each point), the points were measured repeatedly after about 2 hours. The resulting coordinates of the points are then the average of these two measurements. The stated accuracy of the measured control points is m_{xy} = 1 cm, m_h = 1 – 2 cm. However, only the Z coordinate is evaluated to evaluate the quality of LiDAR data. X and Y coordinates cannot be verified on this type of signalling. As part of the scanning in January 2025, experimental "folding" GCPs were deployed within the site of interest (see Fig. 3-B). Using them, we are able to perform a basic evaluation of the effect of the presence of a low number of GCPs on the resulting point cloud.

In order to determine the influence of individual approaches to smoothing and optimization of the point cloud during its processing, the processed point cloud was evaluated within the defined asphalt road - always visually and in comparison, with the surveyed points. We tested the effect of incremental optimization using the features implemented in DJI Terra Pro, Terra Solid, and Cloud Compare (see Figure 7). The optimization method that produces the most accurate and smoothest data was then used for all processed datasets, which are evaluated within other criteria.

Another factor that affects the accuracy of the resulting cloud is the "bare ground" filtering method. Here, we tested different approaches implemented in TerraSolid, ArcGIS Pro and CloudCompare. Control points (more than 4500) were surveyed by RTK GNSS technology within the entire test site. With regard to the number of points, individual points were measured using 5 observations.

In January 2025, laser scanning was also supplemented with validation measurements with a snow probe (see Fig. 4). Using this data, we will try to validate the data processed according to the created methodology.

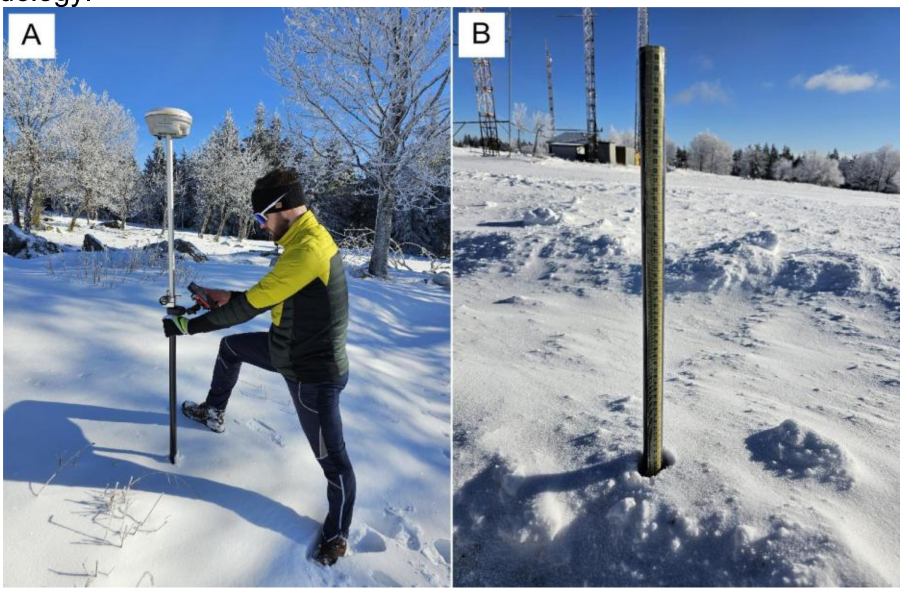

Fig. 4 - Snow probe verification measurements

Statistical methods

Geostatistical methods applied to differences in coordinates were used to evaluate the quality of individual datasets. Three main quality aspects of model errors (i.e., differences between modelled and reference coordinates) were evaluated [33]:

1. Model errors should not be spatially autocorrelated, meaning they should be randomly distributed in space. To evaluate this aspect, the Global Moran's Index was calculated. The statistical significance of the index was evaluated based on the p-value derived from a normally distributed z-score. The analysis was conducted using the *Spatial Autocorrelation (Global Moran's I)* tool in ArcGIS Pro (version 3.2.0).
2. Model errors should be normally or at least symmetrically distributed, with a central tendency close to zero**.** The Jarque–Bera test was used to assess the univariate normality of the errors. In addition, standardized skewness and standardized kurtosis were computed to examine

the shape of error distribution. Basic descriptive statistics including the mean, median, standard deviation, and RMSE were also calculated to characterize the accuracy and variability of the modelled data. All computations were carried out using PAST software (version 4.16c).

3. There should be no significant dependency between model errors and altitude. For this purpose, the Pearson correlation coefficient was calculated to assess potential linear relationships. The coefficient also allows for straightforward significance testing. The analysis was performed in PAST software (version 4.16c).

RESULTS

Within this chapter, the results of the presented methodology for the collection and validation of snow cover data will be evaluated. With regard to the detailed geostatistical analysis of the processed data, other tables and graphs are available in Appendix.

Reference Networks

As introduced in the chapter Data and methods - during the measurement we used a total of two GNSS RTK reference networks - national Czepos and commercial TopNet. The aim of the comparison is to obtain an objective overview of the accuracy of individual GNSS reference networks during measurements carried out under the same conditions: at the same time, at the same location and under the same satellite configuration. Within the selected area, 7 points were signaled that were surveyed (and will be used to evaluate X, Y and Z coordinates) and 75 points measured without signalling, which were used only for the evaluation of the quality of the Z coordinate. This area was then photogrammetrically scanned using a drone and a DJI P1 camera in two aerial missions (using different reference networks). The data were then photogrammetrically processed into orthophoto and digital surface model. Details on measurement, data collection and processing are given in the Data and methods chapter.

Differences in X, Y and Z coordinates were then used for the accuracy analysis. An example of measured coordinates and coordinates derived from orthophoto (location of points within a signaled control point) is shown at Fig. 5.

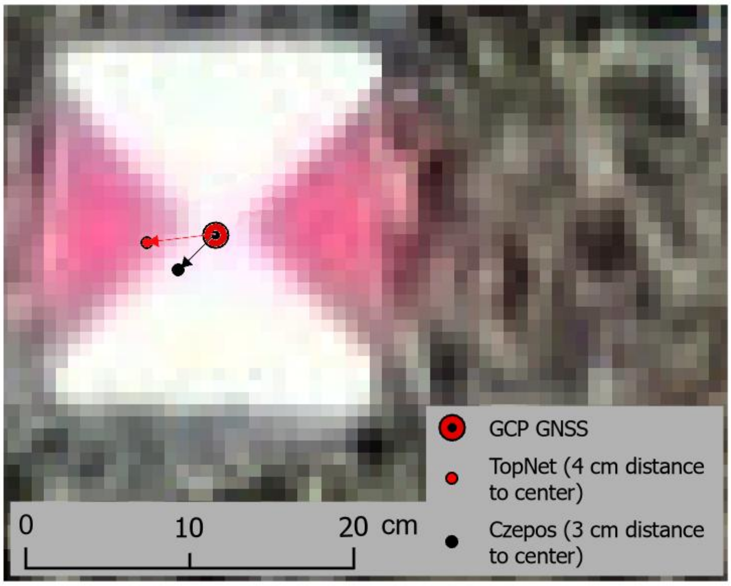

Fig. 5 - Positional differences of Ground Control Point center derived from photogrammetric processing using different GNSS correction networks.

Within the framework of a detailed geostatistical analysis (according to the methodology presented above), 3 qualitative aspects were evaluated. A detailed statistical evaluation, including tables and graphs, is available in Appendix.

According to the Moran indexes and its p-values (Appendix Table 1), spatial autocorrelation is statistically significant in both models, but in different components. While the TopNet network shows significant autocorrelation in the X coordinate, the spatial structure of the Czepos network is more pronounced in the Y axis. The remaining components do not show spatial clustering of errors and can be considered randomly distributed.

The normality condition was explored using skewness and kurtosis and subsequently tested by the Jarque–Bera test. In all cases, no significant deviations from the normal distribution were found (p-values > 0.1).

Pearson correlation coefficients between errors and altitude show a very strong linear dependence in all cases, with the highest correlation recorded in the Y coordinate for both networks.

The results of our qualitative test confirmed the announced accuracies of the reference networks (with regard to the influence of the distance from the reference station), even though the centers of the control points are shifted by a distance of 3 cm in the case of the Czepos network and 4 cm in the case of the TopNet network.

Both reference networks exhibit statistically significant positive vertical biases, with Czepos showing slightly larger systematic errors and RMSE compared to TopNet. Although TopNet performs marginally better in terms of overall accuracy, both datasets are affected by significant spatial autocorrelation and non-normal error distributions. The observed weak negative correlation with elevation suggests a minor trend toward increasing underestimation of height at higher elevations

Concerning the Z coordinate accuracy - both Czepos and TopNet reference networks show a statistically significant positive bias in elevation, with TopNet demonstrating slightly better overall accuracy and stability (lower RMSE and standard deviation). The spatial distribution of errors is non-random, exhibiting strong spatial autocorrelation in both systems. Error distributions are non-normal, negatively skewed, and slightly leptokurtic, indicating a majority of values slightly below the mean and the presence of a few large positive outliers. Additionally, a weak negative correlation between error and altitude suggests a minor tendency to underestimate elevations at higher altitudes. Overall, while both systems introduce systematic elevation overestimation, TopNet provides marginally more precise and consistent results, making it the preferable option for height data acquisition in this context.

Influence of post-processing operations on LiDAR data

As mentioned in the methodological part of the article, when processing LiDAR data, we verified the influence of standard and less standard post-processing tools on the quality of the resulting data. For this purpose, 46 points were signaled and coordinates measured with RTK GNSS within the area of interest (see Fig. 3-A), which are used for qualitative evaluation of the output data. Given the overlap of individual datasets, it is possible that a lower number of control points were used in some accuracy analyses.

From the information available in DJI Terra Pro, the positions of the virtual reference stations that were used for GNSS corrections within individual data collection campaigns were visualized. As can be seen in Fig. 6-A, the 2 centers of the virtual stations are shifted by about 15 km from the scanning area. These are datasets obtained 6/2023 and 12/2023.

Furthermore, we tested the effect of using one folding GCP with dimensions of 40 x 40 cm on increasing the quality of the processed point cloud. As can be seen in Fig. 6-B, the center of the GCP identified in the processed cloud is shifted by about 15 cm from its real position surveyed by GNSS.

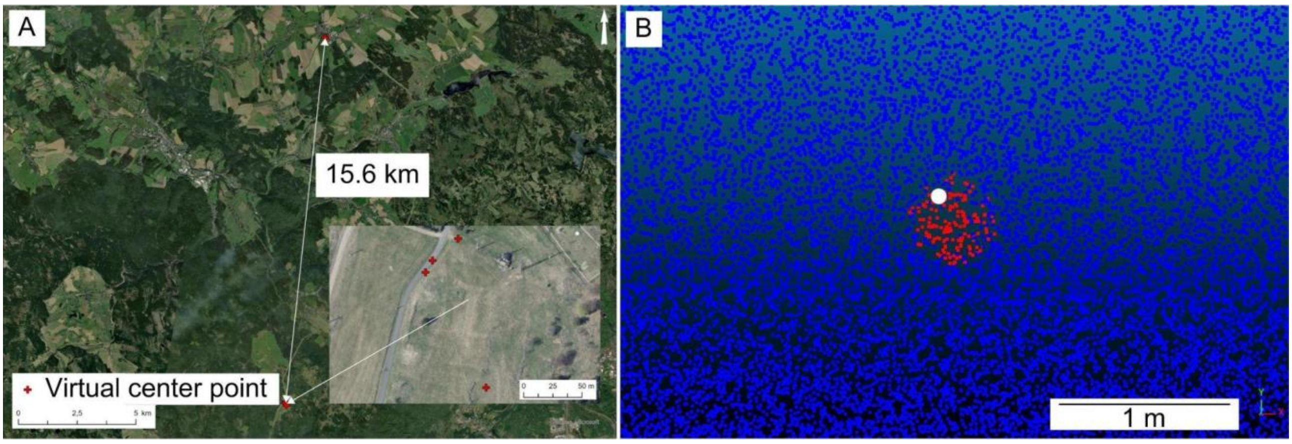

Fig. 6 A - Virtual GNSS correction stations centers; B - Ground Control Point (red square) identified based on the LiDAR intensity and the GNSS measured center (white point).

The results of the applied post processing approaches were evaluated visually and using statistical analyses of Z-coordinate differences on 46 control points within the processed datasets. The RMSE indicator was used for each step (see Figure 7) and a detailed geostatistical evaluation was then used for the best performing approach.

Raw data entering the post processing are presented in Figure 7-A (Smooth 1). In the first step, smoothing (point cloud optimalization) in DJI Terra Pro (Figure 7-B; Smooth 2), smoothing in TerraSolid (Figure 7-C; Smooth 3), smoothing in DJI Terra Pro and then in TerraSolid (Figure 7-D; Smooth 4) were applied to the data. A SOR filter was then applied to the data from Figure 7-D (Smooth 4) in the CloudCompare environment (Figure 7-E; Smooth 5). Detailed description of the applied filters is given in Appendix – Table 3.

According to the evaluation of the RMSE results, the best data set is based on Figure 7-C - data that was smoothed only by the function in TerraSolid. However, based on visual evaluation, the data to which the smoothing filters have been applied in DJI Terra Pro, TerraSolid and the Cloud Compare SOR filter come out best. In order to thoroughly verify the quality of data filtration, a detailed statistical evaluation of the data from 6/2023 presented on Figure 7-C and E was performed. Furthermore, the same approach was applied to the dataset from January 24, 2025. This dataset was chosen with regard to the use of an experimental folding control point. Quality evaluation was carried out also on the derived point cloud, manually shifted by the detected correction vector in the sense of the center shift of the identified center of the control point and its measured position (see Fig. 6-B).

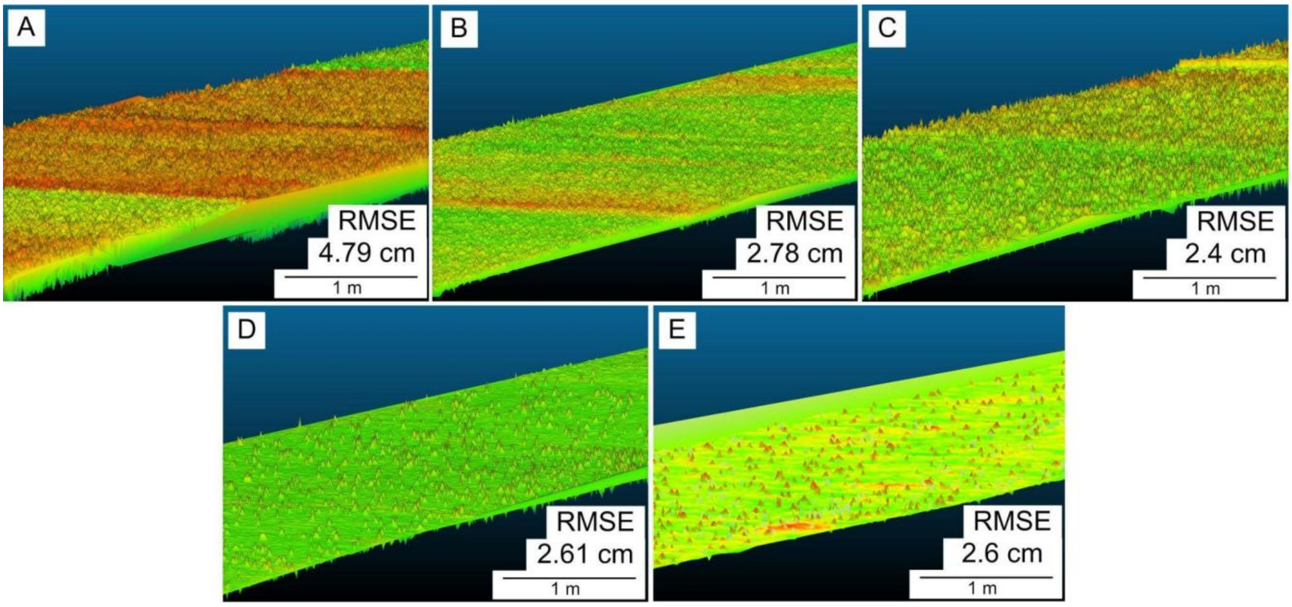

Figure 7 Results of application of methods for post-processing of LiDAR data. A - input data (without optimization); B - smoothing (point cloud optimalization) in DJI Terra Pro. C - smoothing in TerraSolid; D – point cloud optimalization in DJI Terra Pro and then smoothing in TerraSolid; E – data from D with Statistical Outlier Removal function applied.

Statistical evaluation of postprocessing operations

The differences found in the Z coordinate were subjected to a geostatistical analysis according to defined criteria. A detailed analysis of the results, including tables and graphs, is in Appendix (Figure 4, Table 4, Table 5, Figure 6).

The spatial autocorrelation of model errors was statistically significant for both smoothing methods (Smooth 3 and Smooth 5), which confirms the significant spatial clustering of the errors. The central tendency was negligible – the average and median of the Smooth 3 were zero, the Smooth 5 slightly above zero. Both methods achieved low dispersion with RMSE below 3 cm (0.024 m and 0.026 m), with a narrow, symmetrical distribution and no outliers. Normality tests showed no significant deviations from the normal distribution. Visual and quantitative analysis showed that the application of smoothing algorithms significantly improves accuracy compared to the unsmoothed model (RMSE 4.79 cm). The Smooth 3 and Smooth 5 methods show the best results, with Smooth 3 having the advantage of completely symmetrical error distribution and lower variability, making it the most balanced choice. Methods with DJI Terra optimization achieved fewer outliers, but slightly higher deviations due to the suppression of height details. The highest internal consistency is confirmed by the interquartile range (IQR) for Smooth 3, while outliers are more common for Smooth 1, 4 and 5. The Smooth 3 seems to be a suitable choice, especially where maintaining the height details of the surface is key. On the other hand, Figure 7-C shows that the Smooth 3 method still leaves the surface noisy. The Tab. 5 (in Appendix) clearly shows that the use of control points (even if only one) significantly increases the quality of the cloud. The Smooth 5 method supplemented by moving the cloud to the control point was therefore used for further data processing.

The impact of "bare earth" filtering on data quality

Within the framework of continuous experimental testing of the accuracy of the obtained data, it was shown that with regard to the ruggedness of the terrain of the area of interest (pits, ditches, stone walls but as well high grass), the method of filtering the cloud to the "bare ground" has an impact on the resulting structure of the point cloud. Points classified as ground are important for deriving a summer data set ("snow-free" data. For this purpose, several algorithms for filtering "bare ground" points were tested, which are contained in software products that are available for research and that are commonly used - TerraSolid (Spatix), CloudCompare and ArcGIS Pro (Clasif1 – TerraSolid (Spatix)-based workflow with additional height-from-ground classification and SOR filtering in CloudCompare; Clasif2 – ArcGIS Pro Standard Classification combined with SOR filtering; Clasif3 – ArcGIS Pro Conservative Classification and SOR filtering; Clasif4 – ArcGIS Pro Aggressive Classification and SOR filtering; Clasif5 – TerraSolid (Spatix) Classify Ground function with custom terrain settings (e.g., max building size, terrain angle); Clasif6 – Same as Clasif5 with additional SOR filtering in CloudCompare; Clasif7 – Pure CloudCompare-based classification using SOR filter and CSF (Cloth Simulation Filtering) plugin with Relief method. Detailed description of the filtering methods is presented in Appendix – Table 6.

The quality assessment was based on more than 4,500 RTK GNSS points and 46 road-marked points used to verify the impact of filtering algorithms on point cloud smoothing. The analysis was conducted using three qualitative parameters. All methods showed significant spatial autocorrelation of errors (Moran's I between 0.107 and 0.180; $p < 0.01$), indicating a clustered spatial structure. The error distribution deviated from normality (Jarque-Bera test $p < 0.01$), with pronounced kurtosis (kurtosis > 20) and negative skewness; the most extreme characteristics were observed for the "Clasif 7" variant (kurtosis = 67.9; skewness = -4.664). This variant also exhibited the highest negative central tendency and RMSE (0.301 m). The lowest RMSE values were observed for the "Clasif 1" and "Clasif 5" variants (0.247 m and 0.250 m, respectively). A high correlation ($r > 0.99$) was found between the "Clasif 2–4" methods, while "Clasif 7" correlated minimally with the others ($r < 0.1$), indicating its fundamentally different character. Most methods yielded comparable results, except for "Clasif 7," which showed the greatest variance and deviations. The best balance of accuracy, stability, and consistency was performed by the "Clasif 1 Spatix" method, which achieved the lowest RMSE, low variability, and strong correlation with other variants.

However, when these filters were applied to snow-covered landscapes, they caused a significant removal of point cloud data representing the snow surface. For the purpose of isolating snow cover from LiDAR data, a combination of filters was applied in CloudCompare, based on point height above terrain, surface roughness, point density, and normal orientation. Height above ground was used as a basic criterion to separate the snow layer from taller vegetation, while the calculation of surface roughness in a small window helped distinguish the smooth snow surface from the irregular structure of vegetation. Tree branches were further identified using their differing slope—points with deviating surface normals were detected and subsequently removed. Point density can also used to eliminate sparse structures typical of branches. By combining these criteria within CloudCompare's visualization environment, vegetation was effectively suppressed while maintaining a continuous (dense) snow cover point cloud. The detailed filtering procedure is provided in the Appendix – section "Methodology for filtering "bare ground" with snow cover".

Measurement with a snow gauge stick, map of snow cover thickness and other possible approaches

Validation of the measured data using a snow probe was carried out during two monitoring campaigns in January 2025. During the LiDAR scanning on January 13, 2025, a total of 43 test points were measured, and on January 24, 2025, 42 points were surveyed. Prior to the second data collection, a thaw followed by new snowfall occurred—this caused the lower snow layers to refreeze, introducing uncertainty as to whether the snow probe reached the actual ground surface. Therefore, these data were excluded from the accuracy evaluation. The point was first surveyed using RTK GNSS and then with snow probe. The resulting map is shown on Fig. 8. Snow depths measured with a snow pole are represented by points. The used (winter) point cloud (January 13, 2025) was also shifted based on the differences found on the folding GCP.

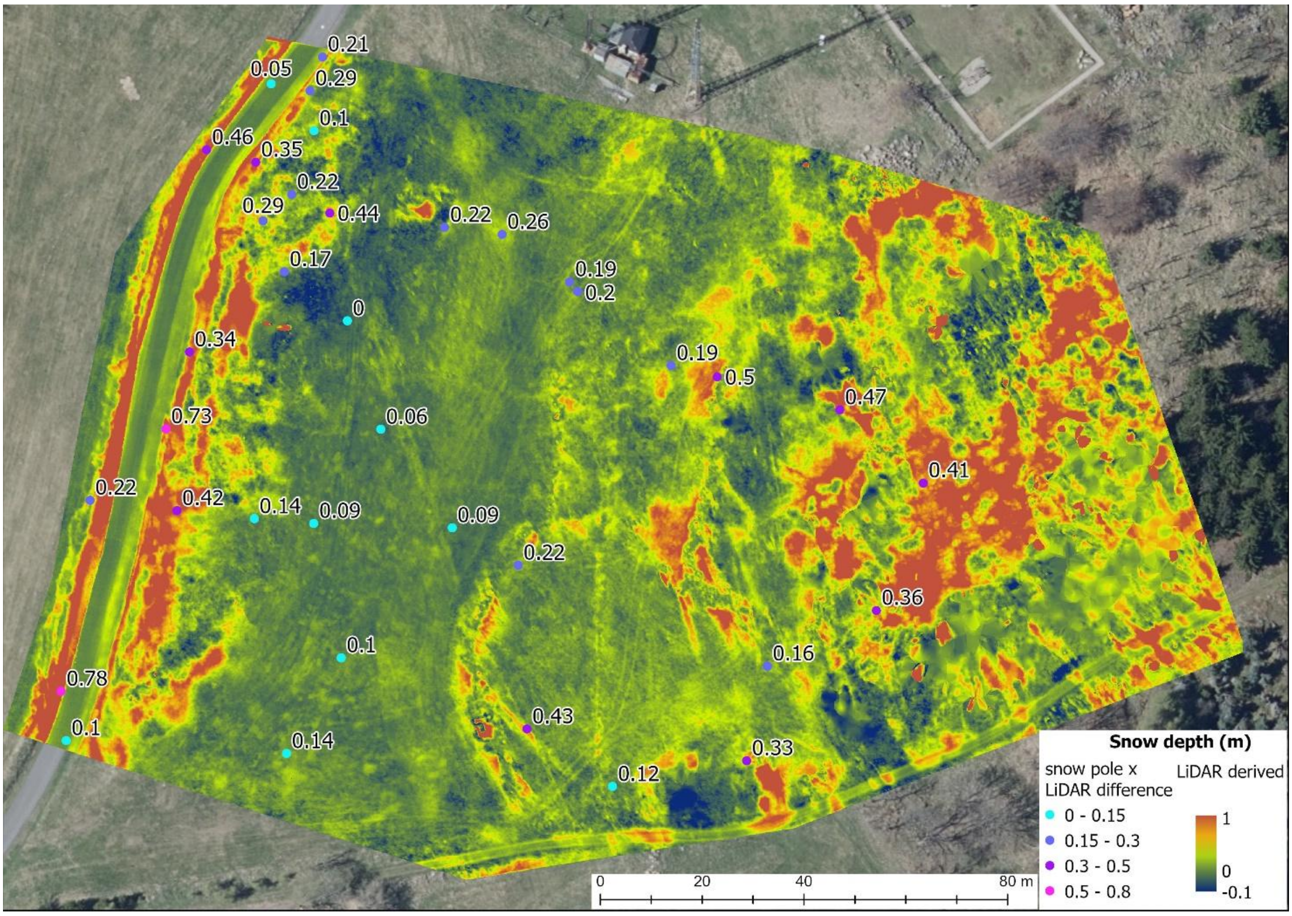

Fig. 8 - Snow depth map including snow depth measurements using the snow pole

DISCUSSION

Our comparative analysis of the Czepos and TopNet GNSS correction networks revealed subtle but systematic differences in positional accuracy. While both networks fulfilled the expected precision requirements for UAV-based RTK measurements, TopNet demonstrated slightly lower RMSE and standard deviation in elevation data, as well as a lower level of spatial autocorrelation in the X-Y plane. This is consistent with findings by authors such as [33], who emphasize the importance of network density and real-time signal quality in mountainous terrain. Notably, both networks exhibited a consistent positive elevation bias of 8–11 cm, likely related to the virtual base station location, which was ~15 km from the area of interest in some campaigns. These biases are particularly important when no ground control points are available to compensate for such systematic errors.

Our tests showed that the application of smoothing algorithms significantly improves LiDAR data accuracy. The unsmoothed model (Smooth 1) had an RMSE of 4.79 cm, whereas all smoothed variants reduced errors to approximately 2.5 cm. Among them, Smooth 3 (TerraSolid only) provided the most balanced results, with zero mean and median error, and symmetrical distribution of residuals. However, visual analysis revealed that the Smooth 5 method (a combination of DJI Terra, TerraSolid, and CloudCompare SOR) yielded the most aesthetically consistent and least noisy surface. This highlights an important trade-off: numerical indicators such as RMSE may not fully capture the surface smoothness or visual interpretability, which are often critical in hydrological or environmental applications.

An important methodological insight is that UAV LiDAR campaigns without ground control points are feasible, but subject to cumulative vertical errors. Our analysis shows that even a single foldable GCP, if accurately positioned using RTK GNSS, can significantly improve vertical alignment when used as a co-registration anchor for the point cloud. Moreover, point cloud smoothing in DJI Terra Pro appears to slightly overestimate elevation values, as shown by consistent positive shifts in error distributions. For this reason, we recommend using TerraSolid-based smoothing followed by intensity and geometry-based filtering, especially in areas where no GCPs can be deployed.

Ground classification algorithms proved useful not only for identifying terrain but also for suppressing noise in the point cloud. However, in snow-covered landscapes, standard bare-ground filters tended to mistakenly classify snow surfaces as terrain, particularly in open meadows. Our custom filtering method based on CloudCompare allowed for more accurate separation of snow from vegetation by combining height above ground, surface roughness, return number, and normal orientation. This multi-criteria approach proved essential for isolating snow cover in complex forest–meadow mosaics.

Snow depth estimation from LiDAR requires precise subtraction of snow-free and snow-covered surfaces. However, the variability in vegetation height, especially in summer datasets, complicates this process. Tall grass tufts and uneven ground structures often remain partially unfiltered, resulting in false negatives (i.e., negative snow depth). We recommend collecting snow-free data during late autumn or after frost events when vegetation is flattened and less influential on terrain modeling. Although meteorological and logistical constraints may limit such campaigns, their added value in reducing ground surface uncertainty is considerable.

While snow probes remain a useful tool for in-situ snow depth validation, our study identified several uncertainties. First, GNSS survey poles used to define terrain elevation may penetrate deeply into soil or vegetation, producing biased ground values. Second, snow probes may not reliably indicate the true base of the snowpack, especially after thaw-refreeze events that form ice layers or cause probe deflection. These factors limit the reliability of manual measurements as validation for LiDAR-derived snow thickness. Future field campaigns may benefit from integrated sensor probes or repeated time-series observations to reduce ambiguity.

The outcomes of this study go beyond methodological refinement and have direct implications for applied environmental monitoring. The presented UAV-based LiDAR workflow offers a scalable and replicable approach to snow documentation in mountainous regions with limited ground access. Regional water authorities, environmental protection agencies, and land-use planners may benefit from the spatially explicit data generated through this approach. In particular, accurate snow thickness mapping supports improved hydrological modeling, flood risk estimation, and planning of adaptation strategies in response to climate change. Moreover, the ability to document snowpack variability across open and forested terrain can inform conservation management in protected areas, such as national parks or nature reserves, where ground-based sensors are often infeasible. Although the study area covers 3.1 hectares, it encompasses a representative range of terrain variability and snow depths (0–1 m). This diversity, combined with the availability of historical ground measurements, makes it a suitable site for detailed methodological validation. Data obtained through this methodology are already being applied in hydrological studies to assess snow water equivalent (SWE) and related flood risks. Additional results, including analyses of SWE measurements performed in the Beskids Mountains, will be published separately.

The current methodology involves multiple software environments and manual processing steps, including point cloud filtering, noise removal, classification, and validation. While each step ensures high-quality outputs, the process remains time-intensive and requires significant operator expertise. Future work should explore the integration of automated workflows using open-source libraries (e.g., PDAL, Open3D) or batch-processing tools in CloudCompare and TerraSolid. Such developments could facilitate near-real-time snow monitoring over large areas and support operational deployment in remote sensing programs by governmental or academic institutions.

Operating UAVs in ecologically sensitive regions such as mountain ridges, forests, and protected landscape areas presents a range of logistical and ethical challenges. Our methodology was developed with careful attention to environmental regulations and conservation priorities. Equipment was transported manually to minimize disturbance, flight durations were kept minimal, and sensor deployments avoided critical habitats (e.g., wintering grounds of wildlife). These constraints, while challenging, underscore the importance of designing monitoring approaches that are both technologically effective and environmentally responsible. Future work should further investigate how UAV-based methods can be harmonized with nature protection policies to enable sustainable long-term monitoring.

CONCLUSION

This study presents a validated methodology for UAV-based LiDAR documentation of snow cover in the complex environmental conditions of Central European Mountain regions. The results highlight the importance of multiple technical and methodological factors that significantly influence the quality and usability of derived snow depth data.

First, the choice of GNSS correction network plays a measurable role in positional accuracy. While both tested networks (Czepos and TopNet) met expected standards, they exhibited systematic elevation biases and significant spatial autocorrelation. TopNet showed marginally better performance, particularly in elevation accuracy and error dispersion, making it a preferable choice for height-sensitive applications when ground control points are unavailable.

Second, the study demonstrates that point cloud post-processing has a critical effect on model quality. Among the tested approaches, the TerraSolid smoothing method (Smooth 3) provided the most balanced numerical results, while a more comprehensive workflow including DJI Terra, TerraSolid, and CloudCompare filtering (Smooth 5) yielded visually superior and less noisy outputs. When supported by a single ground control point, the quality of the resulting surface model improved significantly, confirming the utility of even limited GCP integration.

Third, the filtering of "bare ground" in snow-free datasets was shown to be a decisive step for the accurate estimation of snow depth. The Spatix-based filtering approach (Clasif 1) achieved the most stable results across more than 4,500 GNSS-validated points. In snow-covered scenes, standard ground classification algorithms often failed due to confusion between snow and vegetation. A combination of geometric criteria (e.g., roughness, normal orientation, and height above ground) in CloudCompare proved effective for isolating the snow surface while minimizing vegetation artifacts.

Finally, the study identified limitations in both the reference (snow-free) and validation (snow pole) data. Tall vegetation in summer months introduced negative snow depth values, suggesting that snow-free scanning is best conducted in late autumn or winter. Manual snow depth measurements also suffered from uncertainties related to ground contact and snowpack structure, underscoring the need for more robust in-situ validation techniques in future work.

Overall, this research contributes to the development of practical, field-tested workflows for high-resolution snow cover monitoring using UAV LiDAR systems. The proposed methodology is applicable in mountainous, remote, and protected landscapes, and offers valuable insights for hydrologists, environmental scientists, and land managers. Future research should aim to automate key processing steps, explore alternative validation methods, and extend the approach to different climatic zones and terrain types.

ACKNOWLEDGEMENTS

This research was supported by project TA ČR "Analysis of spatio-temporal dynamics of snow cover for the purposes of prediction and prevention of hydrological extremes and dimensioning of adaptation measures within land consolidation", reg. No. SS05010157.

REFERENCES

[1] Lizama, E., Somos-Valenzuela, M., Rivera, D., Lillo, M., Morales, B., Baraër, M., & Fernández, A. (2024). Role of mountain glaciers in the hydrological dynamics of headwater basins in the Wet Andes. Journal of Hydrology, 132413. doi:10.1016/j.jhydrol.2024.132413

[2] Sunita, N., Gupta, P. K., Gusain, H. S., Gill, A. S., & Sidhu, O. S. (2024). Snow Cover Variability in the Beas River Basin and its relation with climate parameters during 2007-2018. IOP Conference Series Earth and Environmental Science, 1326(1), 012147. doi:10.1088/1755-1315/1326/1/012147

[3] Schilling, S., Dietz, A., & Kuenzer, C. (2024). Snow Water Equivalent Monitoring—A Review of Large-Scale Remote Sensing Applications. Remote Sensing, 16(6), 1085. doi:10.3390/rs16061085

[4] Jenicek, M., & Ledvinka, O. (2020). Importance of snowmelt contribution to seasonal runoff and summer low flows in Czechia. Hydrology and Earth System Sciences, 24(7), 3475–3491.

[5] Slatyer, R. A., Umbers, K. D. L., & Arnold, P. A. (2024). Ecological responses to variation in seasonal snow cover. Conservation Biology, 38(2), e13727. doi:10.1111/cobl.13727

[6] Taheri, M., & Mohammadian, A. (2022). An Overview of Snow Water Equivalent: Methods, Challenges, and Future Outlook. Sustainability, 14(18). https://www.mdpi.com/2071-1050/14/18/11395

[7] Zha, H., Zhang, F., Tang, S., Zhang, L., & Luo, L. (2025). Unraveling the Distinct Roles of Snowmelt and Glacier-Melt on Agricultural Water Availability. AGU, 61(1). doi:10.1029/2023WR036898

[8] Poschlod, B., & Daloz, A. S. (2024). Snow depth in high-resolution regional climate model simulations over southern Germany – suitable for extremes and impact-related research? European Geosciences Union, 18(4). doi:10.5194/tc-18-1959-2024

[9] PAVELKA, Karel; ŠEDINA, Jaroslav a PAVELKA, Karel. Knud Rasmussen Glacier Status Analysis Based on Historical Data and Moving Detection Using RPAS. Online. *Applied Sciences*. 2021, roč. 11, č. 2. ISSN 2076-3417. Dostupné z: https://doi.org/10.3390/app11020754

[10] Wieder, W. R., Kennedy, D., Lehner, F., & Yamaguchi, R. (2022). Pervasive alterations to snow-dominated ecosystem functions under climate change. Proceedings of the National Academy of Sciences, 119(30). doi:10.1073/pnas.2202393119

[11] Lute, A. C., Abatzoglou, J., & Link, T. (2022). High-resolution snow model SnowClim: Dataset and applications for climate adaptation. Geoscientific Model Development, 15(13), 5045-5071. doi:10.5194/gmd-15-5045-2022

[12] Mitterwallner, V., Steinbauer, M., Mathes, G., & Walentowitz, A. (2024). Global reduction of snow cover in ski areas under climate change. PLOS ONE, 19(3). doi:10.1371/journal.pone.0299735

[13] Vionnet, V., Martin, E., Masson, V., Guyomarc'h, G., Naaim-Bouvet, F., Prokop, A., Durand, Y., & Lac, C. (2014). Simulation of wind-induced snow transport and sublimation in alpine terrain using a fully coupled snowpack/atmosphere model. The Cryosphere, 8(2). doi:10.5194/tc-8-395-2014

[14] Nousu, J. -P., Lafaysse, M., Mazzotti, G., Ala-aho, P., & Marttila, H. (2024). Modeling snowpack dynamics and surface energy budget in boreal and subarctic peatlands and forests. The Cryosphere, 18(1), 231–256. https://tc.copernicus.org/articles/18/231/2024/

[15] Abe, T., Iwasawa, S., Murakami, T., Ito, K., & Tomonori, U. (2019). Safety measures against snow and ice for safe and secure expressways. doi:10.1016/j.rse.2021.112345

[16] Soomro, S. -e-hyder, Soomro, A. R., Batool, S., & Guo, J. (2024). How does the climate change effect on hydropower potential, freshwater fisheries, and hydrological response of snow on water availability?, 14(65). doi:10.1007/s13201-023-02070-6

[17] Mott, R., Vionnet, V., & Grünewald, T. (2018). The Seasonal Snow Cover Dynamics: Review on Wind-Driven Coupling Processes. Cryospheric Sciences, 197(6). doi:10.3389/feart.2018.00197

[18] Proulx, H., Jacobs, J. M., & Burakowski, E. A. (2023). Brief communication: Comparison of in situ ephemeral snow depth measurements over a mixed-use temperate forest landscape. The Cryosphere, 17(8), 3435-3442. doi:10.5194/tc-17-3435-2023

[19] Mendoza, P. A., Musselman, K. N., & Revuelto, J. (2020). Interannual and Seasonal Variability of Snow Depth Scaling Behavior in a Subalpine Catchment. Advancing earth and space sciences, 56(7). doi:10.1029/2020WR027343

[20] Herla, F., Horton, S., Mair, P., & Haegeli, P. (2021). Snow profile alignment and similarity assessment for aggregating, clustering, and evaluating snowpack model output for avalanche forecasting. European Geosciences Union, 14(1), 239–258. doi:10.5194/gmd-14-239-2021

[21] Ryan, W. A., Doesken, N. J., & Fassnacht, S. R. (2008). Evaluation of Ultrasonic Snow Depth Sensors for U.S. Snow Measurements. Journal of Atmospheric and Oceanic Technology, 9(4), 1005–1015. doi:10.1175/2007JTECHA947.1

[22] Deems, J. S., Painter, T. H., & Finnegan, D. C. (2013). Lidar measurement of snow depth. Journal of Glaciology, 59(215), 467-479. doi:10.3189/2013JoG12J154

[23] Buchelt, S., Skov, K., Rasmussen, K. K., & Ullmann, T. (2022). Sentinel-1 time series for mapping snow cover depletion and timing of snowmelt in Arctic periglacial environments: case study from Zackenberg and Kobbefjord, Greenland. The Cryosphere, 2022(16), 625-646. doi:10.5194/tc-16-625-2022

[24] Postup testování přesnosti služeb a produktů CZEPOS. [Procedure for testing the accuracy of CZEPOS services and products] Czepos. Retrieved May 5, 2025, from https://czepos.cuzk.gov.cz/_postup.aspx

[25] GNSS positioning correction service. (2015). TopCon Positioning. Retrieved May 5, 2025, from https://www.topconpositioning.com/solutions/technology/infrastructure-software-and-services/topnet-live-corrections

[26] Gumilar, I., Bramanto, B., & Rahman, F. F. (2019). Variability and Performance of Short to Long-Range Single Baseline RTK GNSS Positioning in Indonesia. E3S Web of Conferences, 94(01012). doi:10.1051/e3sconf/20199401012

[27] Atiz, O. F., Konukseven, C., Ogutcu, S., & Alcay, S. (2022). Comparative analysis of the performance of Multi-GNSS RTK: A case study in Turkey. International Journal of Engineering and Geosciences, 2022(7), 67-80.

[28] Understanding RTK Accuracy and Its Dependence on Distance from the Base Station. Online. Point One Navigation. Dostupné z: https://support.pointonenav.com/understanding-rtk-accuracy-and-its-dependence-on-distance-from-the-base-station.

[29] BAYBURA, Tamer; TIRYAKIOĞLU, İbrahim a UĞUR, Mehmet Ali. Examining the Accuracy of Network RTK and Long Base RTK Methods with Repetitive Measurements. Journal of Sensors. 2019, roč. 2019.

[30] Ground Control Points- Tutorial. Online. Inflights. Dostupné z: https://help.inflights.com/en/articles/6495854-ground-control-points-tutorial.

[31] DJI Terra Release Notes. 4.5.0. 2025. Available from: https://terra-1-g.djicdn.com/263b7ee0f1fe477c91b7ca44348166fe/releasenotes/DJI%20Terra%20Release%20Notes.pdf.

[32] Martínez-Carricondo, P., Agüera-Vega, F., & Carvajal-Ramírez, F. (2023). Accuracy assessment of RTK/PPK UAV-photogrammetry projects using differential corrections from multiple GNSS fixed base stations. Geocarto International, 38(1). doi:10.1080/10106049.2023.2197507

[33] Pacina, J., Cajthaml, J., Kratochvílová, D., Popelka, J., Dvořák, V. & Janata, T. (2022). Pre-dam valley reconstruction based on archival spatial data sources: Methods, accuracy, and 3D printing possibilities. Transactions in GIS. 26(1), 385-420. ISSN 1361-1682. doi:10.1111/tgis.12854

[34] Schaefer, M. & PEARSON, A. (2021). Accuracy and precision of GNSS in the field. GPS and GNSS Technology in Geosciences. Vol. 2021, no. 19, pp. 393-414. doi:10.1016/B978-0-12-818617-6.00002-0

Article no. X

THE CIVIL ENGINEERING JOURNAL Y-20ZZ

Appendix

Reference Networks

Detailed statistical evaluation of the accuracy of the Czepos and TopNet reference networks used for surveyed points- the evaluation of errors of the X and Y coordinates (7 points used) is in

Tab. 1 and for the Z coordinate (75 points used) is in **Chyba! Nenalezen zdroj odkazů.**. and in box plot graphs in Fig. 1,2 and 3.

Tab. 1 Statistical evaluation of X a Y coordinate accuracy (errors) for the Czepos and TopNet reference network

Method	Czepos		TopNet	
	X	Y	X	Y
Spatial autocorrelation (Moran's Index)	0.518 *	0.709 **	0.742 **	0.437 *
Mean	-0.013 †	0.003 †	-0.033 ***	0.007 †
Median	-0.016 †	-0.004 †	-0.027 **	0.001 †
RMSE	0.023	0.029	0.036	0.020
Standard Deviation	0.021	0.031	0.017	0.021
Standardized Skewness	-0.041	-0.247	-0.242	-1.033
Standardized Kurtosis	-0.042	-1.1	-1.729	0.884
Normality (Jarque-Bera JB)	0.29 †	0.47 †	0.67 †	0.78 †
Pearson correlation	0.827 **	0.965 ***	0.817 **	0.967 ***

Statistical significance if tested: † not significant, * p-value <0.1, ** p-value <0.05, *** p-value < 0.01

The analysis of coordinate errors revealed that CZEPOS provides higher accuracy in the X direction, with a lower mean error (-0.013 m) and no statistically significant deviation from 0 value. In contrast, TopNet shows a significant systematic bias in X (mean value -0.033 m), despite similar overall deviation (RMSE = 0.023 m).

In the Y direction, TopNet performs more reliably, with a lower RMSE (0.020 m), reduced skewness, and weaker spatial autocorrelation compared to CZEPOS. The mean Y errors for both networks are small and not significantly biased. CZEPOS exhibits higher clustering of error values (Moran's I = 0.709 **). Importantly, errors in both coordinates strongly correlate with elevation (Z), indicating that accuracy decreases with increasing height, regardless of the reference network used.

Tab. 2 Statistical evaluation of Z coordinate accuracy (errors) for the Czepos and TopNet reference network

Method	***Czepos***	***TopNet***
	Z (altitude)	**Z (altitude)**
Spatial autocorrelation (Moran's Index)	0.521***	0.501***
Mean	0.107 ***	0.082 ***
Median	0.114 ***	0.086 ***
RMSE	0.119	0.095
Standard Deviation	0.053	0.048
Standardized Skewness	-0.985	-0.848
Standardized Kurtosis	1.4	1.01
Normality (Jarque-Bera JB)	18.07***	12.09***
Pearson correlation	-0.189*	-0.156 †

Statistical significance if tested: † not significant, * p-value <0.1, ** p-value <0.05, *** p-value < 0.01.

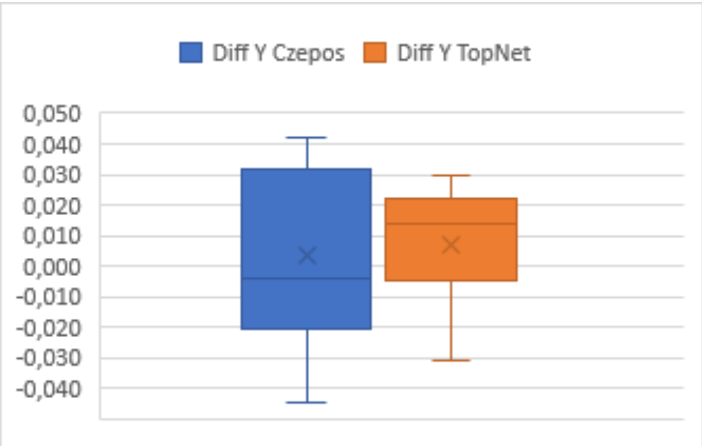

Fig. 1 Box plot showing the differences for the Y coordinate

DOI 10.14311/CEJ.20XX.0X.XXXX

Fig. 2 Box plot showing the differences for the X coordinate

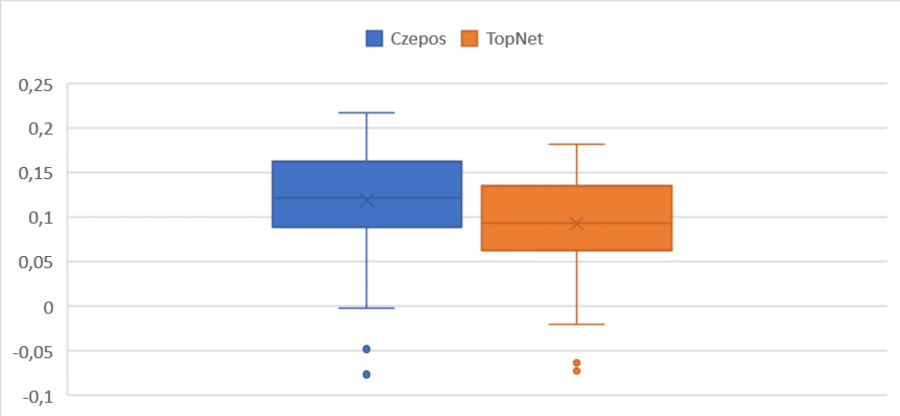

Fig. 3 Box plot showing the differences for the z coordinate

Accuracy and Systematic Errors of the Z coordinate analysis

Both reference networks exhibit a systematic overestimation of elevation values. For CZEPOS, the mean deviation is 0.107 m and the median is 0.114 m. For TopNet, the mean is 0.082 m and the median is 0.086 m. In all cases, the deviation of mean and median from 0 value is statistically significant at the $p < 0.01$ level, indicating a consistent positive bias in elevation measurements.

Accuracy and Error Dispersion

TopNet achieved a lower overall error compared to CZEPOS. The root mean square error (RMSE) for TopNet was 0.095 m, while CZEPOS recorded a RMSE of 0.119 m. Similarly, the standard deviation was slightly lower for TopNet (0.048 m) than for CZEPOS (0.053 m), suggesting a marginally higher precision and stability in TopNet's elevation data.

Spatial Behavior of Errors

Both methods display significant spatial autocorrelation of errors. Moran’s I values were 0.521 for CZEPOS and 0.501 for TopNet, both significantly different from 0 value. This indicates that errors are not randomly distributed and form locally clustered patterns.

Statistical Properties of Error Distribution

The distribution of errors is not normal as confirmed by the Jarque-Bera test: 18.07 for CZEPOS and 12.09 for TopNet. (both statistically significant). The characteristics of skewness are negative (-0.985

for CZEPOS and -0.848 for TopNet). suggesting that most values are slightly below the mean with some larger positive outliers. Additionally, both distributions show a slightly increased kurtosis (values above 1), indicating a sharper peak and heavier tails than a normal distribution.

Error Dependency on Elevation

There is a weak negative correlation between elevation errors and altitude. For CZEPOS, the correlation coefficient is -0.189 and is significantly different from 0 value. This suggests a slight tendency for elevation underestimation in higher terrain. For TopNet, the correlation is −0.156 and is not statistically significant.

Influence of post-processing operations on LiDAR data

Tab. 3 Methods used to post-process LiDAR data

Smooth1	No smoothing applied.
Smooth2	Only the *Optimize Point Cloud Accuracy* function in DJI Terra Pro was used.
Smooth3	Without using the *Optimize Point Cloud Accuracy* function in DJI Terra Pro; instead, TerraSolid (Spatix) was used with the *Smoothen and Remove Noise* tool.
Smooth4	Combination of Smooth2 and Smooth3; smoothing applied both in DJI Terra Pro and in TerraSolid (Spatix).
Smooth5	Combined approach including SOR filtering in CloudCompare (SOR parameters: 8 neighbors, standard deviation multiplier 1.5).

Visual inspection of the 3D difference models (Main text – Fig. 7 A–E) confirms the quantitative finding: a significant deviation is only evident in the unsmoothed model (RMSE = 4.79 cm), while all tested smoothing variants achieve an RMSE between 2.4–2.78 cm. The results show a consistent improvement in accuracy due to the application of smoothing algorithms. The detailed description of the used post-processing methods is in Tab. 3.

When comparing smoothing methods over communications the best results are achieved by *the Smooth 3* and *Smooth 5* variants, both with an RMSE of around 2.5 cm. The differences between them are minimal, but *the Smooth 3 method* is characterized by a completely symmetrical distribution of errors (mean = median = 0) and slightly lower variability which makes it the most balanced choice – see Tab. 4

Methods using DJI Terra optimization show lower dispersion and fewer outliers. but achieve slightly higher deviations compared to *the Smooth 3* method. probably due to smoothing that suppresses fine height details of the surface. See Fig. 4.
On further visual analysis presented on Fig. 4. outliers are prominent in *Smooth 1*. but also occur in *Smooth 5* and *Smooth 4*. which may indicate local errors in classification or a less appropriate selection of points in some segments of communication.
The symmetry of the distribution is best in the *Smooth 3*. where the median lies almost exactly in the middle of the box. On the other hand, there *is a noticeable hint of a positive shift in the Smooth 4* and *Smooth 5* (the median is closer to the lower limit of the box) which may indicate a tendency to overestimate the height.
The visualization also confirms earlier quantitative results – *Smooth 3* is the only method without DJI optimization that achieves very good results and can be preferred where maintaining height details is a priority. On the other hand, FigFig. 5 shows the structure of the point cloud (both the original and the spatially repaired one using the control point) and the position of the control point. The control point always comes out into the space between the LiDAR points of the cloud so the verified value of the Z coordinate is always interpolated from the cloud under test.

The Smooth 3 and Smooth 5 methods were subjected to detailed geostatical analysis. The spatial autocorrelation of model errors was statistically significant in both compared methods (Moran's I = 0.487 and 0.694 respectively; p-values < 0.01) indicating a significant spatial structure of the residuals.

The central tendency was negligible – the mean and median error for the *Smooth 3* method was 0 while for *the Smooth 5* they reached values of 0.014 m and 0.016 m respectively.

The variance of errors was low for both methods with RMSE below 3 cm (0.024 m for *Smooth 3* and 0.026 m for *Smooth 5*) which is fully consistent with the expected accuracy over communications. Standardized skewness and kurtosis and the box plots show a narrow distribution around zero with a minimum of outliers.

The normality test (Jarque-Bera) did not reveal significant deviations from the normal distribution for any of the methods (p > 0.1).

The "peaks" visible in Fig. 7-C (in the main text) are always outside the control points and even though the statistical evaluation values of the Smooth 3 method come out better than the Smooth 5 method. This method wins in terms of visual quality (smoothness).
The effect of point cloud co-registration on only one ground control point was also evaluated as part of the statistical analysis. Box plot difference of Z coordinates (their significant improvement after the implementation of GCP into processing) within the Smooth 5 method is on Fig. 6

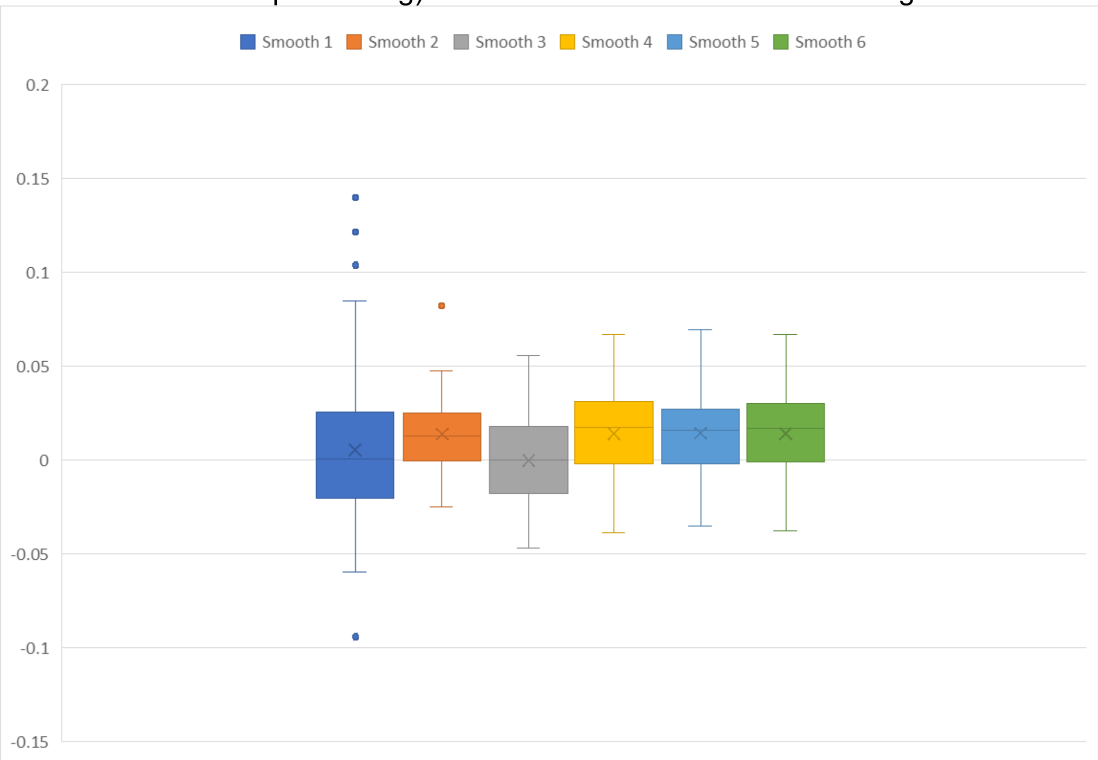

Fig. 4 Box plot of errors of tested smoothing methods (Smooth 1 – Smooth 6) referring to data in Tab. 4.

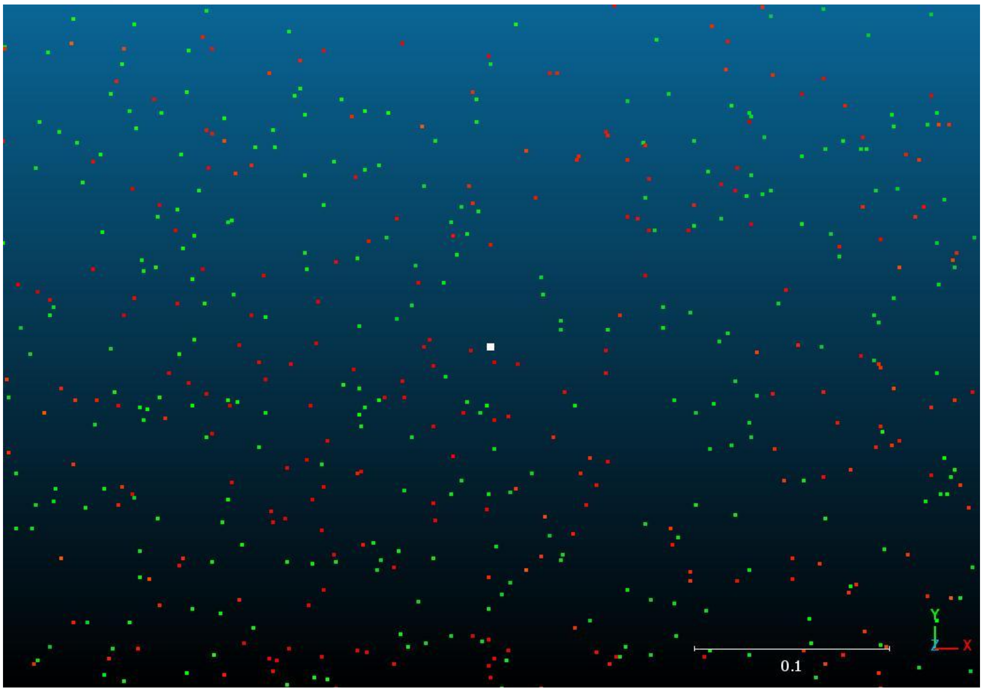

Fig. 5 GNSS measured control point (white), original point cloud (red), positionally corrected point cloud (green).

Tab. 4 Detailed statistical analysis of errors of Smoothing 3 and Smoothing 5 methods on summer data (June 19, 2023)

Method	**Smooth 3**	**Smooth 5**
Spatial autocorrelation (Moran's Index)	0.487 ***	0.694 ***
Mean	0.000	0.014
Median	0.000	0.016
RMSE	0.024	0.026
Standard Deviation	0.024	0.022
Standardized Skewness	0.068	0.09
Standardized Kurtosis	-0.378	0.4
Normality (Jarque-Bera JB)	0.416 †	0.106 †
Pearson correlation	0.452	0.452

Statistical significance if tested: † not significant, * p-value <0.1, ** p-value <0.05, *** p-value < 0.01.

DOI 10.14311/CEJ.20XX.0X.XXXX

Tab. 5 Detailed statistical analysis of errors of Smoothing 3 and Smoothing 5 methods on winter data (January 24, 2025)

Method	**Smooth 5**	**Smooth 5 GCP used**
Spatial autocorrelation (Moran's Index)	0.849 ***	0.773 ***
Mean	-0.119	0.011
Median	-0.111	0.013
RMSE	0.121	0.025
Standard Deviation	0.020	0.022
Standardized Skewness	-0.416	-0.273
Standardized Kurtosis	2.135	2.173
Normality (Jarque-Bera JB)	2.765 †	1.881 †
Pearson correlation	0.946	0.946

Statistical significance if tested: † not significant, * p-value <0.1, ** p-value <0.05, *** p-value < 0.01.

Fig. 6 Box plot of errors in Z coordinate on point cloud without Ground Control Point co-registration (blue) and with Ground Control Point co-registration (right).

The impact of "bare earth" filtering on data quality

Point cloud processing software products include various methods of "bare ground" filtering. As part of our processing. we tested algorithms in our available (and widespread) tools. An overview of the tested methods is in **Chyba! Chybný odkaz na záložku.**.

Tab. 6 Tested methods for filtering "bare ground"

Clasif 1	1. Spatix: Process Drone Data – used Thin Points to Inactive, Classify Ground (value: 10), Classify Height from Ground (1;5) 2. CloudCompare: SOR filter (8 neighbors, standard deviation multiplier 1.5)
Clasif 2	1. ArcGIS Pro: Classify LAS Ground – Standard Classification method 2. CloudCompare: SOR filter (8 neighbors, standard deviation multiplier 1.5)
Clasif 3	1. ArcGIS Pro: Classify LAS Ground – Conservative Classification method 2. CloudCompare: SOR filter (8 neighbors, standard deviation multiplier 1.5)
Clasif 4	1. ArcGIS Pro: Classify LAS Ground – Aggressive Classification method 2. CloudCompare: SOR filter (8 neighbors, standard deviation multiplier 1.5)
Clasif 5	1. Spatix: *Classify Ground* – default settings, modified: Max building size 8 m, Terrain angle 15°, Iteration angle 10°, Iteration distance 100 m
Clasif 6	1. Spatix: same as Clasif5 2. CloudCompare: SOR filter (8 neighbors, standard deviation multiplier 1.5)
Clasif 7	1. CloudCompare: SOR filter (8 neighbors, standard deviation multiplier 1.5) 2. CloudCompare (CSF plugin): *Relief* method; advanced settings – *Cloth resolution*: 0.5, *Max iterations*: 500, *Classification threshold*: 0.5

Tab. 7 Detailed statistical analysis of Z-coordinate errors for individual bare ground filtering methods

Method	Clasif 1	Clasif 2	Clasif 3	Clasif 4	Clasif 5	Clasif 6	Clasif 7
Spatial autocorrelation (Moran's Index)	0.107 ***	0.110 ***	0.114 ***	0.113 ***	0.178 ***	0.180 ***	0.108 ***
Mean	-0.148	-0.150	-0.149	-0.149	-0.085	-0.085	-0.241
Median	-0.167	-0.171	-0.169	-0.170	-0.101	-0.102	-0.253
RMSE	0.247	0.251	0.253	0.250	0.250	0.251	0.301
Standard Deviation	0.198	0.201	0.205	0.201	0.235	0.236	0.180
Standardized Skewness	-1.816	-1.772	-1.673	-1.710	-0.647	-0.588	-4.664
Standardized Kurtosis	37.254	35.852	34.387	35.650	23.102	22.508	67.900
Normality (Jarque-Bera JB)	219710.876 ***	202171.294 ***	184492.956 ***	199561.912 ***	75133.823 ***	70723.017 ***	796 039.946 ***
Pearson correlation	1 ***	0.992 ***	0.988 ***	0.995 ***	0.839 ***	0.835 ***	0.063 ***

Statistical significance if tested: † not significant, * p-value <0.1, ** p-value <0.05, *** p-value < 0.01.

Quality was evaluated on the basis of more than 4500 points measured by RTK GNSS within the test area of interest. This analysis also included 46 road-focused points (and used to evaluate point cloud smoothing) to verify the possible effect of filtering algorithms on the overall quality of the point cloud. The quality of the filtered point cloud was again evaluated using three defined qualitative parameters. The results are presented in Tab. 7.

The spatial autocorrelation of errors was statistically significant in all tested methods (p-values < 0.01) with Moran index values ranging from 0.107 to 0.180. This indicates that the errors are not randomly distributed in space and exhibit a spatial structure.

The normality of the error distribution has not been confirmed for any of the methods. Jarque-Bera statisticsachieved extremely high values and were significantly different from normality in all cases (p-values < 0.01). This corresponds to high values of standardized kurtosis exceeding 20 and negative skewness in all cases. The most significant deviations from normality were recorded in *Clasif 7* (kurtosis = 67.9; skewness = - 4.664) as confirmed by the box plot with numerous outliers (see Fig. 7).

The central tendency (mean and median) was negative for all methods with the lowest values again for *Clasif 7* (mean = - 0.241; median = - 0.253). The variance of errors (RMSE) was also highest for this variant (0.301) while the lowest RMSE values were achieved for Clasif *1* and Clasif *5* (0.247 and 0.250 respectively).

The relationships between the methods errors and elevation were expressed by Pearson's correlation coefficient. A high correlation (r > 0.99) was observed between most variants of standard processing (*Clasif 2*, *Clasif 3* and *Clasif 4*). On the other hand the *Clasif 7 method* showed a low correlation (r = 0.063), which indicates a fundamentally different nature of the resulting errors.

Although the individual classification methods differ slightly in accuracy most of them give very similar results. The largest deviations and variance of errors are shown by *the variant Clasif 7* while the other approaches differ mainly in lower variability and better symmetry of errors. In practice, most of the tested methods can be considered comparably applicable if they are applied consistently and with regard to the specific conditions of the given area.

Of all the approaches tested, the Clasif 1 method shows the best ratio between accuracy, stability and a reasonable degree of variability as it achieves the lowest RMSE (0.247 m).

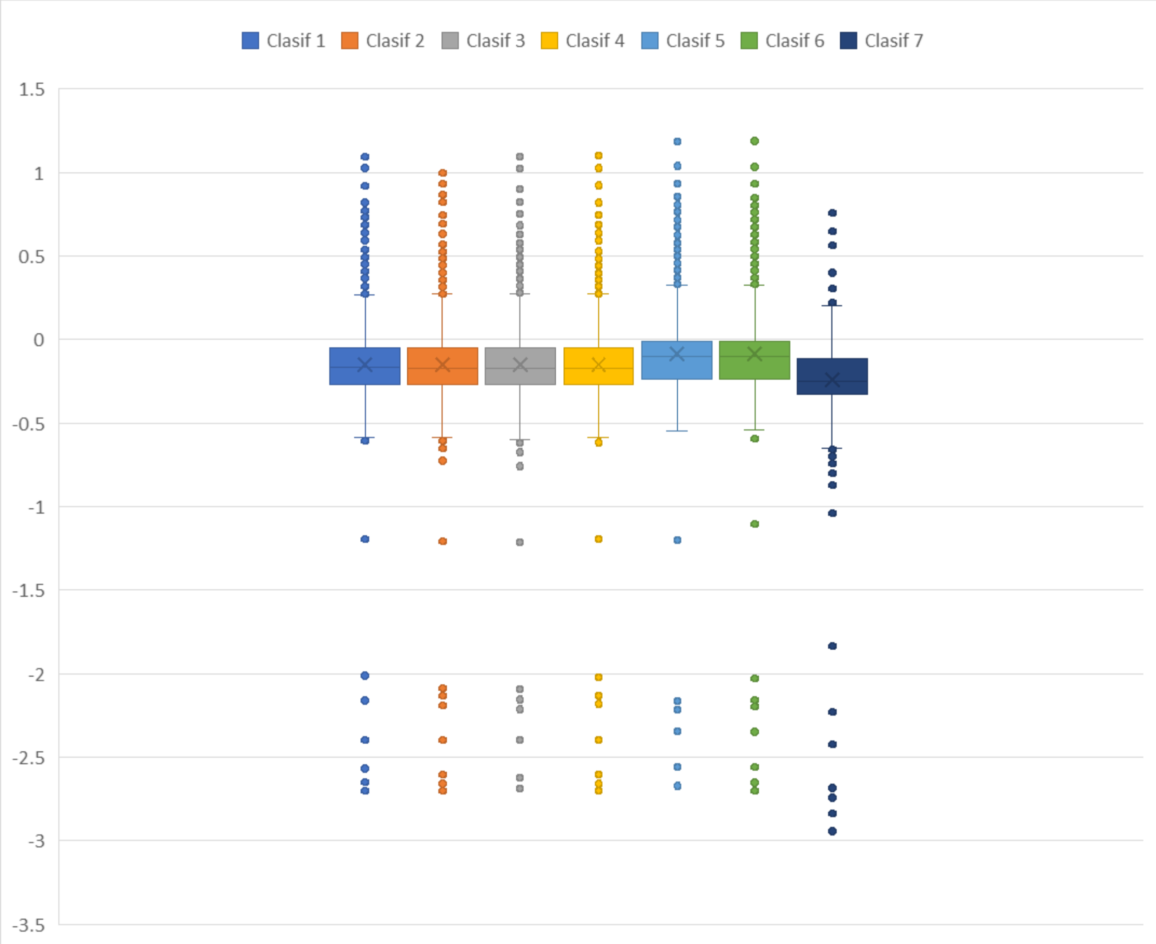

Fig. 7 Box plots of errors in the Z coordinate for individual classification approaches

Methodology for filtering "bare ground" with snow cover

To remove vegetation in the case of a point cloud with snow cover. It is advisable to use a point cloud from the period without vegetation in combination with a cloud with snow. Calculation of the approximate maximum thickness of snow cover – a "snow-free" cloud with filtered vegetation is converted to mesh and then the "Cloud to Mesh distance" is calculated. From the winter cloud we extract only points that are in the range of +/- 0 to the maximum snow depth. This will filter out most of the vegetation. This step can only be replaced by estimating the snow depth – i.e. filtering points that lie within our estimated interval. In the following steps it is necessary to remove the remains of vegetation.

1. Filtering according to Roughness around the points (Tools > Other > Compute Geometric Features) and choose a window size of 0.5 – 1 m (in our case 0.5 m). Snow has low roughness, vegetation significantly higher. We filter points with low Roughness (Edit > Scalar Fields > Filter By Value (in our case < 0.05)).

2. Filtering by return number - snow usually reflects only one pulse (last return). while vegetation often causes multiple reflections. Filter only Last Return (Edit > Scalar Fields > Filter By Value (in our case = 1)).

3. If the sensor has recorded intensity. we check the histogram (Edit > Scalar Fields > Show Histogram). We filter values with typical snow intensity - it is usually higher but it depends on the specific scan (Edit > Scalar Fields > Filter By Value (in our case > 100)).

The previous procedure will filter out most of the vegetation but it is still necessary to focus on the remnants of branches.

4. We will use the "local roughness" function again. Branches often change the slope and shape of the surface – even if they are low – they have a different geometry than smooth snow. In the "Compute Geometric Features" tool. select "Roughness" but this time in a small area (0.1 – 0.3 m). We then filter the points with a Roughness > 0.01.

5. It is also advisable to filter the cloud according to the normals. Normals need to be computed first (Edit > Normals > Compute). Other parameters - Neighborhood radius (depending on cloud density. „Auto“ can be selected); Preferred orientation: +Z. In CloudCompare normals need to be exported as a Scalar Field (Edit > Normals > Export Normals to SF(s)). We export points with a normal value. e.g. 0.95 – 1.0. That is we keep only points that have normals almost perpendicularly upwards (typically snow).

   After these two steps. most of the vegetation points should be filtered out. However. if there are still some left – usually isolated points – we will use the next step.

6. The SOR (Statistical Outlier Removal) filter can be applied to the individual points that remained after the previous filtration process in the Tools > Clean > SOR menu. In the parameters we need to set "k" which is the number of nearest neighbors (in our case 10) and Sigma - the number of standard deviations from the average distance (in our case 1.5).

CIVIL ENGINEERING JOURNAL

Article no. 15

THE CIVIL ENGINEERING JOURNAL 2-2025

RESEARCH ON FLEXURAL CALCULATION THEORY OF REINFORCED CONCRETE T-BEAM STRENGTHENED BY STEEL WIRE MESH AND POLYURETHANE CEMENT (SWM-PUC) COMPOSITE

Yi Wang[1], Kenxin Zhang[1], Liangxiang Guo[2], Dianye Cao[3], Shiyu Chen[3] and Longsheng Bao[3]

1. *Shenyang Jianzhu University, School of Transportation and Geomatics Engineering, Shenyang, No.25 Hunnan Zhong Road, China;*
2. *Guangzhou Highway Engineering Group Co. LTD, Engineering Department, Guangzhou, No. 6, Shuiyin Erheng Road, China;*
3. *Shenyang Jianzhu University, School of Transportation and Geomatics Engineering, Shenyang, No.25 Hunnan Zhong Road, China; baolongsheng710605@163.com*

Received:	*21.10.2024*
Received in revised form:	*09.04.2025*
Accepted:	*17.06.2025*

ABSTRACT

In order to solve the problem of poor bonding and easy peeling of reinforced concrete structure strengthened by steel wire mesh and polymer mortar (SWM-PM). In this paper, a steel wire mesh and polyurethane cement (SWM-PUC) composite strengthening technique is presented. The flexural properties of one unreinforced beam, two SWM-PM strengthened beams and four SWM-PUC composite strengthened beams were studied experimentally. The experimental results show that the SWM-PUC composite reinforcement layer can improve the load carrying capacity and rigidity of reinforced concrete beams and limit the unfolding cracks significantly. The SWM-PUC composite strengthened beams have pure bending damage and peeling damage between the strengthening layer and the concrete has not occurred. However, SWM-PM strengthened beams with the same SWM reinforcement ratio occurred with peeling damage between the reinforcement and the concrete. On basis of an experimental study, the theoretical formulas for cracking load, ultimate load, deflection and width of crack of SWM-PUC composite strengthened beams are proposed by the simplified stress-strain constitutive relation of the material and the theoretical formulas are deduced with the code. By contrasting the test results with the theoretical computation results, the accuracy of the experiment results and the reliability of the theoretical formulas were verified.

KEYWORDS

Steel Wire Mesh and Polyurethane (SWM-PUC) Cement Composite, Flexural Strengthening, Reinforced Concrete Beam, Calculation Theory

INTRODUCTION

Bridges play a vital role in highway transportation and are indispensable infrastructure. However, with the passage of time and the influence of the natural environment, coupled with the overloading of vehicles and outdated design standards, concrete bridges are subject to problems such as material aging, cracking and insufficient bearing capacity [1-3]. From the economic and environmental point of view, adopting a reasonable method of maintenance and reinforcement can produce good economic and social benefits.

At present, the main reinforcement methods for reinforced concrete bridges [4-5] are pasting carbon fiber plates [6-7] and pasting steel plates [8]. Pasted steel plate reinforcement method and pasted carbon fiber plate reinforcement method are convenient in construction, both of which can greatly increase the bearing capacity of specimens and hardly affect the structural headroom height. However, the aging resistance of the carbon fiber plate material itself is poor, and the steel plate is prone to corrosion in the environment of nature. Because of the uneven surface of the concrete beam, the steel plate and carbon fiber plate are difficult to fit well with the concrete surface. There is an urgent need to solve the problem of durability after the strengthening of pasted carbon fiber plates and pasted steel plates.

Steel wire mesh (SWM) is used for bridge structural strengthening due to its good tensile strength, toughness and durability [9-11], often using cement-based such as polymer mortar [12-14] and engineered cementitious composite (ECC) as its bonding and anchoring material with concrete [15-16], polymer mortar and ECC have good film-forming properties, which can adapt to the uneven surfaces of the concrete structure being strengthened. Fang Y, through the experimental study on the flexural strength of beams reinforced with high-strength wire mesh and ECC composite materials, found that the SWM and engineered cementitious composite (SWM-ECC) strengthening layer can significantly increase the flexural resistance and stiffness of the reinforced beams, and decrease the width of the cracks in the composite layer and delay the development of the concrete cracks [17]. However, ECC is a cement-based material that requires wet work, which has problems with long curing time and low early strength. In addition, the poor bonding of ECC materials to the strengthened beams results in peeling damage to the SWM-ECC strengthening layer and the strengthened beams, which reduces the utilization rate of the SWM [18-19]. Xing G, conducted a flexural loading experimental study on steel wire mesh and polymer mortar (SWM-PM) strengthened RC beams, and SWM-PM was found to be effective in improving the load carrying capacity and rigidity of RC beams, but the tentative strength and bonding properties of polymer mortar material have certain limitations, and cracking of the SWM-PM reinforcement layer and stripping of the reinforcement layer from the concrete surface occur, affecting the durability of the reinforced bridge structure [20].

To solve the problem that the bonding between the strengthening layer and concrete of reinforced concrete T-beam strengthened by SWM is poor and easy to peel off, the strengthening efficiency of reinforced concrete T-beam strengthened by SWM is further improved. In this paper, a method of strengthening existing reinforced concrete beams by using steel wire mesh and polyurethane cement (SWM-PUC) composite materials is proposed. Through the flexural experiment of SWM-PUC composite strengthened reinforced concrete T-beams, the change law of flexural performance of strengthened beam is explored, and to clarify the crack development, damage mode and load carrying capacity of the SWM-PUC composite strengthened reinforced concrete T-beams are clarified. Based on the experimental study, the flexural calculation method of the strengthened reinforced concrete T-beam by SWM-PUC composite strengthening is proposed.

TEST PROFILE

Material Properties

Concrete

Ordinary silicate cement was used for cement, natural river sand was used for fine aggregate, and two kinds of graded crushed stone with diameters ranging from 5 to 25 mm and 25 to 31.5 mm were used for coarse aggregate. The 28-day cubic compressive strength and flexural strength of the concrete are measured to be 31.8 MPa and 5.30 MPa, respectively. The modulus of elasticity of the concrete was 30 GPa and Poisson's ratio was 0.2.

Steel

The diameter of the tensile reinforcement is 18 mm, and the diameter of the stirrups and erection reinforcement is 8 mm. The yield strengths of the 18 mm and 8 mm diameter reinforcement is 400 MPa and 335 MPa, respectively, and the ultimate strengths are 600 MPa and 510 MPa, respectively. The modulus of elasticity of the reinforcement is 200 GPa and Poisson's ratio is 0.3.

SWM

The type of steel wire is 6 x 7 + IWS (a steel wire has 6 strands, each consisting of 7 steel wires, with IWS as the center metal strand core). The steel wires mesh is made of steel wires with a diameter of 2.4 mm, the area of a single steel wire is 4.52 mm^2, the tensile strength is 1520 MPa, the elastic modulus is 140 GPa, and the ultimate tensile strain is 0.0187.

Polymer Mortar

Polymer mortar is made by mixing cement, fine aggregate, polymer emulsion and admixtures. Polymer emulsion is an important component of polymer mortar. The compressive and flexural strengths of the polymer mortar are measured to be 55 MPa and 5.6 MPa, respectively. The modulus of elasticity of polymer mortar is 23.1 GPa.

PUC Material

PUC material is polymerized from polyester polyols, isocyanates and cement. The combination PUC as presented in Table 1. The axial tensile test of the PUC material measured a tensile strength of 35.6 MPa. PUC has a tensile modulus of elasticity of 5500 MPa and an ultimate tensile strain of 7000 με. The expression of PUC obtained by fitting the result data is as follows:

$$\sigma_{\mathrm{PUC}} = -0.24566\varepsilon_{\mathrm{PUC}}^{\ 2} + 6.85318\varepsilon_{\mathrm{PUC}} - 0.34356 \tag{1}$$

where σ_{PUC} is the stress of PUC material, ε_{PUC} is Strain of PUC material.

Tab. 1 - The mix ratio of PUC material

Components of PUC	Ratio/%
Polyester polyol	25
Isocyanate	25
Concrete	40
Molecular sieve	10

Specimens Design

A total of seven reinforced concrete (RC) beams were designed for the experiment, including one unreinforced beam, two SWM-PM reinforced beams, and four SWM-PUC composite strengthened beams. The beam length is 3800 mm, the upper flange width is 360 mm and the beam height is 320 mm. The thickness of the concrete protective layer is 25 mm. The distance of the loading point from the support is 1500 mm and the shear span ratio is 5.5.

The main parameters of the test were in addition to the type of bonding anchorage material in the reinforcement layer. The reinforcement ratio of the SWM, the thickness of the PUC, the anchoring method and the loading method were also considered. For a beam with initial damage, the beam is preloaded before strengthening so that the maximum crack width of the beam is 0.2 mm. After unloading, the beam is strengthened. After the strengthening and maintenance are completed, the graded loading is carried out. The specimen design parameters are presented in Table 2.

Tab. 2 - Specimens design parameters

Beam	Bonded anchoring materials	Bonded anchoring materials thickness(mm)	Number of longitudinal steel wires	End anchoring method	Loading method
CB	-	-	-	-	-
B1	Polymer mortar	20	8	-	-
B2	Polymer mortar	20	8	End U-shaped anchorage	-
B3	PUC	20	5	-	-
B4	PUC	20	8	-	-
B5	PUC	30	5	-	-
B6	PUC	20	8	-	Preload

Loading and Measuring Programs

The loading method of the test was four-point bending loading, and the loading device as presented in Figure 1. There test beams were all simply supported beams with a 3600 mm span and a distance of 600 mm between the two loading points. Preload the test beam before official loading and inspect all the test instruments and meters to see if they work properly. Before cracking of the test beams, the loading level was 2 kN. The loading level after cracking of the test beams was 5 kN, and the loading was stopped when the maximum crack of the test beams exceeded 1 mm. Displacement gauges were arranged at the center of the beam span and at the loading point location to measure the deflection during the loading process. Concrete strain gauges were arranged along the beam height of the experimental beam to measure the concrete strain during the loading process. Strain gauges were placed in the tension reinforcement to measure the reinforcement strain. Strain gauges were arranged at the strand position in the middle of the span to measure the strain of the strand during loading. All measurements were collected by a static strain collection box.

Fig. 1 - Test loading device diagram

TEST RESULTS AND ANALYSIS

Cracking Load

The cracking loads of all the specimens are presented in Table 3. The cracking load of beam CB was 10 kN. The cracking load of beam B1 reinforced with SWM-PUC was 14 kN, which was a 40% increase over beam CB. The cracking load of beam B2 reinforced with SWM-PM was 16 kN, which was a 60% increase over beam CB. Due to the U-shaped anchorage of beam B2, the cracking load of beam B2 was elevated by 2kN compared to beam B1. Beam B3 was strengthened with a SWM-PUC composite with a cracking load of 18 kN. Beam B4 had a cracking load of 20 kN. With the same thickness of the strengthening layer, the reinforcement ratio of the SWM in the strengthening layer of beam B4 was larger than that of beam B3, so the cracking load of beam B4 was elevated by 2 kN compared with that of beam B3. The cracking load of beam B5 was 22 kN,

DOI 10.14311/CEJ.2025.02.0015

and the thickness of the strengthening layer of beam B5 was larger than that of beam B3 with the same configuration of the strengthening layer's SWM, and the cracking load of beam B5 was elevated by 4kN compared with that of beam B3.

Tab. 3 - Characteristic load test value

Beam	Cracking load/kN	Increase relative to CB/%	Yield load/kN	Increase relative to CB/%	Ultimate load/kN	Increase relative to CB/%
CB	10	-	60	-	80	-
B1	14	40	70	16.6	85	6.3
B2	16	60	75	25	94	17.5
B3	18	80	79	31.6	112.8	41
B4	20	100	85.8	43	122.6	53.3
B5	22	120	98	63.3	140	75
B6	-	-	84	40	120	50

Yield Load and Ultimate Load

(1) Yield load

The yield loads for all specimens are shown in Table 3. The yield load of beam CB was 60 kN. The yield loads of beams B1 and B2 were 70 kN and 75 kN, respectively, and the yield loads were elevated by 16.6% and 25%, respectively, compared with beam CB. Showing that the SWM-PM reinforcement method can enhance the yield load of the strengthened beams. Beam B2 was anchored with U-shaped anchor, beam B2 had a 5 kN higher yield load than beam B1. The thickness of the strengthening layer of beam B1 and beam B4 was the same as the reinforcement ratio of the SWM in the strengthening layer, and the yield load was 70 kN and 85.8 kN, respectively. The yield load of beam B4 was 22.6% higher than that of beam B1. It indicates that the SWM-PUC composite can better enhance the yield load of strengthened beams. The thickness of the strengthening layer was the same for beam B3 and beam B4, and the yield loads were 79 kN and 85.6 kN, respectively. The yield load of beam B4 was elevated by 8.6% compared to beam B3. The reinforcement ratio of the SWM in the strengthening layer of beam B3 and beam B5 was the same, and the yield load was 79 kN and 98 kN, respectively. The yield load of beam B5 was elevated by 24.1% compared to beam B3. Beam B6 was a preloaded beam. The ultimate loads of beam B6 and beam B4 were 43 kN and 40 kN, respectively. It shows that SWM-PUC strengthening had a good strengthening effect on beams with initial damage.

(2) Ultimate load

The ultimate loads of the specimens are shown in Table 3. The thickness of the strengthening layer of beam B1 and beam B4 was the same as the reinforcement ratio of the SWM in the strengthening layer. The ultimate loads were 86 kN and 122.6 kN, respectively, and the difference in ultimate load was 36.6 kN. The thickness of the strengthening layer was the same for beam B3 and beam B4. The ultimate load of beam B4 was elevated by 8.7% compared to beam B3. The reinforcement ratio of the SWM in the strengthening layer of beam B3 and beam B5 was the same, and the ultimate load was 112.8 kN and 140 kN, respectively. The ultimate load of beam B5 was elevated by 24.1% compared to beam B3. The thickness of the strengthening layer of beam B4 and beam B6 was the same as the reinforcement ratio of the SWM in the strengthening layer. The ultimate load increase of the preloaded beam B6 was 50%. The ultimate load increase of beam B4 without preloading is 53.3%. The increase in the ultimate load of both was almost the same.

Load-Strain Curve Analysis

Longitudinal Reinforcement Strain

It can be seen from Figure 2 that the longitudinal reinforcement strain is linearly related to the load before cracking of the specimen. When the load reached 40 kN. The strain in the unreinforced beam was 1585 με. The strains of beams B1 and B2 strengthened with SWM-PM were 1,288 με and 1,127 με. At this time, the strains of B3, B4, B5 and beam B6 strengthened by SWM-PUC composite were 853 με, 697 με, 632 με and 750 με, respectively. Under the same load, the strain change of the SWM-PUC composite strengthening specimen was small. The reason is that the SWM shares part of the load during the loading process so that the load increment of the strengthened beam is smaller for the same longitudinal reinforcement strain. With the increase in load, the reinforcement yielded and the constraint of the concrete by the SWM became more obvious. The load continued to increase and the SWM-PM strengthening layer peeled away from the concrete. However, the PUC remained well bonded to the concrete, and the slope of its load-reinforcement strain curve decreased slowly.

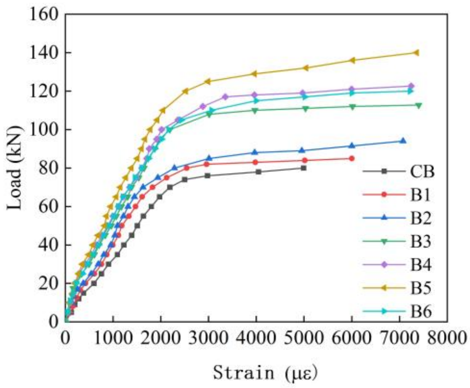

Fig. 2 - Load-reinforcement strain curve

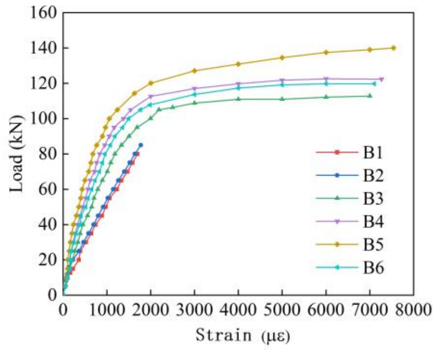

Fig. 3 - Load- steel wire strain curve

Longitudinal Reinforcement Strain

The load-steel wire strain curve as presented in Figure 3. The SWM is involved in the force throughout the loading process, and the load is linearly related to the strain in the steel wire before the beam cracks. With the increase of load, the cracks develop and expand gradually, the neutralization axis moves upward, and the strain in the SWM increases. When the steel wire yields, the strain of the SWM increases rapidly. This is because the stress of the steel wire remains constant and the load is shared between the SWM and the PUC until the composite reinforcement breaks. Among them, the SWM-PM strengthened beams B1 and B2, the strength of the SWM was not fully utilized because the strengthening layer was damaged by peeling off from the concrete, and the SWM was not pulled off.

PUC Strain

The load- PUC strain curves for beams B3, B4, B5 and B6 are shown in Figure 4. Under the same load, the strain of PUC of beam B5 was less than that of PUC of beam B3. It shows that the stiffness of the test beam increases as the thickness of polyurethane increases. Among them, the load-PUC strain curves of test beams B4 and B6 almost overlapped, indicating that they had the same stiffness. Furthermore, it showed that the beam still had good stiffness after being reinforced with cracks after preloading. The ultimate bearing capacity was the same as that of the test beam which had not been preloaded. The ultimate damage loads of the test beams for the four different working conditions were 112.8 kN, 122.6 kN, 140 kN, and 120 kN, respectively. At that time, the corresponding PUC strains were 7000 με, 7140 με, 7336 με, and 7071 με, respectively. Compared with polymer mortar materials, PUC materials had better bonding properties and tensile strength and had a better effect on bearing capacity when combined with steel wire strengthening.

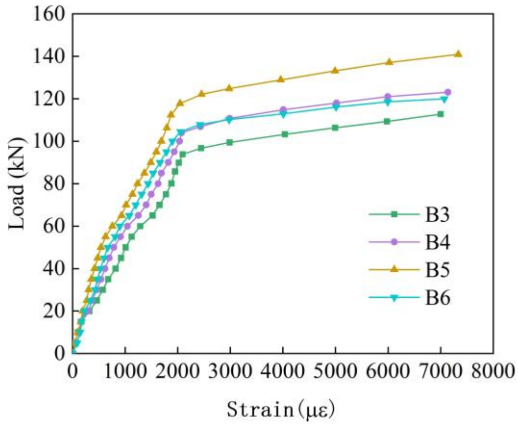

Fig. 4 - Load- PUC strain curve

DERIVATION OF THEORETICAL FORMULAS OF SWM-PUC COMPOSITE STRENGTHENED REINFORCED CONCRETE BEAMS.

Basic Assumptions

The following fundamental assumptions are made for the computation of the bending capacity of the reinforced concrete T-beam in its normal section during bending after strengthening:

1. Neglect the bond-slip of the SWM-PUC composite strengthening layer in the contact area with the concrete.
2. Equivalent stress plot is used for concrete instead of actual curve stress plot. The height is the height of the compression zone and the width is the design value of concrete strength.
3. Before a flexural member reaches the limit state of load bearing capacity, the section strains are essentially consistent with the flat section assumption.
4. The constitutive relationship of concrete refers to the design code standard for concrete structures [26], as shown in Figure 5. After the concrete cracks, the tensile effect of the concrete is ignored.

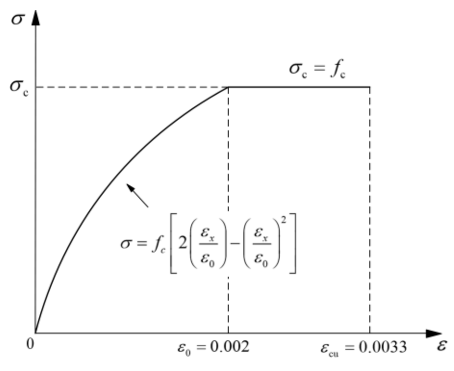

(a) Compressive constitutive model

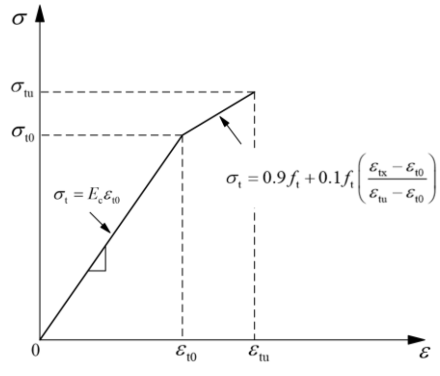

(b) Tensile constitutive model

Fig. 5 - Constitutive relation model of concrete

5. The three-stage stress-strain constitutive relationship model is used for the reinforcement. The elastic phase, yielding phase, and strengthening phase, in that order, are presented in Figure 6.

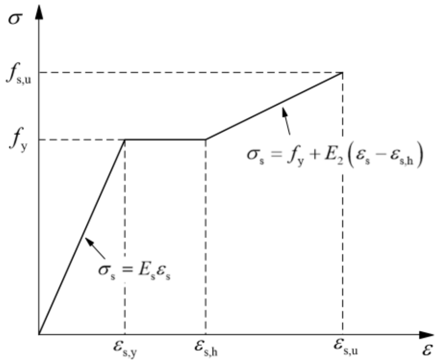

Fig. 6 - Constitutive relation model of reinforcement

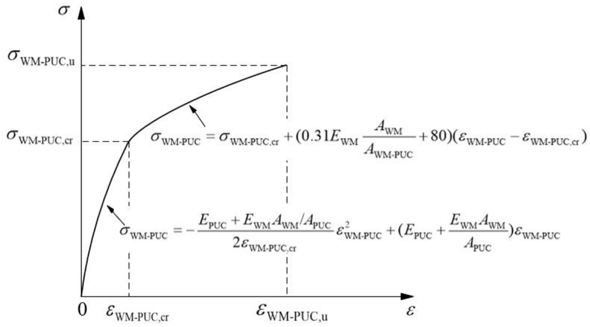

Fig. 7 - Constitutive relation model of SWM-PUC composites

6. The stress-strain constitutive relationship model of the SWM-PUC composite layer as presented in Figure 7. The model is divided into two segments, a rising segment and a strengthening segment for the elastic-plastic change of the PUC material. The calculation formula is as follows:

$$\sigma_{\mathrm{WM-PUC}} = \begin{cases} \alpha\varepsilon^2_{\mathrm{WM-PUC}} + \beta\varepsilon_{\mathrm{WM\text{-}PUC}} & \left(0 \le \varepsilon_{\mathrm{WM-PUC}} \le \varepsilon_{\mathrm{WM-PUC,cr}}\right) \\ \gamma\left(\varepsilon_{\mathrm{WM-PUC}} - \varepsilon_{\mathrm{WM-PUC,cr}}\right) + \sigma_{\mathrm{WM-PUC,cr}} & \left(\varepsilon_{\mathrm{WM-PUC,cr}} \le \varepsilon_{\mathrm{WM-PUC}} \le \varepsilon_{\mathrm{WM-PUC,u}}\right) \end{cases} \tag{2}$$

$$\begin{cases} \alpha = -\dfrac{E_{\mathrm{PUC}} + \dfrac{E_{\mathrm{WM}}A_{\mathrm{WM}}}{A_{\mathrm{PUC}}}}{2\varepsilon_{\mathrm{WM\text{-}PUC,cr}}} \\ \beta = E_{\mathrm{PUC}} + E_{\mathrm{WM}}A_{\mathrm{WM}} / A_{\mathrm{PUC}} \\ \gamma = 0.31E_{\mathrm{WM}}A_{\mathrm{WM}} / A_{\mathrm{WM\text{-}PUC}} + 80 \end{cases} \tag{3}$$

Bearing Capacity Analysis

Cracking Load

The structural mechanics method was used to analyze the internal forces of the strengthened beams under load. The stress relations for the strengthened T-beam are presented in Figure 8.

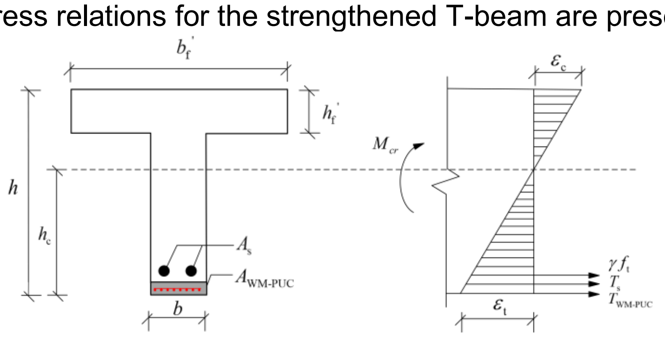

Fig. 8 - Cracking moment stress diagram

The split load of SWM-PUC reinforced RC-T beams can be computed according to the following equation:

$$M_{\mathrm{cr}} = \gamma f_{\mathrm{t}} W_0 \tag{4}$$

DOI 10.14311/CEJ.2025.02.0015

where γ is the coefficient of influence of plasticity of concrete under load, f_t is the concrete axial tensile strength, W_0 is the elastic resistance moment of the tension edge should be obtained by conversion. The conversion formula is as follows (5) ~ (9).

T-section beams with members in the elastic phase before cracking, the converted cross-sectional area A_0 is computed by the equation below:

$$A_0 = b_f^{'} h_f^{'} + b\left(h - h_f^{'}\right) + \left(n_s - 1\right) A_s + \left(n_{WM\text{-}PUC} - 1\right) A_{WM\text{-}PUC} \tag{5}$$

The static moment S_0 of the T-beam section is:

$$S_0 = b_f^{'} h_f^{'} \left(h - \frac{h_f^{'}}{2}\right) + b\left(h - h_f^{'}\right)\left(\frac{h - h_f^{'}}{2}\right) \tag{6}$$

The neutral axis h_c of the T-beam is:

$$h_c = \frac{S_0}{A_0} = \frac{b_f^{'} h_f^{'} \left(h - \frac{h_f^{'}}{2}\right) + b\left(h - h_f^{'}\right)\left(\frac{h - h_f^{'}}{2}\right)}{b_f^{'} h_f^{'} + b\left(h - h_f^{'}\right) + \left(n_s - 1\right) A_s + \left(n_{WM\text{-}PUC} - 1\right) A_{WM\text{-}PUC}} \tag{7}$$

Through the parallel shift formula, the moment of inertia I_0 of the converted section is obtained as:

Using the parallel shift equation, the expression for the moment of inertia1 of the converted section is derived as.

$$I_0 = \frac{b_f^{'} \left(h_f^{'}\right)^3}{12} + b_f^{'} h_f^{'} \left(h - h_c - \frac{h_f^{'}}{2}\right) + \left(n_s - 1\right) A_s \left(h_c - a_s^{'}\right)^2 + \left(n_{WM\text{-}PUC} - 1\right) A_{WM\text{-}PUC} \left(h_c - a_{WM\text{-}PUC}^{'}\right)^2 \tag{8}$$

Therefore, the resilient moment of resistance W_0 at the tension margin is:

$$W_0 = \frac{I_0}{h_c} \tag{8}$$

where n_s is the ratio of elastic modulus of steel bar to concrete, $n_s = \frac{E_s}{E_c}$, $n_{WM\text{-}PUC}$ is the ratio of modulus of resilience of SWM-PUC composite to concrete, $n_{WM\text{-}PUC} = \frac{E_{WM\text{-}PUC}}{E_c}$, $b_f^{'}$、 $h_f^{'}$ is the upper flange width, flange thickness, h、h_c is the reinforcement T-beam full section height, neutral axis section height, A_s、 $A_{WM\text{-}PUC}$ is the section area of the steel wire, SWM-PUC composite materials, $a_s^{'}$、$a_{WM\text{-}PUC}^{'}$ is the district from the point of steel wire ensemble to the margin of the tensile area, SWM-PUC ensemble to the margin of the tension area, S_0 is the static moment of T-beam section after reinforcement, h_c is the neutral axis of T-beam after reinforcement, W_0 is the elastic resistance moments of the strengthened T-beam.

The theoretical formula for the cracking load is:

$$F_{cr} = 0.75 M_{cr} \tag{9}$$

The computed and experimental values of splitting loads are presented in Table 4. As presented in Table 4, the cracking loads of T-beams strengthened by SWM-PUC composite showed significant improvement. And the reinforcement layer SWM reinforcement ratio and reinforcement layer PUC thickness the greater the influence. The computed values are in general accord with the experimental values.

Tab. 4 - Comparison of calculated and test values of cracking loads

Beam	CB	B3	B4	B5
Test value/kN	10	18	20	22
Calculated value/kN	9.5	16.5	18.6	20.5
Error value	5%	8.3%	7%	6.8%

Ultimate Load

The bearing capacity of beam CB was 80 kN. The bearing capacity of beam B3 with five longitudinal steel wires was 112.8 kN. The bearing capacity of beam B4 with eight longitudinal steel wires was 122.6 kN. Compared to the unstrengthen beam CB, the load carrying capacity of beams B3 and B4 increased by 41% and 53.3%, respectively. The bearing capacity of beam B5 with five longitudinal steel wires and 30 mm thickness of PUC was 140 kN. It was 75% higher than the unreinforced beam and 22% higher than beam B3 with the same reinforcement ratio. Based on the height of the pressure zone of the equivalent rigid stress map, the flexural components strengthened with SWM-PUC composite were divided into two types. The first type of flexural capacity calculation as presented in Figure 9.

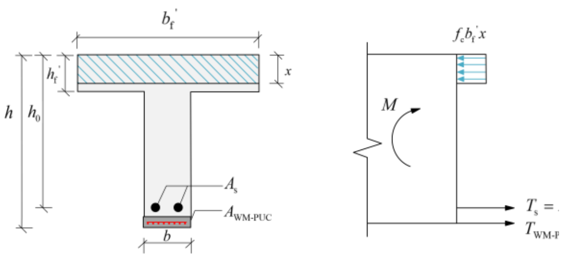

Fig.9 - The first type of flexural load capacity calculation diagram

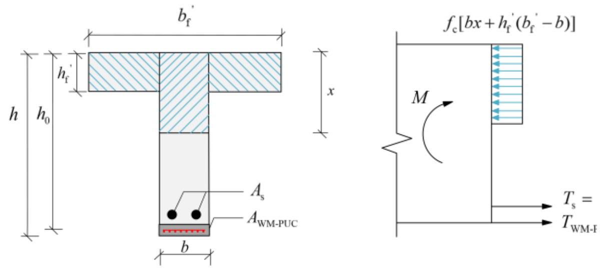

Fig. 10 - The second type of flexural load capacity calculation diagram

If the following equation is met, it is the first type of reinforced T-beam:

$$f_s A_s + \sigma_{\text{WM-PUC}} A_{\text{WM-PUC}} \le f_c b_f' h_f' + f_s' A_s' \tag{10}$$

Find the height of the pressure zone according to this formula:

$$f_s A_s + \sigma_{\text{WM-PUC}} A_{\text{WM-PUC}} \le f_c b_f' x + f_s' A_s' \tag{11}$$

The bending capacity of the normal section is computed according to the following formula:

$$\gamma_0 M \le f_c b_f' x \left(h_0 - \frac{x}{2} \right) + f_s' A_s' \left(h_0 - a_s' \right) \tag{12}$$

The second type of flexural capacity calculation is shown in Figure 10.

If the following equation is not met, it is the second type of reinforced T-beam:

$$f_s A_s + \sigma_{\text{WM-PUC}} A_{\text{WM-PUC}} \le f_c b_f' h_f' + f_s' A_s' \tag{13}$$

The height of the compression zone is calculated according to the following formula:

$$f_s A_s + \sigma_{\text{WM-PUC}} A_{\text{WM-PUC}} = f_c \left[b_f' \left(h_f' - b \right) + bx \right] + f_s' A_s' \tag{14}$$

To ensure that the reinforcement is suitable for the damage of the beam, the height of the compression zone should meet $2a_s' \le x \le \xi h_0$, then the positive section flexural capacity is computed according to the following formula:

$$\gamma_0 M \le f_c bx\left(h_0-\frac{x}{2}\right)+f_c\left(b_f^{'}-b\right)\left(h_0-\frac{h_f^{'}}{2}\right)+f_s^{'}A_s^{'}\left(h_0-a_s^{'}\right) \tag{15}$$

$$h_0=\frac{\left[f_s A_s\left(h-a_s\right)+\sigma_{\text{WM-PUC}}A_{\text{WM-PUC}}\left(h-a_{\text{WM-PUC}}\right)\right]}{\left(f_s A_s+\sigma_{\text{WM-PUC}}A_{\text{WM-PUC}}\right)} \tag{16}$$

where γ_0 is the structural importance factor, M is the positive section bending moment, f_s、$f_s^{'}$、f_c is the design value of tensile strength of tensile reinforcement, the design value of compressive strength of erection bars, the design value of concrete compressive strength, A_s、$A_s^{'}$ is the cross-sectional area of the tensile reinforcement and the cross-sectional area of the compressive reinforcement, $A_{WM\text{-}PUC}$、$\sigma_{WM\text{-}PUC}$ is the sectional area of SWM-PUC composite, the tensile stress of SWM-PUC composite, $b_f^{'}$、$h_f^{'}$、b is the width of the top flange of the T-beam, thickness of the top flange of the T-beam, and width of the ribs of the T-beam, h、h_0、x is the height of full section of reinforced T-beam, effective height of reinforced T-beam section, height of pressurized area of section, a_s、$a_s^{'}$、$a_{WM\text{-}PUC}$ is the distance from the tensile reinforcement to the bottom of the beam, the distance from the compressive reinforcement to the upper flange, and the distance from the total stress point of the SWM-PUC composite to the bottom of the beam.

The ultimate bearing capacity values using the above computation method are in good agreement with the test values, with an error of no more than 10%. As presented in Table 5.

Tab. 5 - Comparison of calculated and test values of load capacity

Beam	CB	B3	B4	B5
Test value/kN	80	112.8	122.6	140
Calculated value/kN	78	108	116	132
Error value	2.6%	4.2%	5.5%	6%

Deflection Analysis

It has been shown experimentally that the load versus deflection curve can be approximated as two linear phases before the reinforcement yields. Therefore, the deflection of the specimens strengthened using the SWM-PUC composite can be accurately computed directly from the bilinear model. The bilinear approach directly maps the load-deflection relationship into two linear approximation expressions. Calculate the partial bending moment M_{cr} before cracking I_0 to obtain the deflection f_1. According to the moment of inertia I_{cr}, calculate the bending moment $M'=M-M_{cr}$ of the other part after cracking to obtain the deflection f_2, and then calculate the total deflection of the specimen as $f=f_1+f_2$. The revised deflection is calculated as follows:

$$f=\lambda l^2\left(\frac{M_{cr}}{\beta_1 E_c I_0}+\frac{M-M_{cr}}{\beta_2 E_c I_{cr}}\right) \tag{17}$$

where β_1、β_2 is the influence coefficient, parsing the experimental data by linear regression yielded the influence coefficient $\beta_1=0.95$、$\beta_2=0.72$. λ is the coefficient of deformation, l is the computed spans of reinforced specimen, M_{cr} is the value of cracking moment, M is the real bending moment value,I_0、I_{cr} is the moment of inertia of the section before and after cracking, E_c is the modulus of elasticity of concrete.

The test results of the SWM-PUC composite strengthened T-beam were contrasted with the calculated results as presented in Figure 11. The corrected deflection calculations were in better agreement with the partial experimental results of the SWM-PUC composite strengthened T-beam.

The results show that the equation can be used to compute and predict the deflection of SWM-PUC composite reinforced T-beams in the yield load range.

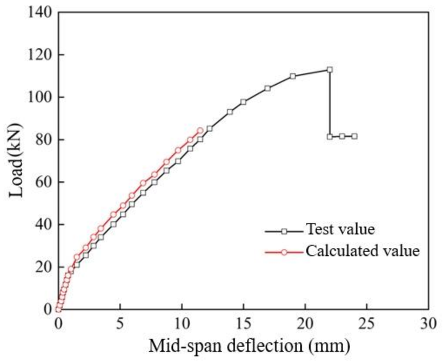

(a) Beam B3

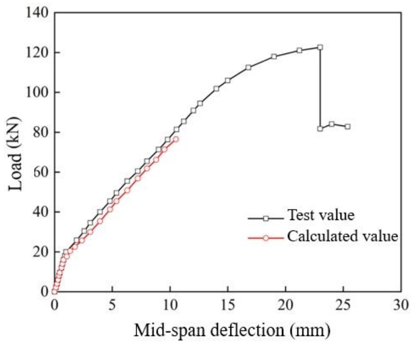

(b) Beam B4

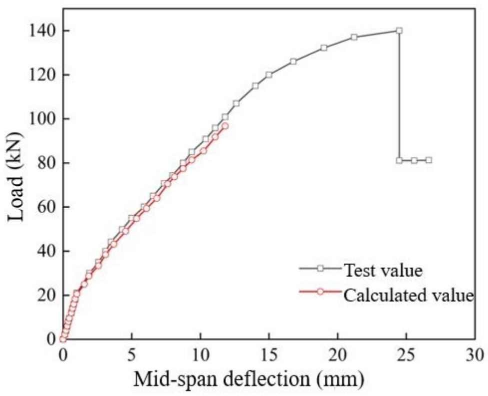

(c) Beam B5

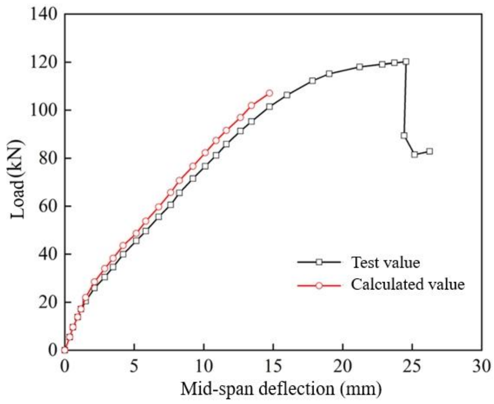

(d) Beam B6

Fig. 11 - Comparison of test and calculated deflections in the yield load range

The ultimate deflection is calculated using the method of structural mechanics, and the deflection of the strengthened test T-beam is computed in accordance with the following equation:

$$B = \frac{B_0}{(\frac{M_{cr}}{M_s})^2 + [1 - \left(\frac{M_{cr}}{M_s}\right)^2\Bigg]\frac{B_0}{B_{cr}}} \tag{18}$$

$$M_{cr} = \gamma f_t W \tag{19}$$

$$\gamma = \frac{2S_0}{W_0} \tag{20}$$

$$f = \frac{243M}{320B} \tag{21}$$

where S_0 is the static torque of T-beam after strengthening in section, γ is the coefficient of plastic influence of tensile zone concrete, W_0 is the moment of elastic resistance at the tension margin, B_0 is the full-section bending stiffness, B_0=0.95E_c+I_0, B_{cr} is the bending stiffness of cracked section, B_{cr}=$E_{cr}I_{cr}$.

The comparison of the deflection values using the above calculation method with the test values as presented in Table 6. The error between the computed value of ultimate deflection and the test value does not exceed 10%, which is within reasonable limits.

Tab. 6 - The calculated values of deflection are compared with the test values

Beam	CB	B3	B4	B5	B6
Test value/kN	26.1	26.3	27.5	28.8	26.2
Calculated value/kN	25	25.5	26	26.6	24.5
Error value	4.2%	3%	5.5%	7.6%	6.5%

Section Stiffness Analysis

Effect of Reinforcement Ratio of SWM on Strengthened Concrete T-beam

The influence of the reinforcement ratio of the SWM on the section stiffness as presented in Figure 12. Specimen A and specimen B have the same parameters of ordinary steel reinforcement ratio and PUC, but different reinforcement ratios for the SWM. It can be seen from equation (4), the bending moment of cracking of specimen B is larger than the cracking moment of specimen A. Since both specimens had the same reinforcement rate of ordinary steel bars, the two straight lines after cracking had the same slope. At the equivalent bending moment, the lower section rigidity of specimen B is higher than that of specimen A It is observed that the stiffness increases with the increase in the reinforcement ratio of the SWM for the same common steel reinforcement ratio.

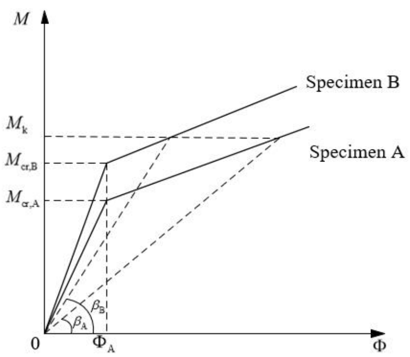

Fig.12 - Effect of reinforcement ratio of SWM on section stiffness

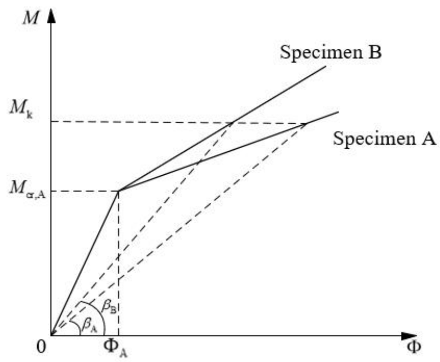

Fig. 13 - Effect of reinforcement ratio of ordinary steel on section stiffness

Effect of Common Reinforcement Ratio on Strengthened Concrete T-beams

The influence of the reinforcement ratio of ordinary steel on section stiffness as presented in Figure 13. The reinforcement ratio of the SWM and the thickness of the PUC of specimen A and specimen B are the same, and the reinforcement ratio of ordinary steel in specimen B is larger than that in specimen A. The bending moment at cracking of specimen A and specimen B are equal. The reinforcement ratio of the section plays a major role in influencing the slope of the line in the second stage after cracking. The greater the ratio is, the greater the slope is. The rigidity of specimen B in the second stage is larger than that of specimen A. Therefore, the cross-sectional stiffness of specimen B will be greater than that of specimen A for the same bending moment.

Effect of PUC on Reinforced Concrete T-beams

The effect of PUC thickness on section stiffness as presented in Figure 14. The reinforcement ratio of the SWM and the reinforcement ratio of the ordinary reinforcement are the same parameters for both specimen A and specimen B, but the thickness of the PUC is different. From the graph, it is clear that the cracking load of specimen B is larger than the cracking load a of specimen. The sectional stiffness of specimen B is greater than that of specimen A. The findings indicate that the use of PUC as a bond anchoring material can appropriately increase the cracking load and rigidity of the second stage.

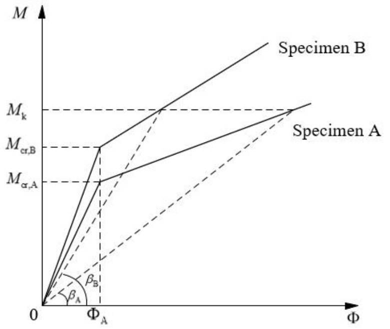

Fig. 14 - Effect of PUC thickness on section stiffness

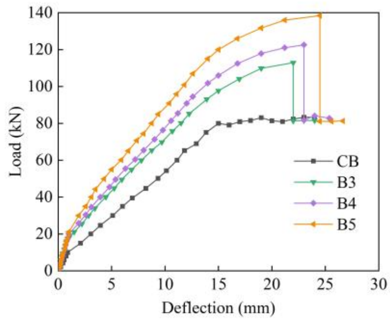

Fig. 15 - Load-deflection curves for CB, B3, B4 and beam B5

Effect of SWM-PUC Strengthening Layer on Reinforced Concrete T-Beam

In order to investigate the influence of using SWM-PUC composite reinforcement on the flexural stiffness of the test beams, the load-deflection curves of beams CB, B3, B4 and B5 were compared, as presented in Figure15. The results show that the SWM-PUC composite reinforcement method can improve the stiffness of plain reinforced concrete T-beams significantly. Largely because: (1) The use of the steel wire mesh increased the cracking load of the beams, thus substantially increasing their service stage stiffness; (2) The use of SWM for reinforcement is tantamount to increasing the reinforcement ratio of the beams, thus increasing the stiffness of the beams during the service phase; (3) PUC has some flexural properties and durability, and it can hold the SWM better, thus increasing the stiffness of the beam.

Crack Width Analysis

Referring to the concrete structure design code [26], the crack width of strengthened concrete is calculated as follows:

$$\begin{aligned} \varpi_{\max} &= \alpha_{cr}\psi\frac{\sigma_{ss}}{E_s}\left(1.9c+0.08\frac{1+\alpha}{1+\theta}\frac{d_{eq}}{\rho_{te}}\right) \\ \psi &= 1.1-\frac{0.65 f_{tk}}{\rho_{te}\sigma_{ss}} \\ \sigma_{ss} &= \frac{M_s}{(1+\alpha)A_s\eta h_0} \end{aligned} \tag{22}$$

where a_{cr} is the characteristic coefficient of stress for beam, a_{cr}=1.7, E_s is the elastic modulus of longitudinal reinforcement, c is the thickness of the protective layer, a is the equivalent rigidity coefficients of SWM-PUC composite strengthening layer, θ is the SWM-PUC composite reinforcement layer impact factor, ψ is the reinforcement strain coefficient, when ψ <0.2, let ψ = 0.2, and when ψ >1.0, let ψ = 1.0, f_{tk} is the standard tensile strength of concrete axis, σ_{ss} is the equivalent stress of composite reinforcement in the tension zone, M_s is the value of moment under standard load combinations.

Formulas based on crack spacing and crack width. In this paper, a method of strengthening reinforced concrete T-beams with SWM-PUC composite was presented. Calculations were carried out for beams reinforced with different proportions of SWM reinforcement ratio and PUC thickness, and the results of split width calculations were compared with the measured results, as presented in Table 7. From the table, it is seen that the calculation method of the modified formula matches well with the measured value, and it can be closer to the actual split width than the actual crack width.

Tab. 7 - The calculated value of crack width compared with the test value

Beam	CB	B3	B4	B5	B6
Test value/kN	0.58	0.49	0.48	0.45	0.47
Calculated value/kN	0.54	0.47	0.46	0.44	0.45
Error value	6.9%	4%	4.1%	2.2%	4.3%

CONCLUSION

In view of some problems in the strengthening of reinforced concrete structures by SWM-PM. The composite reinforcement technology combining SWM-PUC material was proposed. To verify the practicability of this composite reinforcement technique, the research on the bending properties of reinforced concrete beams strengthened by SWM-PUC was emphasized, and the main findings were as follows:

(1) The cracking load of the SWM-PUC composite strengthening layer on the test beams was significantly better than that of the SWM-PM strengthening layer. When the thickness of the strengthening layer was 20 mm and eight steel wires were configured. The cracking load of the beams strengthened with SWM-PUC composite was 42.8% higher than that of the beams strengthened with SWM-PM. When there were three fewer steel wires, the cracking load of the SWM-PUC strengthened beam was still 28.6% higher than that of the SWM-PM strengthened beam.

(2) The SWM-PUC composite strengthening was more effective in lifting the yield load of the strengthened beams. The yield load increases with the increase in the reinforcement ratio of the SWM and the thickness of the strengthening layer. When the thickness of the strengthening layer was 20 mm and eight steel wires were configured. The yield load of the beams strengthened with SWM-PUC composite was 22.6% higher than that of the beams strengthened with SWM-PM. At a strengthening layer thickness of 20 mm, increase in steel wires from five to eight. The yield load increase was 8.6%. When eight steel wires were configured, the thickness of the strengthening layer was increased from 20 mm to 30 mm yield load was increased by 24.1%.

(3) The SWM-PUC composite strengthening can effectively enhance the load bearing capacity of the specimens more than the SWM-PM strengthening. And the yield load increased with the increase of the reinforcement ratio of the SWM and the thickness of the strengthening layer. When the thickness of the strengthening layer was 20 mm and eight steel wires were configured. The ultimate load of the SWM-PUC composite strengthening beams was 44.2% higher than that of the SWM-PM strengthening beams. At a strengthening layer thickness of 20 mm, increase in steel wires from five to eight. The ultimate load increase was 8.7%. When eight steel wires were configured, the thickness of the strengthening layer was increased from 20 mm to 30 mm ultimate load was increased by 24.1%.

(4) The theoretical formulas for cracking load, ultimate load, deflection, and crack width of reinforced concrete T-beams strengthened with SWM-PUC composite reinforcement were derived in conjunction with existing codes. The test results are within 10% error of the theoretical calculations.

ACKNOWLEDGEMENTS

The authors are grateful for the financial support of the Basic Research Projects of Liaoning Provincial Department of Education in 2024 (Project No. LJ212410153003), the Doctoral Start-up Fund Projects of Liaoning Province (Project No. 2021-BS-168) and Shenyang Science and Technology Project Fund（23-407-3-19）.

REFERENCES

[1] Qeshta I M I, Shafigh P, Jumaat M Z., 2015. Flexural behavior of RC beams strengthened with wire mesh-epoxy composite. Construction and Building Materials, vol. 79, p.104-114.

[2] Bergamo O, Pignat M, Puca C., 2018 Passive methods for the fast seismic characterization of structures: the case of Silea Bridge. International Journal of Civil Engineering, vol. 16, p. 807-822.

[3] Rahman M M, Jumaat M Z, Rahman M A, Qeshta I M., 2015. Innovative hybrid bonding method for strengthening reinforced concrete beam in flexure. Construction and Building Materials, vol. 79, p. 370-378.

[4] Cardinale G, Orlando M., 2004. Structural evaluation and strengthening of a reinforced concrete bridge. Journal of Bridge Engineering, vol. 9(1), p. 35-42.

[5] Naser M Z, Hawileh R A, Abdalla J A., 2019 Fiber-reinforced polymer composites in strengthening reinforced concrete structures: A critical review[J]. Engineering Structures, vol. 198, p. 109542.

[6] Lee J K, Lee J H., 2002. Nondestructive evaluation on damage of carbon fiber sheet reinforced concrete. Composite structures, vol. 58(1), p. 139-147.

[7] Ge W, Tang R, Wang Y, Zhang Z, Sun C, Yao S, Lu W., 2022. Flexural performance of ECC-concrete composite beams strengthened with carbon fiber sheet. Results in Engineering, vol. 13, p. 100334.

[8] Zheng X, Wan B, Huang P, Huang J., 2019. Experimental study of hybrid strengthening technique using carbon fiber laminates and steel plates for reinforced concrete slabs. Construction and Building Materials, vol. 210, p. 324-337.

[9] Qeshta I M, Shafigh P, Jumaat M Z, Abdulla A I, Ibrahim Z, Alengaram U J., 2014. The use of wire mesh–epoxy composite for enhancing the flexural performance of concrete beams. Materials & Design, vol. 60, p. 250-259.

[10] Xing G, Wu T, Liu B, Huang H, Gu S., 2010. Experimental investigation of reinforced concrete T-beams strengthened with steel wire mesh embedded in polymer mortar overlay. Advances in structural Engineering, vol. 13(1), p. 69-79.

[11] LIN Y D, ZONG Z H, LIN Q F., 2012. Experiment study on flexural behavior of RC/PRC beams strengthened with high strength steel wire mesh and permeable polymer mortar. Engineering Mechanics, vol. 29(9), p. 141-149.

[12] Ma H, Li Z., 2013. Microstructures and mechanical properties of polymer modified mortars under distinct mechanisms. Construction and Building Materials, vol. 47, p. 579-587.

[13] Aggarwal L K, Thapliyal P C, Karade S R., 2007. Properties of polymer-modified mortars using epoxy and acrylic emulsions. Construction and Building Materials, vol. 21(2), p. 379-383.

[14] Mahdi F, Abbas H, Khan A A., 2010. Strength characteristics of polymer mortar and concrete using different compositions of resins derived from post-consumer PET bottles. Construction and Building Materials, vol. 24(1), p. 25-36.

[15] Araujo C A M, Loriggio D D, Da Camara J M M N., 2011. Anchorage failure and shear design of hollow-core slabs. Structural Concrete, vol. 12(2), p. 109-119.

[16] Cao Q, Jiang H, Wei R, Deng Y., 2016. Shear behavior of anchor blocks in externally prestressed concrete bridges. Proceedings of the Institution of Civil Engineers-Structures and Buildings, vol. 169(9), p. 657-668.

[17] Yuan F, Chen M, Pan J., 2020. Flexural strengthening of reinforced concrete beams with high-strength steel wire and engineered cementitious composites. Construction and Building Materials, vol. 254, p. 119284.

[18] Fischer G, Li V C., 2007. Effect of fiber reinforcement on the response of structural members. Engineering Fracture Mechanics, vol. 74(1-2), p. 258-272.

[19] Ranade R, Li V C, Heard W F., 2015. Tensile rate effects in high strength-high ductility concrete. Cement and Concrete Research, vol. 68, p. 94-104.

[20] Xing G, Wu T, Liu B, Huang H, Gu S., 2010. Experimental investigation of reinforced concrete T-beams strengthened with steel wire mesh embedded in polymer mortar overlay. Advances in structural Engineering, vol. 13(1), p. 69-79.

[21] Wang Y, Sun Q, Ding H, Leng S, Cui H, Xu B, Cui H., 2022. Investigation of interfacial bonding properties of polyurethane concrete and cement concrete/steel reinforcement. Advances in Materials Science and Engineering, vol. 2022(1), p. 5644468.

[22] Li L, Yu T, Wu Y, Wang Y, Guo C, Li J., 2022. Research on the properties of a new type of polyurethane concrete for steel bridge deck in seasonally frozen areas. Coatings, vol. 12(11), p. 1732.

[23] Hussain H K, Zhang L Z, Liu G W., 2013. An experimental study on strengthening reinforced concrete T-beams using new material poly-urethane-cement (PUC). Construction and Building Materials, vol. 40, p. 104-117.

[24] Hussain H K, Liu G W, Yong Y W., 2014. Experimental study to investigate mechanical properties of new material polyurethane–cement composite (PUC). Construction and Building materials, vol. 50, p. 200-208.

[25] Kexin Z, Quansheng S., 2016. Strengthening of a reinforced concrete bridge with polyurethane-cement composite (PUC). The Open Civil Engineering Journal, vol.10(1).

[26] National Standard of the People’s Republic of China. 2011. GB 50010-2011. Code for Design of Concrete Structures. Beijing: China Architecture & Building Press.

Article no. 16

THE CIVIL ENGINEERING JOURNAL 2-2025

NUMERICAL STUDY ON THE TBM MUCKING PERFORMANCE IN THE EH PROJECT AND OPTIMIZATION OF THE SUPPORTING RIBS

Zheng Jiaxing[1], Geng Qi[2], Ni Zhihua[1], Wu Wei[1], Li Lei[2], Zhao Xiangbo[1], Guo Chenghao[1], Xue Lu[1] and He Tao[1]*

1. *Sinohydro Bureau 3 Co., LTD. Xi'an, Shaan Xi 710024, China*
2. *School of Construction Machinery, Chang'an University, Xi'an, Shaan Xi 710064, China; 2023125089@chd.edu.cn*

Received: *22.10.2024*

Received in revised form: *04.04.2025*

Accepted: *22.05.2025*

ABSTRACT

To study the cutterhead's muck transfer performance of the TBM applied in the EH project, in China, a discrete element method (DEM) based numerical model was built and the mucking process was simulated at different penetration rates and cutterhead rotational speed. It was found that the conventional straight-supporting-rib cutterhead performed well at different penetration rates and low RPMs, but the muck excessive throwing issue was serious when the RPM was higher than 10 rev/min. To overcome this problem, a new arched-supporting-rib cutterhead was proposed. The curvature radius of the arched supporting ribs is suggested between 1.25 m and 1.75 m, and the offset angle is suggested between 40° and 45°. The newly proposed arched-supporting-rib cutterhead can perform well in muck transfer at a greater RPM range of 4~13 rev/min, which allows the TBM to be excavated at low, medium, and high RPMs considering ground conditions and requirements of construction progress.

KEYWORDS

TBM, Muck transfer, Discrete element method, EDEM, Supporting rib

INTRODUCTION

As a kind of heavy professional engineering equipment, the full-section hard rock tunnel boring machine (TBM) has been widely used in the fields of hydropower, mining, highway, and railway engineering. The TBM cutterhead has key functions such as rock cutting, tunnel support, and muck transport. The muck transfer process is of vital importance for TBM tunneling because it directly affects the advancing speed, cutterhead blockage, cutter wear, and cutterhead design. The muck transfer components on a cutterhead mainly include the mucking buckets, mucking chutes, and supporting ribs. During TBM excavation, the rock muck and chips are first scooped up by the muck buckets, then pass the mucking chutes, and finally slide into a hopper through the supporting ribs. The literature is reviewed considering the three muck transfer components.

Representative studies on the muck buckets are as follows. Qi et al [1] focused on the modification and renovation of the worn muck buckets on a TB880E type TBM after its application in the Qinling tunnel and Taohuapu tunnel projects, in China. The renovated TBM was then applied in the excavation of the Zhongtianshan tunnel in Xinjiang Autonomous Region, China. Mao [2] found that the modified buckets were frequently damaged under fractured ground conditions due to the repeated strong impact of large rock blocks on the buckets. The bucket saddles and bolts were strengthened to solve this problem. Zhang [3] verified the application of a new low-alloy wear-resisting cast steel in TBM muck buckets and found that the service life can be improved by 60%. Geng et al. [4] built a numerical model of the TBM mucking process using PFC3D software to analyze the influence of bucket structure, height, and width on the cutterhead mucking performance considering the average mucking speed and passing rate. According to the aforementioned research, it is found that the muck bucket structure has been basically settled and thus the key problem lies in the bucket installation and metal wear resistance.

Representative studies on the mucking chutes and supporting ribs are as follows. Geng et al. [5-7] built the numerical models of the TBM mucking process using PFC3D and EDEM software considering the flat-face, conical-shaped, multi-stage, and corrugated cutterheads respectively. The influences of the number, length, width, and area of the mucking chutes on the mucking performance were investigated comprehensively. Xia et al [8-12] simulated the TBM mucking process using EDEM software and the results were compared with field TBM mucking tests. The influence mechanism of the structural parameters of mucking chutes on mucking performance and bucket wear was revealed, and an optimization design method for mucking chute layout was proposed. Based on the TBM mucking simulations using PFC3D software, Huo et al. [13-16] proposed a fuzzy evaluation method for the mucking performance. The influences of the mucking chutes and supporting ribs on the mucking performance were studied and the structures were optimized. Li et al. [17] simulated the TBM mucking process using the ABAQUS software to reveal the influence of supporting rib angle and cutterhead revolutions per minute (RPM) on mucking performance. According to the aforementioned research, it is found that the particle-based discrete element method (DEM) is widely used to simulate the TBM mucking process. Owing to the advantage of GPU calculation, the EDEM software seems to be more adequate to simulate the large-scale TBM mucking problem with millions of particles. As TBMs are large customized equipment, the design of the mucking components should be conducted and evaluated according to the mucking performance in specific ground conditions with different operation parameters.

In this study, the mucking process of an open-type TBM applied in Erhe (EH) project in Xinjiang Autonomous Region, China, was simulated using the EDEM software and its GPU calculation technique. The mucking performance considering the mucking rate and the muck residual quantity was evaluated when the cutterhead was rotated at different penetration rates and RPMs. To improve the mucking performance with high cutterhead RPMs, an arched supporting rib was proposed, and the structures were optimized via groups of mucking simulations. This study provides new insights and guides for the design of the cutterhead's supporting ribs considering the mucking performance.

PROJECT OVERVIEW

Brief description of the sites

The total length of the Keshuang section tunnel in the second phase of the Xinjiang EH Water Supply Project is about 283.4 kilometers, rendering it the world's longest water supply tunnel. The project crosses the low mountains and hilly areas between the south slope of the Altay Mountain and the north slope of the East Tianshan Mountain. The landscape features high elevations in the northern regions and lower ones in the southern parts, with the east being elevated and the west lower in altitude. The overall terrain gradually decreases from northeast to southwest, with the altitude ranging from 750 to 1300 meters.

The total construction length of the bid-II section is 23.34 kilometers. As shown in Figure 1, the tunnel was first bored with a TBM from the northwest exit to the middle for 10840 m. Upon completion of the central 2000-meter stretch using the drill and blast (D & B) technique, the TBM was overhauled and stepped through this section and then bored the next section of 10500 m toward the southeast exit. The tunnel route's geological composition primarily consists of tuff and tuffaceous sandstone from the Carboniferous and Devonian periods, as well as intrusive granite from the Variscan period. The rocks are hard and the rock mass is intact, mostly of medium to hard grade, belonging to Class II and III surrounding rocks. It is suitable for the application of a TBM because the maximum buried depth is no more than 150 m and thus the rock burst risk is low. However, there are 10 fracture zones along the tunnel alignment and the width of fracture zones is from 4 m to 35 m. Meanwhile, the inclination angles of the fracture zones are at least 55 degrees. When the TBM excavates in the fracture zones, the rock muck amount is possibly large and the rock chips are possibly massive in size, which may cause the stuck of the TBM. As a result, it is necessary to analyze the mucking performance and verify the mucking ability of the TBM cutterhead.

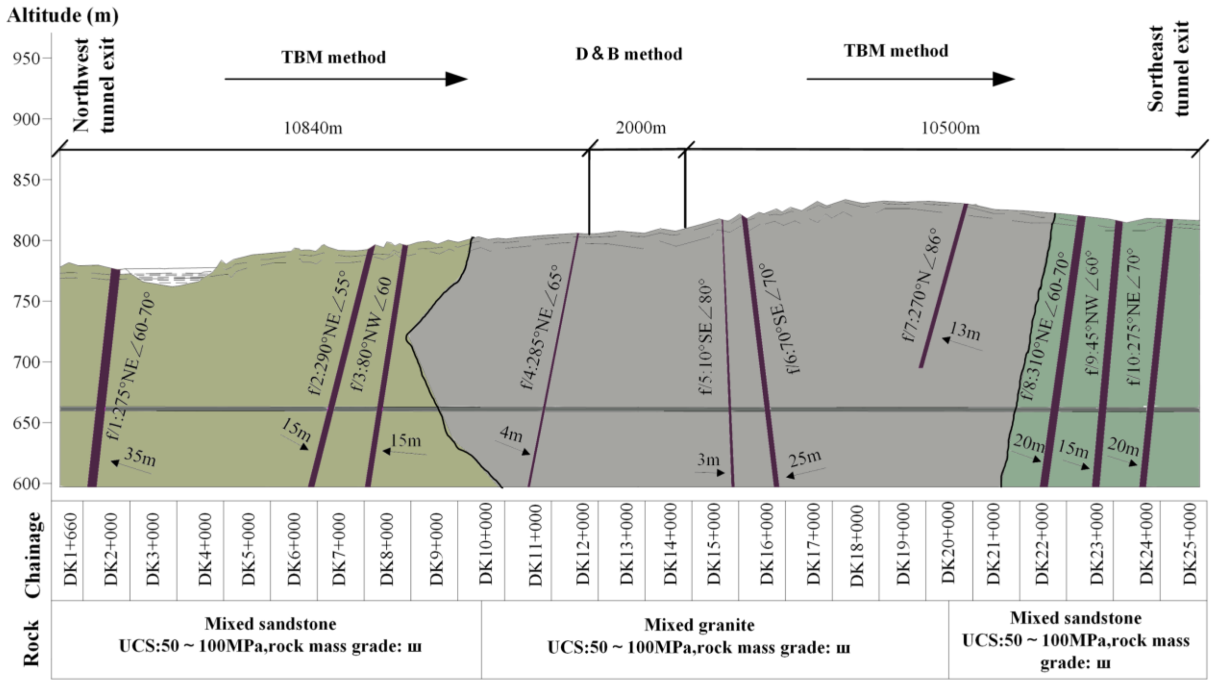

Fig. 1 - Geological profile along the tunnel alignment of bid-II section (the scale ratio of the horizontal to the vertical axis is 25:1)

Brief description of the applied TBM and field penetration data

The applied 'ZTT7030' open-type hard rock TBM was manufactured by China Railway Construction Heavy Industry (CRCHI) corporation limited. As shown in Figure 2, the total length and weight of the TBM are 220 m and 1300 t, respectively. The length and weight of the TBM host from the cutterhead to the rear support are 23.8 m and 600 t, respectively. The total installing power is approximately 4403 kW. The maximum excavation diameter is 7.03 m when new gauge cutters are equipped. A cutterhead is equipped with a total of 48 constant cross section (CCS) disc cutters, comprising 8 central cutters (i.e. 4 double disc cutters with 17 inches in diameter), 28 face cutters with 19 inches in diameter, and 12 gage cutters with 19 inches in diameter. A total of 6 mucking chutes are set on the outer circumference of the cutterhead and the mucking buckets are mounted respectively. The chips allowed to pass the mucking chutes are smaller than 250 mm in the middle axis. The cutterhead is driven by eight 350-kW motors, resulting in the cutterhead revolutions per minute (RPM) of 0~10.9 rev/min, rated torque of 4410 kN·m (at 5.5-rev/min RPM), and extricating torque of 6620 kN·m (at 0.5-rev/min RPM). The cutterhead is pushed via the main beam by 4 thrust cylinders of 2000 mm in stroke, resulting in the rated and maximum thrust of 23562kN and 27489 kN, respectively. The muck conveying ability of the main belt conveyer is 1000 t/h.

The field penetration data, including the torque, thrust, RPM, and penetration of the cutterhead are shown in Figure 3 when the TBM excavated in a successive excavation chainage from DK15462 to DK15488. The data were exported from the industrial computer for one time per minute. This period lasted for 500 min and the advancing distance was 26 m. During this period, the excavation was stopped 9 times, including 6 regular step changes which lasted 5 min for each, and 3 rests for regular tunnel support works which lasted 30 min for each. The time for net penetration counted for 73.8% of the total period, indicating a high machine utilization ratio. During the regular penetration, the average cutterhead thrust and torque were 11953 kN and 1678 kN·m respectively, which account for 51% and 38% of the rated thrust and torque respectively. The rock-breaking ability of the TBM was not fully exploited considering the influences of rock mass stability, cutter wear, and tunnel support speed. The cutterhead RPM was stable whose average value was 6.2 rev/min. The average penetration was 7.1 mm/rev. The field penetration data can guide the parameter setting of the mucking numerical model in the next section.

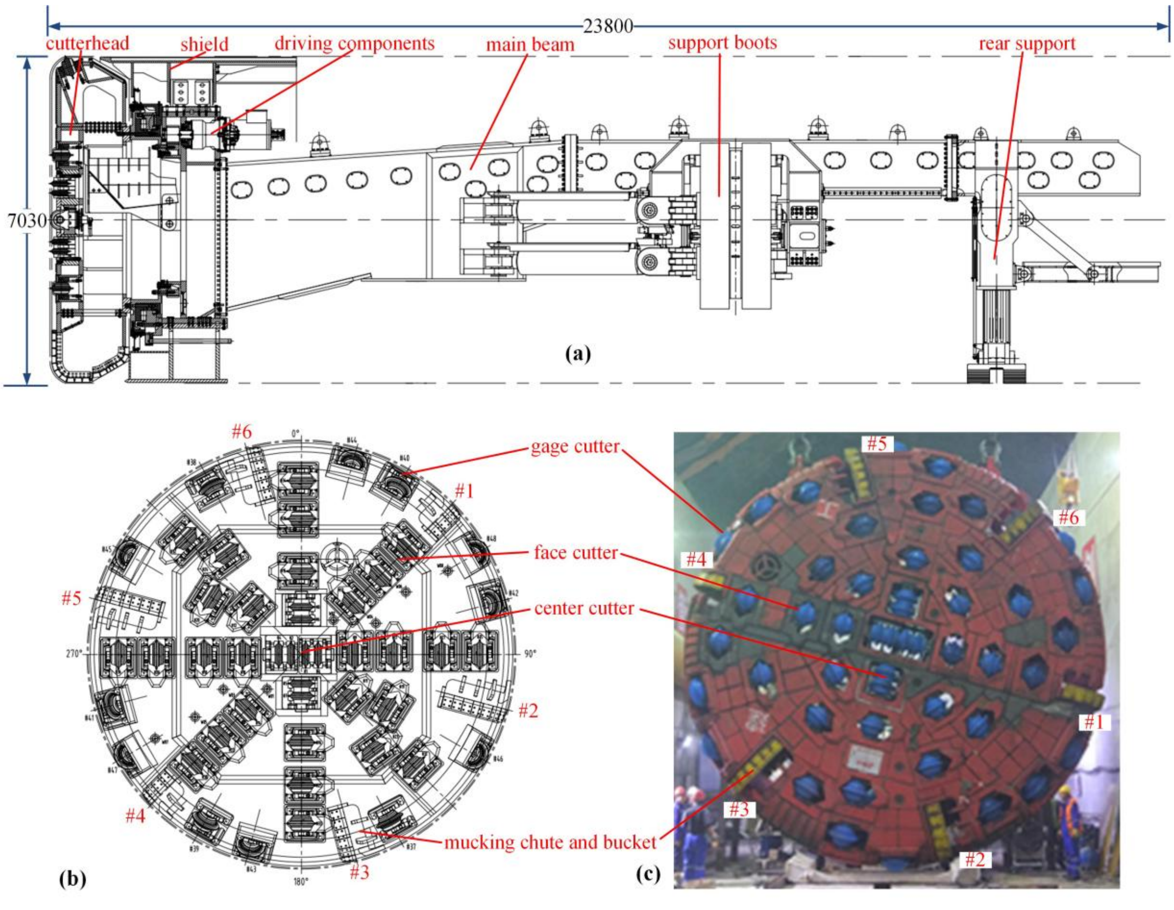

Fig. 2 - The applied ZTT7030 TBM, (a) the host machine, (b) layout of cutters and mucking chutes on the cutterhead, (c) hoisting and installation of the cutterhead on site.

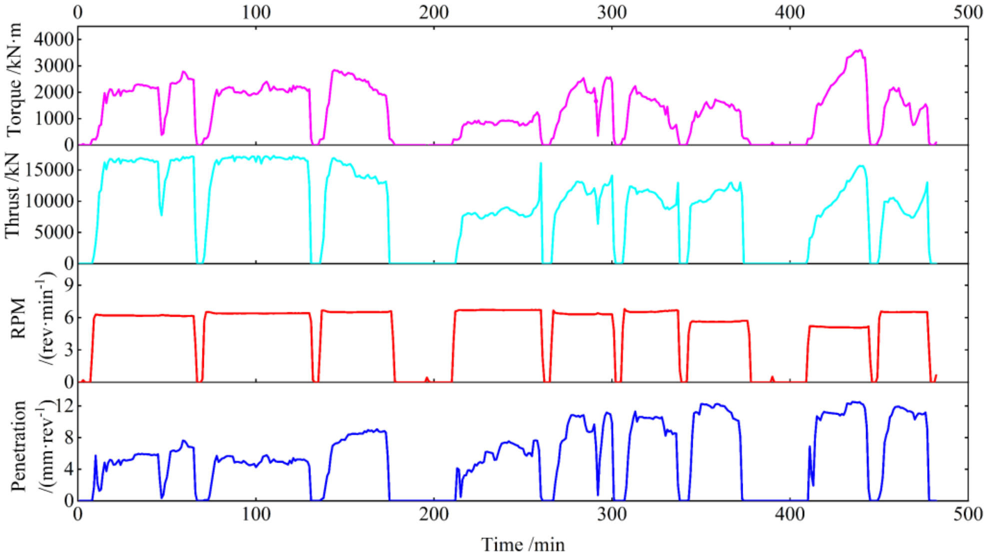

Fig. 3 - The TBM field penetration data in DK15462-15488.

NUMERICAL ANALYSIS OF THE CUTTERHEAD MUCKING PERFORMANCE

Model setup

The particle-based DEM software EDEM^{3D} was used to build the numerical model of the rock muck transfer process. According to Geng et al. [6], the rock mucking performance was not affected by the disc cutters. Thus, the cutters and their installing boxes were not modeled to improve the calculation speed. The cutterhead was modeled according to the drawing shown in Figure 2. The structure and dimension of the mucking components including the mucking chutes, mucking buckets, and supporting ribs were in accordance with the drawing. The intricate cutterhead and muck hopper were crafted in binary stereolithography (STL for short) format with Creo software and subsequently brought into EDEM^{3D} software as rigid components. The tunnel face and surrounding face are directly modeled in the EDEM^{3D} software.

According to Geng et al. [5], the simulation result of the rock mucking process is strongly affected by the dimension and shape of the rock chips. To improve the simulation accuracy, the rock chips were statistically modeled using a 3D reconstruction technology. As shown in Figure 4, a group of rock chips were randomly collected from the project site. The chips were then scanned using a 3D scanner to reconstruct the STL-format models. Next, the STL-format chips were imported into the EDEM^{3D} software and filled with particles to accomplish the particle-aggregated chip templates. During the simulation, the number of chips generated based on each template was controlled by the volume of each template as well as the cutterhead diameter, RPM, and penetration. The physical properties and contact parameters are shown in Table. 1.

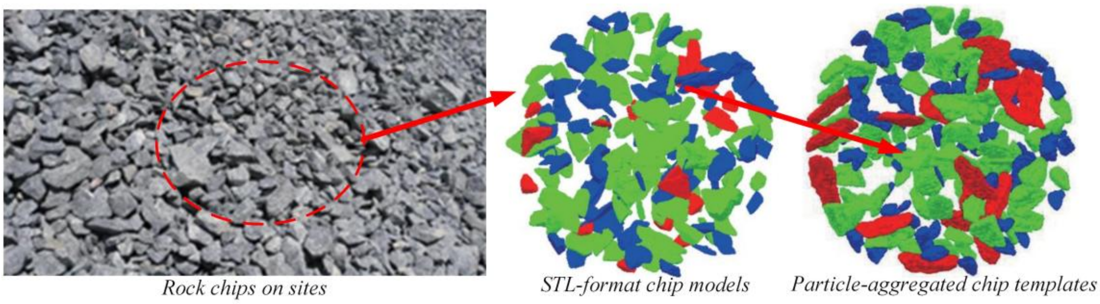

Fig. - 4 Process of the rock chip modelling.

Tab. 1 - Model physical properties and contact parameters

Model parts	Poisson's ratio		Density/(kg·m-3)	Young's modulus/GPa
Structural elements	0.3		7850	210
Rock chips	0.25		2600	55
Contact group	Contact model	Restore coefficient	Static friction coefficient	Sliding friction coefficient
Chip-chip	Hertz- Mindlin	0.3	0.5	0.05
Steel-chip		0.5	0.4	0.03

During the EDEM simulation process, the rock debris can be set as either unbreakable or breakable, referred to as particle blocks and particle clusters respectively. Setting the rock debris as breakable particle clusters allows for the simulation of secondary breakage during the stirring and discharge processes, which more closely resembles the actual debris discharge process. However, the rock debris used in this study was sourced from a conveyor belt and had already undergone secondary breakage, thus there was no need to simulate the secondary breakage process of the debris. If the rock debris were set as breakable particle clusters, it would consume a significant amount of time in steps such as contact traversal and bond analysis, greatly increasing the computational cost. Therefore, the rock debris was set as unbreakable.

Based on the above settings, the numerical model for rock muck transfer of the TBM cutterhead is illustrated in Figure 5. The structural elements include a cutterhead body colored in grey, a muck hopper colored in yellow, and the tunnel and surrounding surfaces represented in meshes. The cutterhead body is composed of the front panel, mucking chutes and buckets, supporting ribs, the back cone, and the flange. The distance between the front surface of the cutterhead and the tunnel face is set as 145 mm, which is identical to the height of the center and face cutters. The muck hopper is composed of a funnel and a slide to collect the muck from the supporting ribs and transfer it out of the model domain in order to improve the calculation speed. The muck is generated from a particle factory that is located near the tunnel face. The muck falls to the tunnel bottom by gravity is scooped up by the mucking buckets, and then passes the mucking chutes, and then glides into the hopper via the supporting ribs. The simulation lasts for 40 s. To evaluate the mucking performance, the weight of muck at the base of the space between the cutterhead and tunnel face (M_F, kg), the weight of the muck in the cutterhead chamber (M_C, kg), and the weight of the muck transferred from the hopper (M_T, kg) were recorded every 0.1 s during the simulation. The muck passing rate (PR) can be calculated as the ratio of M_T to the weight of the generated muck (M_G, kg) in the time period from 20 s to 40 s when the mucking process is stable.

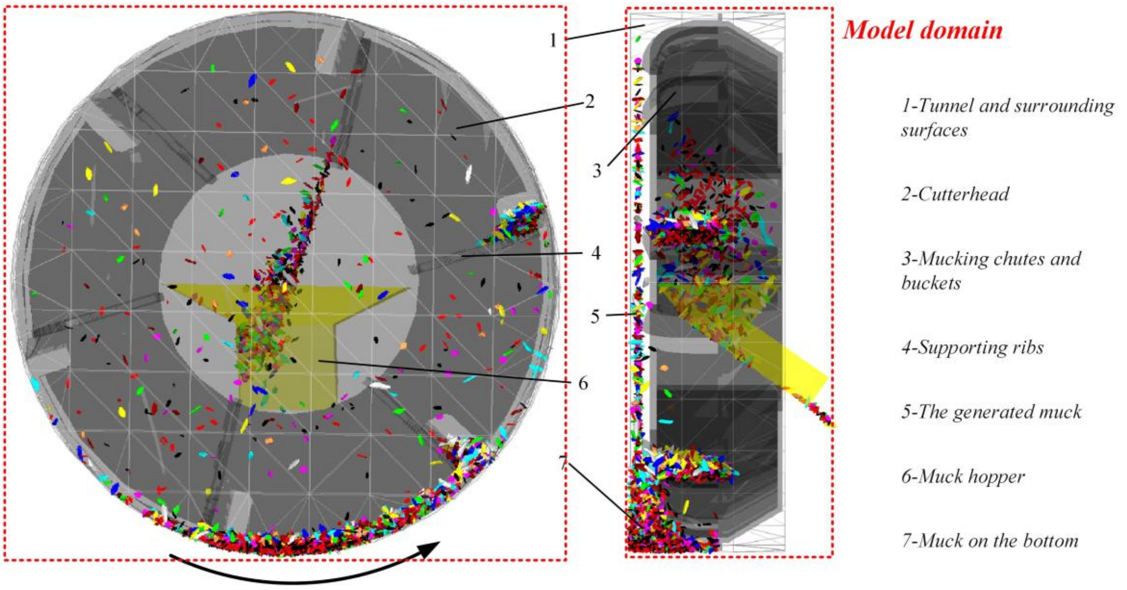

Fig. 5 - Illustration of the numerical model for rock muck transfer of the TBM cutterhead.

Influence of the penetration rate on mucking performance

According to Figure 3, the cutterhead's RPM was generally stable with an average value of 6.2 rev/min. However, the penetration rate varied from 4 mm/rev to 12 mm/rev. To examine how the penetration rate affects mucking efficiency, five simulations were conducted using the model shown in Figure 5 by setting the penetration rate as 4, 6, 8, 10, and 12 mm/rev, respectively. The cutterhead's RPM was kept at 6.2 rev/min. The mucking performance under different penetration rate is shown in Figure 6. Each figure was captured at 24.5 s when the mucking process was stable. The increase of muck generate rate from 41.4 kg/s to 124.1 kg/s can be observed from the front of the models. According to Figure 6 and Figure 7, as the penetration rate increases, the amount of the muck accumulated in the tunnel bottom (M_F) increases obviously, which may exacerbate the secondary wear of the gage cutters. Besides, the weight of the muck removed by each mucking bucket and the M_C increase with the increasing penetration rate, which may bring in additional resistance moments for the cutterhead. For each penetration rate, the fluctuation of M_F and M_C becomes stable after 15 s, indicating that the muck generation and transfer enter a dynamic balance mode. It means that the muck in the tunnel bottom and cutterhead chamber will not keep accumulating and increasing, indicating that the ability of the cutterhead to transfer muck is sufficient under the studied conditions with different penetration rates. This is also proved by Figure 7c, which shows that the muck passing rate (PR) is near 100% for different penetration rates. For each model, the fluctuation frequency of M_F and M_C is 0.63 Hz, which equals the product of the amount of mucking chute and cutterhead revolutions per minute.

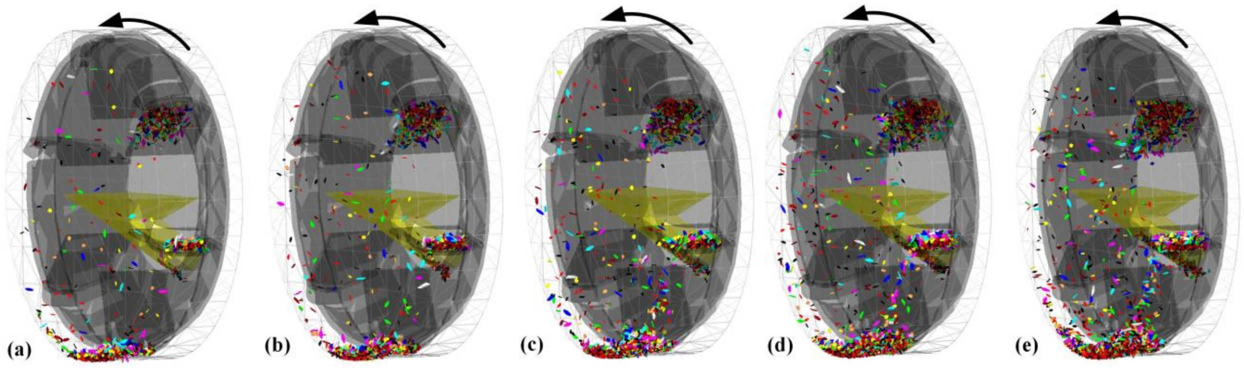

Fig. 6 - Mucking performance under different penetration rates, (a) 4mm/rev; (b) 6 mm/rev; (c) 8 mm/rev; (d) 10 mm/rev; (e) 12 mm/rev.

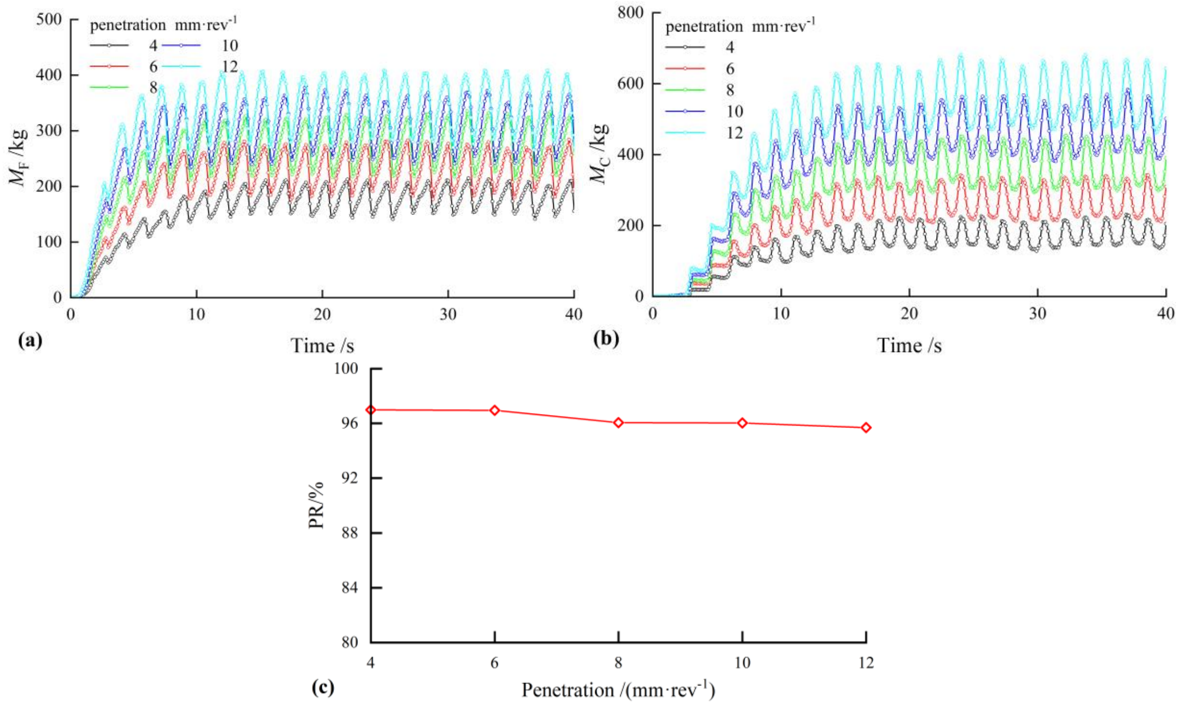

Fig. 7 - Indicators to evaluate the mucking performance under different penetration rates, (a) M_F; (b) M_C; (c) PR.

Influence of cutterhead's RPM on mucking performance

Although the cutterhead's RPM was generally stable during the given stage in Figure 3, it can be improved properly in some stable and not-so-hard ground conditions in order to increase the TBM advance rate on the premise of not serious cutter wear. To examine the impact of the cutterhead's RPM on mucking performance, four simulations were conducted using the model shown in Figure 5 by setting the RPM as 4, 7, 10, and 13 rev/min, respectively. The penetration rate was kept at 7 mm/rev. The mucking performance under different cutterhead's RPM is shown in Figure 8. Each figure was captured at 24.5 s when the mucking process was stable. The increase of muck generate rate from 70 kg/s to 227.5 kg/s can be observed from the front of the models. According to Figure 8 and Figure 9a, as the RPM increases, the amount of the muck accumulated in the tunnel bottom (M_F) is generally the same for different models. This occurs because although the muck generates rate increases with the increase of RPM, the scooping frequency of the muck buckets also increases with the increase of RPM. When the RPM is lower than 10 rev/min, the fluctuation of M_C is stable for different models after 15 s (Figure 9b), and the PR is near 100% (Figure 9c), which indicates that the muck generation and transfer can enter a dynamic balance mode. For the model with an RPM of 10 rev/min, although the PR is near 100%, the muck mainly falls on the left side of the hopper and is about to be thrown out of the hooper. For the model with an RPM of 13 rev/min, a large amount of muck remains on the mucking chutes and supporting ribs and accumulates in the cutterhead chamber. The M_C increases as the simulation progresses and its value is much larger than the other three models. Meanwhile, the PR is only about 86%, indicating the insufficient mucking ability of the cutterhead. This is because that much muck is thrown out of the hopper and keeps accumulating in the cutterhead chamber due to the high linear velocity, which can be observed in Figure 8d. It indicates that the RPM of the studied 7.03-m-diameter cutterhead should better be lower than 10 rev/min, which agrees with the designed RPM range (0~10.9 rev/min) of the TBM.

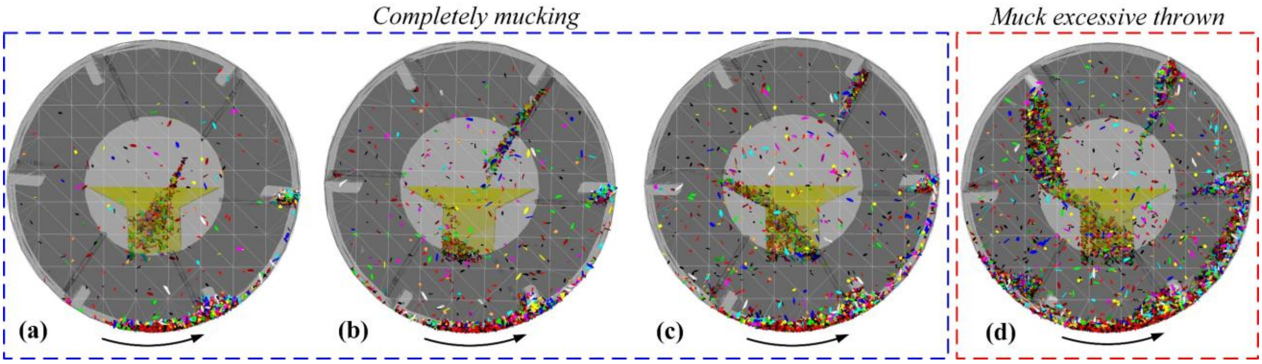

Fig. 8 - Mucking performance under different cutterhead's RPM, (a) 4 rev/min; (b) 7 rev/min; (c) 10 rev/min; (d) 13 rev/min.

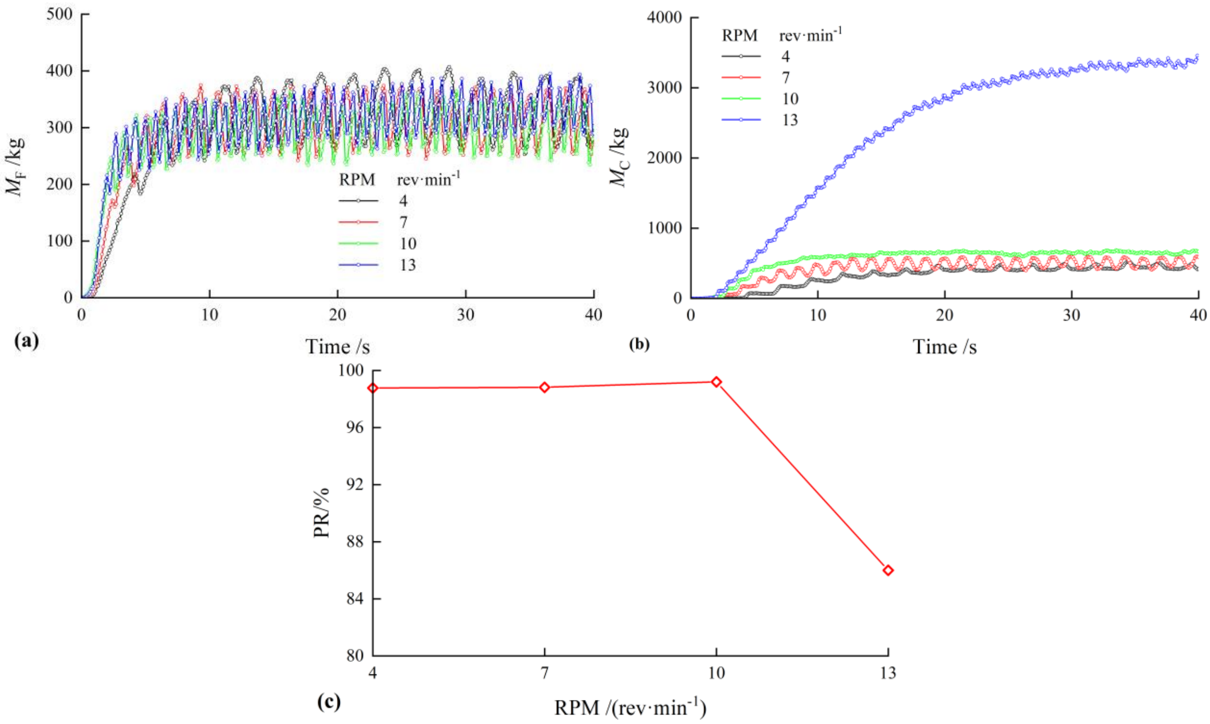

Fig. 9 - Indicators to evaluate the mucking performance under cutterhead's RPM, (a) M_F; (b) M_C; (c) PR.

DESIGN AND OPTIMIZATION OF ARCHED SUPPORTING RIBS

Based on the above analysis, the unsuitable of the straight-supporting-rib cutterhead for high RPM operation is caused by the long-distance throw of the muck due to the high linear velocity of the outer circumference of the cutterhead. In contrast, the arched-supporting-rib cutterhead may perform better which is illustrated in Figure 10. Compared with a conventional cutterhead and its cutter layout, the position angles of some cutter holes should be slightly adjusted to avoid interference. Two parameters, i.e., the offset angle α and curvature radius ρ may affect the mucking performance and thus should be carefully designed.

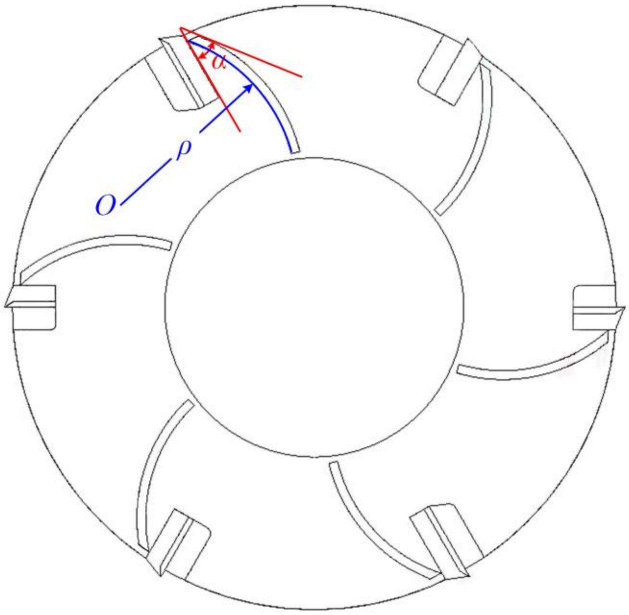

Fig. 10 - Illustration of the position of the arched supporting ribs on the TBM cutterhead.

Influence of curvature radius on mucking performance

To study the influence of ρ on the arched supporting ribs, five simulations were conducted by setting the ρ as 1.0, 1.25, 1.5, 1.75, and 2.0 m, respectively. The α, penetration rate, and RPM were set as 60°, 7 mm/rev, and 13 rev/min, respectively. The other cutterhead structure and parameters were the same as the model shown in Figure 5. The mucking performance of cutterheads with different ρ is shown in Figure 11. Each figure was captured at 30 s when the mucking process was stable. When the ρ was 1.0 m, some muck was thrown out of the hopper (excessively thrown) and fell on the convex side of the arched supporting ribs. As the cutterhead rotated, the muck fell on the concave side of the neighbouring supporting ribs and entered the next cycle. Thus, the M_C value was much higher and the PR was lower (Figure 12b) than the other models (Figure 12a) respectively. As the ρ improved, the falling position of the muck into the hopper moved right and the excessive throwing issue was mitigated. Thus, the M_C was low and the PR was almost 100%. When the ρ was 2.0 m, a little muck could not fall into the hopper (insufficient thrown) during the first 15 s due to its relatively low linear speed. However, as the mucking progressed, the muck could still fully flow into the hopper during the following cutterhead revolutions. This is why the M_C value of the 2.0-m-ρ model was relatively low but a little higher than the models with ρ of 1.25 m, 1.5 m, and 1.75 m. Meanwhile, the PR of this model can achieve almost 100%. These results indicate that the mucking performance of the arched supporting ribs is significantly affected by the curvature radius ρ. The smaller the ρ, the excessive throwing issue will be more prone to occur. The larger the ρ, the insufficient-thrown problem will be more prone to occur. For a certain α value, there exist proper ρ values with which the mucking performs well at high cutterhead RPM.

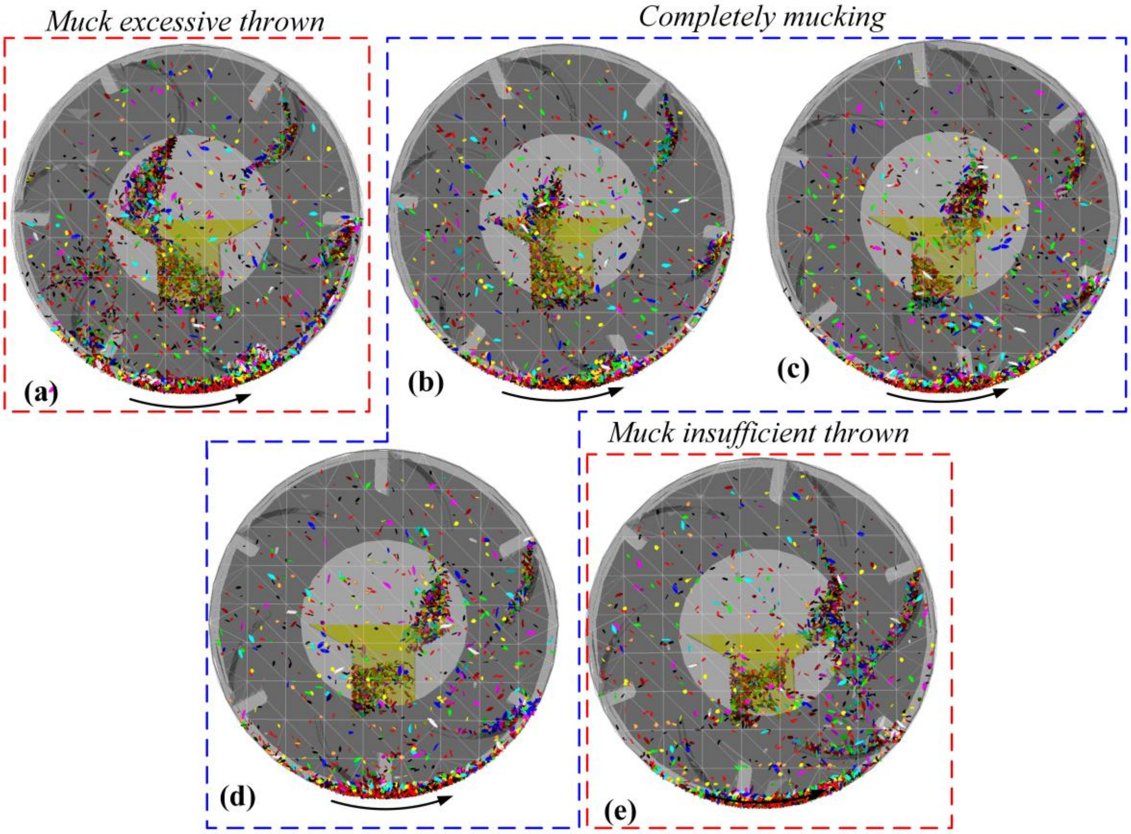

Fig. 11 - Mucking performance of cutterhead with different curvature radius of the arched supporting ribs at RPM of 13 rev/min, (a) 1 m; (b) 1.25 m; (c) 1.5 m; (d) 1.75 m; (e) 2 m.

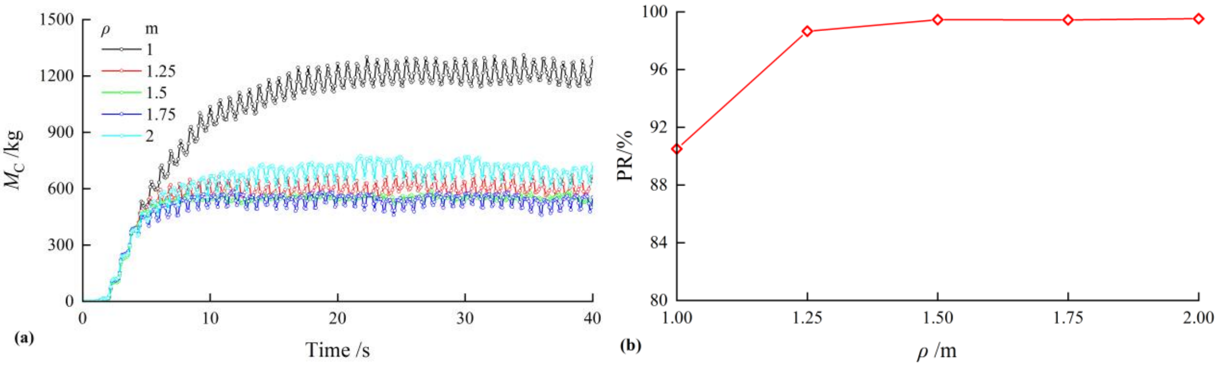

Fig. 12 - Indicators to evaluate the mucking performance of cutterhead with different curvature radius of the arched supporting ribs at RPM of 13 rev/min, (a) M_C; (b) PR.

Influence of offset angle on mucking performance

To study the influence of α on the arched supporting ribs, six simulations were conducted by setting the α as 35°, 40°, 45°, 50°, 55°, and 60°, respectively. The ρ, penetration rate, and RPM were set as 1.75 m, 7 mm/rev, and 13 rev/min, respectively. The other cutterhead structure and parameters were the same as the model shown in Figure 5. The mucking performance of cutterheads with different α is shown in Figure 13. Each figure was captured at 30 s when the mucking process was stable. When the α was 35°, a little muck was thrown out of the hopper, which caused muck accumulation in the cutterhead chamber and thus a high M_C value. Even so, the accumulated muck can be further transferred into the hopper during the following cutterhead revolutions. Compared with the straight-supporting-rib model shown in Figure 8d, the M_C was much

DOI 10.14311/CEJ.2025.02.0016

lower and the PR was much higher. This indicates that the arched-supporting-rib cutterhead performed better in mucking at high RPMs. As the *α* improved, the falling position of the muck into the hopper moved right and the excessive throwing issue was mitigated. Thus, the M_C was low and the PR was almost 100%. When the *α* is 60°, the muck can fully fall into the hopper but the insufficient-thrown problem will possibly appear for models with higher *α* values. These results indicate that the mucking performance of the arched supporting ribs is significantly affected by the offset angle *α*. The smaller the *α*, the excessive throwing issue will be more prone to occur. The larger the *α*, the insufficient-thrown problem will be more prone to occur. For a certain *ρ* value, there exists a proper *α* value with which the mucking performs well at high cutterhead RPM.

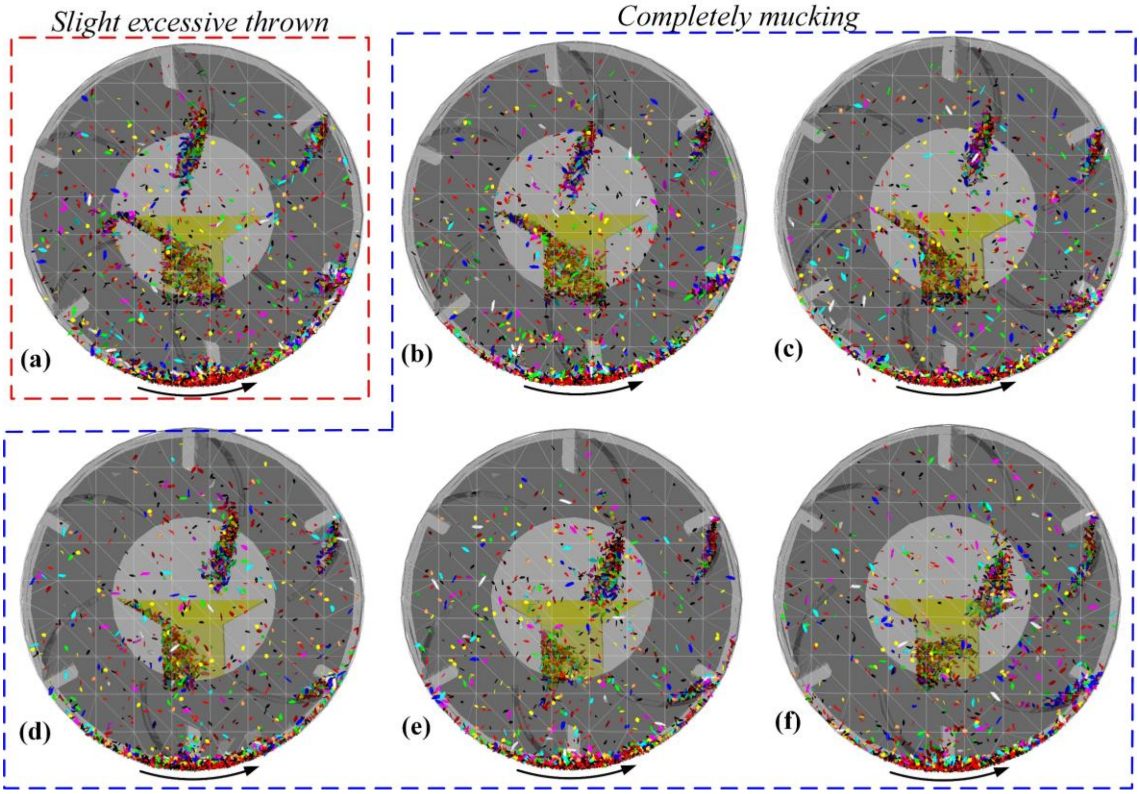

Fig. 13 - Mucking performance of cutterhead with different offset angles of the arched supporting ribs at RPM of 13 rev/min, (a) 35°; (b) 40°; (c) 45°; (d) 50°; (e) 55°; (f) 60°.

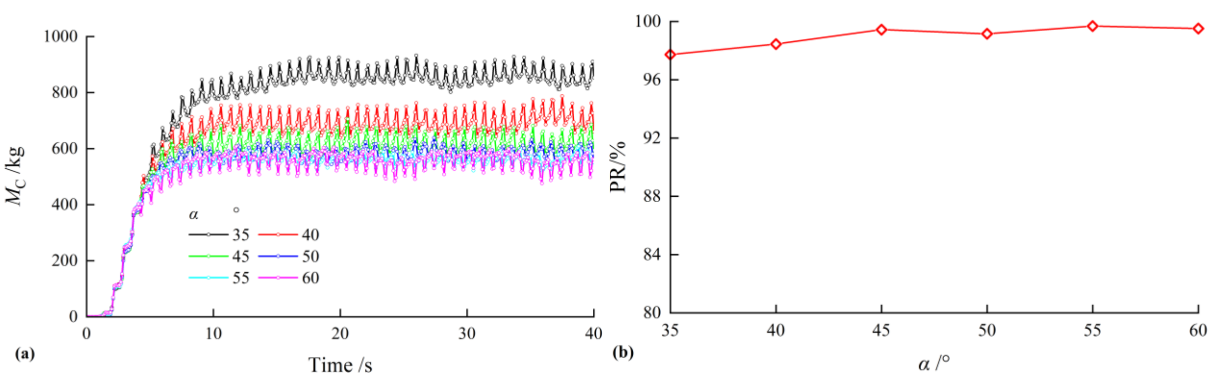

Fig. 14 - Indicators to evaluate the mucking performance of cutterhead with different offset angles of the arched supporting ribs at RPM of 13 rev/min, (a) M_C; (b) PR.

Mucking performance of arched-supporting-rib cutterhead at low RPMs

The simulations in the above two sections were conducted at a high RPM of 13 rev/min. However, the insufficient-thrown problem of muck will possibly occur at low RPMs for the arched-supporting-rib cutterhead. As a result, four simulations were conducted using the models shown in Figure 13 (b)~(e) by setting the RPM as 4 rev/min. The penetration rate was the same with previous models of 7 mm/rev. The mucking performance of cutterheads with different α is shown in Figure 15. Each figure was captured at 30 s when the mucking process was stable. When the α was 40°, the muck fully fell into the hopper, resulting in a low M_C value and almost 100% PR. When the α was 45°, an insufficient-thrown problem began to occur in the beginning, which caused slight muck accumulation in the cutterhead chamber and thus a higher M_C value than the 40°-α model. Even so, the accumulated muck can be further transferred into the hopper during the following cutterhead revolutions. Thus, the PR is still almost 100%. For the models with α of 50° and 55°, the muck insufficient-thrown problem was very obvious. The M_C kept increasing during the simulation, indicating that the muck kept accumulating in the cutterhead chamfer since the muck transfer and generation cannot enter a dynamic balance state. Thus, the PR was much reduced especially for the 55°-α model the PR was 0, indicating no muck transferred outside. Based on the above analysis, the ρ is suggested between 1.25 m and 1.75 m, and the α is suggested between 40° and 45°. Using these designs, the studied 7.03-m-diameter cutterhead with arched supporting ribs can perform well in muck transfer at an RPM range of 4~13 rev/min.

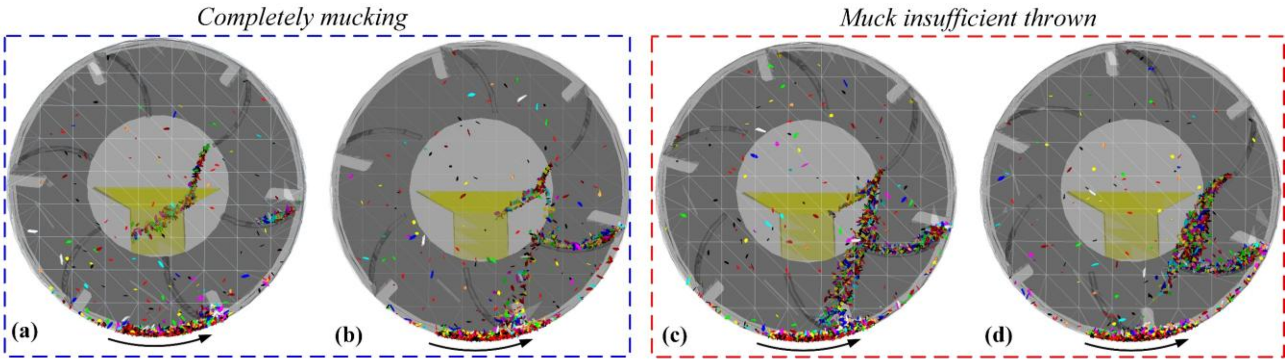

Fig. 15 - Mucking performance of cutterhead with different offset angles of the arched supporting ribs at RPM of 4 rev/min, (a) 40°; (b) 45°; (c) 50°; (d) 55°.

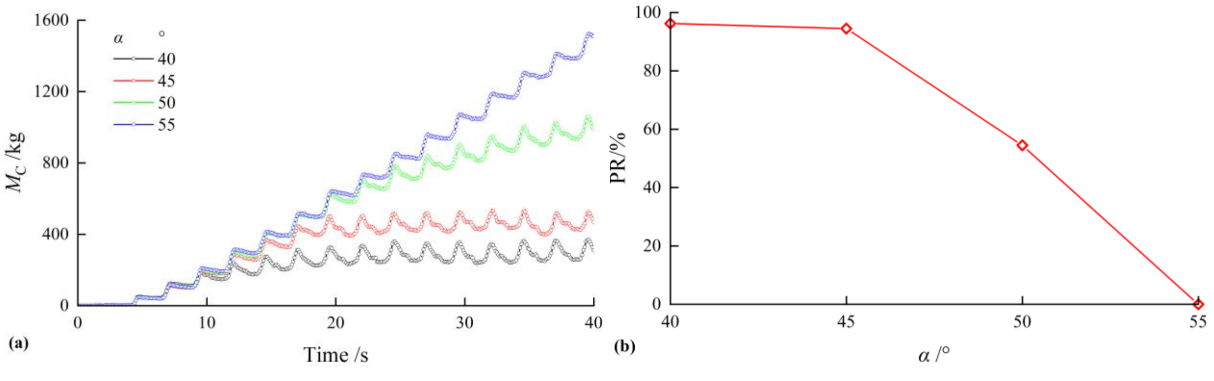

Fig. 16 - Indicators to evaluate the mucking performance of cutterhead with different offset angles of the arched supporting ribs at RPM of 4 rev/min, (a) M_C; (b) PR.

DOI 10.14311/CEJ.2025.02.0016

CONCLUSIONS

In this study, the cutterhead's muck transfer performance of the TBM applied in the EH project, in China, was investigated using a DEM numerical model, and a new arched supporting rib was proposed and designed. For the studied 7.03-m-diameter TBM, the conventional straight-supporting-rib cutterhead performed well at different penetration rates and low RPMs, but the muck excessive throwing issue was serious when the RPM was higher than 10 rev/min. As a comparison, the newly proposed arched-supporting-rib cutterhead can perform well at a greater RPM range of 4~13 rev/min if the supporting ribs are specifically designed. The curvature radius of the arched supporting ribs is suggested between 1.25 m and 1.75 m, and the offset angle is suggested between 40° and 45°. The increase of the curvature radius and offset angle can mitigate the muck excessive throwing issue but aggregate the muck insufficient-thrown problem.

ACKNOWLEDGMENTS

This work was supported by The National Natural Science Foundation of China (52278390) and Sinohydro Bureau 3 Co., LTD. Project (SDSJ-KSJF2024-001).

REFERENCES

[1] Qi M.X., Wang Y.J., Li H.L., et al., 2009. Research and application of overall refit of open type TBM. Modern Tunnelling Technology, vol. 46(04): 64-70.

[2] MAO B.Q., 2013, Improvement of the tool and scraper system for TBM under abnormal geological conditions. Construction Machinery, vol. (11): 99-102+107.

[3] Zhang J, 2019, Production of TBM ballast scraper using low alloy wear-resistant cast steel. Building Technique Development, vol. 46(04): 54-55.

[4] Geng Q, Zhang H.J., Liu X.H., et al., 2019. Numerical study on the rock muck transfer process of TBM cutterhead with clump strategy based on discrete element method. Tunnelling and Underground Space Technology, vol. 91

[5] Geng Q, Xie L.Y., Zhang Z.Y., et al., 2020. Influence of tunnel boring machine scraper bucket structure on the mucking performance. Journal of Xi'an Jiaotong University, vol. 54(11): 149-157.

[6] Geng Q, Zhang X.Y., Zhang Z.Y., et al., 2023. A numerical simulation study on the mucking mechanism of tbm two-stage spiral cutterhead. Modern Tunnelling Technology, vol. 60(02): 1-10.

[7] Zhang X.Y., 2023. Research on ballast discharging mechanism and performance of opposite-type cutter of full-section rock tunnel boring machine. Xi'an: Chang'an University.

[8] Xia Y.M., Yang M., Wu D., et al., 2018. Influence of the TBM mucking slots structure on the discharge characteristics of ballasts. Journal of Harbin Engineering University, vol. 39(9): 1561-1567.

[9] Xia Y.M., Yang M., Lin L.K., et al., 2021. Effect of blade angles on the shovel muck capacity and wear characteristics for TBM scraper. Arabian Journal for Science and Engineering, vol. 46(5): 5203-5218.

[10] Xia Y.M., Yang M., Mei Y.B., et al., 2022. Influence of geological properties and operational parameters on TBM muck removal performance for yinsong tunnel. Geotechnical and Geological Engineering, vol. 40(4): 2291-2306.

[11] Yang M., Xia Y.M., Lin L.K., et al. ,2020. Optimal design for buckets layout based on muck removal analysis of TBM cutterhead. Journal of Central South University, vol. 27(6): 1729-1741.

[12] Yang M., Xia Y.M., et al., 2017. Comprehensive performance evaluation method of mucking structure for TBM cutterhead//International Conference on Tunnel Boring Machines in Difficult Grounds. Wuhan: TBM DiGs, vol. 1-14.

[13] Huo J.Z., Chen W., OuYang X.Y., et al., 2015. Optimum design of TBM mucking slot based on the rock ballast fluidity. Journal of Northeastern University (Natural Science), vol. 36(5): 715-718.

[14] Chen W., 2015. TBM mucking process simulation based on the discrete element method and a new mucking structure design. Dalian: Dalian University of Technology.

[15] Chen W., Sun W., Huo J.Z.,et al., 2015. The open area determination of TBM cutterhead. Machinery Design & Manufacture, vol. (5): 29-31+35.

[16] Nie X.D., Hu J., Nie S.W., et al., 2018. Optimization method for the structural design of the mucking plate. Chinese Journal of Construction Machinery, vol. 16(5): 421-426.

[17] Li D.P., 2013. Process simulation of the TBM knife disc slip to be based on Abaqus. Construction Machinery Technology & Management, vol. 26(6): 101-106.

EXPERIMENTAL VERIFICATION OF THE INFLUENCE OF THE QUALITY OF INPUT IMAGES ON THE PROCESSING OF THE PHOTOGRAMMETRIC MODEL

Alice Adamcová

Czech Technical University in Prague, Faculty of Civil Engineering, Department of Special Geodesy, Thákurova 7, 166 29, Praha 6, Czech Republic; alice.adamcova@fsv.cvut.cz

Received: *09.01.2025*
Received in revised form: *30.04.2025*
Accepted: *24.07.2025*

ABSTRACT

Photogrammetric acquisition and subsequent data processing have become increasingly common in recent years. However, this method of documentation is affected by many circumstances that can negatively influence the results. This paper is devoted to the experimental determination of the influence of the quality of input images on the processing of a photogrammetric model, because the quality of input images is essential for the accuracy of the final product and can be influenced by various factors. The effect of different image quality on the ability of software to align these images and on the accuracy of this alignment and subsequent processing was tested practically in this case. Three specific interior surfaces and three specific exterior surfaces were used for the experiment, each of which was photographed in four series - one series was taken with high quality images, while the remaining three were specifically degraded in quality. Three photogrammetric software, Agisoft Metashape Professional, iTwin Capture Modeler and Pix4Dmapper, were selected for processing. In all software, all acquired series were processed and the ability to perform image orientation and the subsequent quality of this orientation was mainly monitored, where reprojection error was the main criterion. In the case of successfully aligned series, a dense point cloud was produced, which was also subjected to analysis. Based on these results, appropriate procedures for photogrammetric processing were determined when conditions that may negatively affect image quality are known in advance.

KEYWORDS

Photogrammetry, Image quality, Alignment, Dense point cloud

INTRODUCTION

Photogrammetry has nowadays established itself in many scientific fields, where it is increasingly used, e.g., for documentation of historical monuments [1, 2], its use in combination with various types of UAVs [3] for capturing the Earth's surface is very widespread, its use in landscape monitoring for natural hazards is no less frequent [4, 5], but it can also be used in healthcare [6].

Nowadays, with the development of technology, the possibilities by which photogrammetric data can be acquired are expanding and the range of tools that can improve the quality of the resulting photogrammetric model and improve its accuracy is widening.

The different uses and processing conditions in the case of photogrammetry also differ in the data acquisition strategy. The use of terrestrial photogrammetry is common [7, 8, 9], while nowadays photogrammetry using UAVs [10, 11, 12] or a combination of both methods is gaining prominence. Another option is to combine photogrammetry with LiDAR (Light Detection And Ranging) technology [13, 14] or to combine the resulting product with laser scanning output [15] or satellite imagery [16]. It is now common practice to use UAVs with a built-in GNSS receiver [17], which helps to georeference the resulting model more efficiently, while different methods of receiver position processing can be used [5, 18]. Although georeferencing using GCPs (ground control points) is still common today [10, 19], paths to direct georeferencing without the use of GCPs are being developed [20, 21].

However, the wide range of applications of this technology also entails different conditions under which photogrammetric documentation takes place. These conditions can affect the quality of the images, which are then used as an input into the processing. A photogrammetric model can only be produced from images that capture the same scene. The quality of the images is therefore crucial for successful processing, as reduced image quality (e. g. because of blurring) means degraded conditions for the alignment of the images due to their ambiguity.

Each of the photogrammetric software has a different computational kernel, so the same series of images will be produced differently in different software.

The quality of the images can be calculated in different ways [22], some photogrammetric software already has this function directly integrated [23], and this technology will be used later in this paper.

This paper aims to experimentally analyse the sensitivity to reduced quality of input images and the ability to process these images for three selected software. A total of 24 image series capturing six different surfaces are used for this purpose - each surface is imaged in four series with different image quality. The quality of the images is assessed using a coefficient that is generated in Agisoft Metashape Professional software.

The aspects monitored are in particular the ability of each software to process the reduced quality images and the quality of this processing. From these results, conclusions are then drawn regarding the suitability of the use of each software for processing degraded images and, in particular, recommendations for imaging under previously known degraded imaging conditions that may have a negative impact on image quality.

MATHERIALS AND METHODS

This chapter will describe the instruments and software used for the experiment and specify the testing methodology and results.

Equipment and software

The processing was carried out using three different software as shown in Table 1.

Tab. 1 - Used software

Software	Version
Agisoft Metashape Professional	2.0.1
iTwin Capture Modeler	24.0.0
Pix4Dmapper	4.7.5

Imaging was performed with a Canon EOS 450D camera with Canon EF 40 mm f/2.8 STM lens, whose parameters are listed in Table 2.

Tab. 2 - Parameters of used camera

Parameter	Value
Focal length	40 mm
Sensor type	CMOS

Sensor size	22,3 x 14,9 mm
Image resolution	4272 x 2848 pix
Pixel size	5,21 x 5,21 μm

Workflow

The quality of the dense cloud is influenced by the number of tie points, i.e., the points used for the alignment of the individual images. In order to correctly assign positions to images relative to others, these points need to be correctly identified in the image, and this depends on the quality of the images. Using blurry images for processing negatively affects the ability of feature detection, thus negatively affects the count of tie points.

The image quality factor can be calculated in Agisoft Metashape Professional and is an indicator of the sharpness of the images [23], which is calculated as the ratio between the pixels of the original image and the image to which a Gaussian filter has been applied [24]. Factor acquires values from 0 to 1, higher factor implicates higher quality (sharpness) of the particular image. According to [23], it is recommended not to use images that have a quality factor lower than 0.5 for the calculation.

For the purpose of this paper, three different indoor surfaces, namely two types of wood (a slightly varnished cabinet and a table) and a carpet (Figures. 1-3), and three different outdoor surfaces, gravel, concrete and grass (Figures. 4-6), were selected and imaged with different quality, each in a total of four series.

Fig. 1 – Cabinet surface

Fig. 2 – Table surface

Fig. 3 – Carpet surface

Fig. 4 – Gravel surface

Fig. 5 – Concrete surface

Fig. 6 – Grass surface

The indoor shooting was done with as much light as possible entering the room, while the outdoor shooting was done in cloudy weather.

The aim of this experiment was to test the alignment for aerial topographic mapping, that is why the images were taken from a single distance of approximately 1.2 m from the surface, only nearly orthogonal to the surface, and although handheld, the imaging procedure simulated the flight of a drone during nadir imaging.

Six images were taken in the longitudinal direction (four in the case of the 'Table' series) and four images were taken in the lateral direction. To illustrate the imaging method, the camera positions for the Gravel 4 series are shown in Figure 7, including the number of overlapping images in each part of the cloud, Figure 8 shows diagram of images axes; the same configuration of camera positions was followed for the other series. Thus, each image was taken with sufficient overlaps in

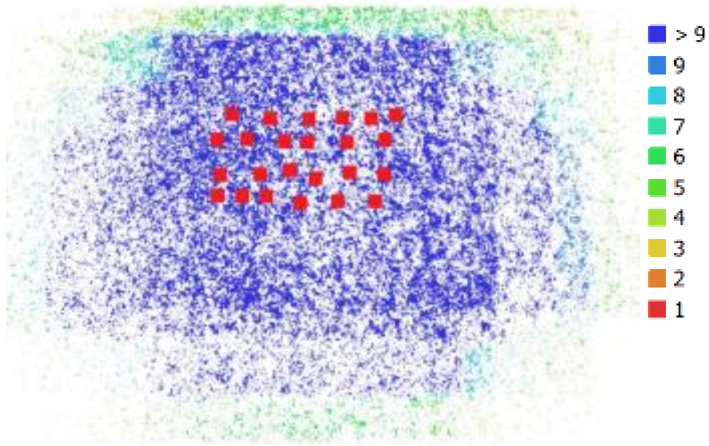

terms of processing the photogrammetric model.

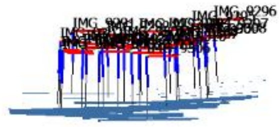

Fig. 7 – Camera positions for the Gravel 4 series (red markers) and image overlap

Fig. 8 - Axes positions for the Gravel 4 series

First, the surfaces were photographed with the camera automatically set and in the highest possible quality, i.e., all images in the series had a quality factor greater than 0.5.

Then, two series were taken where the quality was artificially reduced. The camera was set to priority of time - in the case of one series the shutter was set to 1/25 s, in the case of the other to 1/8 s, ISO was set to 200 and aperture value was changing automatically in range of value f/2,8 - f/9 in case of interior series and f/2,8 - f/7 in case of exterior series. With these settings, the camera was moving when taking the picture. Finally, a series was taken where the quality was degraded only by manual blurring. The degradation of the images was always almost identical.

All images were taken with autofocus on and lightning off.

The count of images of each series together with the extreme values of their quality factors are shown in Table 3 and Table 4, and Figures 9-14 show images with different quality of the selected surfaces.

Tab. 3 - Count of images and their quality factors for interior series

Series	Image count	Lowest quality factor	Highest quality factor	Average quality factor	Way of image degradation
Cabinet 1	24	0.55	0.83	0.75	
Cabinet 2	24	0.00	0.95	0.31	Exposure + movement
Cabinet 3	24	0.00	0.24	0.10	Exposure + movement
Cabinet 4	24	0.00	0.00	0.00	Blurring
Table 1	16	0.57	0.74	0.64	
Table 2	16	0.48	0.58	0.55	Exposure + movement
Table 3	16	0.00	1.00	0.43	Exposure + movement
Table 4	16	0.00	0.00	0.00	Blurring
Carpet 1	24	0.52	0.83	0.73	
Carpet 2	24	0.64	0.73	0.70	Exposure + movement
Carpet 3	24	0.54	0.73	0.63	Exposure + movement
Carpet 4	24	0.00	1.00	0.22	Blurring

Tab. 4 - Count of images and their quality factors for exterior series

Series	Image count	Lowest quality factor	Highest quality factor	Average quality factor	Way of image degradation
Concrete 1	24	0.57	0.81	0.78	
Concrete 2	24	0.48	0.64	0.58	Exposure + movement
Concrete 3	24	0.37	0.70	0.60	Exposure + movement
Concrete 4	24	0.00	0.42	0.13	Blurring
Gravel 1	24	0.53	0.72	0.63	
Gravel 2	24	0.49	0.66	0.58	Exposure + movement
Gravel 3	24	0.44	0.70	0.50	Exposure + movement
Gravel 4	24	0.31	0.35	0.33	Blurring
Grass 1	24	0.67	0.82	0.76	
Grass 2	24	0.54	0.67	0.60	Exposure + movement
Grass 3	24	0.52	0.68	0.59	Exposure + movement
Grass 4	24	0.21	0.40	0.27	Blurring

Fig. 9 – Concrete - factor 0.23

Fig. 10 – Concrete - factor 0.58

Fig. 11 – Concrete - factor 0.80

Fig. 12 – Table - factor 0.00

Fig. 13 – Table - factor 0.53

Fig. 14 – Table - factor 0.73

All series were oriented in Agisoft Metashape Professional, iTwin Capture Modeler and Pix4Dmapper and in case of successfully oriented series (i.e., series where at least 2/3 of the images were oriented) a dense cloud was generated.

The alignment in Agisoft Metashape Professional was set to the Highest accuracy and there was no limit to the number of tie points per image to be generated. In the case of orientation in iTwin Capture Modeler, the number of tie points was set to High and in the case of orientation in Pix4Dmapper, the number of tie points was set to Automatic. There was no tie points filtering done after the alignment. Though Agisoft Metashape Professional offers function that filters tie points with low accuracy, which can increase the accuracy of following model / dense cloud, but the other two software do not include this function, so it was done in no software to achieve more comparable results.

Furthermore, if a dense point cloud was generated, it was generated with a quality of Ultra high in Agisoft Metashape Professional, sampling was set to 1 in iTwin Context Capture Modeler and in Pix4Dmapper the dense cloud was calculated from the original image resolution and with the point density set to High.

The subsequent comparison of the results examined the ability of the software to process each series and the quality of these processes, both visually and in terms of accuracy, where the main criterion was the quadratic mean of the reprojection error, i.e., the distance between the actual and the adjusted point position.

RESULTS

Tables 5 and 6 show the parameters of interior orientation for chosen series in all software, including optimized values for focal length in millimetres and distortion coefficients.

Figures 15 and 16 show distribution of tie points in two different series in all software. Figure 15 shows Grass 4 series (taken with manual blurring), where distribution of tie points through all software looks very similar, which happens in almost all series. On the other hand, Figure 16 shows one of two exceptions, where the distribution looks very different in different software and does not depict the shape of surface in Pix4Dmapper. These exceptions occur in case of Cabinet 1 (shown) and Grass 1, e. g. series taken with hight quality.

Tables 7 and 8 show the number of aligned images and the number of tie points from each series. In the case of successfully oriented series, the number of dense cloud points is also given.

Tab. 5 - Parameters of interior orientation for Cabinet series

Series	Parameter		Software		
			Agisoft Metashape Professional	iTwin Capture Modeler	Pix4Dmapper
Cabinet 1	Focal length [mm]		34,604	39,468	61,955
	Radial distortion coefficients	K1	-0,079	-0,095	-0,381
		K2	0,172	0,277	3,173
		K3	-0,035	-0,243	-8,111
	Tangential distortion coefficients	P1	0,000	-0,002	-0,010
		P2	0,003	0,002	0,001
Cabinet 2	Focal length [mm]		29,141	23,022	43,853
	Radial distortion coefficients	K1	-0,009	-0,003	0,068
		K2	-0,155	-0,076	-1,433
		K3	0,822	0,339	7,295
	Tangential distortion coefficients	P1	-0,009	0,020	-0,010
		P2	-0,005	0,027	0,013
Cabinet 3	Focal length [mm]		29,471	---	---
	Radial distortion coefficients	K1	-0,014	---	---
		K2	0,037	---	---
		K3	-0,265	---	---
	Tangential distortion coefficients	P1	0,020	---	---
		P2	-0,002	---	---
Cabinet 4	Focal length [mm]		65,679	25,036	42,048
	Radial distortion coefficients	K1	0,027	-0,042	0,013
		K2	-0,308	0,125	-1,122
		K3	1,359	-0,405	9,753
	Tangential distortion coefficients	P1	-0,031	-0,010	-0,002
		P2	0,033	0,011	0,006

Tab. 6 - Parameters of interior orientation for Concrete series

Series	Parameter		Software: Agisoft Metashape Professional	Software: iTwin Capture Modeler	Software: Pix4Dmapper
Concrete 1	Focal length [mm]		40,652	40,339	39,010
	Radial distortion coefficients	K1	-0,075	-0,077	-0,075
		K2	0,111	0,130	0,098
		K3	0,196	0,076	0,158
	Tangential distortion coefficients	P1	0,000	0,001	-0,004
		P2	0,001	0,000	0,001
Concrete 2	Focal length [mm]		68,240	58,543	40,912
	Radial distortion coefficients	K1	-0,179	0,052	-0,073
		K2	1,815	-0,620	0,808
		K3	-13,288	1,642	-5,636
	Tangential distortion coefficients	P1	0,009	-0,024	0,004
		P2	0,057	0,051	-0,004
Concrete 3	Focal length [mm]		39,631	28,212	38,753
	Radial distortion coefficients	K1	-0,027	-0,007	-0,015
		K2	0,041	-0,279	-0,361
		K3	0,019	1,028	2,824
	Tangential distortion coefficients	P1	-0,001	0,004	0,000
		P2	0,005	-0,020	0,001
Concrete 4	Focal length [mm]		41,446	31,069	---
	Radial distortion coefficients	K1	-0,074	-0,049	---
		K2	-0,292	-0,035	---
		K3	4,082	0,359	---
	Tangential distortion coefficients	P1	0,001	0,001	---
		P2	0,005	0,003	---

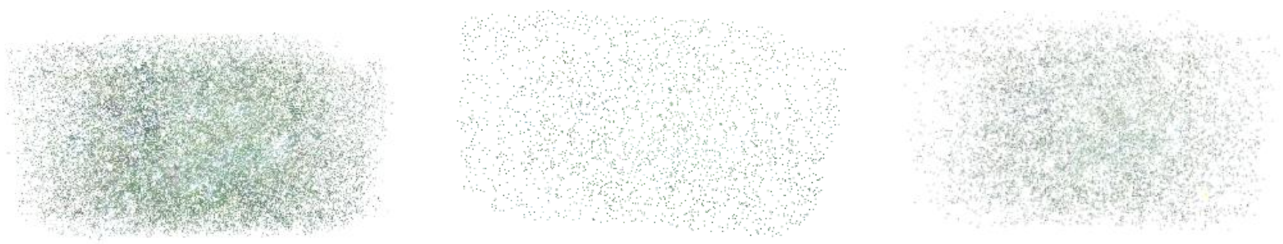

Fig. 15 - Tie points distribution for Grass 4 - top view - software (from the left) Agisoft Metashape Professional, iTwin Capture Modeler a Pix4DMapper

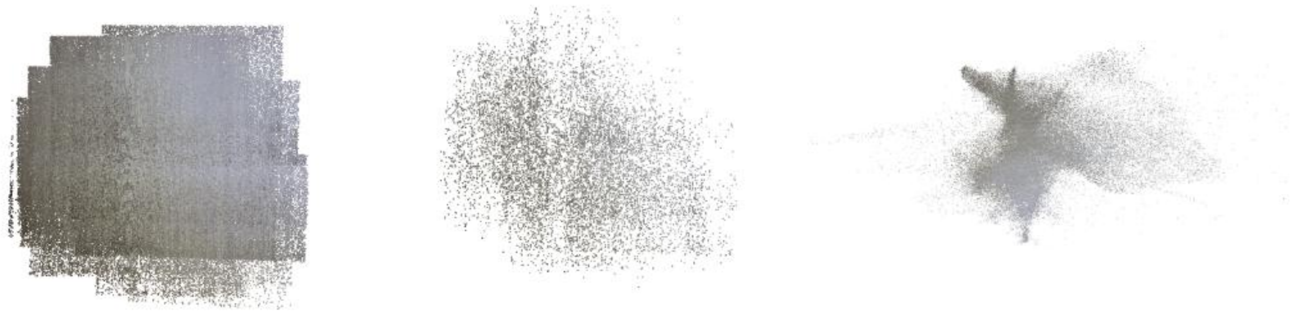

Fig. 16 - Tie points distribution for Cabinet 1 - top view - software (from the left) Agisoft Metashape Professional, iTwin Capture Modeler a Pix4DMapper

Tab. 7 - Counts of aligned images and points of sparse and dense clouds for interior series

		Agisoft Metashape Professional			iTwin Capture Modeler			Pix4Dmapper		
Series	Way of degradation	Images aligned	Tie points count	Dense cloud points count	Images aligned	Tie points count	Dense cloud points count	Images aligned	Tie points count	Dense cloud points count
Cabinet 1		24/24	296 343	37 916 525	24/24	10 788	33 192 366	24/24	281 177	5 562 177
Cabinet 2	time, moving	24/24	18 342	10 602 892	8/24	152	---	10/24	7 796	80 650
Cabinet 3	time, moving	5/24	540		0/24	---	---	0/24	---	---
Cabinet 4	blurring	24/24	8 157	5 721	24/24	142	1 617 774	24/24	3 424	---
Table 1		16/16	135 620	21 903 710	16/16	5 255	22 055 999	16/16	138 511	36 427
Table 2	time, moving	5/16	701		0/16	---	---	0/16	---	---
Table 3	time, moving	2/16	13		0/16	---	---	0/16	---	---
Table 4	blurring	16/16	2 686	1 303	16/16	165	3 507 995	0/16	---	--
Carpet 1		24/24	588 601	31 583 814	24/24	17 792	25 749 335	24/24	304 902	12 666
Carpet 2	time, moving	2/24	15		0/24	---	---	0/24	---	---
Carpet 3	time, moving	23/24	59 133	16 461 716	20/24	1 415	7 933 943	18/24	60 421	5 109
Carpet 4	blurring	24/24	6 838	58 859	24/24	592	22 235 142	18/24	2 816	---

Tab. 8 - Counts of aligned images and points of sparse and dense clouds for exterior series

		Agisoft Metashape Professional			iTwin Capture Modeler			Pix4Dmapper		
Series	Way of degradation	Images aligned	Tie points count	Dense cloud points count	Images aligned	Tie points count	Dense cloud points count	Images aligned	Tie points count	Dense cloud points count
Concrete 1		24/24	835 420	23 800 971	24/24	15 271	20 282 290	24/24	164 805	---
Concrete 2	time, moving	15/24	6 321	---	8/24	625	---	9/24	4 752	---
Concrete 3	time, moving	24/24	64 934	17 385 536	20/24	1 600	22 493 185	20/24	24 690	2 753
Concrete 4	blurring	24/24	10 985	888 389	24/24	844	21 577 319	0/24	---	---
Gravel 1		24/24	587 177	43 860 040	24/24	20 194	33 490 022	24/24	289 441	14 041 698
Gravel 2	time, moving	11/24	11 505	---	8/24	104	---	0/24	---	---
Gravel 3	time, moving	22/24	75 646	24 568 448	20/24	1 530	---	19/24	108 026	12 770
Gravel 4	blurring	24/24	67 044	8 691 866	24/24	6 946	21 135 779	24/24	61 524	---
Grass 1		24/24	675 243	23 822 714	24/24	11 406	45 103 792	24/24	200 509	950
Grass 2	time, moving	21/24	6 861	2 014 327	20/24	380	---	0/24	---	---
Grass 3	time, moving	14/24	21 574	---	15/24	540	---	11/24	26 006	2 359
Grass 4	blurring	24/24	35 961	44 873 542	24/24	2 725	22 150 156	24/24	36 590	---

From Tables 7 and 8, it can be seen that with the exception of the Grass 3 series, Agisoft Metashape Professional was able to orient more images than the other two software. Regarding the number of tie points, in four cases Pix4Dmapper software generated the highest number of points, but in the remaining cases Agisoft Metashape Professional again generated the highest number. In the case where a dense cloud was produced by both Agisoft Metashape Professional and iTwin Capture Modeler, Agisoft Metashape Professional generated the higher number of dense cloud points in six cases, iTwin Capture Modeler in eight cases. Pix4Dmapper generated very sparse clouds in all cases or did not generate them at all despite successful orientation. This also occurred in three cases in iTwin Capture Modeler.

The reprojection errors for each series are shown in Tables 9 and 10 below. At first glance, it can be seen that the error values generated by Pix4Dmapper are significantly lower than those of the remaining software. The series that were photographed with high accuracy (marked as 1) show very similar error values for the other two software, while the other series, with one exception, show smaller errors for iTwin Capture Modeler, in some cases very significantly.

Tab. 9 - RMS of reprojection errors for interior series

Series	RMS of reprojection error [pix]		
	Agisoft Metashape Professional	iTwin Capture Modeler	Pix4Dmapper
Cabinet 1	0.83	0.70	0.33
Cabinet 2	2.28	1.11	0.28
Cabinet 3	1.84	---	---
Cabinet 4	4.51	1.42	0.23
Table 1	0.85	0.66	0.20
Table 2	2.31	---	---
Table 3	1.24	---	---
Table 4	3.58	1.59	---
Carpet 1	0.53	0.51	0.16
Carpet 2	1.35	---	---
Carpet 3	1.37	1.10	0.20
Carpet 4	3.04	1.48	0.20

Tab. 10 - RMS of reprojection errors for exterior series

Series	RMS of reprojection error [pix]		
	Agisoft Metashape Professional	iTwin Capture Modeler	Pix4Dmapper
Concrete 1	0.32	0.31	---
Concrete 2	1.86	1.40	0.18
Concrete 3	1.54	1.26	0.18
Concrete 4	2.12	0.97	---
Gravel	0.37	0.36	0.11
Gravel 2	1.52	1.25	---
Gravel 3	1.27	0.95	0.23
Gravel 4	1.44	0.93	0.23
Grass 1	0.50	0.55	0.30
Grass 2	2.14	2.31	---
Grass 3	1.92	1.40	0.27
Grass 4	2.04	1.28	0.29

In Figure 17 and Figure 18, dense clouds from the corresponding series are shown. They show that in the case of the lower quality series, the iTwin Capture Modeler produces the visually best clouds.

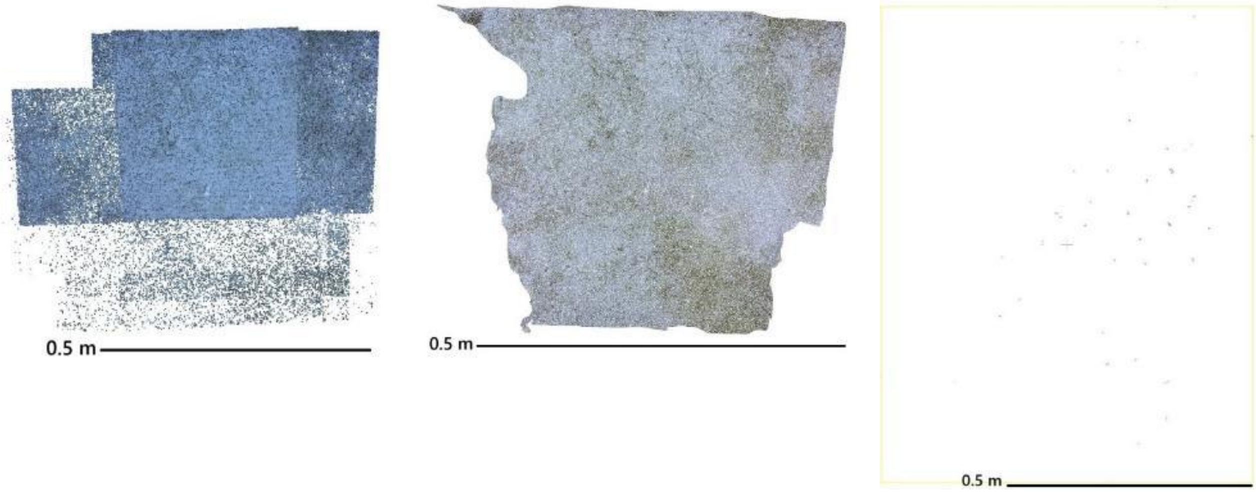

Fig. 17 – Dense cloud for Concrete 3 - software (from the left) Agisoft Metashape Professional, iTwin Capture Modeler a Pix4DMapper

Fig. 18 – Dense cloud for Gravel 1 - software (from the left) Agisoft Metashape Professional, iTwin Capture Modeler a Pix4DMapper

Some images, especially in case of the carpet, that stand out in the quality calculation are those that, although taken at reduced quality (Figure 19), were assessed as being of high quality. However, the orientation and calculation of the dense cloud are already consistent with the reduced quality. This is likely due to the nature of the surface, where the image after the application of the Gaussian filter is already very similar to the original image, so Agisoft Metashape is no longer able to distinguish that the original image is out of focus. However, the surface itself is already too difficult to process, and it is then of poor quality. Inverse case, image with quality calculated lower than 0.5 but in fact with high quality, did not appear in this experiment, but it does not mean, that it cannot happen. This implies that if it is requested to have absolute control over the image quality, it is necessary to do the manual check of all images.

Fig. 19 – Image of carpet with quality factor 0.94

From the reduced quality series all software produced a dense cloud that did not show the entire surface. If the poor conditions are known in advance, it is advisable to increase the number of images and extend the area imaged to ensure the entire area of interest is imaged more than necessary. According to the protocols, the reduced quality images in Agisoft Metashape Professional were usually processed in areas where there was an overlap of at least four images, in the case of iTwin Capture Modeler and Pix4Dmapper software at least three images, but in some cases five images were required for Agisoft Metashape Professional and iTwin Capture Modeler software. Examples of some of the required overlays are shown in Figures 20-22. For the high-quality series, locations with a required overlap of two images were processed in all software.

Despite requiring fewer overlapping images than Agisoft Metashape Professional and exhibiting by far the smallest reprojection errors, Pix4Dmapper was able to orient the fewest series and the resulting dense clouds were in most cases very sparse and thus unusable for further processing. Therefore, under poor conditions and this chosen imaging method, it is not advisable to use Pix4Dmapper for processing.

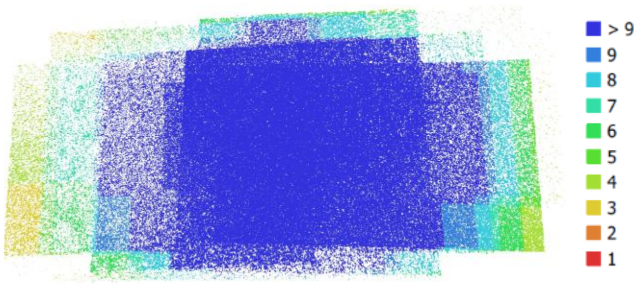

Fig. 20 – Images overlap on the produced parts of the dense cloud from the Gravel 3 series in Agisoft Metashape Professional

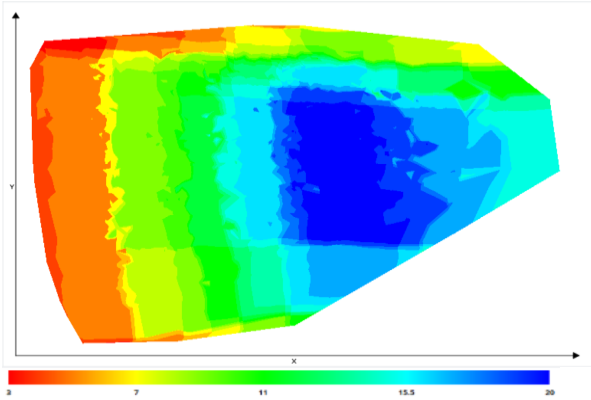

Fig. 21 – Images overlap on the produced parts of the dense cloud from the Gravel 3 series in iTwin Capture Modeler

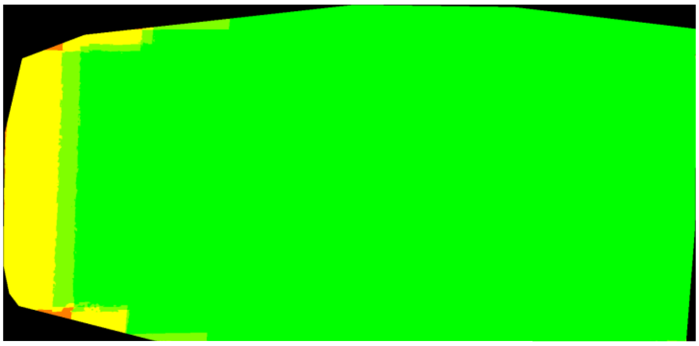

Fig. 22 – Images overlap on the produced parts of the dense cloud from the Gravel 3 series in Pix4Dmapper

CONCLUSION

As base of the testing, six different surfaces were captured with different image quality (4 series with different quality degradation), these series of images were then processed in Agisoft Metashape Professional, iTwin Capture Modeler and Pix4Dmapper. In terms of exterior orientation and number of tie points, Agisoft Metashape Professional performs the best, being able to orient even lower quality images and generate significantly higher numbers of tie points than iTwin Capture Modeler, however, it requires more image overlap than the other two software. iTwin Capture Modeler, on the other hand, produces the highest visual quality dense clouds of all the software tested. Pix4Dmapper has the lowest reprojection errors but oriented the fewest series and most of the dense clouds produced by it were unusable for further processing.

The analysis suggests that if the poor imaging conditions are known in advance, more images should be taken, so that the area of interest is always present in at least three or four images overlapping, depending on the software in which the further processing takes place, instead of the required two. Basically, using two images to create a model allows no control and the quality of alignment then depends on the image quality. When the quality is low, there is no control possible and in extreme cases it makes the alignment impossible. Required count of low-quality images to process the alignment then depends on the algorithms and abilities of particular software.

Thus, if the accuracy requirements do not need to be met, the reduced quality of the input images need not be an obstacle if the more stringent imaging conditions are met. Otherwise, although the software is able to orient the images in some cases, the reprojection error already shows higher values. Therefore, it is advisable to follow the recommended quality factor limit of at least 0.5 and in case of a peculiar surface, the user should check the quality of the images themselves, as even a high-quality factor may not guarantee a good image.

ACKNOWLEDGEMENTS

This research was funded by the Grant Agency of CTU in Prague – grant number SGS24/047/OHK1/1T/11

REFERENCES

[1] Matoušková, E.; Pavelka, K.; Smolík, T. and Pavelka, K. Earthen Jewish Architecture of Southern Morocco: Documentation of Unfired Brick Synagogues and Mellahs in the Drâa-Tafilalet Region. Online. Applied Sciences. 2021, roč. 11, č. 4. ISSN 2076-3417. Dostupné z: https://doi.org/10.3390/app11041712. [cit. 2025-01-07].

[2] Šedina, J.; Hůlková, M.; Pavelka, K. and Pavelka, Jr, K. RPAS for documentation of Nazca aqueducts. Online. European Journal of Remote Sensing. 2019, roč. 52, č. sup1, s. 174-181. ISSN 2279-7254. Dostupné z: https://doi.org/10.1080/22797254.2018.1537684. [cit. 2025-01-09].

[3] Jon, J.; Koska, B. and Pospíšil, J. (2013) Autonomous Airship Equipped by Multi-sensor Mapping Platform, The International Archives of the Photogrammetry, Remote Sensing and Spatial Information Sciences, XL-5/W1, pp. 119-124. doi: 10.5194/isprsarchives-xl-5-w1-119-2013. [cit. 2025-01-09].

[4] Kovanič, Ľ.; Štroner, M.; Urban, R. and Blišťan, P. Methodology and Results of Staged UAS Photogrammetric Rockslide Monitoring in the Alpine Terrain in High Tatras, Slovakia, after the Hydrological Event in 2022. Online. Land. 2023, roč. 12, č. 5. ISSN 2073-445X. Dostupné z: https://doi.org/10.3390/land12050977. [cit. 2025-01-07].

[5] Žabota B. and Kobal, M. (2021) Accuracy Assessment of UAV-Photogrammetric-Derived Products Using PPK and GCPs in Challenging Terrains: In Search of Optimized Rockfall Mapping, Remote Sensing, 13(19), p. 3812. doi: 10.3390/rs13193812. [cit. 2025-01-07].

[6] Lim, Y. Ch.; Abdul Shakor, A. S. and Shaharudin, R. Reliability and Accuracy of 2D Photogrammetry: A Comparison With Direct Measurement. Online. Frontiers in Public Health. 2022, roč. 9. ISSN 2296-2565. Dostupné z: https://doi.org/10.3389/fpubh.2021.813058. [cit. 2025-01-07].

[7] Sánchez-García, E.; Balaguer-Beser, A.; Taborda, R. and Pardo-Pascual, J. E. Modelling Landscape Morphodynamics by Terrestrial Photogrammetry: An Application to Beach and Fluvial Systems. Online. ISPRS - International Archives of the Photogrammetry, Remote Sensing and Spatial Information Sciences. 2016, roč. XLI-B8, s. 1175-1182. ISSN 2194-9034. Dostupné z: https://doi.org/10.5194/isprsarchives-XLI-B8-1175-2016. [cit. 2025-01-09].

[8] Terrugi, L. B.; Rinaldi, M.; Chiaverini, I. and Ostuni, D. Application of Terrestrial Photogrammetry to the Measurement of a Riverbank Retreat. Online. ITALIAN JOURNAL OF ENGINEERING GEOLOGY AND ENVIRONMENT. 2011, s. 115-122. Dostupné z: https://doi.org/10.4408/IJEGE.2011-01.S-09. [cit. 2025-01-09].

[9] Nero, M. A.; Pinto Rocha, A.; Guerra Mamede, C.; Borba Schuler, C. A.; Da Costa Temba, P. et al. Positional accuracy in close-range photogrammetry through Topography and Geodesy. Online. Revista de Arquitectura. 2023, roč. 25, č. 2. ISSN 2357-626X. Dostupné z: https://doi.org/10.14718/RevArq.2023.25.3659. [cit. 2025-01-09].

[10] Chen, X.; Pan, S. and Chen, G. 3D model construction and accuracy analysis based on UAV tilt photogrammetry. Online. IOP Conference Series: Earth and Environmental Science. 2022, roč. 1087, č. 1. ISSN 1755-1307. Dostupné z: https://doi.org/10.1088/1755-1315/1087/1/012047. [cit. 2025-01-09].

[11] Vacca, G.; Dessì, A. and Sacco, A. (2017) The Use of Nadir and Oblique UAV Images for Building Knowledge, ISPRS International Journal of Geo-Information, 6(12), p. 393. doi: 10.3390/ijgi6120393. [cit. 2025-01-07].

[12] Blistan, P.; Kovanič, Ľ.; Zelizňaková, V. and Palková, J. Using UAV photogrammetry to document rock outcrops. Online. Acta Montanistica Slovaca. Roč. 21, č. 2, s. 154-161. Dostupné z: https://www.researchgate.net/profile/Peter-Blistan/publication/305781724_Using_UAV_photogrammetry_to_document_rock_outcrops/links/57a1b40408aeb16048331a5a/Using-UAV-photogrammetry-to-document-rock-outcrops.pdf. [cit. 2025-01-09].

[13] Štroner, M.; Urban, R.; Křemen, T.; Braun, J. UAV DTM Acquisition in a Forested Area—Comparison of Low-Cost Photogrammetry (DJI Zenmuse P1) and LiDAR Solutions (DJI Zenmuse L1). Eur. J. Remote Sens. 2023, 56, 2179942. [cit. 2025-01-07].

[14] Fuad, N. A., Ismail, Z., Majid, Z., Darwin, N., Ariff, M. F. M., Idris, K. M., a Yusoff, A. R. (2018, July 31). Accuracy evaluation of digital terrain model based on different flying altitudes and conditional of terrain using UAV LiDAR technology. IOP Conference Series: Earth and Environmental Science, 169, 012100. https://doi.org/10.1088/1755-1315/169/1/012100. [cit. 2025-01-07].

[15] Majid, Z.; Ariff, M. F. M.; Idris, K. M.; Yusoff, A. R.; Idris, K. M. et al. Three-Dimensional Mapping of an Ancient Cave Paintings Using Close-Range Photogrammetry and Terrestrial Laser Scanning Technologies. Online. The International Archives of the Photogrammetry, Remote Sensing and Spatial Information Sciences. 2017, roč. XLII-2/W3, s. 453-457. ISSN 2194-9034. Dostupné z: https://doi.org/10.5194/isprs-archives-XLII-2-W3-453-2017. [cit. 2025-01-09].

[16] Chen, Ch.; Tian, B.; Wu, W.; Duan, Y.; Zhou, Y. et al. UAV Photogrammetry in Intertidal Mudflats: Accuracy, Efficiency, and Potential for Integration with Satellite Imagery. Online. Remote Sensing. 2023, roč. 15, č. 7. ISSN 2072-4292. Dostupné z: https://doi.org/10.3390/rs15071814. [cit. 2025-01-09].

[17] Forlani, G., Dall'asta, E., Diotri, F., Cella, U. M. D., Roncella R., and Santise, M. (2018, February 17). Quality Assessment of DSMs Produced from UAV Flights Georeferenced with On-Board RTK Positioning. Remote Sensing, 10(2), 311. https://doi.org/10.3390/rs10020311. [cit. 2025-01-07].

[18] Dinkov, D. Accuracy assessment of high-resolution terrain data produced from UAV images georeferenced with on-board PPK positioning. Online. Journal of the Bulgarian Geographical Society. 2023, roč. 48, s. 43-53. ISSN 2738-8115. Dostupné z: https://doi.org/10.3897/jbgs.e89878. [cit. 2025-01-09].

[19] Güngör, R.; Uzar, M.; Atak, B.; Yilmaz, O. S. and Gümüş, E. Orthophoto production and accuracy analysis with UAV photogrammetry. Online. Mersin Photogrammetry Journal. 2022, roč. 4, č. 1, s. 1-6. ISSN 2687-654X. Dostupné z: https://doi.org/10.53093/mephoj.1122615. [cit. 2025-01-09].

[20] Teppati Losè, L.; Chiabrando, F. and Giulio Tonolo, F. (2020) Boosting the Timeliness of UAV Large Scale Mapping. Direct Georeferencing Approaches: Operational Strategies and Best Practices, ISPRS International Journal of Geo-Information, 9(10), p. 578. doi: 10.3390/ijgi9100578. [cit. 2025-01-07].

[21] Štroner, M., Urban, R., Seidl, J., Reindl, T., and Brouček, J. (2021, March 31). Photogrammetry Using UAV-Mounted GNSS RTK: Georeferencing Strategies without GCPs. Remote Sensing, 13(7), 1336. https://doi.org/10.3390/rs13071336. [cit. 2025-01-07].

[22] Matuzevičius, D.; Urbanavičius, V.; Miniotas, D.; Mikučionis, Š.; Laptik, R. et al. Key-Point-Descriptor-Based Image Quality Evaluation in Photogrammetry Workflows. Online. Electronics. 2024, roč. 13, č. 11. ISSN 2079-9292. Dostupné z: https://doi.org/10.3390/electronics13112112. [cit. 2025-01-09].

[23] Online. In: Agisoft Metashape User Manual - Professional Edition, Version 2.0. Agisoft Metashape, s. 25. Dostupné z: https://www.agisoft.com/pdf/metashape-pro_2_0_en.pdf. [cit. 2024-07-13].

[24] Topic: What causes an Estimated Image Quality value >1? Online. Agisoft Metashape. Dostupné z: https://www.agisoft.com/forum/index.php?topic=9889.0. [cit. 2024-11-01].

Article no. 18

THE CIVIL ENGINEERING JOURNAL 2-2025

KEY TECHNOLOGY OF SUPER-LARGE DIAMETER SHIELD PILE FOUNDATION REPLACEMENT CONSTRUCTION

Jian Ouyang[1], Haijun Wang[1], Luxiang Wu[1], Xingwei Xue[2] and Kexin Zhang[2]

1. *Guanzhou Expressway Co., LTD, Engineering Department, Guangzhou, China; OuYJian666@163.com*
2. *Shenyang Jianzhu University, School of Transportation and Surveying Engineering, No. 25, Hunnan Zhong Road, Shenyang, Liaoning Province, China*

Received: *30.11.2024*
Received in revised form: *23.05.2025*
Accepted: *17.06.2025*

ABSTRACT

This study investigates the critical technologies for large-span pile foundation replacement construction under super-large diameter shield tunneling conditions, using the Guangzhou Haizhu Wan Shield Tunnel Project as a case study. A novel "active buttressing-pile truncation" integrated methodology was developed, featuring a 20.8m-span composite buttress system comprising pile groups, pre-stressed double-beam structures, and bearing platforms. The research emphasizes the active buttressing phase, which critically influences superstructure deformation. Maximum settlement of existing buildings reached -6.1mm (negative denotes downward movement) with no differential settlement detected. Structural Performance: Joist stress-strain responses and building inclinations remained within 65% of warning thresholds. The proposed system demonstrated superior settlement control efficacy, reducing superstructure displacements by 42% compared with conventional methods. The findings confirm that this large-span pre-stressed double-beam buttress pile foundation system provides an effective technical solution for urban underground construction involving complex foundation replacement, offering both theoretical and practical references for similar projects.

KEYWORDS

Super-large diameter shield tunnel, Pile foundation underpinning, Construction monitoring, Monitoring and analysis

INTRODUCTION

With the rapid development of China's economy and the improvement of residents' living standards, many large and medium-sized cities have experienced a proliferation of vehicles and insufficient road transportation capacity, which in turn leads to the increasingly obvious problem of traffic congestion, and thus the structure of the underground space and transportation system plays an increasingly important role [1-3]. In urban planning and development, it is necessary to avoid the existing underground structures, but for the development of earlier urban underground space is more complex, will inevitably conflict with the existing underground buildings [4-6]. If such conflicts are resolved by demolishing and reconstructing existing buildings, it increases the cost and duration of the project. Therefore, when planning underground space, it is necessary to comprehensively consider the economic and technical feasibility, and the most cost-effective way to solve this problem is generally the pile foundation underpinning technology [7].

Underground space development and utilization has been further developed by the emergence of pile foundation underpinning technology, and the birth of this technology has brought new scientific research directions in the design of the scheme of the required structure, on-site construction, safety monitoring, etc. [8-9]. With the increasing maturity of pile foundation underpinning technology, more and more countries are using pile foundation underpinning in their underground projects. For pile foundation underpinning, it is actually to make the load of the superstructure redistributed on the new structure after the existing pile foundation is cut off during the construction process, for a reinforced concrete structure, it is necessary to try to ensure that the settlement and deformation of the original structure and the replacement structure during the construction of the pile foundation underpinning comply with the specification requirements [10-12]. Frequently, there will be settlement differences between the old and new structures, and settlement differences that exceed a certain value will adversely affect the normal use and safety of the structure [13]. Moreover, load bearing condition and load transfer pattern of the old and new structures in the process of buttress replacement are also important factors to judge whether the buttress replacement is successful or not. Therefore, numerical simulation analysis and real-time monitoring of the old and new structures in pile foundation underpinning are necessary [14-15]. Pile foundation underpinning has been a great help for many complex projects, however, in the past pile foundation underpinning projects, there are more pile and beam underpinning programs of “two to one”, and there are fewer projects that use large-span pre-stressed underpinning beams to underpin group pile foundations under super-large diameter shield tunneling conditions, and most of the scholars have only studied the load transfer, foundation settlement, building deformation, etc. before and after the overall underpinning project [16-18]. For this kind of project, most scholars only studied the load transfer, foundation settlement and building deformation before and after the whole replacement. For the case of single-span pile foundation underpinning with multiple existing pile foundations, the different excision order of existing pile foundation means that the system conversion of pile foundation underpinning is carried out in a different way, and the impacts on the replacement structure as well as the pre-stressing tendons of the pile foundation underpinning are also different, so it is very necessary to study and propose a reasonable sequence of pile excision for this kind of project [19-20].

This paper takes Guangzhou Haizhu Wan shield tunneling project as the engineering background, systematically summarizes the key technology of super-large diameter shield large-span pile foundation underpinning construction, establishes the numerical simulation of the underpinning construction process, analyzes and carries out the research on different parameters such as jacking force, prestressing steel beam configuration and the sequence of the removal of the old piles, etc., and puts forward the reasonable pre-stressing steel beam underpinning construction according to the influence on the deformation of the super-structure and the stress and deformation of underpinning girder. According to its influence on the deformation of the superstructure, stress and deformation of the joist, a reasonable pre-stressing beam configuration and pile removal sequence at the bottom of the beam are proposed.

PROJECT OVERVIEW

Haizhu Wan Tunnel Project is the northern section of Guangzhou South Railway Station Fast Track, connecting the existing Dongxiaonan Elevated Road in the north and Nanpu Avenue in the south. Total length of the project line is 4348 m. Design speed of the main line is 60 km/h. It is mainly constructed by shield tunneling method, open cut method and bridge method. From north to south, the project crosses Nanzhou Road, Metro Line 2 and South Ring Elevated in turn through bridges, and then goes into the ground in the form of tunnels to cross the Pearl River Lijiao Waterway, Luoxi Island, Sanzhixiang Waterway and Nampo Boulevard. Tunneling length is 3463 m, of which the length of the Nam Chau cut section is 541 m, the length of the Nam Po cut section is 845 m. Shield

DOI 10.14311/CEJ.2025.02.0018

tunneling length is 2093 m in the west line and 2102 m in the east line, and the project schematic diagram is shown in Figure. 1.

Fig. 1 - Engineering diagram of Haizhu Wan Tunnel shield section

Design of the shield tunneling section is a 6 lane east-west two-lane tunnel with a single shield tunnel outside diameter is 14.5 m. It is constructed with two mud-water balanced shield machines, with a minimum flat surface radius of 1000 m and a maximum gradient of 4%. Among them, the west line is a Herrenknecht mud-water balanced shield tunneling machine, with a cutter diameter of 15.07 m, a cutter with a pressure change function, a panel type structure, and an opening rate of 30%. East line is a mud-water balanced shield tunneling machine of Iron Construction Heavy Industry, the diameter of the cutter plate is 15.07 m, the structure is star spoke type, and the opening rate is 35%. Figure 2 shows the east-west line shield tunneling cutter plate diagram.

(a) West line "Avenue Pioneer"

(b) East line " Route Pioneer "

Fig. 2 - Engineering diagram of Haizhu WanTunnel shield section

KEY AND DIFFICULT POINTS of THE PROJECT: SUPER-LARGE DIAMETER SHIELD TUNNELING THROUGH A PILE FOUNDATION

The shield tunneling penetrated the CNNC Business Building after 200 m, as shown in Figure 3. Underground of the building is a poured pile foundation, which is divided into two phases. Above ground is a 6-story reinforced concrete frame structure. Adjacent frame columns of the house have a span of 7.9 m and an average floor height of 3.9 m. The use of the house is for office purposes. A total of 88 piles (49 in the east line and 39 in the west line) were affected within the excavation.

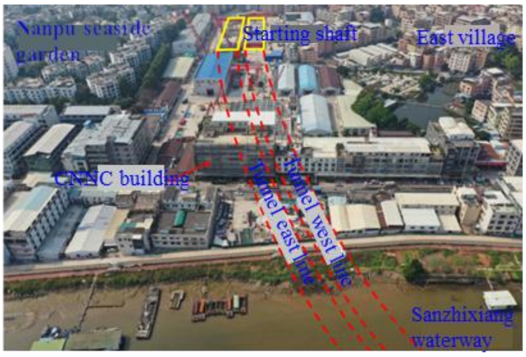

(a) Location map

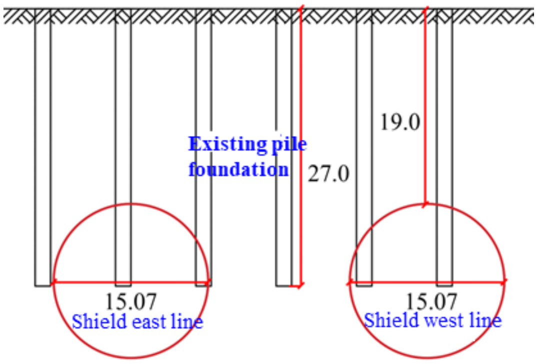

(b) Cross section diagram (unit: m)

Fig. 3 - General plan of pile foundation of shield crossing building

A total of 67 grinding piles (30 in the east line and 37 in the west line), which intruded into the tunnel for about 3 m to 9 m, were located within the excavation area. CNNC Phase I is A480 mm cast-in piles with a pile length of 23 m and 6 C16 steel cages in the upper 8 m. CNNC Phase II is A600 mm to A1500 mm cast-in piles with a pile length of 24 m. The steel cages are arranged in a longitudinal arrangement, with the main bars of C16,18 and 20. Below the free-standing foundations of Building 33 are A 300 tubular piles with a length of 23 m and a main reinforcement of C14. See Table 1 for details.

Tab. 1 - Commercial building pile foundation statistics table

Serial number	Diameter (mm)	Pile length (m)	Main reinforcement (mm)	Length of steel cage (m)	Depth of tunnel intrusion (m)	Root	Number of ground piles	Number of Eastern Lines	Number of western lines	Concrete grade
1	A480	23	16	8	3-4	80	37	10	27	C25
2	A600	27	18	27	8-9	11	5	5	0	C35
3	A800	27	20	27	8-9	4	4	2	2	C35
4	A1000	27	20	27	8-9	12	6	3	3	C35
5	A1200	27	20	27	8-9	2	0	0	0	C35
6	A1500	27	20	27	8-9	10	7	2	5	C35
7	A300	23	14	23	3-4	20	8	5	0	C25

DESIGN of PILE FOUNDATION UNDERPINNING

Underpinning structure consists of two parts, underpinning pile and underpinning beam, underpinning beam includes underpinning main beam and underpinning secondary beam. Micro steel pipe slurry pile is used for underpinning, the diameter of the hole is 250 mm, the steel pipe is made of Q235B steel with diameter of 220 mm, and the pile diameter is filled with pure cement slurry with strength class M30.Main girder span of underpinning are more than 18 m, is about 20.8 m, underpinning main girder cross-section width × height: 0.6 m ~ 0.8 m × 2.2 m, underpinning secondary girder cross-section width × height: 0.6 m × 2.2 m, underpinning girder and underpinning bearing platform adopt C40 grade concrete, reinforcement adopts HRB400 grade reinforcement and HRB300 grade reinforcing steel. Overall underpinning structure plan is shown in Figure 4 (expansion on the existing bearing platform to get a new bearing platform is called extension bearing platform).

DOI 10.14311/CEJ.2025.02.0018

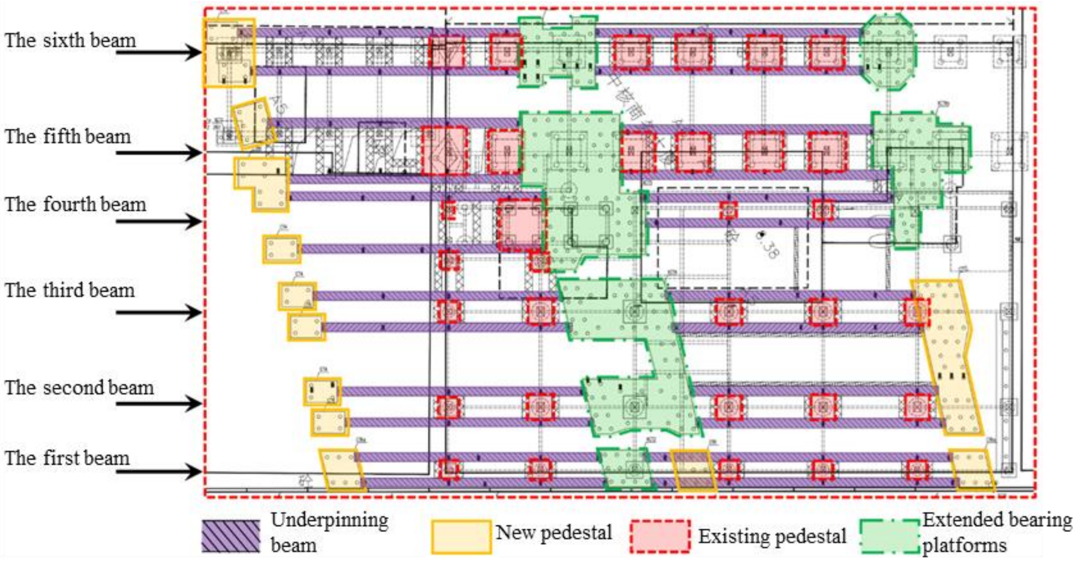

Fig. 4 - Building replacement structure plan

Between the underpinning structure and the underpinned structure is mainly designed for shear resistance: with the help of occlusion between the underpinning beam and the old bearing platform, interface treatment and reinforcement planting, the surface of the original bearing platform is chiselled to within the height of the underpinning beam, the diameter of the drilled holes is 14~42 mm, and the holes are cleaned up of dust and dirt using high compressed air or high-pressure water gun, and the processed rebar is inserted after putting in reinforcement adhesive, and then the reinforcing adhesive is cured. Pour the concrete of the solid section.

PILE FOUNDATION UNDERPINNING CONSTRUCTION

Underpinning Construction Points

This project is a super-large diameter shield tunneling conditions, the use of large-span prestressed double girder buttress buttressing method buttressing the pile foundation of the building group, different from the usual "two drag a" pile and girder structure buttressing, this project single-span buttress buttressing at least buttressing two existing pile foundation, buttressing a maximum of 16 existing pile foundation, the buttressing process of structural stability put forward higher requirements for the whole buttressing process. The maximum number of existing piles to be replaced is 16. Foundation underpinning construction process is shown in Figure 5.

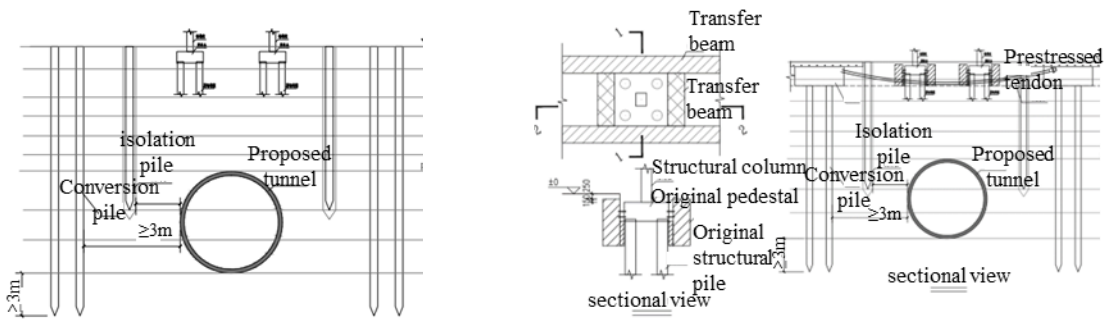

(a) Surrounding soil reinforcement, construction of conversion pile and isolation pile

(b) Construction of beam replacement and new cap, tensile prestress

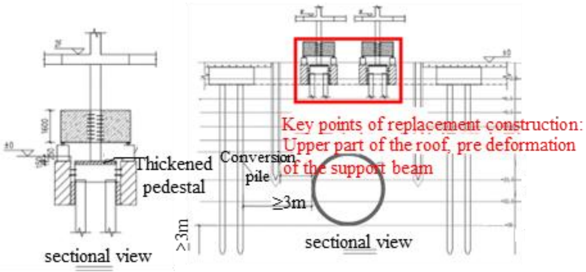

(c) Back to the top of the supporting beam pre-deformation, thickening the original cap

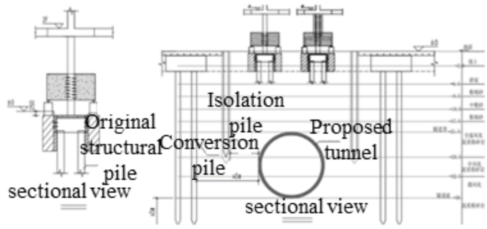

(d) The cap and the bearing beam are sealed twice

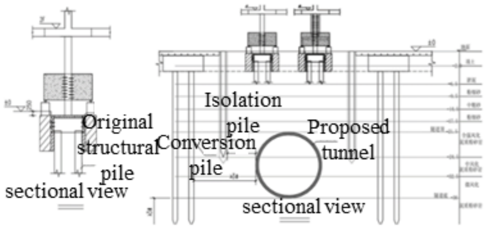

(e) Remove bracket

Fig. 5 - Foundation replacement construction process

Implementation of Underpinning Project

In this project, the active underpinning method is adopted, which needs to set up temporary reaction frame under the first floor columns before connecting the underpinning beams with the old bearing platforms, and use the underpinning beams to go back to the top of the upper part of the main body, so as to make the deformation of the underpinning beams stabilized, and then carry out the construction of the connection between the underpinning beams and the old bearing platforms, in which the most important construction process is to go back to the top of the upper part of the body by means of the following methods:

(1) In this building underpinning reconstruction construction, the jacking synchronization can control the insufficient bending deformation hazard of the superstructure in the building underpinning reconstruction construction. After the reinforced concrete pre-roof crossbeam reaches the design strength, four jacks with load-bearing capacity not less than 150 T are arranged between the corners of the pre-roof crossbeam and the joist beams, and temporary steel supports are to be installed on both sides of the jacks, as shown in Figure 6.

(2) Sequence of back jacking: All topping operations were carried out after the prestressing was tensioned and the design strength was reached. Topping back is done according to the location of prestressing beams from south to north, in batches of 6 sub-synchronized topping back. As shown in Figure 7.

(3) Back jacking process: construction preparation → pre-placement of jack position → installation of temporary steel support → installation of monitoring equipment → test jacking → formal jacking → completion of the first jacking → graded loading jacking to the design pressure (simultaneous monitoring).

(4) Points to back jacking: ① Before jacking, calculate the weight of each jacking point; calculate the amount of arching oil at each point; test the top before jacking. Pay attention to the top of the test top and the speed of each top, not enough to raise more oil can be divided. Rise too fast to tighten the oil valve. Trial top, before synchronized jacking. ② Synchronized pressurized jacking, jacking back to the bracket, underpinning back to the top of the load using the principle of graded loading, a total of ten levels of loading, each level of load increase of 10% of the upper limit value of the jack, cannot be loaded to the maximum value at a time. Each level of loading needs to be

maintained for 10 min, such as structural stability before adding secondary loads. ③ Closely monitor the generation and development of cracks in the underpinning in the process of roof return, and stop loading immediately when the maximum crack width is more than 0.1 mm. ④ Underpinning back jacking force requirements, that is, the maximum back jacking force at each original structural column cannot exceed the column underpinning force, the column underpinning force measurements provided by the design institute are shown in Figure 8.⑤ Observe that the change in settlement of the pile foundation and the deformation of the superstructure remain unchanged before proceeding with the second pouring of the conversion beam to connect the original structure at the bearing platform.

Fig. 6 - Top return diagram

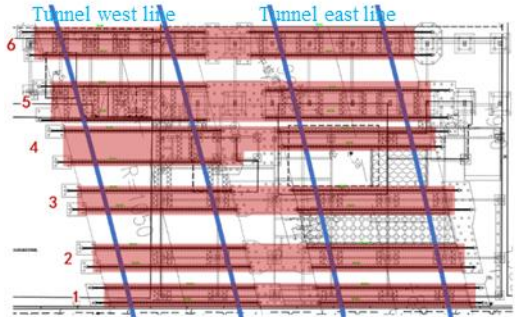

Fig. 7 - Topping sequence

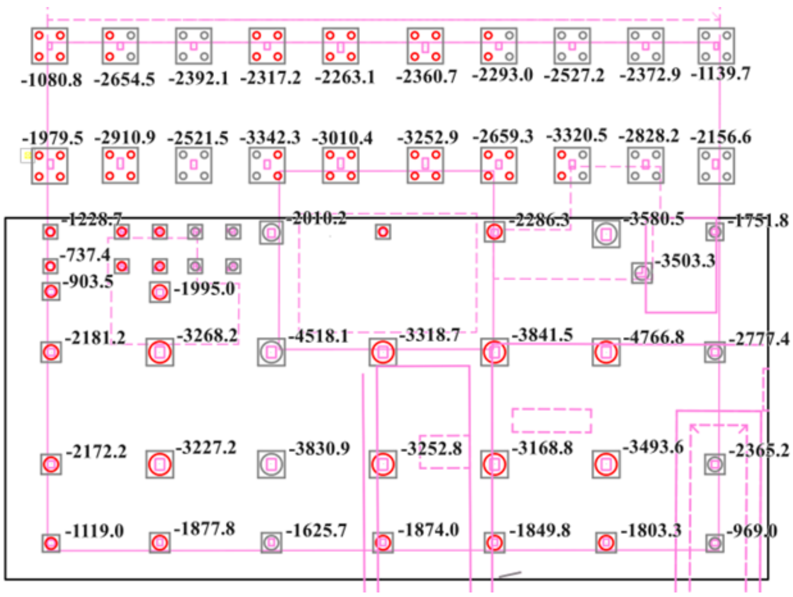

Fig. 8 - Building column base force (unit: kN)

Demolition of Existing Pile Foundations

Original pile removal adopts static cutting method to break the pile, and the removal should be done symmetrically on both sides of the tunnel at the same time. During the demolition process, the original structural columns, underpinning beams, and bearing platform settlement and crack monitoring must be strictly monitored. Once the structure produces cracks or there are any signs of instability, immediately stop construction and organize the evacuation of site personnel. After feedback to the design unit to analyze the causes and forces, new measures will be formulated before entering the construction site.

(1) Demolition process

DOI 10.14311/CEJ.2025.02.0018

①On-site review of construction plan data: Measurement and determination of cutting position, calculation of deformation settlement; ② Control settlement observation points: Calculate and discipline the arrangement of settlement observation points; ③ Calculate cutting data; calculate data such as cutting position and cutting depth; ④ Installation of cutting machinery: Installation of cutting machinery in accordance with drawings or programs; ⑤ Cutting and real-time monitoring of deformation data: Start the cutting operation, gradually release the structural load of the column, and monitor the deformation data in real time; ⑥ Lifting and removing concrete test blocks; ⑦ Structural settlement observation: an important monitoring measure to ensure structural safety.

(2) Existing pile removal sequence

In the original pile excision, although through the jacking back jacking the upper part of the prestressing beam and new pile foundation pre-stressing, so that the original bearing column force system converted to the new underpinning system, theoretically from any position to start excision of the original pile will not have an impact on the existing building itself, but the reality is often do not jacking up the existing pile foundation after the "zero internal force" in order to further ensure the safety of the original pile excision, this project in accordance with the principle of "first dense area then non-dense area, first the middle and then both sides, jump pile excision". In order to further ensure the safety of original pile removal, this project is carried out in accordance with the principle of "first dense area then non-dense area, first the middle and then both sides, jump pile removal". The sequence diagram is shown in Figure 9.

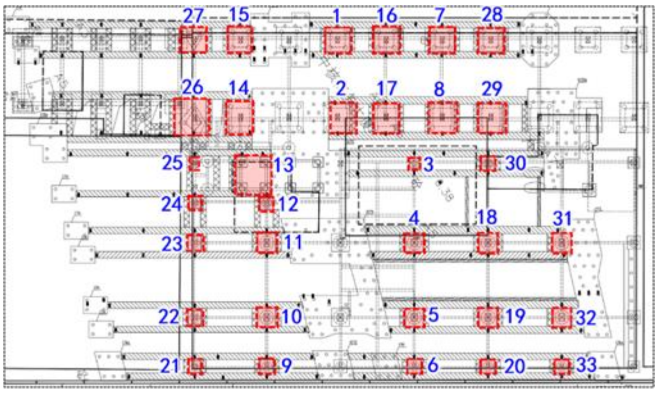

Fig. 9 - Old pile removal sequence diagram

(3) Construction without support and replacement

1. Excavate 1.5 m downwards at the original bearing platform and install the rope saw cutting equipment.
2. The first knife from left to right cutting to pile cross-section of about 75%, due to the structure of the pile by the cutting machine cutting surface gradually increased, pile force area gradually reduced, when the pile force surface is less than 25% or so, the pile vertical force eccentricity, this time, the pile and the conversion beam superstructure will be released tiny downward deflection of the force, resulting in the corded saw jammed locks, and then converted to cut the second knife;
3. Second cut is made at an interval of 150 mm between the top and bottom of the pile, and the second cut is made from right to left to about 95% of the pile cross-section, and the saw is locked to convert the cutting seam. The third cut is made at an interval of 150 mm between the top and bottom, and the third cut is made from right to left to cut through the whole pile section. Underpinning pile and superstructure stripping, cut off the pile in pieces 1 m. Pile foundation underpinning is basically completed.

ANALYSIS of SITE MONITORING for PILE FOUNDATION UNDERPINNING WORKS

Monitoring Arrangement

1. **Settlement monitoring arrangement for existing buildings**

Ninety-one settlement monitoring points were deployed for this project. Settlement observation layout is shown in Figure 10.

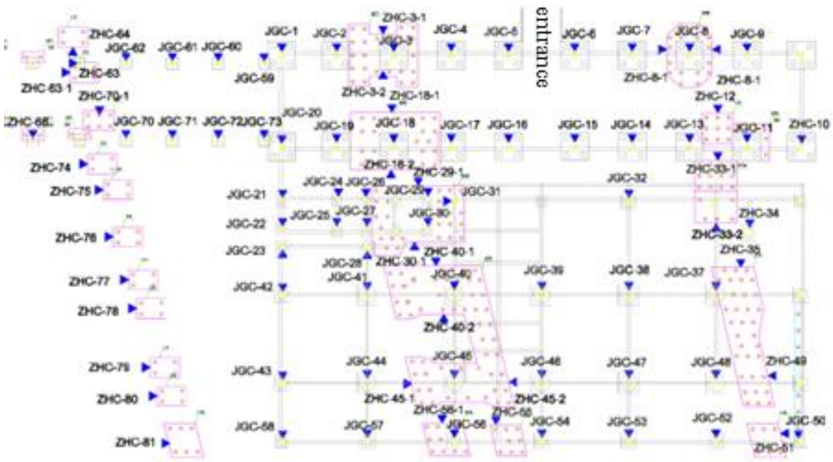

Fig. 10 - Settlement observation point layout

Construction monitoring activities commence from the initiation of pile foundation work. During the construction phase, observations of underpinning beam construction and underground tunnel work are conducted twice daily. For the remainder of the construction period, these observations are reduced to once per day. Special monitoring is required for the following events: once each during the suspension and resumption of construction activities, once monthly during periods of work stoppage, three times per month during the first two months of the operational phase, once per month from the third to the sixth month, once every two months from the sixth to the twelfth month, two to three times per year in the second year, and once per year from the third year onward until the construction reaches a stable state.

2. **Stress monitoring of underpinning beams**

There are 135 stress observation points laid out for this project. Stress monitoring layout is shown in Figure 11.

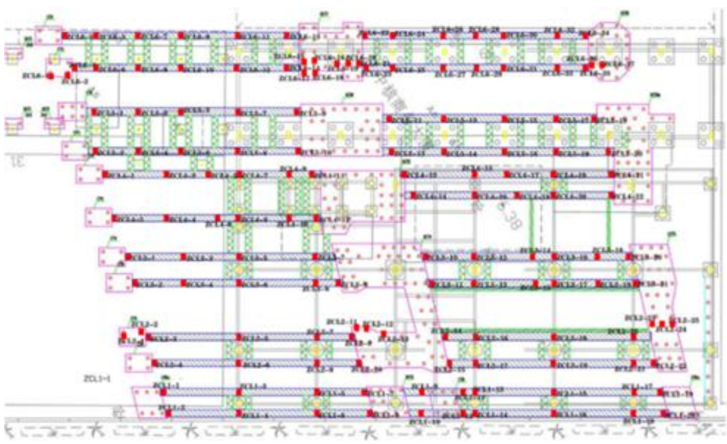

Fig. 11 - Layout of stress monitoring points

DOI 10.14311/CEJ.2025.02.0018

3. Tilt monitoring of existing buildings

There are 18 building tilt points laid out for this project. Building tilt point layout is shown in Figure 12.

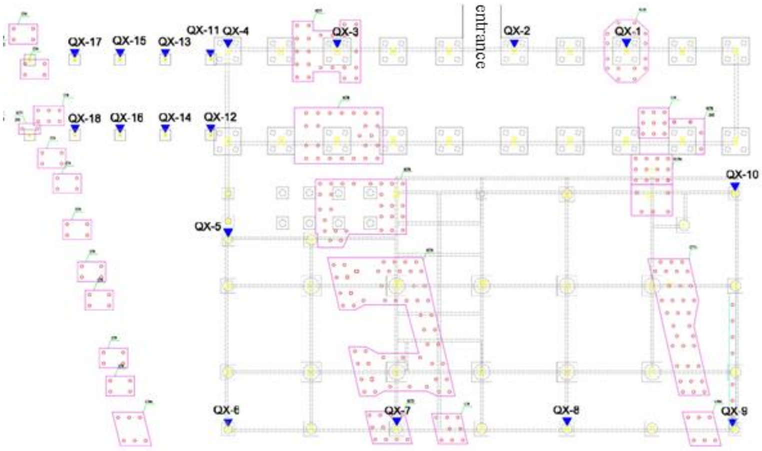

Fig. 12 - Building tilt monitoring layout

4. Surface crack monitoring

There are several crack monitoring points for this project, and crack monitoring shall include crack location, orientation, length, width, and changes. For crack width monitoring, steel nails can be embedded on both sides of the crack, and the distance of the nails can be used to observe whether the crack is further developed. It is also important to focus on the areas where cracks are likely to occur. Timely detection of new cracks, good records and observation marking tracking observation, through the existing cracks on the surface or due to engineering construction cracks to carry out width monitoring, to assess the degree of impact of engineering construction on the surrounding safety and normal use.

Analysis of Settlement Monitoring Data for Existing Buildings

Monitoring point settlement values were selected for key nodes at the end of the joist construction, the end of the back jacking upper construction, and the end of the old pile removal construction during the entire underpinning construction process, as shown in Figure 13.

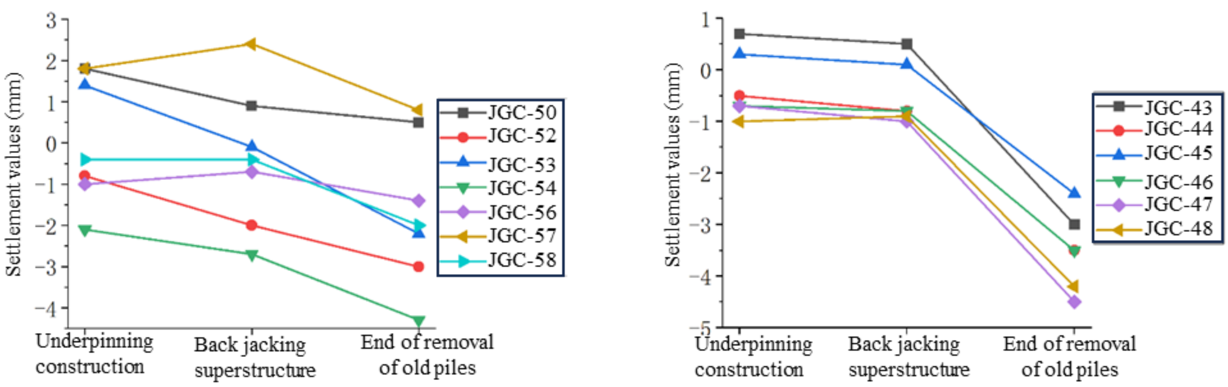

(a)The first beam *(b)The second beam*

DOI 10.14311/CEJ.2025.02.0018

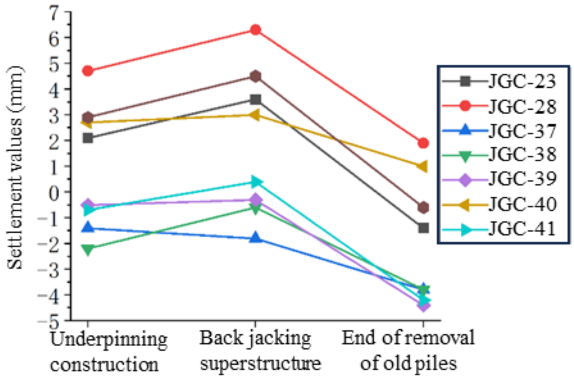

(c)The third beam

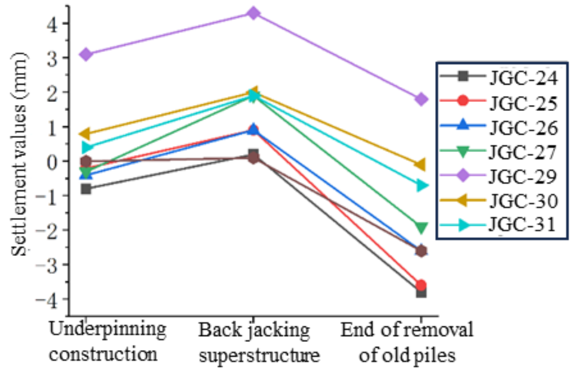

(d)The fourth beam

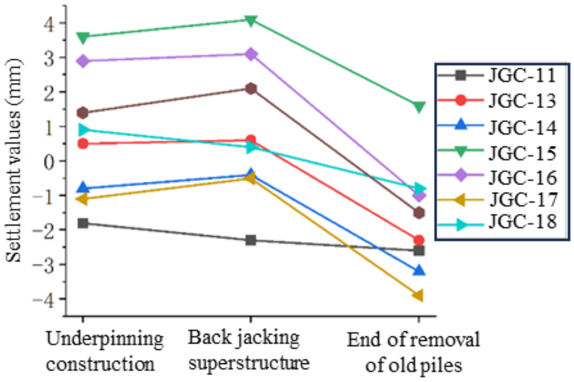

(e)The fifth beam

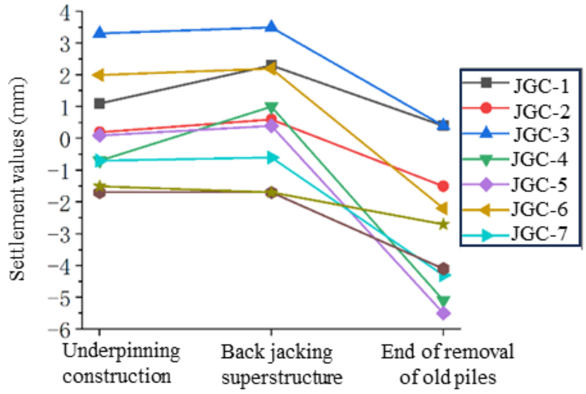

(f)The sixth beam

Fig. 13 - Settlement value of building monitoring point

Maximum deformation values of the six underpinning beams at the critical nodes of construction and maximum cumulative deformation values are shown in Table 2.

Tab. 2 - Maximum change value of settlement and maximum cumulative change value

Deformation value	Maximum deformation value		Maximum cumulative deformation value	
	Point number	Deformation value（mm）	Point number	Deformation value（mm）
The first beam	JGC-53	-2.1	JGC-54	-4.3
The second beam	JGC-44	-3.5	JGC-46	-3.8
The third beam	JGC-42	-5.1	JGC-28	6.3
The fourth beam	JGC-25	-4.5	JGC-37	4.3
The fifth beam	JGC-19	-3.6	JGC-15	4.1
The sixth beam	JGC-4	-6.1	JGC-4	-6.1

From the figure, it can be seen that after back jacking the upper part and making the predeformation construction of the underpinning beams finished, most of the measuring point elevations were basically unchanged or had a change of about 1 mm; after removing the old piles, all the measuring point elevations decreased, but the changes of the measuring points on each beam were roughly the same, and most of the remaining measuring points were between 2~4 mm except for some measuring points, and there was no uneven settlement of the CNA Building underpinning the whole period. All the deformation values are less than the warning value ±10 mm warning value.

Tilt Monitoring of Existing Buildings

Monitoring point tilt values were selected for key nodes during the entire underpinning construction process, the end of the joist construction, the end of the back jacking upper construction, and the end of the old pile removal construction, as shown in Figure 14.

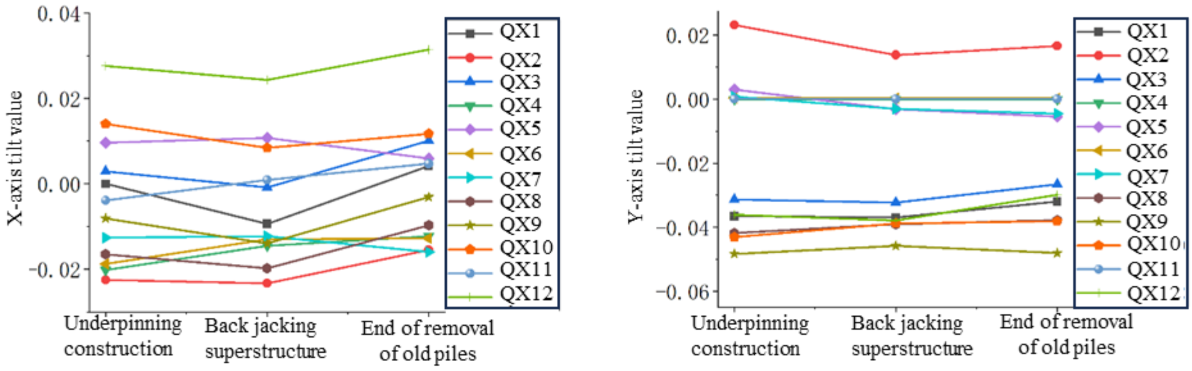

(a) X-axis (b) Y-axis

Fig. 14 - Inclination value of building monitoring site

Maximum change in tilt and maximum cumulative change in tilt at the nuclear building measurement points in the critical nodes of construction are shown in Table 3.

Tab. 3 - Maximum change value of tilt and maximum cumulative change value

Deformation value	Maximum change value		Maximum cumulative change value	
	Point number	Change value (°)	Point number	Change value (°)
X-axis	QX-1	0.0136	QX-12	0.0314
Y-axis	QX-17	0.0256	QX-9	-0.0481

Maximum change in X-axis and maximum cumulative change in all measurement points is less than ±0.2292° warning value, maximum change in Y-axis and maximum cumulative change in Y-axis is less than ±0.2865° warning value.

Stress-Strain Monitoring of Underpinning Beams

Underpinning beam construction was completed to the end of the old pile removal construction, and the measurement points are shown in Figure 15.

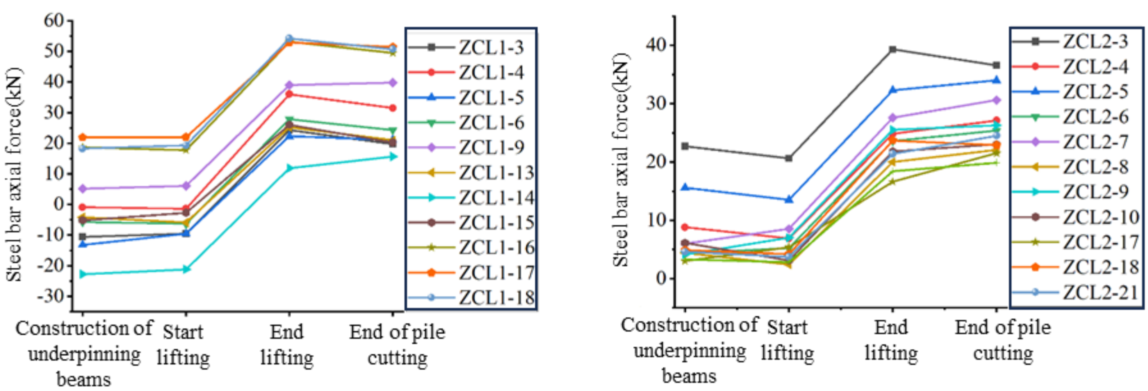

(a)The first beam (b)The second beam

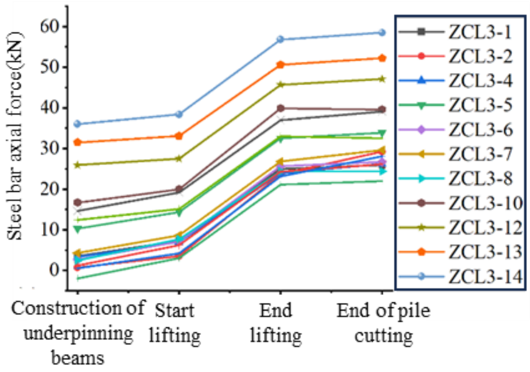

(c)The third beam

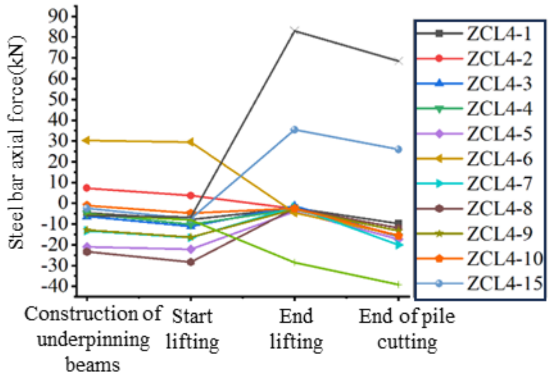

(d)The fourth beam

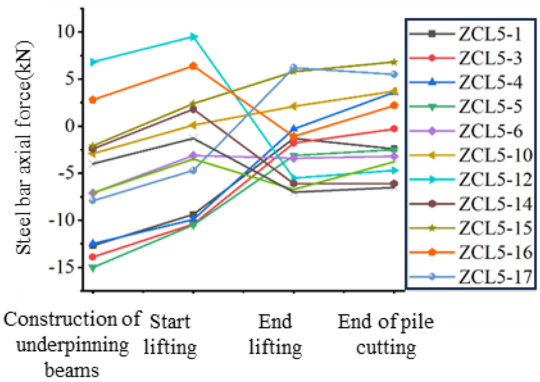

(e)The fifth beam

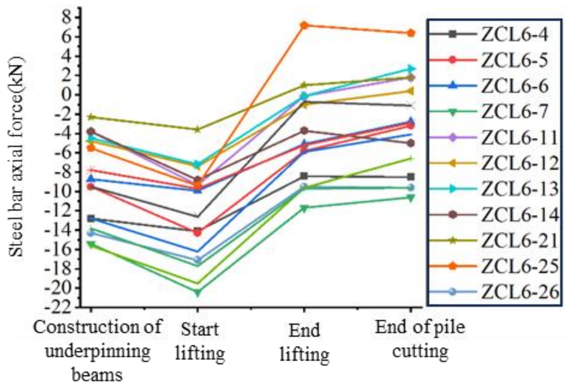

(f)The sixth beam

Fig. 15 - The monitoring value of stress and strain measuring point of underpinning beam

For each beam, the support axial force calculated from the measured values of the stress-strain monitoring points of the beams remained basically unchanged from the end of the construction of the beams to the end of underpinning jacking. During the jacking process, the deformation of the beams caused the measured values to undergo a large change, and after the end of jacking to the end of the pile cut-off, there was basically no change in the support axial force calculated from the measured values. The maximum values of cumulative changes in axial force of each beam are shown in Table 4.

Tab. 4 - Change in tension/pressure of the underpinning beam

Underpinning beam	Cumulative maximum change value	
	Point number	Change value（kN）
The first beam	ZCL1-18	65.3
The second beam	ZCL2-3	39.3
The third beam	ZCL3-14	59.1
The fourth beam	ZCL4-20	83.2
The fifth beam	ZCL5-20	-16.5
The sixth beam	ZCL6-7	-20.4

Maximum value of cumulative change was measured at the fourth beam, ZCL4-20, with a maximum value of 83.2 kN. Cumulative change of tension/pressure at all stress-strain measurement points was much less than the ±687 kN warning value.

From the results of settlement monitoring, tilt monitoring, and stress-strain monitoring of the beams underpinning, the construction results of the pile foundation underpinning of CNNC Building by the double beam underpinning method are good.

CONCLUSIONS

In this paper, for the super-large diameter shield tunneling conditions, large-span prestressed double-beam buttress replacement of pile foundations underpinning buildings, unlike the usual “two-tow-one” pile-beam structural buttressing, the single-span buttress beam of this project is at least buttressing two existing pile foundations, and at most buttressing 16 existing pile foundations, which puts forward a higher requirement for the structural stability in the whole process of buttressing.

(1) Settlement monitoring data, tilt monitoring data, and stress-strain monitoring data of the underpinning beams for the existing building were carried out and collected on site during the underpinning construction. Subsidence of the CNNC building did not show large settlement before and after several construction phases, and the maximum deformation value was 6.3 mm.

(2) Maximum change in X-axis and maximum cumulative change in all measurement points is less than ±0.2292° warning value, maximum change in Y-axis and maximum cumulative change in Y-axis is less than ±0.2865° warning value. There is no overall uneven settlement, and all deformation values are less than the warning value ±10 mm warning value. For the tilt monitoring data, the tilt values of X-axis and Y-axis are less than the warning value.

(3) Maximum value of cumulative change was measured at the fourth beam, ZCL4-20, with a maximum value of 83.2 kN. Cumulative change of tension/pressure at all stress-strain measurement points was much less than the ±687 kN warning value. Underpinning beam stress-strain monitoring, the cumulative change of tension/pressure calculated from all stress-strain measurement points is much smaller than the warning value. From the results of settlement monitoring, tilt monitoring, and stress-strain monitoring of the beams, the construction result of using double-beam underpinning method to underpin the pile foundation of CNNC Building is good.

REFERENCE

[1] Xia H, Du G, Cai J, et al. Comparison between bearing characteristics of pervious concrete pile composite foundations with different replacement ratios[J]. Geohazard Mechanics, 2023, 1(3): 255-261.

[2] Yang Q, Li Z, Li L J, et al. Comprehensive Experimental Investigation of Improved Clay Ground by Sand Compaction Pile Varying from Low to High Area Replacement Ratios[J]. International Journal of Geomechanics, 2023, 23(9): 04023155.

[3] Yan L, Gou X, Guo Z, et al. Experimental and numerical investigation on pile foundation underpinning structure system in urban overpass [J]. Materials, 2023, 16(19): 6576.

[4] Randolph M F. Science and empiricism in pile foundation design [J]. Géotechnique, 2003, 53(10): 847-875.

[5] Cheng X, Chen W, Jing W, et al. Influence of area replacement ratio on settlement and stability of oil storage tank composite foundation treated with compaction piles [J]. Electronic Journal of Geotechnical Engineering, 2015, 20(11): 4665-4678.

[6] Polańska B, Rainer J. Rigid inclusion ground improvements as an alternative to pile foundation[C]//IOP Conference Series: Materials Science and Engineering. IOP Publishing, 2020, 869(5): 052080.

[7] Zhang M, Zhang X. A field experimental study of composite foundation with CFG pile+ vibro-replacement stone column pile in liquefaction area[C]//2017 2nd International Symposium on Advances in Electrical, Electronics and Computer Engineering (ISAEECE 2017). Atlantis Press, 2017: 75-78.

[8] Zhang C, Liu S, Zhang D, et al. A modified equal-strain solution for consolidation behavior of composite foundation reinforced by precast concrete piles improved with cement-treated soil[J]. Computers and Geotechnics, 2022, 150: 104905.

[9] Kim S, Whang S W, Kim S. Pile foundation design through the increased bearing capacity of extended end pile[J]. Journal of Asian Architecture and Building Engineering, 2017, 16(2): 395-402.

[10] Ng C W W, Gunawan A, Shi C, et al. Centrifuge modelling of displacement and replacement energy piles constructed in saturated sand: a comparative study [J]. Géotechnique Letters, 2016, 6(1): 34-38.

[11] Cheng Z, Li S, Wang J. Controlled rocking pile foundation system with replaceable bar fuses for seismic resilience [J]. Earthquake Engineering and Engineering Vibration, 2022, 21(3): 683-696.

[12] Yang Z, Shen F, Yin P, et al. A new approach for improving lateral performance of pile foundations in seasonally frozen regions [J]. Cold Regions Science and Technology, 2023, 207: 103778.

[13] Tian X, Song Z, Huaizheng W, et al. Deformation and mechanical characteristics of tunnel-slope systems with existing anti-slide piles under the replacement structure of pile-wall [J]. Tunnelling and Underground Space Technology, 2024, 153: 105995.

[14] Yang W, Ni P, Chen Z, et al. Consolidation analysis of composite ground improved by granular piles with a high replacement ratio considering overlapping smear zones[J]. Computers and Geotechnics, 2023, 162: 105636.

[15] Zhang C, Zhao Y, Zhang Z, et al. Case study of underground shield tunnels in interchange piles foundation underpinning construction [J]. Applied Sciences, 2021, 11(4): 1611.

[16] Xiao D, Jiang G L, Liao D, et al. Influence of cement-fly ash-gravel pile-supported approach embankment on abutment piles in soft ground [J]. Journal of Rock Mechanics and Geotechnical Engineering, 2018, 10(5): 977-985.

[17] Tehrani F S, Nguyen P, Brinkgreve R B J, et al. Comparison of press-replace method and material point method for analysis of jacked piles [J]. Computers and Geotechnics, 2016, 78: 38-53.

[18] Russo G, Marone G, Di Girolamo L. Hybrid energy piles as a smart and sustainable foundation [J]. Journal of Human, Earth, and Future, 2021, 2(3): 306-322.

[19] Hokmabadi A S, Fatahi B, Samali B. Assessment of soil–pile–structure interaction influencing seismic response of mid-rise buildings sitting on floating pile foundations[J]. Computers and Geotechnics, 2014, 55: 172-186.

[20] Hokmabadi A S, Fatahi B, Samali B. Assessment of soil–pile–structure interaction influencing seismic response of mid-rise buildings sitting on floating pile foundations[J]. Computers and Geotechnics, 2014, 55: 172-186.

CIVIL ENGINEERING JOURNAL

Article no. 19

THE CIVIL ENGINEERING JOURNAL 2-2025

CASE STUDY: ROCKFALL MITIGATION AT A HIGHWAY SLOPE IN SUICHUAN COUNTY, CHINA

Shuisheng Yang[1], Shalu Huang[1], Zhibin Tian[1] and Wanhao Yu[2]

1. *Jiangxi Provincial Highway Research and Design Institute Co., Ltd, Nanchang, 330002, Jiangxi, China*
2. *School of Civil Engineering, Sichuan University of Science & Engineering, Zigong, 643000, Sichuan, China; 1203945563@qq.com*

Received:	*02.12.2024*
Received in revised form:	*15.04.2025*
Accepted:	*17.06.2025*

ABSTRACT

Conducting proper stability analysis of potential rockfall hazards and implementing appropriate prevention measures are crucial for ensuring highway safety. This study investigated a rock slope along the G105 National Highway in Suichuan, Jiangxi, China. The stability of the slope was evaluated through a combination of theoretical analysis and field investigation. The slope is stable under normal conditions but transitions to a state of partial instability or instability during extreme weather events or seismic activities, necessitating protective measures. To assess the risk of rockfall, a Rock-fally simulation was conducted. The deposition distribution, kinetic energy, translational velocity, and bounce height of rocks with varying volumes during the fall were simulated. The kinetic energy of rockfall is primarily influenced by the volume of the rock mass, while translational velocity, bounce height, and deposition distribution are closely associated with the cross-sectional conditions. Based on the evaluation results, appropriate reinforcement measures were selected, and the slope was monitored using InSAR and automatic monitoring technologies. The combination of drone scanning, modeling, automated monitoring techniques, and InSAR technology effectively reduces uncertainties in risk assessment. Based on the evaluation results, the application of active energy-absorbing protection nets and other preventive measures were proposed, demonstrating a satisfactory protective effect. The case study will provide valuable engineering guidance for rockfall analysis and prevention on highway slopes.

KEYWORDS

Rockfall, Slope monitoring, InSAR, Prevention engineering

INTRODUCTION

In the densely populated regions, where land resources are scarce, buildings and pathways were constructed along the mountains to maximize the utilization of the land. Nevertheless, the utilization of the mountain area endanger the stability of the slopes, of which the susceptibility to collapse and rockfall incidents is high [1]. This issue is particularly evident along the G105 National Highway, especially in the Suichuan segment, Jiangxi, China. Which is characterized by a complex geological environment and unstable slopes. These slopes, especially in areas with high gradients and loose rock formations, are highly prone to rockfalls and landslides. Additionally, natural factors such as rainfall and seismic events can trigger further instability, posing a significant threat to traffic safety. The complexities are inextricably of rock fall linked to factors such as the site-specific characterisitcs of rockfalls, a lack of history rockfall datasets, and the difficulties of quantifying rockfall stability in diverse risk-coupling scenarios [2-5].

In previous years, rockfall research was limited by the limitations of technology, and rockfall prevention was predominantly based on experience and empirical approaches. Practices such as retaining walls, drainage systems and slope reinforcement have been used to increase the stability of rocky slopes. Furthermore, rock removal and periodic slope inspections were essential to promptly identify potential risks. Later, empirical approaches proved effective in initial slope assessments. However, relying solely on these methods to prevent collapses and rockfalls, reliance has often resulted in suboptimal results. The main uncertainties are that predicting rock displacement trajectories at different locations is difficult, which is a crucial factor in assessing rockfall hazards [6-8]. Therefore, scholars focus on computational modeling and introduced numerical simulation methods to evaluate the slope stability and predict disaster occurrences. The objective was to predict high-risk zones and support decision-making in implementing protective measures. Currently, the most used software for rockfall simulation is Rocfall. It conducts analyses involving translational velocity, rebound height, kinetic energy, and debris distribution caused by rockfalls [9-11].

Numerical simulation methods overcome the disadvantages of empirical approaches. However, these methodologies are not immune to inherent limitations that significantly affect the accuracy and reliability of simulation results. The effectiveness of the numerical model depends on the quality of the input data. Building a reliable rockfall model requires an extensive compilation of geological parameters and comprehensive monitoring data. However, the spatial and temporal variability of geological factors presents challenges in achieving forecast accuracy. Rockfall monitoring is typically required, which includes Global Navigation Satellite Systems (GNSS) or inclinometers. Automatic monitoring methods can be used in tracking movements of individual blocks and offer a high frequency of data acquisition. However, the application is limited to the specific points on the rock slope, meaning difficult to obtain the comprehensive capture of slope deformative characteristics [12]. Consequently, critical data relating to regions of unstable slopes may be omitted during monitoring, resulting in deficiencies in the numerical model's slope assessment. The latest technology in slope monitoring is Interferometric Synthetic Aperture Radar (InSAR). Compared to conventional methods, InSAR offers advantages such as improved spatial resolution, resilience to interference, broad coverage and monitoring capabilities in all weather conditions [13]. With continuous advancements and practical applications, InSAR has demonstrated advantages in monitoring rockfalls, landslides, and catastrophic scenarios. However, InSAR also has limitations, for example, its spatial resolution may be inadequate to accurately detect small rockfalls or localized deformations. Furthermore, the specifics of the terrain and dense vegetation can obstruct the visibility of slopes, increasing the challenges faced in monitoring rockfall [14-16]. In summary, numerical simulation techniques have been significantly improved, as an alternative method to empirical methods. However, the uncertainties of both the numerical simulation and the empirical method largely arise from the uncertainties inherent in monitoring data [17]. Improving the reliability, comprehensiveness and effectiveness of monitoring data in the context of rockfall management will now be useful for assessing the stability of rock slope.

In light of these considerations, this study focuses on a rocky slope along National Road G105 in Suichuan County and evaluates automated monitoring techniques together with InSAR technology. The study combines UAV remote sensing, 3D modeling, automated monitoring and InSAR, forming a basis for slope stability surveillance. Data collection is used to analyze rockfall incidents across multiple rock volumes and profiles, examining movement trajectories, velocities, rebound heights, kinetic energies, and debris distribution. It proposes several fortification strategies, including active and passive networks, shelters, and hazard reduction methods [18-19]. Through InSAR and automated monitoring, a comprehensive surveillance regime is established for the rockfall-prone region, offering continuous all- weather data for early warnings. These preventative measures have proven to be effective in mitigating slope collapses and rockfall incidents, providing valuable engineering insights for rockfall prevention.

OVERVIEW OF THE ROCK SLOPE

The rocky slope is located next to the G105 National Highway in Suichuan County, Jiangxi Province. The rock formation on the right side of the highway appears as a steep cliff, indicating the potential for rockfall. The geological hazard associated with this slope is classified as high-level rockfall, located on the steep cliff to the right of the highway. Through a comprehensive field investigation, three specific regions that present an elevated rockfall risk were pinpointed and denoted as WY1, WY2, and the concave cavity Figure 1 and Table 1 illustrate the location and attributes of the rock mass at this location.

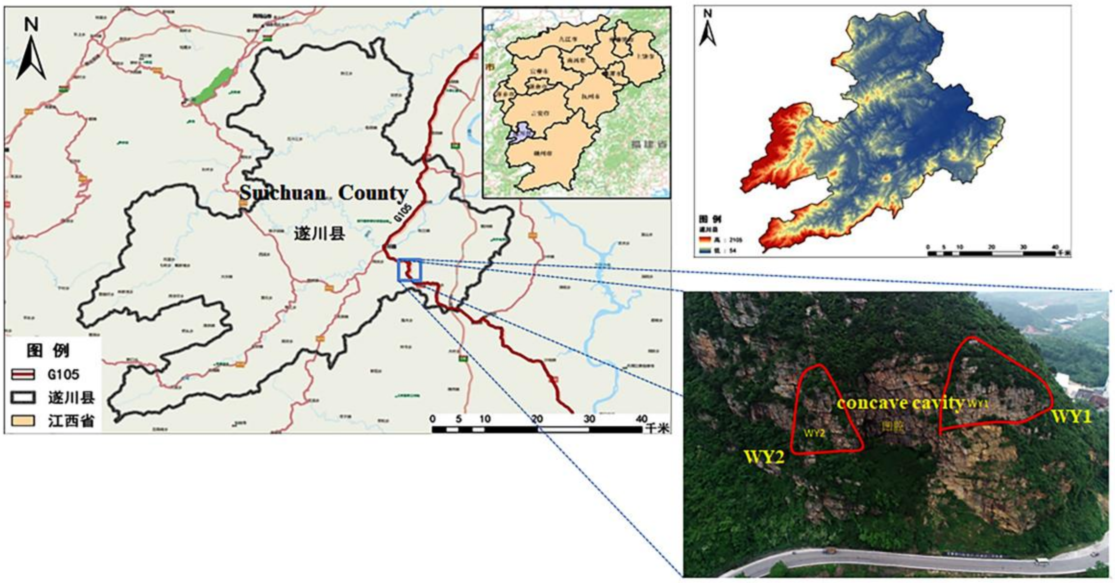

Fig. 1 - Location and illustration of the rockfall

Tab. 1 - Characteristics of regional rock masses

Characterization	WY1	WY2	Concave cavity
Height of the rock mass on the right	100-120m	150-170m	130-150m
Slope bottom features	The rock mass at the bottom of the cliff remains relatively intact with a higher vegetation cover, and scattered rock debris	The rock mass at the bottom of the cliff remains relatively intact with a higher vegetation cover, and scattered rock debris	Slope 50-65°, with a high vegetation cover and relatively intact rock mass, along with visible accumulations of rock debris.
Characteristics of rock mass cracks	70m from the ground, vertically extended, yielding 74°∠61°, about 30m in length and 50-80cm in width, with plant roots	70-75m from the ground, vertically extended, in line with WY1, length about 30m, width about 50-100cm	No obvious cracks were found, but gravity produced localized chipping and falling blocks

Dimensions of the bottom of the rock mass	Width about 36m, height about 30-35m, thickness about 7-10m, volume about 7560m^3	Width about 30m, height about 35-38m, thickness about 7.5m, volume about 3250m^3	

ROCK MASS STABILITY ANALYSIS

Qualitative Analysis

Based on field investigations and stereographic projection analysis, the rock mass structure in the study area is primarily controlled by the original bedding planes and two sets of high-angle joints (J1: 143°∠76°, J2: 25°∠88°). The bedding planes, with an orientation of 195°∠2°, form a typical counter-slope relationship with the slope surface (74°∠61°), and their dip angle is significantly lower than the critical friction angle required for sliding (typically >15°), effectively excluding the possibility of bedding-parallel slip.

In contrast, the two joint sets (J1 and J2) are densely developed (joint trace frequency > 5/m) and exhibit strong geometric compatibility with the slope surface. The angles between their strike directions and the slope orientation are approximately 69° and 49°, respectively, while their dip angles (76°–88°) are nearly parallel to the slope inclination (61°). This structural alignment facilitates tensile stress concentration along the joint planes under external loading, significantly reducing the tensile strength of the rock mass, and thereby promoting tensile failure along the joints.

Stability Calculation

According to site investigation, rockfall on this slope aligns with rotational landslide collapse. The center of gravity of the rock masses in WY1 and WY2 is positioned within the pivot point. Equation (1) is used for calculation when the stability is controlled by the tensile strength of the rear rock mass and the center of gravity of the hazardous rock mass lies within the overturning point. This equation is derived from the overturning stability calculation formula for hazardous rock slopes specified in the specification [20].

$$F=\frac{\frac{1}{2}f_{lk}\cdot\frac{H-h}{\sin\beta}\left(\frac{2}{3}\frac{(H-h)}{\sin\beta}+\frac{b}{\cos\alpha}\cos(\beta-\alpha)\right)+W\cdot a}{Q.h_0+V\left(\frac{H-h}{\sin\beta}+\frac{h_w}{3\sin\beta}+\frac{b}{\cos\alpha}\cos(\beta-\alpha)\right)} \tag{1}$$

Here's the meanings of the parameters:

f_{lk}--- the standard tensile strength of the unstable rock mass (kPa), determined by multiplying the standard tensile strength of the rock by a reduction coefficient of 0.40;

h--- Depth of the rear edge crack (m);

h_w--- Water filling height of the rear edge crack (m);

h_0--- Vertical distance from center of gravity to tipping point (m);

H---Vertical distance from the upper end of the rear edge crack to the lower end of the unpenetrated segment (m);

W--- Self-weight of rock mass;

Q--- Seismic force(kN/m);

V--- Pressure of fractured water (kN/m);

a---Horizontal distance from the barycenter of mass of the unstable rock mass to the overturning point (m);

b---Horizontal distance from the lower end of the unpenetrated segment of the rear edge crack to the overturning point (m);

α---Angle (°) between the contact surface of the unstable rock mass and the foundation. It takes a positive value when the rock mass is outwardly inclined and a negative value when inwardly inclined;

β---Angle (°) of the rear edge crack.

The inherent density of the rock is assumed to be 24 kN/m³, while the saturated density is set at 24.5 kN/m³. The tensile strength is estimated to be 400 kPa. Three distinct scenarios are considered for the calculations: the existing condition, the rainstorm condition and the seismic condition. For the existing condition, the calculations are based on the state observed during the investigation period, accounting only for the self-weight of the rock mass. In rainstorm conditions, the calculations take into account both the self-weight of the rock mass and the hydrostatic pressure within the fissures induced by heavy rainfall. This pressure, calculated using the hydrostatic pressure formula, is applied to the fracture surfaces and incorporated into the driving force generated by the self-weight of rock mass to assess the potential for sliding under heavy rainfall. Duri this scenario, the water level is presumed to range from 1/3 to 1/2 of the fissure depth. In the seismic condition, the calculations encompass the self-weight of the rock mass, seismic forces, and the influence of fissure water pressure. For seismic conditions, seismic inertial forces in both horizontal and vertical directions—derived from the product of the weight of rock mass and the seismic acceleration—are introduced to simulate earthquake-induced disturbances. In this scenario, the total driving force or adverse load is composed of the self-weight of rock mass, seismic inertial forces, and fracture water pressure. This total force is then compared with the resisting force, which includes cohesion and frictional resistance, to calculate the factor of safety. The stability outcomes are presented in Table 2, adhering to the guidelines delineated in the relevant standards for rock stability assessment [20].

Tab. 2 - Calculation results of rock mass stability

Rock mass number	Destruction mode	Working condition	Stability coefficient *Fs* of rock mass	Prevention and control safety level	Stability evaluation
WY1	Tilting type	Current conditions	3.12	Secondary	Stable
		Rainstorm condition	1.19		Unstable
		Seismic conditions	0.89		Unstable
WY2	Tilting type	Current conditions	2.85	Secondary	Stable
		Rainstorm condition	1.26		Approximately stable
		Seismic conditions	0.96		Unstable

The aforementioned results collectively suggest that the rock mass currently maintains a condition ranging from stable to moderate stability, meaning that the safety factor is not high, but still greater than 1.0. However, this state changes from a state of moderate stability to potential instability during rainstorm conditions, and changes to a fully unstable state during seismic events. Under such a circumstance, this could lead to disruptions in daily transportation or complete road closures when a storm or earthquake hits this area.

DOI 10.14311/CEJ.2025.02.0019

ROCKFALL SIMULATION

To accurately model rockfall behavior during descent, a detailed understanding of its complex influencing factors is required. To support data collection, fixed aerial control points were set up at the slope site, and an unmanned aerial vehicle (UAV) was used to capture images of the hillside rock mass. Based on these images, a 3D model of the slope was generated, as shown in Figure 2. The slope was divided into 29 sections from left to right for detailed analysis.

In model construction, appropriate values for parameters including slope slip coefficients, roughness, tangential damping coefficients, rockfall geometric attributes, rock dimensions, and density are selected based on data collected from field monitoring. The ensuing analysis that follows provides information on the distribution of rockfall stopping points across various slope cross-sections, along with assessments of kinetic energy, translational speed, and rebound height.

In Rock-fally simulations, rockfall modeling can intuitively illustrate the movement trajectories and impact locations of falling rocks, aiding in the assessment of risk zones and the effectiveness of protective measures. It offers advantages such as operational flexibility, low cost, and high repeatability. However, its strong dependence on input parameters and the simplifications inherent in the modeling process may lead to deviations from real-world conditions. Therefore, when applying such simulations, it is essential to incorporate field data and set parameters appropriately to enhance the reliability of the results.

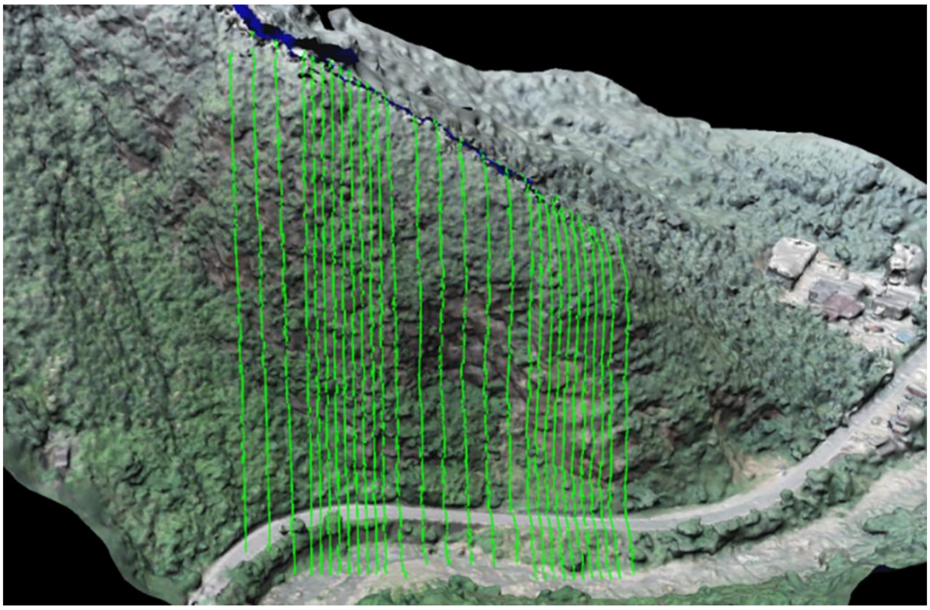

Fig. 2 - Location of simulated characteristic cross-section of slope

Three main cross-sections have been chosen for rockfall analysis, employing Rockfall software. To identify the influence of rocks with varying volumes, simulations have been carried out using rocks with dimensions of 5m³ and 10m³. The specific cross-sections and simulation models employed are illustrated in Figure 3. The material parameters of the slope in the simulation at three cross-sections are defined as bedrock outcrops, where the coefficient of normal restoration is set to 0.35, the coefficient of frictional restoration is set to 0.85, and the friction angle is set to 30.

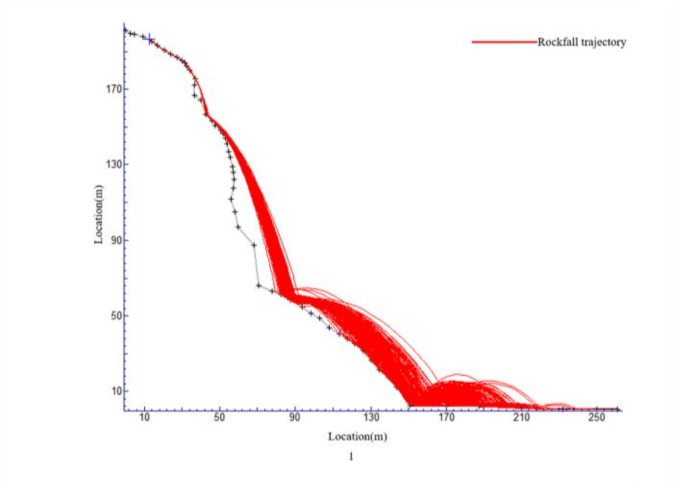

（a）Dimensions of 5m³ in section 1

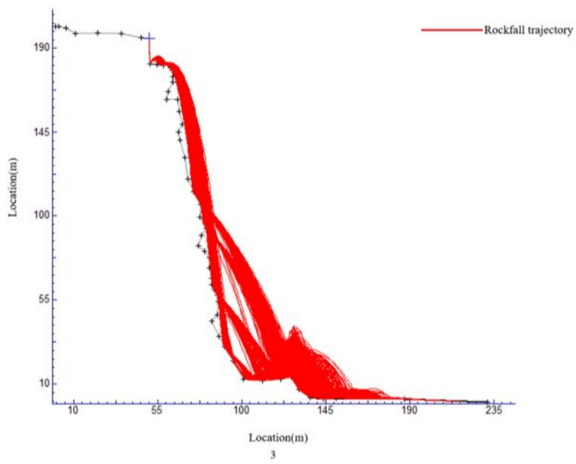

（e）Dimensions of 5m³ in section 3

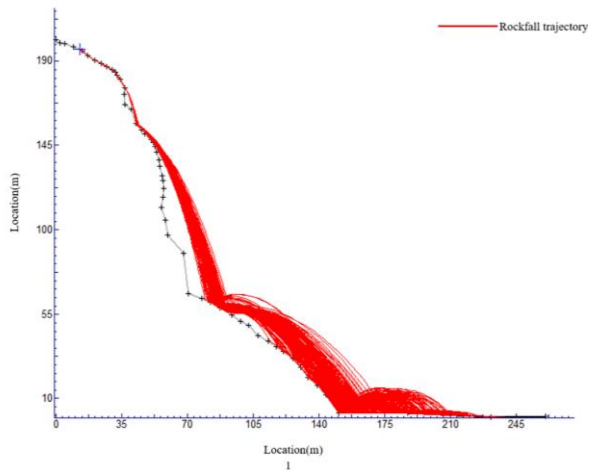

（b）Dimensions of 10m³ in section 1

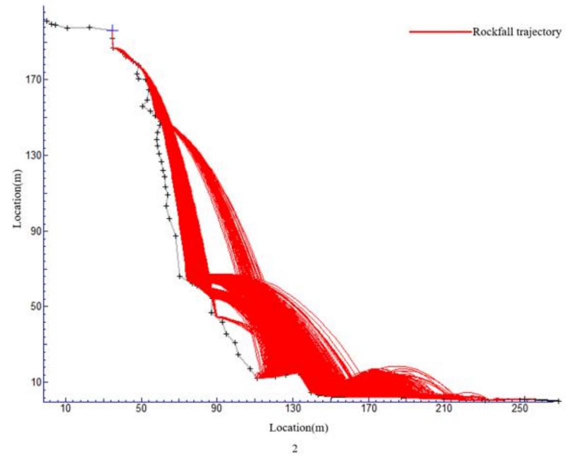

（d）Dimensions of 10m³ in section 2

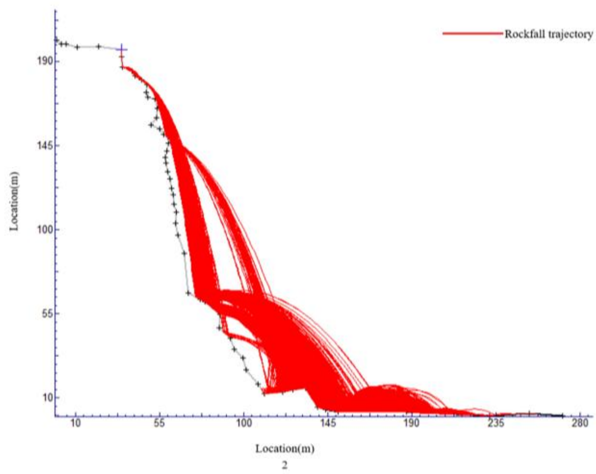

（c）Dimensions of 5m³ in section 2

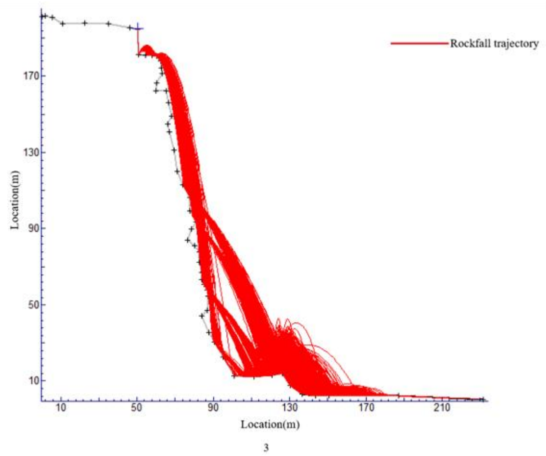

（f）Dimensions of 10m³ in section 3

Fig. 3 - Cross section rockfall trajectory map motion

In the Rocfall software simulation for the most representative sections, the falling rocks are initially set at a velocity of 0 m/s, with the final velocity likewise set at 0 m/s. The initial rotational velocity is also established at 0 m/s. The simulation is conducted over 1000 iterations for each section, allowing for a comprehensive statistical analysis of rockfall incidents. The rock density employed in the simulation is specified at 2500 kg/m³. The normal and tangential restitution coefficients are predominantly contingent on the attributes of the surface of slope covering and vegetation. The values for these coefficients have been derived from the geotechnical investigation papers [21-22].

Model Calculation Results

(1) The influence of Deposition

The simulation results are based on probabilistic statistical analysis. The corresponding number of simulated rockfall sections is shown in Figure 4. In Section 1, for falling rock volumes of 5m³, a portion of them comes to rest within the range of 10-40m, with the highest count of falling points noted at 13m, totaling 579. When the volume of falling rocks increases to 10m³, some of them accumulate within 10-30m, and the count at 13m is 597.

In Cross-section 2, for a rock volume of 5m³, deposition is predominantly observed between 150-210m, with the peak number of points recorded at approximately 205m, amounting to 132. With a rock volume of 10m³, the maximum number of points is observed between 190-220m, reaching a peak of 119 at 211m.

In Cross-section 3, the rock volume is it 5m³, the points of deposition are concentrated around 152m, with over 227 points. With a rock volume of 10m³, the maximum number of points is observed between 140-170m, reaching a peak of 250 at 153m.

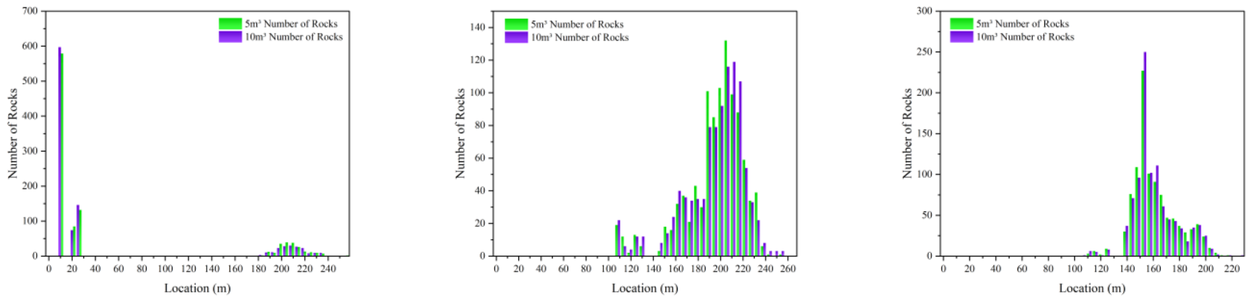

(a) Section 1 (b) Section 2 (c) Section 3

Fig. 4 - Number of falling rocks chart

Based on the statistical analysis of rockfall across the three cross-sections, it is evident that the change in rock volume has a relatively minor effect on deposition distribution, while the geometric and structural characteristics of the slope sections play a more dominant role. Among the three, Cross-section 2 exhibits the highest overall hazard coefficient, as indicated by the greater number and broader spread of rockfall deposition points. This suggests more intense and frequent rockfall activity in that area.

In contrast, although Cross-section 3 has the lowest overall hazard coefficient, it presents the most severe risk of road encroachment. The reason lies in the proximity of its deposition zone to the roadway—many rockfall points are located very close to, or even directly on, the road surface. This concentrated deposition near the road significantly increases the likelihood of traffic obstruction or accidents, even with fewer total events. Therefore, despite its lower general hazard, Cross-section 3 poses a more immediate and tangible threat to road safety. As such, it is strongly recommended to prioritize the implementation of protective measures along this section to mitigate the risk of road blockage caused by rockfall.

(2) The influence of Kinetic Energy

The total kinetic energy diagram is shown in Figure 5. It is evident that in Cross-section 1, the maximum kinetic energy escalates to 5,500 kJ when the rock volume is 5m³, and surges to 11,000 kJ when the volume expands to 10m³. In Cross-section 2, the maximum kinetic energy registers at 7,400 kJ for a rock volume of 5m³, and reaches 15,000 kJ for a volume of 10m³. In Cross-section 3, the highest kinetic energy is recorded at 7,100 kJ for a rock volume of 5m³, and ascends to 1,4000 kJ for a volume of 10m³. The curves illustrating the rise in kinetic energy gradually ascend to a peak before descending, a pattern that closely mirrors the motion characteristics of rockfall during the collapse. With the assumption of consistent variables, such as cross-section attributes, it becomes evident that rock volume exhibits a distinct positive correlation with kinetic energy.

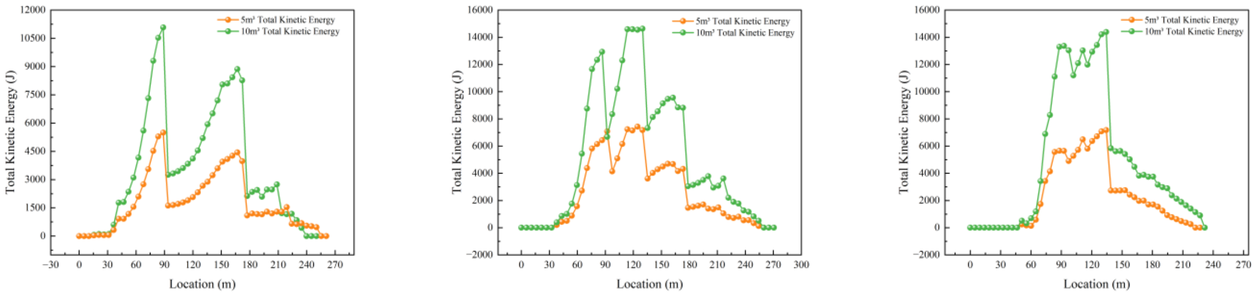

(a) Section 1 *(b) Section 2* *(c) Section 3*

Fig. 5 - Total kinetic energy diagram

An excess of kinetic energy can cause damage upon the road infrastructure, posing a substantial threat to lives and property. A thorough analysis of rockfall kinetic energy serves as a reference for the choice of protective structures, ultimately resulting in an effective reduction in the costs associated with engineering measures.

(3) The influence of Translational Velocity

The horizontal velocity of falling rocks at different cross-sections under different volumes is shown in Figure 6. The rockfall translational velocities as rocks descend from elevated positions, the conversion of potential energy to kinetic energy induces alterations in velocity. These variations in velocity serve as indicators of the roughness of the slope throughout the motion, facilitating an analysis of slope safety.

It is evident that in Cross-section 1, the maximum translational velocity attains 46 m/s for a rock volume of 5 m³, and escalates to 47 m/s for a volume of 10 m³. In Cross-section 2, the utmost translational velocity is recorded at 53 m/s for a rock volume of 5 m³, and slightly higher at 55 m/s for a volume of 10 m³. In Cross-section 3, the highest translational velocity is noted at 55 m/s for a rock volume of 5 m³, and it marginally reduces to 55 m/s for a volume of 10 m³.

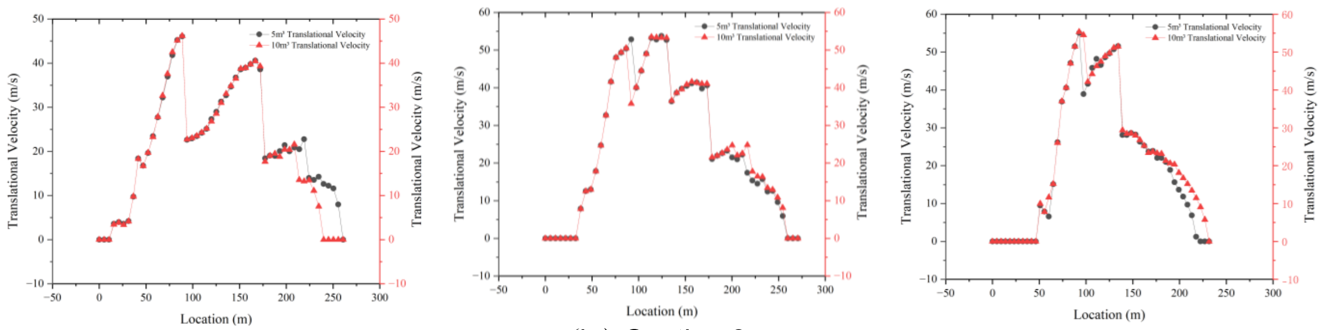

(a) Section 1 *(b) Section 2* *(c) Section 3*

Fig. 6 - Translational velocity of falling rocks

The analysis of peak translational velocities leads to the conclusion that the alteration in rock volume exerts minimal influence, while the characteristics of the cross-section play a more important role in determining translational velocity. Specifically, a higher starting point for the rockfall results in greater translational velocity.

The sequence of peak translational velocities, from highest to lowest, aligns with the analysis of rockfall deposition points, Cross-section 1 exhibits the highest velocity, followed by Cross-section 2, and then Cross-section 3. This sequence further underscores the urgency for mitigation measures to ensure the road safety from the rockfall hazards posed by this slope.

(4) The influence of Bounce Height

The rockfall bounce height corresponding to the section taken is shown in Figure 7. Throughout the descent of rockfall, the rocks may experience multiple rebounds upon striking various surfaces. Each bounce has the potential to cause damage to the slope and lead to a dissipation of energy.

It is evident that in Cross-section 1, the maximum bounce height reaches 53m for a rock volume of 5m³ and 55m for a volume of 10m³. In Cross-section 2, the maximum bounce height attains 72m for both rock volumes (5m³ and 10m³). In Cross-section 3, the highest bounce height is measured at 65m for a rock volume of 5m³ and 66m for a volume of 10m³. The examination of bounce height across different cross-sections indicates that rock volume has a marginal effect on bounce height, whereas the characteristics of the cross-section exert a more substantial influence.

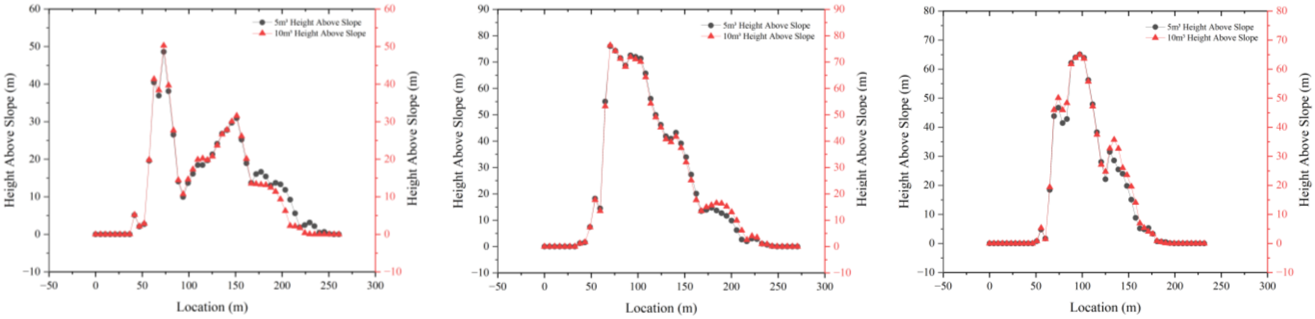

（a）Section 1 （b）Section 2 （c）Section 3

Fig. 7 - Rockfall rebound height chart

In summary, the distribution of rockfall deposition, translational velocities, and bounce heights are briefly determined by cross-section itself, such as initial elevation and slope friction coefficient. Meanwhile, rockfall kinetic energy is predominantly influenced by rock volume. The rockfall simulations and subsequent analysis affirm that in the selected three representative cross-sections, the maximum bounce height is 72m, the peak translational velocity is 55m/s, and the highest kinetic energy is 15,000 kJ, all of which are observed in Cross-section 2. This analysis concurs with prior calculations and field surveys, indication that rockfall poses a great threat to the use of the road.

DEFORMATION MONITORING BASED ON INSAR

To evaluate the deformation of the rock slope in the Suichuan segment of the G105 National Highway, the analysis made use of both D-InSAR and SBAS-InSAR methodologies for comprehensive area monitoring. A total of 15 ascending orbit data scenes sourced from Sentinel-1A were selected and subsequently processed. The study adopted the wide-swath interferometric mode with VV polarization, generating Single Look Complex data in Level-1. The chosen mode was Scan SAR-interferometric wide-swath (IW), covering a time duration of 168 days. InSAR technology offers significant cost advantages and spatial continuity for large-scale slope monitoring, with its millimeter-level accuracy meeting the early warning requirements for highway slopes. Compared to traditional methods, the automated InSAR system enhances data acquisition efficiency by approximately six times and is not limited by terrain accessibility. While the GNSS reference station provides a point monitoring accuracy of ±2 mm, its deployment density is limited; total stations, though capable of sub-millimeter precision, require manual periodic measurements, and data acquisition may be interrupted by extreme weather conditions, such as heavy rainfall. The construction cost of traditional monitoring networks (GNSS combined with total station) is approximately USD 36,000/km, while the cost of InSAR in this study is only 17% of the traditional method. Particularly in high and steep slope areas, where manual monitoring poses safety risks, InSAR technology demonstrates significant advantages.

D-InSAR

Differential Interferometric Synthetic Aperture Radar (D-InSAR) technology primarily needs integrating external Digital Elevation Model (DEM) data to remove the terrain phase from the interferogram derived from InSAR. At present, three primary D-InSAR techniques are commonly employed: two-pass, three-pass, and four-pass interferometry. Among them, the two-pass interferometric method is regarded as the most reliable due to its relatively simple implementation and high accuracy.

Following the D-InSAR analysis, the Sentinel-1A data were processed with two-pass interferometric method. This led to the generation of a surface deformation map, which unveiled non-uniform ground deformation along the entirety of the road. The severely impacted regions primarily cluster in the northern section, showcasing surface uplift with the maximum deformation measuring 0.219 m. In comparison, the deformation in the southern section is slightly lesser than that in the northern section, with most deformations falling below 0.06 m. Within the central urban area, the road segment indicates subsidence of approximately less than 0.08 m.

SBAS-InSAR

SBAS-InSAR stands for Small BAseline Subset InSAR, through the combination of a substantial amount of SAR data, a series of differential interferograms with short spatial baselines can be derived. This effectively avoids spatial decorrelation, enhancing the accuracy of the deformation analysis.

Following the two-pass interferometric processing of the Sentinel-1A data, the average deformation rates along the G105 Suichuan section were computed. The overall deformation along the road corridor is relatively modest, with the majority of regions displaying an annual average deformation rate of approximately ±50mm/year. The regions experiencing severe deformation are primarily concentrated in the northeastern section, where the maximum subsidence rate reaches 50mm/year. Deformation rates in the southern section generally remain below 30mm/year, while in the central urban area, the road segments undergo minimal deformation, with an average deformation rate of around ±10mm/year.

For a more detailed analysis of the deformation characteristics in the high-altitude collapse areas along the G105 Suichuan section, seven key points of interest were selected. These points encompass locations along the road alignment and within the range of the slope collapse, as shown in Figure 8.

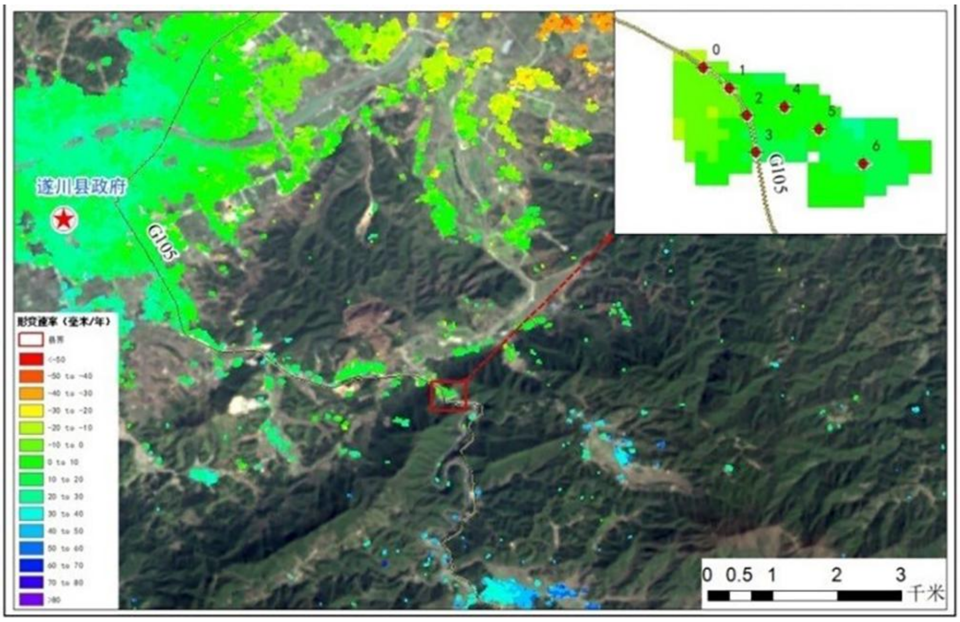

Fig. 8 - Deformation rate diagram of the collapse points of Suichuan section G105 during the monitoring period

Through monitoring the deformation of high-risk collapse points, all seven monitoring locations exhibited distinct deformation behaviors during the entire observation period. Generally, points 0 and 1 showed noticeable subsidence, while the remaining five points exhibited slight uplift.

Among these, point 3 demonstrated the greatest subsidence, reaching approximately 20 mm between April 8 and April 20. Point 1 followed with a subsidence of 13 mm between July 1 and August 6. Point 2 remained relatively stable, with fluctuations confined within 8 mm throughout the monitoring period, although a significant uplift was observed after August 6.

The deformation behavior at all monitoring points exhibited fluctuating patterns, which may indicate episodic instability, potentially linked to anthropogenic activities. Several monitoring points exhibited synchronized deformation trends, with abrupt subsidence or uplift occurring at specific intervals. These significant deformation events underscore the importance of implementing timely protective measures to ensure the safety of both vehicular traffic and pedestrians in the affected areas.

MITIGATION MEASURES

Guided by theoretical calculations and assessments conducted through simulation software, this study proposes the implementation of an actively controlled energy dissipation net in conjunction with a rockfall protection system as well as the tunnel construction. In the case of rocks WY1 and WY2, primarily due to their substantial volume and the emergence of unloading cracks at the rear edge, it is advisable to initiate manual rock extraction as the preliminary measures. Furthermore, a primary energy dissipation net will be strategically installed beneath the rocks. The lower section of the net will feature an open design, while the remaining sections will be closed. This will result in a total length of 260 meters and an average height of 155 meters. The protective area will encompass 40,300 square meters.

In the construction of the tunnel, an open-cut method will be employed, strategically positioned at the most severely affected areas. The tunnel will take the form of an integral, single-aisle, two-way driving structure, spanning a total length of 210 meters. The design takes into account a 2-meter diameter rock block falling from a height of 100 meters, resulting in an impact force of approximately 838kN/m. To support the outer side of the tunnel, pile foundations will be employed, while the top will be filled with crushed stones at a slope ratio of 50% [23]. In order to ensure the rationality and feasibility of the proposed protection measures, a preliminary cost estimation has been conducted. The estimated investment includes the following components: Manual removal of unstable rocks (WY1 and WY2); Energy dissipation net (260m × 155m, covering 40,300 m²); Tunnel construction (210m, open-cut method); Pile foundations; Backfill and slope treatment; Safety monitoring system. The total estimated cost is approximately USD 2.57 million. Considering potential geological uncertainties and implementation risks, it is recommended to set aside an additional 10% contingency, bringing the overall estimate to about USD 2.83 million. These investments are considered necessary and cost-effective, given the potential consequences of rockfall hazards in the project area.

Automated Monitoring

To monitor the potential rockfalls during and post the construction phase, a comprehensive combination of automated monitoring techniques will be deployed. This array includes the monitoring of surface deformation, precipitation levels, rock tilt angles, fractures in the rock, and on-site conditions of the mountain. The primary monitoring method will need the use of GNSS satellite positioning to track the absolute displacement of the slope. For fracture monitoring, points will be strategically installed at locations exhibiting instability and pre-existing cracks.

Moreover, rain gauges will be positioned at higher sections of the slope, isolated from the influence of the surrounding environment. Wireless tilt monitors will provide real-time observations of rock tilt variations. In the event that the tilt of the rock exceeds the predetermined warning threshold, timely alerts will be issued. Video surveillance cameras will be strategically stationed in open and unobstructed areas to provide panoramic views of potential collapse and rockfall zones, enabling real-time and comprehensive monitoring. The layout of the monitoring stations and the monitoring site is depicted in Figure9.

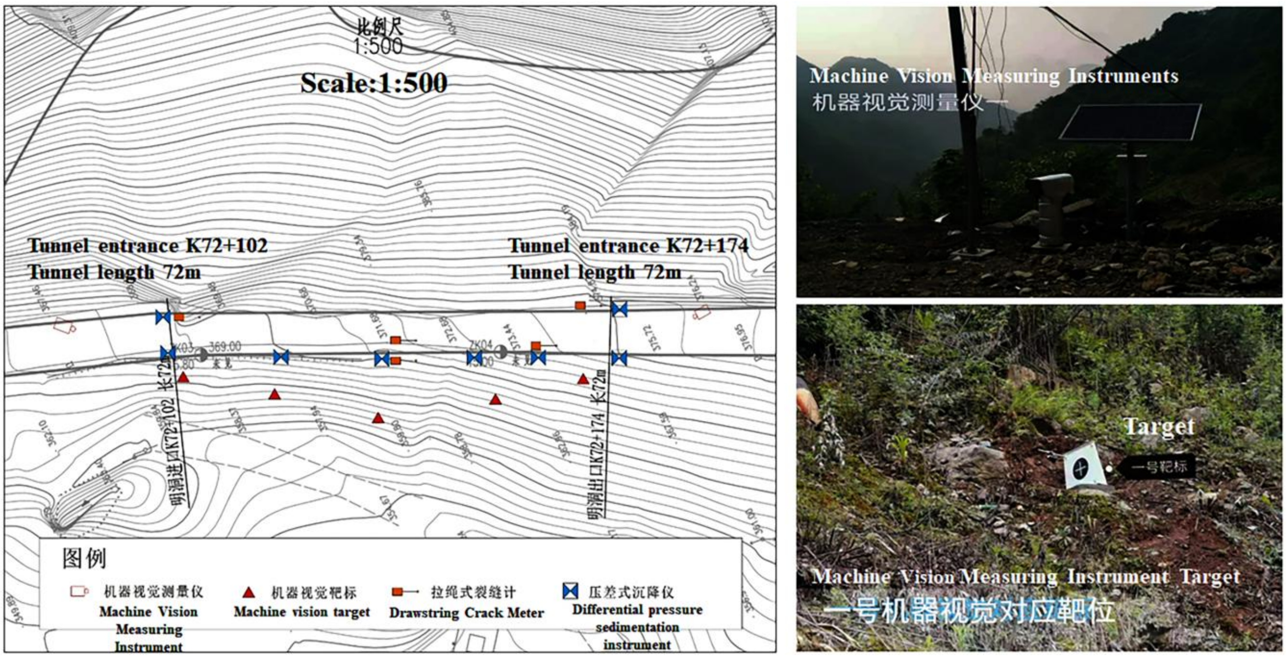

Fig. 9 - Layout of monitoring stations and monitoring sites

The post-construction monitoring outcomes reveal that the machine vision measuring instrument recorded the highest cumulative horizontal displacement at 9.64 mm, while the ground exhibited a vertical displacement of -9.68 mm. The settlement inclinometer detected a maximum cumulative change of -8.33 mm. In the x-direction inclinometer, which comprises one reference point, one turning point, and ten valid points, the maximum cumulative change during the monitoring period is -0.21°. In the y-direction inclinometer, the maximum cumulative change is -0.18°. The rope extensometers registered a maximum cumulative change of 0.48 mm.

Based on the results of automated monitoring, the monitoring system demonstrates relative stability. The measured values at various monitoring points in the slope stabilization project display minor variations, indicating that the slope is in a stable condition. Additionally, no ongoing expansion of cracks in the tunnel is observed, and there are no significant signs of uneven settlement in the tunnel foundation.

CONCLUSION

This study focuses on a rocky slope in the Suichuan segment of the G105 National Highway, conducting a qualitative analysis of the rock mass in the area. A three-dimensional representation of the slope is constructed using unmanned aerial vehicle (UAV) scanning. Rocfall software then analyzes the translational velocity, rebound height, kinetic energy, and deposition distribution for varying rockfall volumes. Additionally, slope stability is monitored through the integration of InSAR and automated monitoring technologies. By combining traditional slope stabilization methods with advanced intelligent monitoring approaches, this study effectively prevents and controls slope instability, leading to the following conclusions.

The rocks WY1 and WY2 on the slope remain stable under normal conditions, showing slight instability during heavy rainfall and becoming prone to instability during seismic events. The slope is particularly vulnerable to high-level collapses, with potential block falls and large-scale collapses along structural planes. Proposed measures, such as active energy dissipation nets, manual rock removal, and strategic tunnel engineering, effectively control and prevent rockfalls.

Simulation results from Rocfall software show a strong positive correlation between the kinetic energy of rockfall and the volume of falling rocks. Meanwhile, translational velocity, rebound height, and deposition distribution are primarily influenced by cross-sectional conditions, such as the height of the falling points and friction coefficients on the impact surface, with no significant relationship to the rockfall volume. The combination of UAV scanning, automated monitoring, and InSAR technology reduces uncertainties in slope risk assessment, making the monitoring data more precise and reliable.

In conclusion, the comprehensive integration of various techniques in this study has been instrumental in assessing and mitigating rockfall risks on the designated slope. The insights gained from this research will provide valuable guidance for similar engineering projects addressing rockfall risks.

ACKNOWLEDGMENTS

This work was Supported by the Development and Application of Landslide Surface Deformation Monitoring System based on High-precision Beidou Technology (No. 2022H0030).

REFERENCES

[1] Zou D, Zheng H., 2005. Fast lagrangian method and its applications in slope stability analysis [J]. Mining Research and Development. 2005(10). https://doi.org/10.3969/j.issn.1005-2763.2005.05.026

[2] Glade T., 2003. Vulnerability assessment in landslide risk analysis. Die Erde 134:121–138.

[3] Crosta G B, Agliardi F., 2004. Parametric evaluation of 3D dispersion of rockfall trajectories. Natural Hazards and Earth System Sciences 4(4):583–598.

[4] Michoud C, Derron M H, Horton P, Jaboyedoff M, Baillifard F J, Loye A, Nicolet P, Pedrazzini A, Queyrel A., 2012. Rockfall hazard and risk assessments along roads at a regional scale: example in Swiss Alps. Natural Hazards and Earth System Science 12(3):615–629.

[5] Frattini P, Crosta G B, Carrara A, Agliardi F., 2008. Assessment of rockfall susceptibility by integr ating statistical and physically-based approaches. Geomorphology 94(3–4):419– 437. https://doi.org/10.1 016/j.geomorph.2006.10.037

[6] Azzoni A, La Barbera G, Zaninetti A., 1995. Analysis and prediction of rockfalls using a mathematical model. International Journal of Rock Mechanics and Mining Sciences & Geomechanics Abstracts 32(7):709–724. https://doi.org/10.1016/0148-9062(95)00018-C

[7] Agliardi F, Crosta G B., 2003. High resolution three-dimensional numerical modelling of rockfalls. International Journal of Rock Mechanics and Mining Sciences 40(4):455–471. https://doi.org/10.1016/S1365-1609(03)00021-2

[8] Frattini P, Crosta G B, Agliardi F., 2012. Rockfall characterization and modeling. In: Clague JJ, Stead D (eds) Landslides types, mechanisms and modeling. Cambridge University Press, Cambridge, pp 267–281, ISBN: 978-1-107-00206-7. https://doi.org/10.1017/CBO9780511740367.023

[9] Dorren, Luuk K A., 2003. A review of rockfall mechanics and modelling approaches [J]. Progress in Physical Geography, 2003, 27(1).

[10] Giani G P, Giacomini A, Migliazza M, et al., 2004. Experimental and Theoretical Studies to Improve Rock Fall Analysis and Protection Work Design[J]. Rock Mechanics & Rock Engineering, 2004, 37(5):369-389.

[11] Lan H, Martin C D, Zhou C, et al., 2010. Rockfall hazard analysis using LiDAR and spatial modeling[J]. Geomorphology, 2010, 118 (1–2):213-223. https://doi.org/10.1016/j.geomorph.2010.01.002

[12] Zhang Q, Huang G W, Yang C S.,2017. Precision space observation technique for geological hazard monitoring and early warning[J]. Acta Geodaetica et Car-tographica Sinica, 2017,46 (10): 1300-1307. https://doi.org/10.11947/j. AGCS.2017.20170453.

[13] Zhu J J, Li Z W, Hu J.,2017. Research progress and methods of InSAR for deformation monitori ng[J]. Acta Geodaetica et Cartographica Sinica, 2017, 46(10): 1717-1733. https://doi.org/10.11947/j.AG

CS.2017.20170350
[14] Zhu J J, Hu J, Li Z W, et al.,2022. Recent progress in landslide monitoring with InSAR[J]. Acta Geodaetica et Cartographica Sinica, 2022 ,51(10) :2001- 2019.
[15] FERRETTI A, PRATI C, ROCCA F.,2001. Permanent scatter-ers in SAR interferometry[J]. IEEE Transactions on Geo-science and Remote Sensing,2001, 39(1): 8-20. https://doi.org/10.1109/IGARSS.1999.772008
[16] B Y K A, B Z L, A C Z, et al.,2023. InSAR monitoring of creeping landslides in mountainous regions: A case study in Eldorado National Forest, California[J]. Remote Sensing of Environment, 258. https://doi.org/10.1016/j.rse.2021.112400
[17] Nadim F, Einstein H, Roberds W., 2005. Probabilistic stability analysis for individual slopes in soil and rock. In: Hungr O, Fell R, Couture R, Eberhardt E (eds) Landslide risk management. Taylor and Francis, London, pp 3–26. https://doi.org/10.1201/9781439833711-6
[18] Gharpure A D, Khan S S., 2022. Rock Fall Prevention by Innovative Products and Technologies [J]. gndec.ac.in, 2022.
[19] Bokati N, Dahal R, Acharya I, et al., 2020. Evaluation of rock fall analysis and suitable protection measures in siddhababa section along siddhartha highway[J].2020.
[20] (DB50/143-2003) Geological Hazard Prevention and Control Engineering Survey Specification [S].
[21] Bozzolo Dopamine R., 1986. Simulation of Rock falls down a Valley side[J]. Acta Mech,1986,63:113-130. https://doi.org/10.1007/BF01182543
[22] Day R W., 1997. Case studies of rockfall in soft versus hard rock [J]. Environmental and Engineering Geoscience,1997,3(1)：133-140. https://doi.org/10.2113/GSEEGEOSCI.III.1.133
[23] (JTG/T D70-2010) Design Rules for Highway Tunnels [S].

CIVIL ENGINEERING JOURNAL

Article no. 20

THE CIVIL ENGINEERING JOURNAL 2-2025

IMPACT OF TERRAIN AND ENVIRONMENT ON THE ACCURACY OF VEHICLE-BASED MOBILE MAPPING SYSTEMS

Lukáš Běloch

Czech Technical University in Prague, Faculty of Civil Engineering, Department of Geomatics, Thákurova 7, Praha 6, Czech Republic; lukas.beloch@fsv.cvut.cz

Received: *14.04.2025*
Received in revised form: *20.06.2025*
Accepted: *24.07.2025*

ABSTRACT

The rapid collection of accurate spatial data and its use in various domains is driving the evolution of Mobile Mapping Systems (MMS). This study evaluates the accuracy of the Riegl VMX-2HA system in three different environments: an urban residential area, an open road section with an unobstructed view of the sky, and a forested roadway where GNSS signals are significantly affected. This research investigates the effect of these environments and different alignment methods on point cloud accuracy. A combination of GNSS, IMU and DMI was used to determine the trajectory, with measurements tied to GCPs. The study compares the results of the processing of the separate sections with the calculation of the entire section and evaluates the differences of the repeated measurements. The results show that aligning measurements without separating sections by environment improves accuracy. The results contribute to the optimisation of MMS-based data collection strategies and provide insight to improve the reliability of spatial data collection.

KEYWORDS

Mobile laser scanning, Mobile mapping system, Point cloud accuracy, Riegl VMX-2HA

INTRODUCTION

The requirement for rapid spatial data collection was behind the creation of the first mobile mapping devices. These devices were initially georeferenced only to ground control points (GCPs); later, additional sensors were integrated for positioning [1; 2; 3]. These methods have a significant impact on overall accuracy. To determine the initial trajectory, a combination of GNSS (Global Navigation Satellite System), IMU (Inertial Measurement Unit), and DMI (Distance Measurement Indicators) are used in vehicle mounted Mobile Mapping Systems (MMS).

Although the GNSS system can achieve absolute centimetre accuracy, the GNSS signal is often degraded by sky obscuration or multipath interference. The IMU is used to obtain accelerations and rotations, and the relative position of the vehicle can be determined from the measurements. However, errors and noise accumulate in these measurements. For optimal computation of the initial trajectory by combining the above methods, it uses the Kalman filter [4; 5; 6]. In addition, the measured trajectory can be transformed into GCPs to ensure accuracy or improve accuracy in sections without a GNSS signal [7; 8]. Another method is to align the point cloud using the Simultaneous Localization and Mapping (SLAM) algorithm [9; 10], but this principle is mostly used for handheld mobile laser scanners, which are mainly used in places without GNSS signals such as buildings [11; 12; 13], forests [14; 15], historical structures [16] or mines [17].

Currently, there are several commercial vehicle-mounted MMS solutions that use panoramic cameras and Light Detection and Ranging (LiDAR) sensors for data acquisition [18]. In testing these devices, the authors of this paper discuss both the accuracy and data quality of the system and its use for specific purposes.

The use of MMS is currently highly relevant. These devices are being developed and improved for several reasons. The first is their use for autonomous vehicle control. This focus involves the relative position of the vehicle (car) in its surroundings, the recognition of traffic signs and the monitoring of traffic [19; 20; 21; 22]. In this context, deep learning tools are widely used for data processing and classification [23; 24; 25; 26; 27; 28].

For surveying purposes, the resulting accuracy of the output is important. In this context, papers deal with the accuracy of the systems [29; 30; 31; 32] especially in terms of the impact of the density of GPSs [33; 34; 35]. These papers imply that the number and quality of GCPs have an important role in the accuracy of the result. However, for effective data collection, it is recommended to use GCPs targeted by the GNSS method with a spacing of 1000 m. This paper focusses on the investigation of the accuracy and behaviour of the MMS device in terrain with different characteristics. [35; 36].

MATERIALS AND METHODS

This chapter describes the characteristics of the test field, the determination of ground point coordinates, and point signalling. Furthermore, it gives a brief description of the work involved in the creation of point clouds, and it concludes with a description of the evaluation of observed values when working with MMS.

Test Field Specification

The test field (Figure 1) dedicated to investigating the properties of the MMS approach using the Riegl VMX-2HA was designed to include various types of area. The test field is in Pilsen, South suburb (Jižní předměstí, 49.7299869N, 13.3574144E). The total length of the test field is 5.5 km with 109 points spaced approximately 50 m apart.

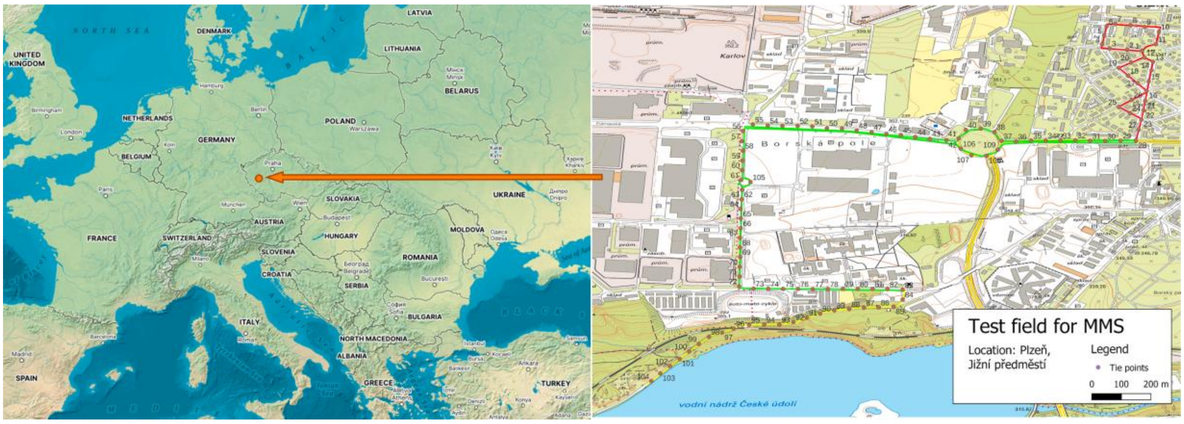

Fig. 1 - Map of the MMS test field

Field Sections

The first section (Figure 2a), 1.5 km long, is in the calm locality of "Na Hvězdě". This area is dominated by residential development and street trees. The second section (Figure 2b) lies along "Sukova", "Folmavská" and "U Letiště" streets and is a multi-lane road with unobstructed views of the sky. The last section of 1 km is then placed in "Dobřanská" Street (Figure 2c). The surrounding area of this street is forested and therefore the GNSS signal is significantly interfered with.

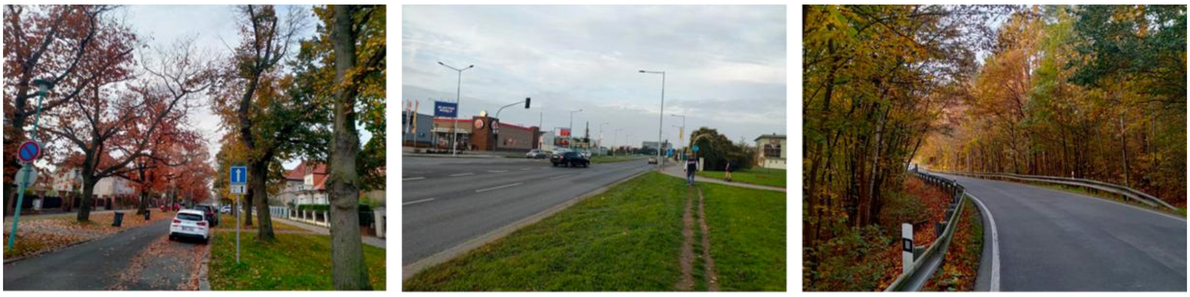

(a) (b) (c)

Fig.2 - Types of area (a – Section 1, b – Section 2, c – Section 3)

Reference and Validation Point Network

Control and check points were stabilised with a measuring steel spike and marked by street lines or a 15x15 cm chequerboard target. The coordinates of the points of all sections were determined by the GNSS RTK method (GNSS points), and the points of the first section were additionally determined by a total station with subsequent alignment (TS points).

Each point was independently measured twice using a Leica GS18. The average standard deviations of the GNSS point determinations were calculated based on these dual measurements. Table 1 presents the standard deviations of the GNSS coordinates derived from the repeated measurements.

Tab.1 - Deviations of GNSS measurement

Field Sections	StDev 2D [mm]	StDev 3D [mm]
Section 1	23	27
Section 2	14	16
Section 3	14	20

Only ground points in Section 1 were measured using the polygon method using a Leica TS1200 total station and then calculated by adjustment in EasyNET software (Version 3.5). Section 1 was assumed to be moderately demanding in terms of GNSS interference. The coordinates determined by this method will be used to calculate the differences between the point-cloud alignment methods. Measuring the entire field using this method would be time consuming, and despite this, it is not expected to be of significant benefit to this work. Table 2 shows the network adjustment parameters in the EasyNet software.

Tab.2 - Adjustment parameters of the tied network

Adjustment method	Tied network
Fixed points	1, 5, 25
Average 2D standard deviation	2.2 mm
Average 3D standard deviation	2.2 mm

Methodology

The data acquisition parameters, the vehicle speed, and the calculation settings affect not only the density of the point cloud but also its overall quality and accuracy. This chapter provides an overview of the fundamental parameters for data collection, as well as the calculation procedure. Detailed descriptions of each parameter can be found in [33].

MMS Data Acquisition

The test field was measured with a Riegl VMX-2HA mobile mapping instrument, attached to a car. The measurements were taken in December 2022. A panoramic camera was not used for the mapping as it was not planned to evaluate the photo data or colour the point clouds. The entire field was surveyed twice (forward and backward). The vehicle moved at an average speed of 20 km/h on the "forward" approach and 35 km/h on the "backward" approach. All significant parameters are listed in Table 3.

Tab.1 - Parameters of data collection

Environmental Factors	
Ambient Temperature	1 °C
Atmospheric Pressure	1020 hPa
Relative Humidity	90 %
Operational Parameters	
Average Vehicle Speed	20 km/h and 35 km/h
Laser Pulse Repeat Frequency	1000 kHz
Use of Panoramic Camera	Not utilized

MMS data processing

The Riegl RiPROCESS data software was used to create point clouds from the measured data and the trajectory from the GNSS/INS data was computed in the Applanix POSpac software. A total of eight point-clouds were computed, two clouds of the entire test field (forward and backward) with GCPs spacing 1km and two clouds for each Section in the same procedure. Figure 3 shows a flow chart of the process with important parameters.

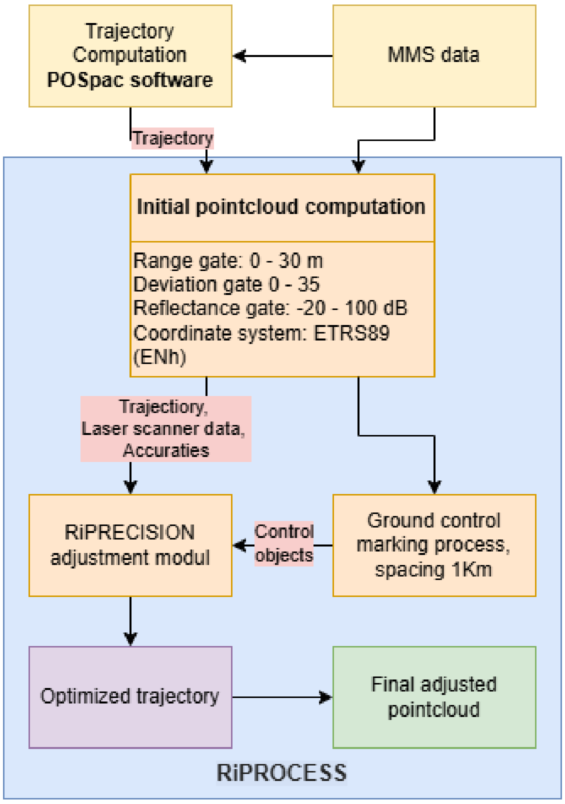

Fig.3 - Data processing flow chart

MMS evaluation

This chapter describes how the results are calculated and evaluated. It focusses on the influence of the alignment method in RiPROCESS software on the resulting cloud accuracy, the quality assumptions of GNSS point clouds, and in the last part to the point clouds and their accuracies.

Determination of accuracy

The deviations were determined by comparing the ground check points with the corresponding points extracted from the point clouds. Equation 1 provides the formula for calculating the Root Mean Square Error (RMSE), while Equation 2 defines the calculation of Standard Deviations.

$$RMSD = \sqrt{\frac{\sum_{i=1}^{n} \Delta x_i^2}{n}},$$
$$where\ \Delta x_i = X_i - \widehat{X_i}, X_i\ are\ the\ coordinates\ of\ the\ check\ point,$$
$$\widehat{X_i}\ are\ the\ coordinates\ of\ the\ point\ obtained\ from\ the\ point\ cloud. (1)$$

$$StDev = \sqrt{\frac{\sum_{i=1}^{n} v_i^2}{n-1}},$$
$$where\ v_i^2 = \Delta \underline{X} - \Delta X_i,$$
$$\Delta X_i\ are\ the\ coordinators\ differences\ between\ the\ check\ points\ and\ the\ points\ obtained\ from\ the\ cloud,$$
$$\Delta \underline{X}\ is\ their\ average. (2)$$

DOI 10.14311/CEJ.2025.02.0020

Influence of the Alignment Method

The initial trajectory is computed from GNSS, INS and DMI data. The absolute position is provided by GNSS, which, especially in places with obscured views of the sky, may show larger deviations from the actual terrain and in some places the trajectory may even be deformed. For these purposes, it is recommended to align the measurements with the ground control points and adjust the entire trajectory. The alignment process utilises GNSS, INS, and DMI data along with their respective accuracies. GCPs are marked on the initial point cloud to refine alignment.

Figure 4a shows the spatial deviations of the initial trajectory; the difference between sections and the impact of GNSS measurements on accuracy are significant. The state after the "non-rigid with translation" adjustment to the GCPs can be seen in Figure 4b. The marked locations of the local minima appear where the ground control points were located. There are four significant maximum deviations in this plot; these deviations are very similar to each other and occur at locations where the vehicle was forced to stop at the road junction. The last thing that can be noticed from comparing these two graphs is that the calculated deviations are reduced after the alignment, but the trends are kept. These graphs were computed in the RiPROCESS software.

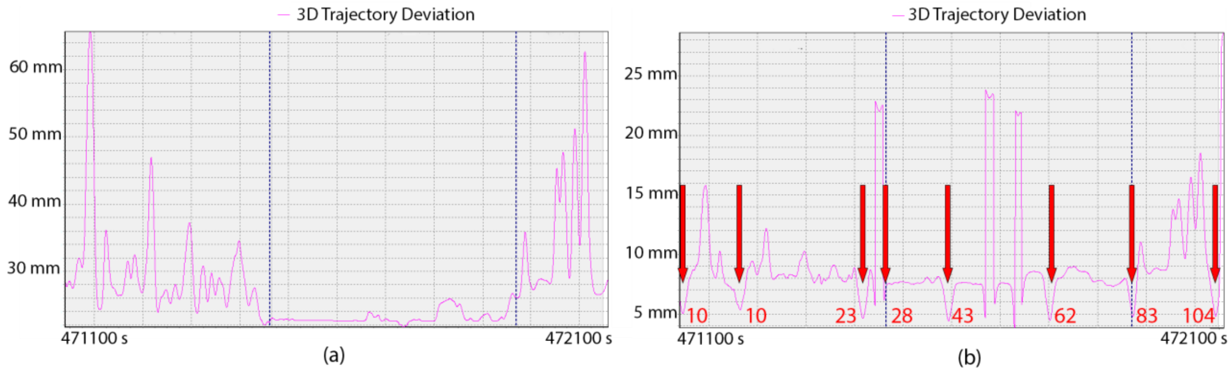

Fig.3 - RiProcess trajectory deviation

RiPRECISION software offers three types of adjustment:

Non-rigid with translation: The entire trajectory is first rotated and translated to minimise deviations at the ground control points, followed by local alignment around the ground control points, and therefore scale adjustment.

Non-rigid: Only local alignment around the ground control points and scale adjustment is performed.

Rigid with translation: The trajectory is rotated and translated to minimise deviations at the ground control points.

For comparison of the adjustment, the point clouds of Section 1 where the TS ground control points are used, and therefore the result will not include the GNSS error. Three clouds were computed, and each point cloud was first aligned at points 10 and 23 (1 km spacing between points), and the trajectories were adjusted according to the methods mentioned. Figure 5 shows the profile of point clouds with checkpoint TS 5.

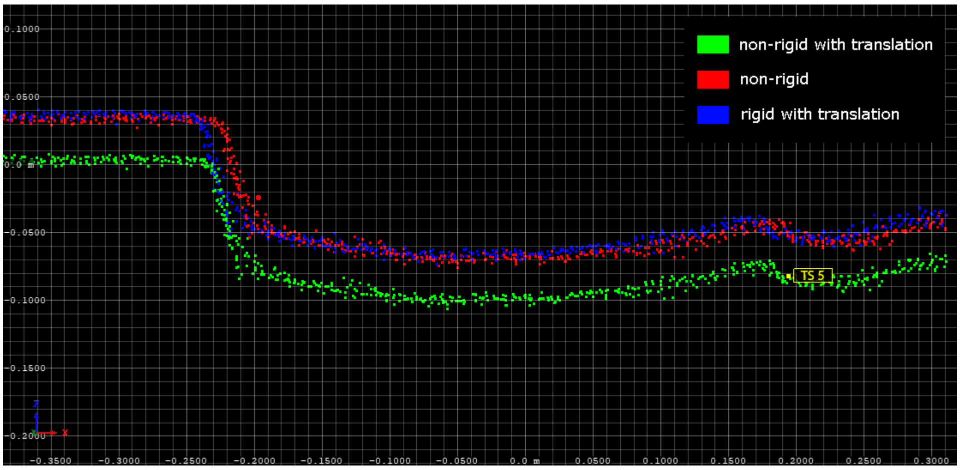

Fig.4 - Profile of various adjustment types

Accuracy of MMS in Various Environments

In this article, three types of environments are studied. The results are expected to show the difference in the point cloud accuracy with the same spacing of the GCPs. This section also focusses on the point cloud accuracy when the section was computed separately (without other sections) and when the section was computed together as one raid.

The last chapter is dedicated to the repeatability of measurements, i.e. the difference of point clouds of the same section that have been measured repeatedly and are tied on identical GCPs. The points taken from the "forward" and "backward" point clouds were compared. Also, in this case, differences were calculated from point clouds computed by sections and point clouds computed as part of the entire field.

RESULTS

Influence of the Alignment Method

Figure 6 illustrates the 3D deviations of each check points distributed along the trajectory. The deviations are calculated here as the difference between the TS point coordinate and a point manually taken from the point cloud. The plot values show similar trends in the deviations, especially between the "non-rigid" and "rigid with translation" methods. The "non-rigid with translation" method shows the smallest deviations during the trajectory, which can be seen in the summary of Table 4.

DOI 10.14311/CEJ.2025.02.0020

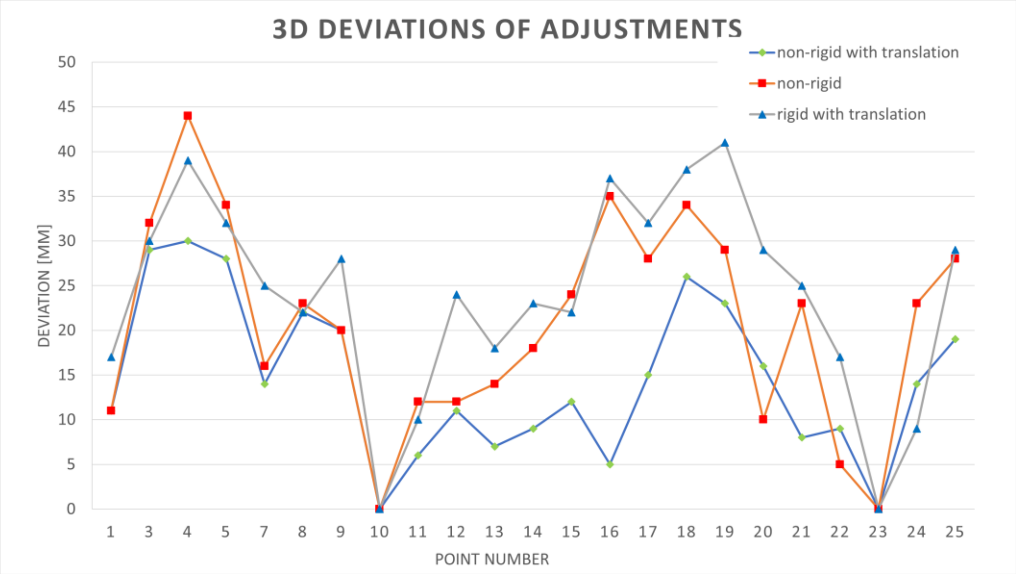

Fig. 5 - Points deviations of various adjustment types

Tab. 2 - Summary deviations of various adjustment types

Alignment method	StDev 3D [mm]	RMSD 3D [mm]
Non-rigid with translation	16	18
Non-rigid	20	25
Rigid with translation	20	27

Accuracy of MMS in Various Environments

Data collection was carried out in three areas. Section 1 was measured in a built-up urban area, Section 2 was carried out on a two-lane road section, without disturbing the view of the sky, and Section 3 data collection was carried out on a forested road. The sections are connected to each other.

Figure 7 shows the deviation plots for these sections. While the line graph represents the deviation of the MLS measured point from the "forward" approach from the point measured by GNSS method, the bar graphs show the 3D deviation of the points from the "forward" and "backward" passes. Compared to the GNSS points, the plot values also show the minimum deviation of the cloud calculated separately and the cloud computed as a group of all sections. The largest difference between these deviations can be seen in the graph of Section 2 at point 40, the difference reaches 26 mm.

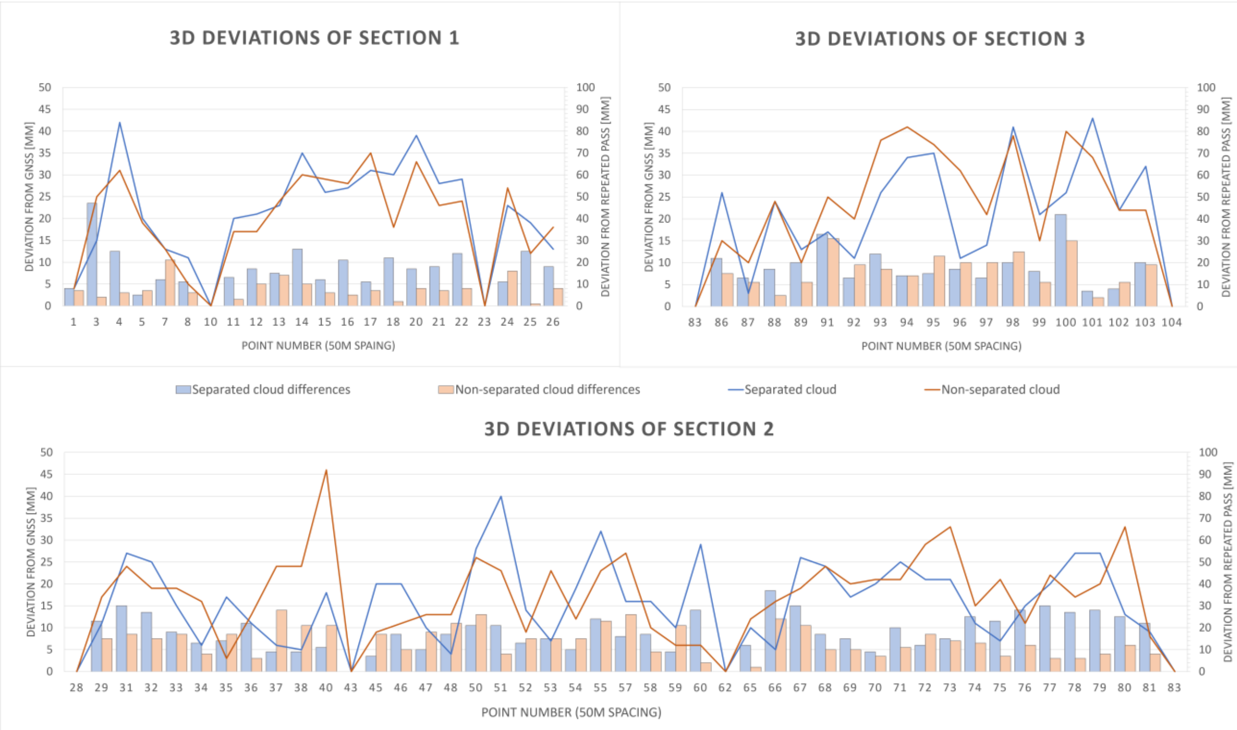

Fig.6 - Point deviations of measured sections

The Table 5 shows in detail the sampling standard deviations (StDev) and Root-mean-square-deviations (RMSD). The plane deviations of the first pass for all environments (compared with GNSS points) are almost identical, StDev 15mm. A more significant difference in this comparison is seen for spatial deviations, because of the height component. However, the difference in deviations between the areas is in the range of millimetres.

The difference in total deviations from the comparison of cloud points from two passes behaves similarly when the clouds are adjusted separately. For all environments, the deviations reach similar values. However, the table shows very small deviations in the height deviation when the clouds were calculated as part of the whole. The height deviations from these repeated passes are below 4 mm.

Tab. 3 - Summary deviations of measured sections

Section	Calc.	2D GNSS [mm]		3D GNSS [mm]		H GNSS [mm]	2D Rep. Pass [mm]		3D Rep. Pass [mm]		H Rep. Pass [mm]
		StDev	RMSD	StDev	RMSD	StDev	StDev	RMSD	StDev	RMSD	StDev
1	Sep.	16	17	21	24	13	14	16	17	19	10
	Tot.	15	17	20	22	13	9	9	9	9	2
2	Sep.	15	15	19	19	11	15	17	18	20	11
	Tot.	15	15	17	19	9	13	15	14	15	4
3	Sep.	15	16	23	27	17	16	19	17	20	6
	Tot.	16	18	21	25	12	15	19	15	19	1
Entire area	-	15	16	20	22	12	13	14	14	15	3

Explanatory notes:
Sep. - point clouds were calculated separately for each section, Tot. - point clouds were computed as part of the entire area.

CONCLUSION

This article was dedicated to comparing the accuracy of the MMS method with the Riegl VMX-2HA in various environments. These areas differed mainly in GNSS interference. The data were acquired on a 5.5 km long test field in Pilsen. The points used for the calculations are spaced at 50 m intervals along this route, and their coordinates were determined by the GNSS method.

In the first step, it was appropriate to determine the method of adjustment of the initial trajectory on the GCPs. An experiment was performed in which the measurements in the first section were aligned to two points (spaced 1000 m apart) and point clouds with different transformations were calculated. For these calculations, very precise points determined by the adjustment of the tied network (TS points) were used. The results show that the most accurate method and the method used further is the "non-rigid with translation" transformation, which achieved a 3D standard deviation of 16 mm.

The results of the sections comparison with GNSS points show several similar results. The first says that the accuracy of the point cloud, computed as part of the whole (with varying environments), increases the accuracy of the results. This was also applicable for Section 2, where linking to sections with worse conditions, there was no degradation in accuracy. The results show an improvement in the 3D standard deviation of 1-2 mm. The change of environment is only slightly reflected in the planar deviations, a more significant change is only seen in the elevation deviation, which affects the spatial accuracy. The best result in this experiment is the accuracy of Section 2 (road without GNSS interference) 3D StDev 17 mm, followed by the built-up area Section 1 3D StDev 20 mm and the forested road Section 3 3D StDev 21 mm.

The deviations from the repeat pass show spatial deviations of about 15 mm, and surprisingly the largest deviations in this comparison are in Section 2. Thus, it can be estimated that more weight was added to GNSS measurements (during MMS measurement) in this section, which were undisturbed here, making the calculation less dependent on the GCPs. An interesting value in this section is the standard deviation of the heights for point clouds computed as an entire area, here it is below the 5 mm. These values again suggest an improvement in accuracy when the sections are not separated.

The results of this work show the greater accuracy of the Riegl VMX-2HA, despite the density of GCPs, compared to its predecessor, the RIEGL VMX-450. The measurements show that this system can be reliably deployed under diverse conditions ranging from urban areas to forested roads. Its simplicity, fast data acquisition and precision make it a suitable primary method for mapping large areas without complex preparation or a high number of control points. The collected data can also be efficiently supplemented with outputs from handheld scanners, drone-based aerial surveys or conventional geodetic measurements. This approach helps to optimise the costs of spatial data collection while ensuring high quality of the final model.

ACKNOWLEDGEMENTS

This work was supported by the Grant Agency of the Czech Technical University in Prague, grants SGS25/046/OHK1/1T/11.

REFERENCES

[1] Chiang, K. W., Tsai, G. J., Zeng, J. C. 2021. Mobile mapping technologies. [online]. In: Urban Informatics. The Urban Book Series. p. 439–465. ISBN 978-981-15-8982-9. https://doi.org/10.1007/978-981-15-8983-6_25

[2] Lapucha, D. 1990. Precise GPS/INS “Positioning for Highway Inventory System”, Report No. 20038. Master’s thesis. [online]. Department of Geomatics Engineering, University of Calgary, Calgary (AB). http://hdl.handle.net/1880/18024

[3] El-Sheimy, N. 1996. The development of VISAT: a mobile survey system for GIS applications. Ph.D. thesis. [online]. University of Calgary, Calgary (AB), Canada. https://prism.ucalgary.ca

[4] Puente, I., González-Jorge, H., Martínez-Sánchez, J., Arias, P. 2013. Review of mobile mapping and surveying technologies. [online]. Measurement. vol. 46, no. 7, p. 2127–2145. ISSN 0263-2241. https://doi.org/10.1016/j.measurement.2013.03.006

[5] Kersting, A. P., Friess, P. 2016. Post-mission quality assurance procedure for survey-grade mobile mapping systems. [online]. The International Archives of the Photogrammetry, Remote Sensing and Spatial Information Sciences. 2016, vol. XLI-B1, p. 647–652. ISSN 2194-9034. Available at: https://doi.org/10.5194/isprs-archives-XLI-B1-647-2016

[6] Kaczmarek, A., Rohm, W.; Klingbeil, L., Tchórzewski, J. 2022. Experimental 2D extended Kalman filter sensor fusion for low-cost GNSS/IMU/odometers precise positioning system. [online]. Measurement. vol. 193, art. 110963. ISSN 0263-2241. https://doi.org/10.1016/j.measurement.2022.110963

[7] Blaser, S., Meyer, J., Nebiker, S., Fricker, L., Weber, D. 2020. Centimetre-accuracy in forests and urban canyons – combining a high-performance image-based mobile mapping backpack with new georeferencing methods. [online]. ISPRS Annals of the Photogrammetry, Remote Sensing and Spatial Information Sciences. vol. V-1-2020, p. 333–341. ISSN 2194-9050. https://doi.org/10.5194/isprs-annals-V-1-2020-333-2020

[8] Cavegn, S., Blaser, S., Nebiker, S., Haala, N. 2018. Robust and accurate image-based georeferencing exploiting relative orientation constraints. [online]. ISPRS Annals of the Photogrammetry, Remote Sensing and Spatial Information Sciences. vol. IV-2, p. 57–64. ISSN 2194-9050. https://doi.org/10.5194/isprs-annals-IV-2-57-2018

[9] Li, S., Li, G.; Wang, L., Qin, Y. 2020. SLAM integrated mobile mapping system in complex urban environments. [online]. ISPRS Journal of Photogrammetry and Remote Sensing. vol. 166, p. 316–332. ISSN 0924-2716. https://doi.org/10.1016/j.isprsjprs.2020.05.012

[10] Xu, X., Zhang, L., Yang, J., Cao, C., Wang, W. et al. 2022. A review of multi-sensor fusion SLAM systems based on 3D LiDAR. [online]. Remote Sensing. vol. 14, no. 12, art. 2835. ISSN 2072-4292. https://doi.org/10.3390/rs14122835

[11] Gharineiat, Z., Tarsha Kurdi, F., Henny, K., Gray, H., Jamieson, A. et al. 2024. Assessment of NavVis VLX and BLK2GO SLAM scanner accuracy for outdoor and indoor surveying tasks. [online]. Remote Sensing. vol. 16, no. 17, art. 3256. ISSN 2072-4292. https://doi.org/10.3390/rs16173256

[12] Vynikal, J., Zahradník, D. 2023. Floor plan creation using a low-cost 360° camera. [online]. The Photogrammetric Record., vol. 38, no. 184, p. 520–536. ISSN 0031-868X. https://doi.org/10.1111/phor.12463

[13] Oniga, V. E., Breaban, A. I., Alexe, E. I., Văsii, C. 2021. Indoor mapping of a complex cultural heritage scene using TLS and HMLS laser scanning. [online]. The International Archives of the Photogrammetry, Remote Sensing and Spatial Information Sciences., vol. XLIII-B2-2021, p. 605–612. ISSN 2194-9034. https://doi.org/10.5194/isprs-archives-XLIII-B2-2021-605-2021

[14] Chudá, J., Výbošťok, J., Tomaštík, J., Chudý, F., Tunák, D. et al. 2024. Prompt mapping tree positions with handheld mobile scanners based on SLAM technology. [online]. Land., vol. 13, no. 1, art. 93. ISSN 2073-445X. https://doi.org/10.3390/land13010093

[15] Pavelka, K., Matoušková, E., Pavelka, K. 2023. Remarks on geomatics measurement methods focused on forestry inventory. [online]. Sensors., vol. 23, no. 17, art. 7376. ISSN 1424-8220. https://doi.org/10.3390/s23177376

[16] Pavelka, K., Pavelka, K., Matoušková, E., Smolík, T. 2021. Earthen Jewish Architecture of Southern Morocco: Documentation of Unfired Brick Synagogues and Mellahs in the Drâa-Tafilalet Region, Applied Sciences., 11(4), 1-25. ISSN 2076-3417. https://doi.org/10.3390/app11041712

[17] Trybała, P., Kasza, D., Wajs, J., Remondino, F. 2023. Comparison of low-cost handheld LiDAR-based SLAM systems for mapping underground tunnels. [online]. The International Archives of the Photogrammetry, Remote Sensing and Spatial Information Sciences., vol. XLVIII-1/W1-2023, p. 517–524. ISSN 2194-9034. https://doi.org/10.5194/isprs-archives-XLVIII-1-W1-2023-517-2023

[18] Di Stefano, F., Chiappini, S., Gorreja, A., Balestra, M., Pierdicca, R. 2021. Mobile 3D scan LiDAR: a literature review. [online]. Geomatics, Natural Hazards and Risk., vol. 12, no. 1, p. 2387–2429. ISSN 1947-5705. https://doi.org/10.1080/19475705.2021.1964617

[19] Yang, B., Dong, Z., Liu, Y., Liang, F., Wang, Y. 2017. Computing multiple aggregation levels and contextual features for road facilities recognition using mobile laser scanning data. [online]. ISPRS Journal of Photogrammetry and Remote Sensing., vol. 126, p. 180–194. ISSN 0924-2716. https://doi.org/10.1016/j.isprsjprs.2017.02.014

[20] Wang, H., Luo, H., Wen, C., Cheng, J., Li, P. et al. 2015. Road boundaries detection based on local normal saliency from mobile laser scanning data. [online]. IEEE Geoscience and Remote Sensing Letters., vol. 12, no. 10, p. 2085–2089. ISSN 1545-598X. https://doi.org/10.1109/LGRS.2015.2449074

[21] Balado, J., Díaz-Vilariño, L., Arias, P., González-Jorge, H. 2018. Automatic classification of urban ground elements from mobile laser scanning data. [online]. Automation in Construction, vol. 86, p. 226–239. ISSN 0926-5805. https://doi.org/10.1016/j.autcon.2017.09.004

[22] Guney, E., Bayilmis, C., Çakan, B. 2022. An implementation of real-time traffic signs and road objects detection based on mobile GPU platforms. [online]. IEEE Access, vol. 10, p. 86191–86203. ISSN 2169-3536. https://doi.org/10.1109/ACCESS.2022.3198954

[23] Ma, Y., Zheng, Y., Easa, S., Wong, Y. D., El-Basyouny, K. 2022. Virtual analysis of urban road visibility using mobile laser scanning data and deep learning. [online]. Automation in Construction, Vol.133, Elsevier, ISSN: 0926-5805, https://doi.org/10.1016/j.autcon.2021.104014

[24] Ma, L., Li, Y., Li, J., Junior, J. M., Goncalves, W. N. et al. 2022. BoundaryNet: extraction and completion of road boundaries with deep learning using mobile laser scanning point clouds and satellite imagery. [online]. IEEE Transactions on Intelligent Transportation Systems., vol. 23, no. 6, p. 5638–5654. ISSN 1524-9050. https://doi.org/10.1109/TITS.2021.3055366

[25] Yao, L., Qin, C., Chen, Q., Wu, H. 2021. Automatic Road marking extraction and vectorization from vehicle-borne laser scanning data. [online]. Remote Sensing., vol. 13, no. 13, art. 2612. ISSN 2072-4292. https://doi.org/10.3390/rs13132612

[26] Li, Q., Yuan, P., Lin, Y., Tong, Y., Liu, X. 2021. Pointwise classification of mobile laser scanning point clouds of urban scenes using raw data. [online]. Journal of Applied Remote Sensing, vol. 15, no. 2, art. 024523. ISSN 1931-3195. https://doi.org/10.1117/1.JRS.15.024523

[27] Reiterer, A., Wäschle, K., Störk, D., Leydecker, A., Gitzen, N. 2020. Fully automated segmentation of 2D and 3D mobile mapping data for reliable modeling of surface structures using deep learning. [online]. Remote Sensing., vol. 12, no. 16, art. 2530. ISSN 2072-4292. https://doi.org/10.3390/rs12162530

[28] Vierhub-Lorenz, V., Kellner, M., Zipfel, O., Reiterer, A. 2022. A study on the effect of multispectral LiDAR data on automated semantic segmentation of 3D point clouds. [online]. Remote Sensing, vol. 14, no. 24, art. 6349. ISSN 2072-4292. https://doi.org/10.3390/rs14246349

[29] Kalvoda, P., Nosek, J., Kuruc, M., Volarik, T., Kalvodova, P. 2020. Accuracy evaluation and comparison of mobile laser scanning and mobile photogrammetry data. [online]. IOP Conference Series: Earth and Environmental Science., vol. 609, no. 1, art. 012091. ISSN 1755-1307. https://doi.org/10.1088/1755-1315/609/1/012091

[30] Puente, I., González-Jorge, H., Riveiro, B., Arias, P. 2013. Accuracy verification of the Lynx mobile mapper system. [online]. Optics & Laser Technology., vol. 45, p. 578–586. ISSN 0030-3992. https://doi.org/10.1016/j.optlastec.2012.05.029

[31] Grešla, O., Jašek, P. 2023. Measuring Road structures using a mobile mapping system. [online]. The International Archives of the Photogrammetry, Remote Sensing and Spatial Information Sciences., vol. XLVIII-5/W2-2023, p. 43–48. ISSN 2194-9034. https://doi.org/10.5194/isprs-archives-XLVIII-5-W2-2023-43-2023

[32] Treccani, D., Adami, A., Brunelli, V., Fregonese, L. 2024. Mobile mapping system for historic built heritage and GIS integration: a challenging case study. [online]. Applied Geomatics., vol. 16, no. 1, p. 293–312. ISSN 1866-9298. https://doi.org/10.1007/s12518-024-00555-w

[33] Běloch, L., Pavelka, K. 2024. Optimizing mobile laser scanning accuracy for urban applications: a comparison by strategy of different measured ground points. [online]. Applied Sciences, vol. 14, no. 8, art. 3387. ISSN 2076-3417. https://doi.org/10.3390/app14083387

[34] Kalvoda, P., Nosek, J., Kalvodova, P. 2021. Influence of control points configuration on the mobile laser scanning accuracy. [online]. IOP Conference Series: Earth and Environmental Science., vol. 906, no. 1, art. 012091. ISSN 1755-1307. https://doi.org/10.1088/1755-1315/906/1/012091

[35] Grešla, O. 2024. Experimental determination of the influence of choosing tie points for mobile mapping in poor conditions. [online]. Geodesy in construction and industry. Prague: Czech Association of Surveyors and Cartographers (Geodézie ve stavebnictví a průmyslu. Praha: Český svaz geodetů a kartografů), p. 70–80. ISBN 978-80-02-03049-2. http://csgk.fce.vutbr.cz/Oakce/A139/prezentace/11_GSP24_Gresla.pdf [accessed 2025-02-15].

[36] Mattheuwsen, L., Bassier, M., Vergauwen, M. 2019. Theoretical accuracy prediction and validation of low-end and high-end mobile mapping system in urban, residential and rural areas. [online]. The International Archives of the Photogrammetry, Remote Sensing and Spatial Information Sciences., vol. XLII-2/W18, p. 121–128. ISSN 2194-9034. https://doi.org/10.5194/isprs-archives-XLII-2-W18-121-2019